

The University of Nottingham

UNITED KINGDOM · CHINA · MALAYSIA

SCHOOL OF CHEMICAL AND ENVIRONMENTAL ENGINEERING

AN OPTIMISED ADVANCED ASH FUSION TEST FOR POWER GENERATORS

Patrick James DALEY

Supervised by Edward LESTER

Thesis submitted to the University of Nottingham for the degree of

Doctor of Engineering

October 2018

"I have not failed. I've just found 10,000 ways that won't work."

- Thomas Edison

Abstract

The Ash Fusion Test (AFT) is considered to be the most popular method of characterising the melt characteristics of solid fuel ash. This thesis shows how pellet preparation can make significant improvements to repeatability and how the optimised advanced ash fusion test (OAAFT) curve can be used to indicate melting properties. A fully automated analysis technique and novel pelleting method have been developed for the advanced ash fusion test (AAFT) and for the first time it has been directly shown that cones and the hand pressed pellets do not have good repeatability and delay the response of the initial deformation temperature (IDT). The optimum shape parameter to track during the AAFT was identified and software was developed to plot this new OAAFT. The second half of this thesis documents an array of investigations to validate and understand the significance of the OAAFT curve. Varying the levels of SiO_2, Al_2O_3, CaO, Fe_2O_3, and MgO within pseudo pellets revealed the impact each component on the curve and aligned well with results from literature. Comparisons of the OAAFT curves with FactSage prediction identified the coals to have excellent correlation whereas the biomass requires further work. Preliminary work on grouping the OAAFT suggested that it can be used to identify links to individual species in samples. The key trends greater levels of SiO_2 and lower levels of CaO and SO_3 result in an expansion phase. An industrial investigation highlighted the potential for the OAAFT to be used in alternative applications. Fuel feed stocks for 2 Colombian stoker furnaces were imaged during combustion to identify swelling, up to 130%, in some of the coals.

Acknowledgments

Firstly, I must thank my sponsors, the Engineering and Physical Sciences Research Council (EPSRC) through the CDT [grant number EP/L016362/1], the Biomass and Fossil Fuel Research Alliance (BF2RA) and the International Young Scientist Research Fellowship, the Natural Science Foundation China (NSFC) [grant number 51650110508] for their sponsorship without whom this would not be possible.

Thank you to my team of co-supervisors over the years in order of appearance; Dr. Richard Smith, Dr. Tom Huddle, Dr. Rachael Hall, Dr. Ewa Marek and Dr. Chengheng Pang for the insight and advice you each have given me. A special thanks to Chengheng whose thesis spawned my research and who has given continual advice and assistance from the Ningbo campus in China.

Thanks to all the people who have aided in data collection and passed on their expertise. A special mention must go to Dr. Jackie Dean, and Dr. Thomas Knott for their assistance and accommodations in my XRF visits. To Joe Meehan, my go-to lab tech to get things done when I was in a bind.

A special thanks to my supervisor Professor Ed Lester, he inspired me to peruse this endeavour and has supported me every step of the way. Although he may not be happy that I traded playing Basketball for American football.

To Eze Benson, you the real MVP.

A huge thanks to Dr. Orla Williams who taught me the ins and outs of writing a paper and improved my writing style, I hope I haven't let you down.

To Dr. Mark Flower, who has his finger on the pulse of coal and biomass power generation, thank you for your invaluable insight into the applications of AFT.

Thank you to my friends on the EngD course, specifically Rob, David, Liam, and Charlie, many a coffee/beer and support during tough times.

To all my teammates on the Tamworth Phoenix, University of Nottingham basketball and American football, and the University of Nottingham scholarship program for support, patience and have made my experience at Nottingham something I will cherish forever.

A quick thank you to my girlfriend Francesca who, for some reason, offered to read through the entire thing a look for grammatical errors. I know we have only been dating for a short time, but you make me so happy and I'm excited by the prospect of our future together, and thanks for introducing me to monopoly deal.

Finally, thank you to my parents, who are the ever-present pillars of strength and have supported me through my 9 years at Nottingham. Even though you told me on the first day that I better not be here that long, apologies. Hopefully it was worth it.

Publications

Patrick Daley; Orla Williams; Cheng Heng Pang; Tao Wu; Ed Lester, *The impact of ash pellet characteristics and pellet processing parameters on ash fusion behaviour*, Research paper, Fuel. Accepted

Patrick J. Daley; Orla Wiliams; Ed Lester; Markus Reinmoller, *Assessing the Link Between the Optimised Advanced Ash Fusion Test Curve and FactSage Modelling for A Range of Coals and pseudo pellets,* Fuel. Pending submission and review

Patrick Daley; Eze Benson; Orla Williams; Cheng Heng Pang; Tao Wu; Ed Lester, *Automated Image Processing and Shape Analysis and Clustering*, Fuel Processing. Pending submission and review

Orla Williams; Patrick Daley; Joe Perkins; Mark Flower; Juan Manuel Barraza; María Patricia Trujillo-Uribe; Cheng Heng Pang; Edward Lester, Automated Ash Fusion Analysis of Stoker Furnace Coals, Fuel. Pending submission and review

Conference Proceedings

Daley P., Huddle T., Lester E., *Image Analysis Based Ash Fusion Testing*, International Conference on Coal Science and Technology 2015, Melbourne, Australia.

Daley P., Huddle T., Lester E., Image Analysis Based Ash Fusion Testing, 2nd International Congress and Expo on Biofuels & Bioenergy 2016, Sao Paulo, Brazil.

Daley P. J., C.H. Pang, T. Wu., Lester E., *Characterizing the AAFT Curve*, Coal geochemistry and mineralogy, coal structure and ash chemistry, International Conference on Coal Science and Technology 2017, Beijing, China.

P. J. Daley, E. Marek, C.H. Pang., T. Wu., E. Lester, *Optimising the AAFT Curve*, Coal geochemistry and mineralogy, coal structure and ash chemistry, International Conference on Coal Science and Technology 2017, Beijing, China.

Patrick J. Daley, Ed Lester, Markus Reinmoller*, Assessing the Link Between The Advanced Ash Fusion Test Curve And FactSage Modelling For A Range Of Coals,* European Conference on Fuel and Energy Research and its Applications 2018, Cardiff, UK

Table of Contents

Abstract ii

Acknowledgments iii

Publications v

Conference Proceedings v

List of Figures xi

List of Tables xiv

Nomenclature xvi

Chapter 1: Introduction 1

1.1 The Origins of Public Power Generation 1

1.2 Current Power Generation 2

1.3 The Ash Fusion Test 3

1.4 Automating the Ash Fusion Test 4

1.5 Thesis Layout 5

Chapter 2 : Literature Review 7

2.1 Executive Summary 7

2.1.1 Ash Fusion Test 7

2.1.2 Slagging and Fouling Prediction 8

2.1.3 The Key Deliverable for The Research 9

2.1.4 Main Goals for Research 9

2.2 A Brief Overview of Slagging and Fouling 11

2.2.1 What Is Slagging and Fouling 11

2.2.2 Where Does It Occur? 12

2.2.3 The Inorganic Path To Deposition 15

2.2.4 Ash Deposition 23

2.2.5 Characteristics Responsible for Slagging And Fouling 30

2.2.6 Cost to Industry of Fouling and Slagging 31

2.2.7 Methods of Mitigating Fouling And Slagging 32

2.3 Ash Fusibility 34

2.3.1 The Standard Ash Fusion Test 35

2.3.2 Predictive Tools and Modelling of Ash Fusion Temperatures 38

2.3.3 Alternative Methodologies for Ash Fusion Testing 41

2.3.4 Automating the ash fusion test 47

2.3.5 Current Market Review 48

2.3.6 Quantitative Understanding of Ash Fusibility 49

2.4 Conclusions 53
Chapter 3 : The Impact of Ash Pellet Characteristics and Pellet Processing Parameters on Ash Fusion Behaviour 55
3.1 Introduction 55
3.2 Materials and Methods 58
3.2.1 Milling and Ashing 58
3.2.2 Pelleting Method Optimisation Study 60
3.2.3 Advanced Ash Fusion Test (AAFT) 62
3.2.4 Thermogravimetric analysis (TGA) 64
3.2.5 Pelleting Mould Type Selection Criteria 65
3.3 Results and discussions 66
3.3.1 Impact of pellet type on the AAFT 66
3.3.2 Impact of material preparation and furnace heating rate for the 5 mm MPPs 73
3.3.3 Cumulative Influence of Pelleting, Preparation and Ashing on 5 Different Fuels 75
3.3.4 The optimised advanced ash fusion test (OAAFT) 80
3.4 Conclusions 81
Chapter 4 : Automated Image Processing and Shape Analysis and Clustering 83
4.1 Introduction 83
4.1.1 Automated Image Analysis 83
4.1.2 Shape Analysis and Clustering 85
4.2 Materials And Methods 87
4.2.1 Thresholding and Edge-Detection Techniques 87
4.2.2 Shapes and Clustering Analysis 88
4.3 Results and Discussions 91
4.3.1 Thresholding and edge detect analysis 91
4.3.2 Clustering the Profile Using Z-Score 100
4.3.3 Ash Fusion Temperature Definitions in Relation To The OAAFT Curve 114
4.3.4 Alternative data collection 115
4.4 Significance of Data 117
4.5 Conclusions 117
Chapter 5 The Impact of Individual Components on Pseudo Ash Pellet AFT Temperatures And OAAFT Curves 118
5.1 Introduction 118

5.2 Materials and Methods....120
5.2.1 Ash Database....120
5.2.2 Synthetic ash samples....120
5.2.3 Ash Fusion Temperatures and Test Curves....121
5.3 Results and Discussions....124
5.3.1 Pseudo Pellet Individual Element analysis....124
5.4 Significance of Data....136
5.5 Conclusions....136
5.6 Further work....137
Chapter 6 : Assessing the Link Between the Optimised Advanced Ash Fusion Test Curve and FactSage Modelling for A Range of Coals and Biomasses....139
6.1 Introduction....139
6.2 Materials and Methods....140
6.2.1 Petrographic Analysis....140
6.2.2 Fused Bead X-ray fluorescence (XRF)....141
6.2.3 FactSage Thermochemical calculations....141
6.2.4 Fuel Characterisation....142
6.3 Results and Discussions....147
6.3.1 FactSage comparison....147
6.3.2 OAAFT grouping....163
6.4 Relevance of Data....170
6.5 Conclusions....172
Chapter 7 : Industrial Case Study OAAFT of Stoker Furnace Coals....173
7.1 Introduction....173
7.2 Materials and Methods....174
7.2.1 Samples Used....174
7.2.2 TMA....175
7.2.3 Coal Combustion Imaging (CCI)....175
7.2.4 Ash Fusion Testing....176
7.3 Results and Discussion....176
7.3.1 Ash Fusion Test with TMA Analysis....176
7.3.2 Coal Combustion Imaging (CCI) with Thermomechanical analysis 182
7.4 Significance of Findings....185
7.5 Conclusions....186
Chapter 8 : Conclusions....187

8.1 Chapter 3 187
8.2 Chapter 4 187
8.3 Chapter 5 188
8.4 Chapter 6 188
8.5 Chapter 7 189
8.6 Future work 189
References cxci
Appendix i
Shape definitions i
Pseudo Pellet Literature Samples Database ii
Top 20 clustering function code v

List of Figures

Figure 2-1: Main locations of ash deposition in a tower boiler and conventional boiler respectively[21], [22].....13
Figure 2-2: Variations In Key Elements In Biomass Types [19], [24], [25].....18
Figure 2-3: Association of Ash Forming Elements Of Solid Fuels.....18
Figure 2-4: Standard characterisation of solid fuels and reference basis.....20
Figure 2-5: Variations in Ash Content For A Range Of Solid Fuel Categories...21
Figure 2-6: Comparison of Imported, UK And Brown Coals.....22
Figure 2-7: Comparison of Different Biomass Groups.....22
Figure 2-8. Typical slagging, fouling, and corrosion found at various locations in the steam generators, by compound [18].....23
Figure 2-9: Ash formation during the combustion of solid fuels [18], [19], [23].....24
Figure 2-10. Thermal Decomposition of Major Coal Minerals [53].....27
Figure 2-11. Phase Diagram of Changes in US Eastern Coal under Reducing Conditions [54].....28
Figure 2-12. The fate of mineral matter in coal during combustion [18].....29
Figure 2-13.Coal consumption by region, million tonnes of oil equivalent [67].....32
Figure 2-14. Characteristic profiles of key deformation events [34].....36
Figure 2-15: Standard AFT Cones Showing Cracks and Flaws.....37
Figure 2-16. The ACIRL Test [79].....41
Figure 2-17. Diagramic representation of the ACRIL test [78].....43
Figure 2-18. The HRL test [79].....44
Figure 2-19. The CSIRO test [79].....45
Figure 2-20: Fingerprint of the ash morphology change with characterised sections/phases.....48
Figure 2-21: Changes of crystal and amorphous minerals in typical samples .51
Figure 2-22: Changes of amorphous substances in low and high ash fusion temperatures ashes at different temperatures [110].....51
Figure 3-1: Profiles for the MPPs tested during the pelleting method optimisation study.....61
Figure 3-2: CAF furnace, images generated, and processed images.....63
Figure 3-3: Typical AAFT profile (250 µm sample, voidage investigation).....64
Figure 3-4: Plots demonstrating the error, morphology, and IDT trigger of each pelleting method; a) 5 mm MPP, b) 10 mm MPP, c) 12 mm cone, d) 18 mm cone, e) CHP, f) CHPD (n=3).....69
Figure 4-1: Ash Fusion Test Shape Guidelines for Coal (Cone) and Biomass (Cylinder).....86
Figure 4-2: Visual Representation of Z-score comparison at IDT.....90
Figure 4-3: Illustration of the clustering groups identified using z-score and clustering.....90
Figure 4-4: 30 cropped images from the CAF test furnace and temperatures at which they were taken.....92
Figure 4-5: Top 5 histogram clusters for image 13 demonstrating analysis functions.....94

Figure 4-6: A) Histogram of pixel counts for the 460 °C Image; B) Top 5 clustered pixel counts from the histogram 95
Figure 4-7: Raw Image, Manual Thresholding and the Top 3 Methods for Image5 96
Figure 4-8:A) Histogram of pixel counts for the 636 °C Image; B) Top 5 clustered pixel counts from the histogram 98
Figure 4-9:Raw Image, Manual Thresholding and the Top 3 Methods for Image 11 99
Figure 4-10: PaNG (H/Hi) curves for the collapsing (Olive cake) and expanding (Kellingley) curves 101
Figure 4-11: Grouping the clusters for the expanding curve SST analysis 101
Figure 4-12: Shrinking phase curve shape comparisons for Perimeter and Area 103
Figure 4-13: Grouping the clusters for the expanding curve IDT analysis 104
Figure 4-14: IDT phase comparisons for Eccentricity and Area 106
Figure 4-15: Grouping the clusters for the expanding curve slope analysis ..106
Figure 4-16: Expanding curve shape comparisons for Aspect ratio and Area109
Figure 4-17: Z-score clustering for shape parameters during the collapsing profile.....110
Figure 4-18: Finalised Expanding and Collapsing Curve Profiles 113
Figure 4-19: Illustration of the shrinkage and expansion calculations.....116
Figure 5-1: Individual component curves from the OAAFT. 125
Figure 5-2: Ash fusion temperatures for CaO at 0-40% 126
Figure 5-3: OAAFT curves for the CaO pseudo pellets ranging from 0 - 40% weight 128
Figure 5-4: Comparison of pseudo pellet deformation temperatures with existing literature.....129
Figure 5-5: OAAFT curves for the Fe2O¬3 pseudo pellets ranging from 0-40% weight 130
Figure 5-6: Comparison of pseudo pellet deformation temperatures with existing literature.....131
Figure 5-7: OAAFT curves for the pseudo pellets ranging from S/A of 0.5 to 4 133
Figure 5-8: Comparison of pseudo pellet deformation temperatures with existing literature.....134
Figure 5-9: OAAFT curves for the pseudo pellets ranging from MgO of 0 to 30 135
Figure 6-1: Illustration of Slag content analysis from FactSage (SlagA with 2 potentially immiscible phases) vs. temperature 142
Figure 6-2: Gedling OAAFT vs FactSage 147
Figure 6-3:Corton Wood OAAFT vs FactSage 147
Figure 6-4: Kellingley OAAFT vs FactSage 148
Figure 6-5: CWD OAAFT vs FactSage 148
Figure 6-6: Cresswell OAAFT vs FactSage 148
Figure 6-7: Jagua OAAFT vs FactSage 149
Figure 6-8: Littleton OAAFT vs FactSage.....149
Figure 6-9: Golden hope OAAFT vs FactSage 149

Figure 6-10: Taff Merth OAAFT vs FactSage 150
Figure 6-11: Tillman Stone OAAFT vs FactSage 150
Figure 6-12: Markham OAAFT vs FactSage.....150
Figure 6-13: Yanoice OAAFT vs FactSage.....151
Figure 6-14: Trentham OAAFT vs FactSage 151
Figure 6-15: Seaham OAAFT vs FactSage 151
Figure 6-16: Indonesian OAAFT vs FactSage.....152
Figure 6-17: Pittsburg No.7 OAAFT vs FactSage 152
Figure 6-18: USA Blue Creek OAAFT vs FactSage 152
Figure 6-19: La Loma OAAFT vs FactSage 153
Figure 6-20: Zondag OAAFT vs FactSage 153
Figure 6-21: Pond Fines OAAFT vs FactSage.....153
Figure 6-22: B139 OAAFT vs FactSage 156
Figure 6-23: MV Flevoborg OAAFT vs FactSage.....157
Figure 6-24: Sunflower OAAFT vs FactSage.....157
Figure 6-25: BKE Palm OAAFT vs FactSage 158
Figure 6-26: Bagasse OAAFT vs FactSage 158
Figure 6-27: B586 OAAFT vs FactSage 159
Figure 6-28: Jatrophe Seed OAAFT vs FactSage 159
Figure 6-29: Eucalyptus OAAFT vs FactSage 160
Figure 6-30: Olive Cake OAAFT vs FactSage 160
Figure 6-31: EC78 OAAFT vs FactSage 161
Figure 6-32: B117 OAAFT vs FactSage 161
Figure 6-33: Traditional Slagging and Fouling Indices 163
Figure 6-34: OAAFT Coal Samples with Sharp Expansion Curve Grouping 164
Figure 6-35: OAAFT Coal Samples with Gradual Transition into Expansion Phase 165
Figure 6-36: OAAFT Coal Samples with an Expansion of >1.5% 166
Figure 6-37: OAAFT Coal Samples with an Expansion of <1.5% 167
Figure 6-38:OAAFT Coal Samples with No Expansion Phase.....167
Figure 6-39:OAAFT Biomass Samples with No Expansion Phase 169
Figure 6-40: OAAFT Biomass Samples with An Expansion Phase.....169
Figure 7-1: A Typical Stoker Furnace To Illustrate Where The Fly Ash And The Furnace Bottom Ash Is Collected – Edited From [173].....175
Figure 7-2: Antioquia OAAFT Curve Plotted with The TMA Analysis 177
Figure 7-3: Blend OAAFT Curve Plotted with The TMA Analysis 177
Figure 7-4: La Cabaña FBA OAAFT Curve Plotted with The TMA Analysis 178
Figure 7-5: La Cabaña Fly ash OAAFT Curve Plotted with The TMA Analysis.178
Figure 7-6: Cundinamarca OAAFT Curve Plotted with The TMA Analysis.....179
Figure 7-7: Mayaguez FBA OAAFT Curve Plotted with The TMA Analysis 179
Figure 7-8: Mayaguez Fly OAAFT Curve Plotted with The TMA Analysis 180
Figure 7-9: Patia OAAFT Curve Plotted with The TMA Analysis 180
Figure 7-10: Valle OAAFT Curve Plotted with The TMA Analysis 181
Figure 7-11: Antioquia Comparison of CCI vs TMA 183
Figure 7-12: Blend Comparison of CCI vs TMA 183
Figure 7-13: Cundinamarca Comparison of CCI vs TMA.....184
Figure 7-14: Patia Comparison of CCI vs TMA 184

Figure 7-15: Valle Comparison of CCI vs TMA 184
Figure 0-1: Demonstration of Where the Foci Of An Ellipse Is.....i

List of Tables

Table 2-1: Factors affecting slagging and fouling in PF boilers 15
Table 2-2: Main Minerals Found in Coal.....17
Table 2-3: Slagging and Fouling Indices.....39
Table 2-4. Comparison of the alternative methodologies for ash fusion testing, modified from[79] 46
Table 2-5: Current market review of ash fusion test systems.....49
Table 3-1: Pelleting shape descriptions.....60
Table 3-2: Sample preparation of the high pressure milled and low pressure un-milled scenarios 62
Table 3-3: Selection criteria for evaluating pelleting process 65
Table 3-4: Selectivity matrix ranks for the pelleting methods in the categories on repeatability, error, morphology, and IDT trigger.....70
Table 3-5: Maximum acceptable differences between results [28].....71
Table 3-6: Selectivity matrix summary for the mould type analysis 73
Table 3-7: IDTs of the particle size, pressure and heating rate investigations on Kellingley coal 74
Table 3-8: Comparison of the change in thermal decomposition with increasing ashing temperature 76
Table 3-9: Comparing pellet preparation methods on IDT trigger.....77
Table 3-10: Comparing effects of ashing temperature on IDT trigger 79
Table 4-1: Raw Size Parameters Obtained from Matlab 89
Table 4-2: Size Parameter Combinations to Create Shape parameters.....89
Table 4-3:Difference in value of the manual threshold and the different threshold techniques for a range of shape parameters.....96
Table 4-4: The variables to be considered from the slope phase of the clustering 102
Table 4-5: The variables to be considered from the slope phase of the clustering 104
Table 4-6: The variables to be considered from the slope phase of the clustering 108
Table 4-7: The variables to be considered from the collapsing curve clustering 111
Table 4-8: Alternative data collection for the OAAFT for the Expanding and Collapsing curves 116
Table 5-1: major oxides in samples 1 - 20 of the pseudo pellets 122
Table 5-2: Line equations and R-squared values for the CaO investigations.127
Table 5-3: Line equations and R-squared values for the Fe_2O_3 investigations 130
Table 5-4: Line equations and R-squared values for the MgO investigations135
Table 6-1: Fused Bead XRF Data for the Coal and Biomass Database.....143

Table 6-2: Maceral Analysis and Vitrinite Reflectance for the Coal Database 145
Table 6-3: Coal Ash Fusion Temperatures and Slag %s at the Key Temperatures 154
Table 6-4: Biomass Ash Fusion Temperatures and Slag %s at the Key Temperatures 162
Table 6-5: Comparing the Averages for the Different OAAFT Curve Groupings 171
Table 7-1: Ash Fusion Temperatures of The Coal Samples 181
Table 7-2: Ash Fusion Temperatures of The Fly Ash And FBA.....182
Table 7-3: Comparing the extent of Swelling between TMA Height, CCI Height and CCI Area 185
Table 0-1: Major oxide compositions of a range of coals and their ash fusion temperatures.....ii

Nomenclature

AAFT	-	Advanced Ash Fusion Test
ACIRL	-	Australian Coal Industry Research Laboratories
ACIRL-IAFT	-	Australian Coal Industry Research Laboratories – Improved Ash Fusion Test
Ach	-	Area of the convex hull
AFT	-	Ash Fusion Test
Ai	-	Initial Area
AI	-	Artificial Intelligent
ANMS	-	Average number of mineral species
Ap	-	Area of the particle
ASTM	-	American Society for Testing and Materials
AXmax	-	Length of the major axis of the ellipse
AXmin	-	Length of the minor axis of the ellipse
AR	-	Aspect Ratio
AXR	-	Axial Ratio
A/ABB	-	Square deviation
B/A	-	Base – acid
BS	-	British Standards
BF2RA	-	Biomass and Fossil Fuel Research Alliance
√C	-	Alt Circularity
CAF	-	Coal Ash Fusibility
CCI	-	Coal Combustion Imaging
Cen	-	Centroid
CHP	-	Carbolite Hand Press
CHPD	-	Carbolite Hand Press with Dextrin
CSIRO	-	Commonwealth Scientific and Industrial Research Organisation

CVX_F	-	Convextity feret
De	-	Diameter of equivalent area circle (Heywood diameter)
DT	-	Deformation Temperature
ECC	-	Eccentricity
FBA	-	Furnace bottom ash
Fmax	-	Maximum Feret Diameter
FT	-	Flow temperature
H	-	Height of the bounding box
HOG	-	Histogram Oriented Gradients
HT	-	Hemisphere Temperature
HRL	-	Hughes Research Laboratories
IDT	-	Initial Deformation Temperature
IUTS	-	Instron Universal Testing System
LOI	-	Loss on ignition
MPPs	-	Machine Pressed Pellets
OAAFT	-	Optimised Advanced Ash Fusion Test
PAnG	-	Picture Analysis and Graphing
PF	-	Pulverised Fuel
Pp	-	Perimeter of the particle
RDN	-	Roundness
RECT	-	Rectangularity
S/A	-	Silica-Alumina
SFP	-	Slagging and fouling propensity
SIFT	-	Scale-Invariant Feature Transform
SLD	-	Solidity
SST	-	Shrinkage Starting Temperature
ST	-	Softening Temperature
SURF	-	Speeded-Up Robust Features

SVM	-	Support Vector Machine
TGA	-	Thermo-gravimetric Analysis
TMA	-	Thermo-mechanical analysis
W	-	Width of the bounding box
XRD	-	X-Ray Diffraction
XRF	-	X-Ray Fluorescence
1/C	-	1/Circularity
ΔH		Change in height
(Av(SD (H/H_i)))		Average standard deviation of height / initial height
(∑ΔH)		Sum of change in height

Chapter 1: Introduction

1.1 The Origins of Public Power Generation

The very first public power station ever to be in operation was actually a hydroelectric power plant, which powered the street lights of Godalming. A simple water mill system attached via pulleys to a generator, it came into use as a public utility for lighting streets, driven by economic factors. The cost of traditional gas lit lamps could be undercut by the use of electricity by means of the HEP [1], [2]. The water source, however, could not sustain the required consistency of output for the lights, and it was swiftly replaced by a portable steam engine. In 1882, shortly after the Godalming HEP plant that Thomas Edison opened the world's first steam powered electricity generating station in London. Later that year he would go 1 step further and open the world's first commercial power station in New York. [2] These systems required the use of boilers to generate steam which then turn a turbine and produce electricity. A boiler can essentially be described as a box that uses heat, usually in the form of a burning fuel to raise water to steam. Over the past 2 centuries this concept has taken many forms. It has been modified to respond to a range of obstacles, whether there has been a need for improvements in safety, steam capacity or general efficiency. The journey to the industrial boiler started as a kettle type boiler, heating a drum of water using an external fire grate, and eventually maturing into the universal pressure and supercritical boilers we use in our power stations today. These are far more sophisticated, with tubed walls, using pulverised fuels which are internally fired and have further tubes being heated

in the flow of the high temperature flue gas. Those early stages of the power industry and the development of the boiler were powered almost exclusively by coal. It was accessible, hugely abundant and hence cheap, solid and easy to handle, and has heating characteristics suitable for boiler combustion, all these factors made it the easy choice as the fuel for the industrial revolution.[3]–[5]

1.2 Current Power Generation

These universal pressure and supercritical power stations produce the electricity for most of the world, and even though there is a move towards renewables there will be a dependency on conventional power stations for many decades to come. There are plenty of problems to overcome when dealing with these industrial scale boilers, from dealing with the emissions for the wide range of different composition fuels that you wish to put through, to the pushing the efficiency of that fuel to optimal levels. With increased restrictions on emissions and the narrow margins between operating costs and electricity prices, ensuring that boiler efficiency is as high as possible for as long as possible is vitally important for power generators. Factors affecting efficiency at an operational level include burning the fuel (boiler conditions) and transferring the heat to the water for steam, and small improvements in efficiency can result in large scale savings for operators.

With the emergence and general acceptance of global warming, momentum for renewable energy has been continually growing. Since the UK government implemented The Climate Change Act 2008 and the Carbon Budget Framework that dictates a gradual reduction in net emissions for power

generators over a 20-year period, [6] there is a strong governmental incentive to promote a switch to more renewable options. The decreasing stores of fossil fuels together with growing concerns for the environment has meant that the use of biomass has received global recognition for its clean renewable potential [7], [8]. Biomass can be burned to produce heat and power without a net contribution to CO_2 emissions, which has been termed as 'carbon neutral' [7], [9]. This has led to biomass being considered as 1 of the most important technologies to combat CO_2 emissions [9]. This is most relevant to the European power sector whereby legislation imparts penalties and provides incentives for reductions in GHGs [10]. It is clear that both coal and biomass still have a large part to play in the global energy mix and will continue to do so in the foreseeable future.

1.3 The Ash Fusion Test

Coal and biomass leave behind roughly 1 – 40% of their components after combustion, known as ash or the inorganic components. This ash melts at boiler temperatures, sticks to heat transfer surfaces and reduces efficiency of heat transferred to the water/steam and availability due to unplanned outages; this process is known as slagging and fouling. It is a major problem for large combustion power stations and leads to substantial losses for the operator. Power stations manage this through fuel selection, boiler design, boiler operating conditions and maintenance during outages. 1 of the ways that slagging and fouling is mitigated is using the ash fusion or fusibility test. The test was invented around the 1890s in order to attempt to predict clinker (large

lumps of coal ash) forming characteristics in lump coal ash [11]. In today's more sophisticated boilers, the test is used as a fuel selection technique with a range of other processes, or as a fault-finding method for understanding unexpected slagging phenomena in the boiler. 4 temperatures are presented by the test, these are used to assess the melting characteristics of the coal or biomass ash in question. The test is carried out by an operator observing pellets of ash either through a window or on a monitor via a camera, each temperature is then noted down based on shapes given by the regional standards. [12]–[15]. Though there are flaws in this the current test, it is seen as the principle method for slagging prediction of solid fuel ash.

1.4 Automating the Ash Fusion Test

Automation of the original processes has clear benefits with respect to precision and standardisation, purely based on the removal of the operator. This is 1 of the key problems identified with the existing ash fusion test, the reliance on visual observation rather than an objective physical measurement. This has been illustrated by discrepancies of up to 400^{o}C between different labs [9], [16]. This can be solved by the use of a camera in the furnace, the images are then analysed in a program based on the trigger points of deformation set out in the regional standards. Each run would then inherently identify the identical point each time. However, Pang et al have taken this approach 1 step further and attempted to characterise the complete behaviour of ashes with a fusion profile based on the height/initial height of the ash pellet sample. Key event 'regions' can easily be identified in the profile and are used to identify

ash characteristics as opposed to individual temperatures [9]. This new form of test shows the most promise in terms of potential to adapt the existing ash fusion test method in a minor way to appeal to industry for ease of applicability, whilst providing more incisive and complete analysis in the identification of ash characteristics.

This thesis aims to develop the AAFT into a robust methodology for power generators to use. Furthermore, the current ash fusion test is scrutinised and the potential improvements around automation are investigated. The key step in this development is establishing the links between coal and biomass mineral components with the behaviour in the AAFT. The final section attempts to demonstrate industrial applications of the AAFT to create a large database of coals and biomasses. The hope is that these profiles will go on to provide a reference for the future tests and link similar curves to behaviours in the boiler.

1.5 Thesis Layout

The thesis is split into 2 sections. The first, documents the development of the OAAFT process. This includes a review of pelleting methods to identify the most repeatable and reliable option, followed by optimising the image processing software to provide reliable output data. The second part of the thesis is a validation of this OAAFT method and a comparison with existing research. This section includes investigations into pseudo coal ash pellet behaviour, a large coal and biomass database study with FactSage comparison and an industrial investigation into the use of the OAAFT for ash, and potential further use for TMA of coal in a stoker furnace.

Chapter 2 : Literature Review

2.1 Executive Summary

2.1.1 Ash Fusion Test

Current pulverised fuel boilers used in industry are a product of a long history of exclusive coal use. In pulverised fuel boilers the primary culprit for reduced efficiency of operation is slagging and fouling. Since the implementation of carbon budgets and the renewables boom, the use of biomass in PF boilers has significantly increased to reduce carbon emissions. Consequently, due to the increased propensity of biomass to cause slagging and fouling, these issues have come into prominence. The existing tool that is used by industry to predict the onset of fouling and slagging, the ash fusion test, has 2 well documented short comings that lead to inconsistencies:

1. Reliance on operator to identify key temperatures
2. Inability of the test, and more accurately the IDT, to represent the onset of fouling and slagging

The adoption of automation using image analysis, in the standard ash fusion test, has removed the first of the 2 short comings. Whereas the attempts at addressing the second of the 2 issues have presented potential answers through the use of shrinking analysis or a more comprehensive analysis as shown by Pang et al., however, further research is required in these areas. There is a clear potential for the development or adoption of these ideas to produce a test that can more accurately and easily assess the slagging and fouling propensity of ash.

2.1.2 Slagging and Fouling Prediction

The heterogeneous nature of solid fuels such as coals and biomasses mean that correlations can be made with respect to mineral or elemental ratios and eutectics. However, a comprehensive tool relies on a huge amount of empirical data of a wide range of feed stocks. There are tools that are attempting to do such work with some success such as, FactSage modelling which uses a 6-mineral thermodynamic database. This predictive method has become a very popular and is continually being improved with increased experimental data. An area over-looked however, is the physical morphology changes during the AFT. There have been a range of investigations into the quantitative mineralogical phase changes during the AFT to aid understanding. Yet, there has been no attempt to link the morphological changes to slagging and fouling by analysing the entire duration of the deformation apart from 1 piece of investigative work. [9] It can be speculated that this has not been attempted due to the inconsistencies and reliability issues experienced with the existing AFT. Therefore, some clear objectives can be drawn from the research to enable slagging and fouling prediction:

1. Create a robust process that is repeatable and reliable
2. Create a portfolio of solid fuels to compare and contrast curve shapes
3. Understand the link between minerology and morphology of ash deformation
4. Link the morphology to industrial slagging and fouling performance

Objective 1 will be the starting point of the investigation. Objective 2 can be feasibly achieved and with aid of industry, it can be used to achieve Objective 4. Objective 3 can be carried out on a few coal sources but as has be shown in previous research analysing the ash quantitatively is time consuming and when the sample size is limited by time the conclusions that can be drawn aren't representative. Therefore, links to the existing empirical samples can be simply achieved and linked to morphology if the sample can be obtained.

2.1.3 The Key Deliverable for The Research

The key deliverable for the project is to create an objective, reliable and repeatable AFT to aid energy generators in the process of fuel selection with respect to slagging and fouling.

2.1.4 Main Goals for Research

The main goals of research can be broken down into 4:

Goal 1 (G1): Create a more repeatable ashing and pelleting process.

Goal 2(G2): Developing software to analysis current AFT.

Goal 3 (G3): Develop alternative test to provide more data than conventional test.

Goal 4 (G4): Find a link between the physical and chemical properties of the ash and slagging and fouling.

The knowledge gaps in the research are summarised as follows:

- Unreliable test repeatability **(G1 & G2)**
    - Improve test repeatability
        - Revise pelleting process
        - Revise ashing process
- Inherently subjective analysis **(G2)**
    - Remove all subjectivity during measurement
- Lack of clarity for test analysis parameters **(G3)**

    - Measure pellet behaviour to provide a fingerprint specific to each fuel type (coal, biomass and blends)
- Lack of understanding between the behaviour of the fingerprint and quantitative and industrial slagging and fouling data **(G4)**
    - Obtain quantitative analysis and links to industrial data.
- Multiple tests include subjective problems **(G3)**
    - Incorporate these test in same analysis
        - Such as quantifying viscosity changes
- No automated process used at large scale **(G3 & G4)**
    - Provide a simple interface using the gathered information into a slagging and fouling predictor
- No representative in-situ deposition analysis **(G3 & G4)**
    - Design a simple method to assess ash deposition mechanism at lab scale

In the work by Pang [9], 4 different temperature regions appear to exist for the ash characteristic profiles; stationary, shrinking, expanding and bubbling. Each region represents a melting/fusion event that is occurring within the sample. The extension of this research with the intention of linking these temperature zones, or another characteristic, to behaviour in the furnace could provide a major step forward in understanding. Such a test would facilitate the production of meaningful data to enable informed decisions around fuel procurement and blending strategies for generators in the UK.

2.2 A Brief Overview of Slagging and Fouling

2.2.1 What Is Slagging and Fouling

The fireside deposition as a result combustion of pulverised fuels (PFs) and the volatilisation and melting of the inorganic matter. Among the forms of deposits in PF boilers, the 2 main forms are called slagging and fouling. Corrosion can be closely linked to these processes as a result of the deposition. [17], [18]

2.2.1.1 Slagging Deposit Types

Deposits in the slagging areas typically consist of an inner powdery layer covered by molten or partly molten ash layer. Wall deposits are usually composed of silicate, iron and alkali species while burner deposits are not completely oxidised fused iron-based minerals. [19] The inability for the furnace to absorb the heat due to insulation by the slagging, increases exit gas temperature and thus causes highly sintered deposits on the heat transfer areas further down the furnace.

2.2.1.2 Fouling Deposit Types

Fouling differs between high (900 – 1300C) and low (300 – 900C) flue gas temperatures. At low temperatures, deposits are loose or slightly sintered, and at high temperatures deposits are semi-fused or sintered. Volatilised inorganics condense and thus the initial layer in deposits are commonly alkali salts which vaporised in the flame. These create a sticky surface encouraging the deposition of non-sticky particles. [19], [20] Sulphated calcium oxides can result in increased mass of these deposits whilst also increasing their strength by binding particles.

2.2.1.3 Corrosion

Corrosion processes take longer to develop than slagging. Chlorine and sulphur rich fuels are the main contributors to fireside corrosion, and the affects can be increased under reducing conditions such as air-staging and low-NOx burners. Furthermore, increased corrosion is seen when low melting alkali iron sulphate or alkali chloride deposits are formed. [19], [20]

2.2.2 Where Does It Occur?

The location in the boiler categorises the deposition (see in Figure 2-1). Each can be linked to different processes and chemicals due to the nature of the area in which it occurs. The 2 terms are described as the following [21]:

> Slagging – deposition of the matter in coal onto surfaces within the furnace that are **directly exposed to the flame radiation.**
>
> Fouling – deposition of the matter in coal onto surfaces within the furnace that are **not directly exposed to the flame radiation.**

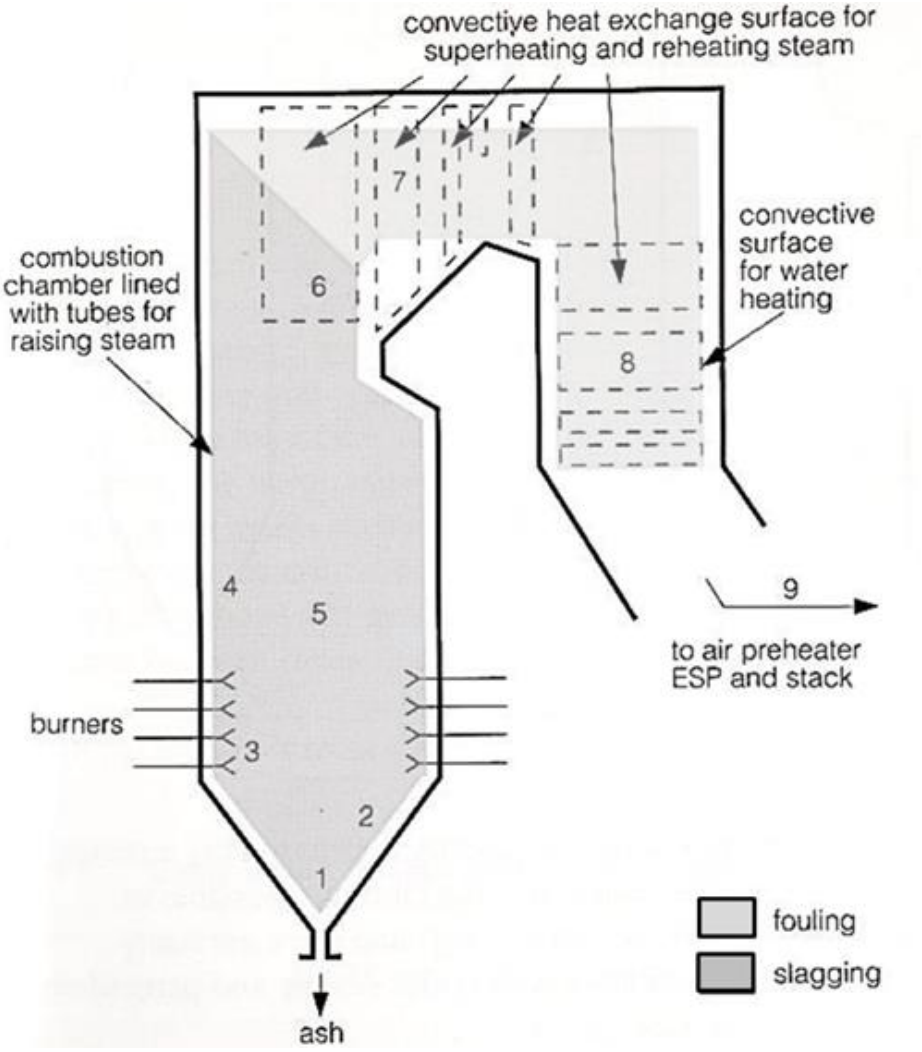


Figure 2-1: Main locations of ash deposition in a tower boiler and conventional boiler respectively[21], [22]

These definitions follow that slagging will take place in the hottest parts of the furnace and fouling will then take place once the flue gas and fly ash in suspension have cooled down.

The illustration by Couch [21] shows the general areas for slagging and fouling respectively in traditional and tower style boilers:

1. Ash hopper (bridging)
    a. Slag dripping down and solidifying or large deposits falling in to the hopper.
2. Ash slope (mechanical damage)
    a. Due to ash lumps dropping down from tubes.
3. Burner (eyebrows)
    a. Can disturb flow pattern and block or damage burner quarl.
4. Wall slag
    a. Boiler/burner design dependant.
5. Division wall slag – where appropriate
    a. Very problematic, sometimes the wall is just removed.
6. Platen (birdnesting)
    a. Due to sintered/fused ash.
7. Convection bank (bonded deposits)
    a. Due to condensing alkali metal sulphates.
8. Economiser (bonded deposits)
    a. Venerable to bonded dust, especially with high calcium coals
9. Air heater (gas inlet fouling)
    a. Usually a product of soot blowing, chunks of low density ash carried over the initial collection point.

2.2.2.1 Boiler Design Considerations

The range in type and location of deposit illustrates the important role that boiler operating conditions and design (geometry) have on slagging and fouling propensities. Furnace size is directly proportional to slagging intensity of a fuel whereas, the convective tube pass (superheat and reheat) spacing and position is based on fouling. Lignite coal boilers generally have to be taller with greater cross-sectional area due to the high quantities of flue gas and slagging propensities. [19]

The factors affecting slagging and fouling were summarised nicely in a graphic modified from [18] by [19] and has been converted to Table 2-1. this is also backed up by [21], [23].

Table 2-1: Factors affecting slagging and fouling in PF boilers

Fuel Quality	PF Boiler Design	Boiler Operation
• **Ash fusion temperatures – melting characteristics** • Viscosity of slag phase • Sintering tendency of ash • Ash burden • Speciation of inorganic material • Particle size distribution and composition	• Furnace exit temperature • Furnace absorption • Furnace configuration • Burner arrangement • Burner size • Tube spacing, orientation and temperature • Steam conditions	• Coal size • Air distribution between burner • Burner operation • Excess air level • Flame impingement • Soot blower operation • Boiler load

The furnace exit gas temperature (FEGT) should be 50C lower than the initial deformation or softening temperature of the ash when designing the boiler. The FEGT for hard coals tend to range from 1150-1200C whereas lignite coals are around 950-1050C. [18], [19] Due to the need to utilise current infrastructure and the competition in the solid fuel market, boilers will now be used with a range of fuels that they may not have been designed for with increased the significance of knowing the characteristics of potential fuels.

2.2.3 The Inorganic Path To Deposition

To link the ash fusion test to slagging and fouling phenomena it is imperative to have an understanding of the overall chemical process. This includes; the

inorganic (incombustible) compositions of solids fuels and the release of ash forming components, formation of the ash, and ash depositions mechanisms.

2.2.3.1 Inorganic Constituents of Coal and Biomass

The inorganic constituents in coal depend on its geological and environmental background which determines its ranks. Whereas for biomass, the growing phases of the plant, origin of agricultural waste, and processing steps are important. [19] Coal is formed by a combination of organic and inorganic matter which undergo physical and chemical changes during a process known as coalification, in which coal increases in rank and the carbon in organic matter increases and becomes denser. This consequently leads to a decrease in inorganic constituents due to formation of clay mineral dispersions in fuel deposits. Table 2-2 contains the main minerals found in coals. [18]–[20]

Table 2-2: Main Minerals Found in Coal

Clay minerals – up to 50%		Chemical formula	
Kaolinite		$Al_2O_3.2SiO_2.H_2O$	
Illite, Muscovite		$K_2O.3Al_2O_3.6SiO_2.2H_2O$	
Montmorillonite		$(1-x)Al_2O_3.x(MgO,Na_2O).4SiO_2.nH_2O$	
Oxides	**Chemical formula**	**Sulphides + Sulphates**	**Chemical formula**
Quartz – 1-15%	SiO_2	Pyrite	FeS_2
Rutile	TiO_2	Pyrrhotite	FeS_x
Magnetite	Fe_3O_4	Gypsum	$CaSO_4.2H_2O$
Hematite	Fe_2O_3	Barytes	$BaSO_4$
Carbonates Up to 20 %	**Chemical formula**	**Chlorides**	**Chemical formula**
Calcite/Aragonite	$CaCO_3$	Halite	NaCl
Dolomite	$CaCO_3.MgCO_3$	Sylvite	KCl
Siderite	$FeCO_3$	**Phosphates**	**Chemical formula**
Ankerite	$CaSO_4.FeCO_3$	Fluorapatite	$Ca_5F(PO_4)_3$

Biomass is a fuel derived from plant or animal matter, and these can include woody biomass, agricultural wastes, animal or domestic residues. Also included in the range of options are sewage sludge and purpose grown energy crops, of herbaceous or woody nature. The inorganic micronutrients in biomass related to growth, above 0.1 wt% (dry matter), are; nitrogen (N), Potassium (K), Calcium (Ca), Magnesium (Mg), and Sulphur (S). [19] Iron (Fe), Molybdenum (Mo), Chlorine (Cl), and Nickel (Ni) are present in lower quantities. Concentrations of K, Cl and N can be significantly increased by the use of

fertilisers. [19], [24], [25] The key inorganic constituents vary widely for each biomass type, this is illustrated in Figure 2-2.

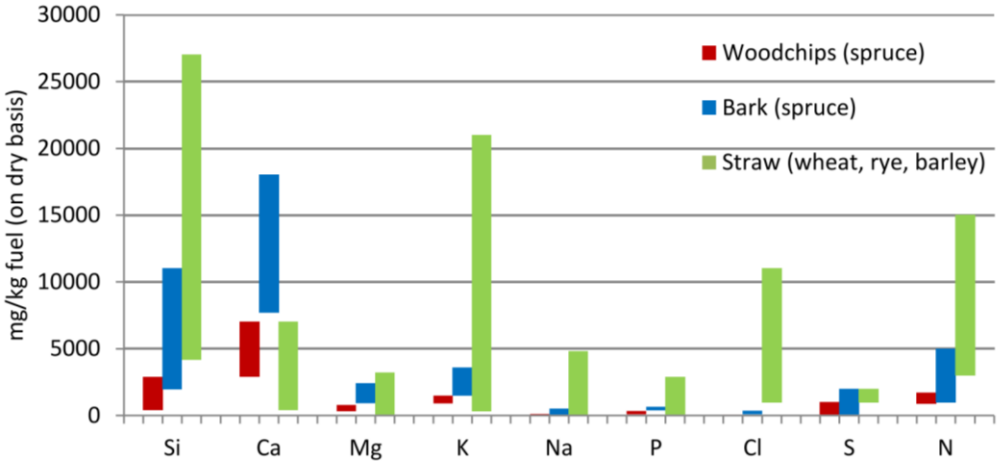


Figure 2-2: Variations In Key Elements In Biomass Types [19], [24], [25]

2.2.3.2 Inorganic Matter Association Within The Fuels

There are 4 types of association for inorganic matter which include; elements organically bound, simple salts dissolved in pore water, and mineral inclusions (more common for coals) which can be included or excluded, this is depicted well in Figure 2-3. [26]–[32].

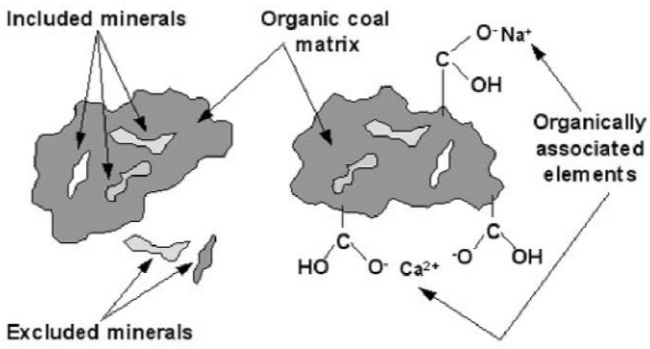


Figure 2-3: Association of Ash Forming Elements Of Solid Fuels

Metals and non-metals associate with the organics, functional groups such as carboxylic acids bond with metals including Na^+, K^+, and Ca^{2+}, whereas non-

metals such as Sulphur, Phosphorus and Chlorine form covalent bonds. The abundance of organically bound metals decreases with rank due to depletion in oxygen for functional groups. With the addition of Mg, these metals are dominant in biomass, as are the non-metals with the exception of Sulphur. The most common salts dissolved are, for the cations, K, Na, and Ca, and for the anions, Cl, HPO_4^{2-}, $H_2PO_4^-$, SO_4^{2-}, $Si(OH)_4$. The mineral inclusion inorganics are dominant in coals and include clay minerals contaminated with K, Na, Ca etc, silicates and other Ca-, Fe-based minerals. [19], [20], [33] Common included minerals in biomass are quartz, calcium oxalate (CaC_2O_4), and iron oxide or hydroxides ($Fe(OH)_3$). Coal minerals can be quantitatively analysed by use of computer controlled scanning electron microscopy (CCSEM) and organically bound minerals and dissolved salts can be analysed by chemical fractionation based on leaching. [19]

2.2.3.3 Ash Content and Composition

The inorganic constituents are the ash-forming species, they undergo transformation during combustion and become part of either the fly ash or the bottom ash. Ash content alongside moisture and volatile content and calorific value is easily obtained under lab conditions and is called the proximate analysis. Ultimate analysis is also done to calculate C, H, N, S, and O content of the fuel. The fuel breakdown is captured concisely in Figure 2-4. [19], [34]

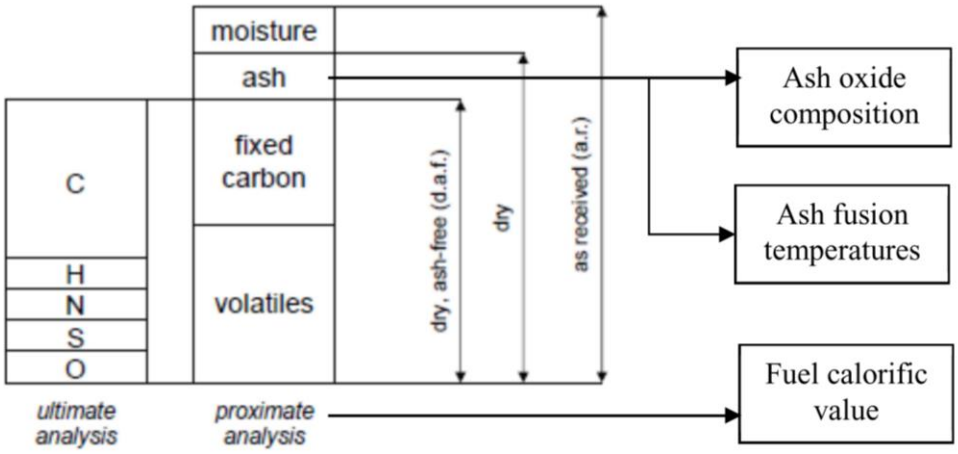


Figure 2-4: Standard characterisation of solid fuels and reference basis

Ash content is determined by heating a representative amount of the solid fuel slowly until only the incombustible matter remains. The temperature for coal is 815C whilst for biomass inorganic matter is volatilised at a lower temperature and thus is ashed at 575C. A drawback of the process is that all inorganic associations with the fuel are destroyed. Inductively coupled plasma-atomic emission spectrometry (ICP-AES) is then used to determine the elemental composition which are then converted into their highest oxidation state. This is commonly 10 oxides: $SiO_2 + Al_2O_3 + TiO_2 + Fe_2O_3 + CaO + MgO + Na_2O + K_2O + P_2O_5 + SO_3 = 100$. Wet digestion is carried out before ICP-AES for raw biomass samples to avoid loss of inorganics during ashing. These oxides can be used as a rough prediction of slagging and fouling based on empirical calculations. Depending on a fuels geological and environmental background, its ash content will change. A study of a range of coal ranks and origins identified that lower coal rank and higher volatile matter yields higher ash content (dry basis), with the exception of biomass fuels as illustrated in Figure 2-5.

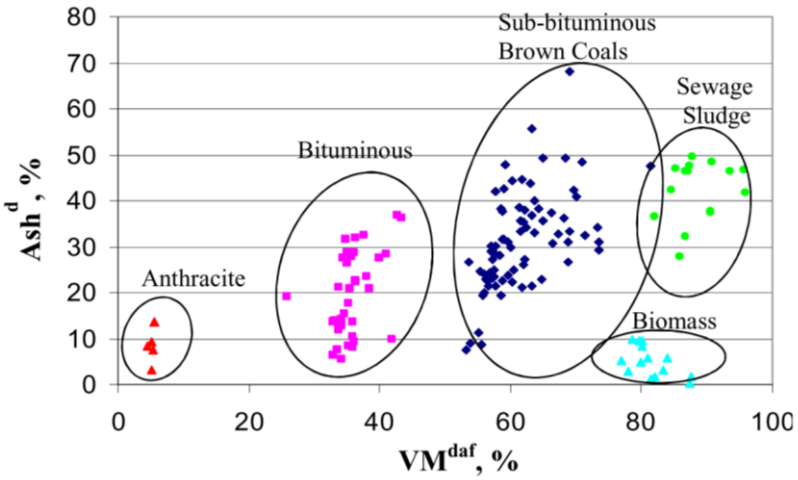


Figure 2-5: Variations in Ash Content For A Range Of Solid Fuel Categories

In summary from low to high, the woody biomass has low ash content 1-10% (average~5%), anthracite 1-20% (~10%), bituminous 5-40% (~20%), subbituminous ranging 9-68% (~30%), and sewage sludge 30-50% (~45%).

A range of bituminous and brown coals for both international and domestic coals were compared with respect to oxides in ashes and the ash fusion temperatures. The links between individual mineral oxides and the IDT are inconsistent but in general with increases in K_2O, SO_3, and Fe_2O_3 the IDT decreases. [19] Plaza also reports from [35] that high calcium contents can lead to highly reflective Ca-silicate/clay based deposits, in addition, high Sulphur US coals contribute to high levels of slagging.

The differences in composition between coal and biomasses such as higher K, P, Ca and lower Fe, clay and general ash content can be clearly seen from Figure 2-6 and Figure 2-7 however, the greater contrast between biomass types is also illustrated.

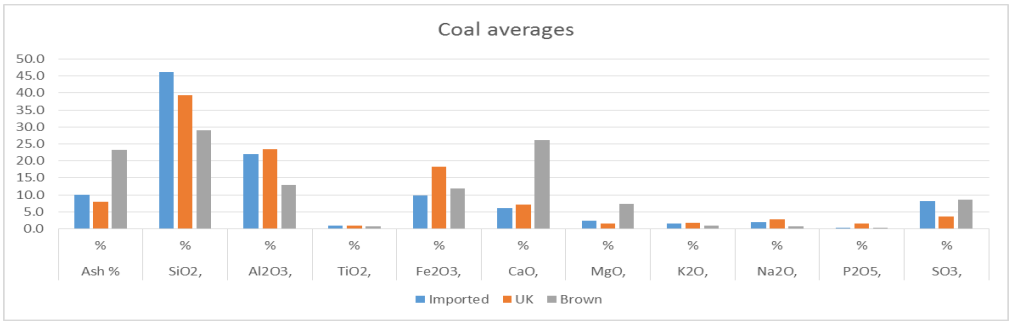


Figure 2-6: Comparison of Imported, UK And Brown Coals

Melting tendencies of biomass ash was compared in a similar way with a range of biomass samples analysed. 3 groups were identified:

1. High silica and alkalis rich ashes with low melting temperatures. (increased S&F risk)
2. Low silica and high calcium ashes with high melting temperatures.
3. Phosphorous-rich biomass/waste fuels. (dependant on ash composition)

Woody biomass with high melt temperatures have been utilised in full conversion power plants however, the other options are only co-fired at low ratios. [36]

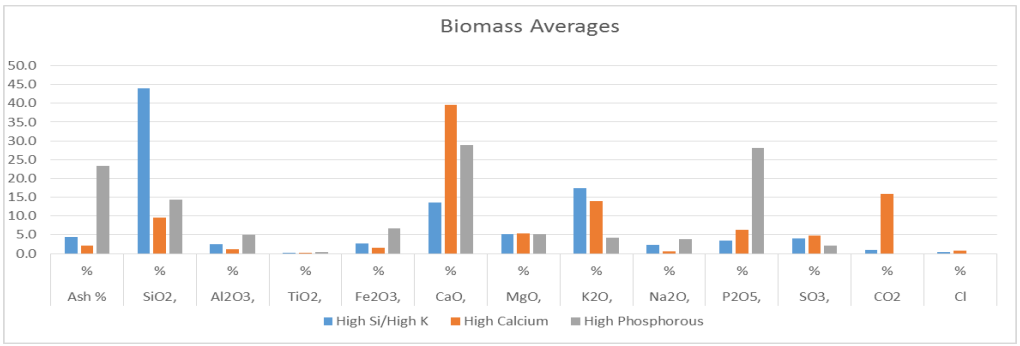


Figure 2-7: Comparison of Different Biomass Groups

2.2.4 Ash Deposition

Ash formation is a very complex process including both chemical and physical interactions, these can be split into 4 steps; the release of ash forming elements during combustion and mineral transformation, transport of particles to surfaces, adhesion, and consolidation. Understanding the onset of the release of ash forming elements will play a vital role in linking ash components and morphological change to slagging and fouling. [18], [19], [23] Typical locations for depositions for specific compound can be seen in Figure 2-8.

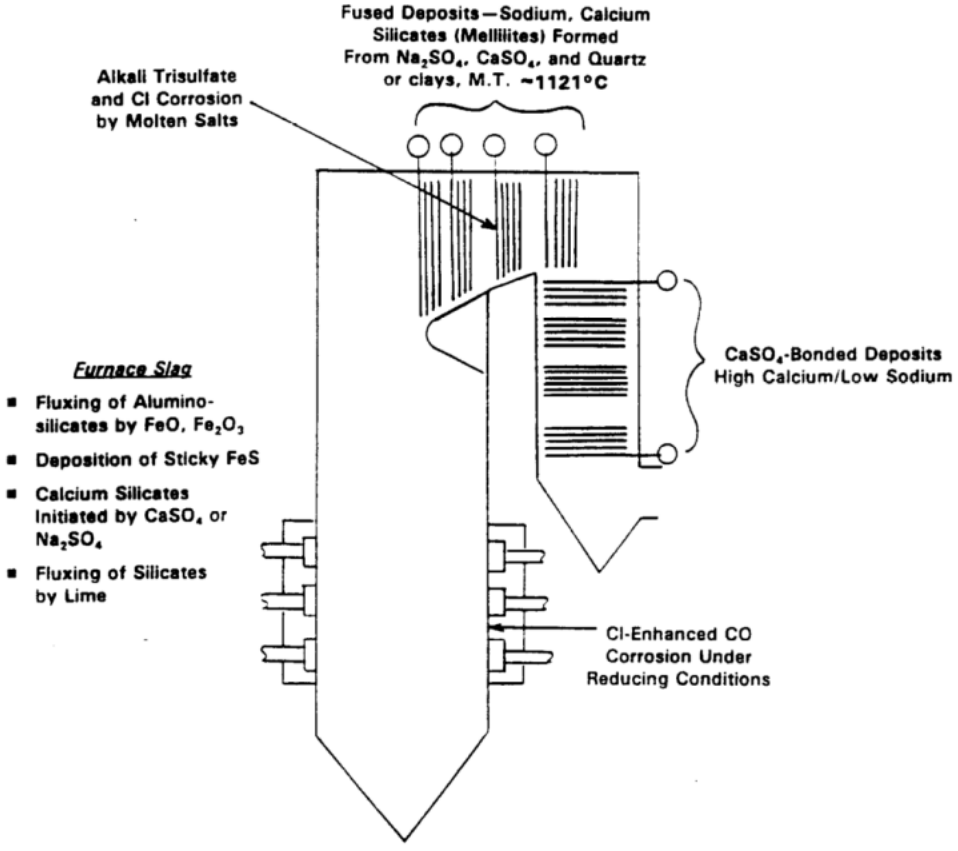


Figure 2-8. Typical slagging, fouling, and corrosion found at various locations in the steam generators, by compound [18]**.**

The fuel undergoes rapid heating (10^6 C/s) and combustion at around 1600C, at which time ionically or organically bound inorganics (such as K, Ca, P, S, and Cl) volatilise with some being recaptured by mineral inclusions. [18], [19] The mineral transformation of the remaining inorganics are various and depend on the ash composition mineral chemistry and residence conditions. The process of fly ash formation takes less than 3 seconds and is represented in Figure 2-9.

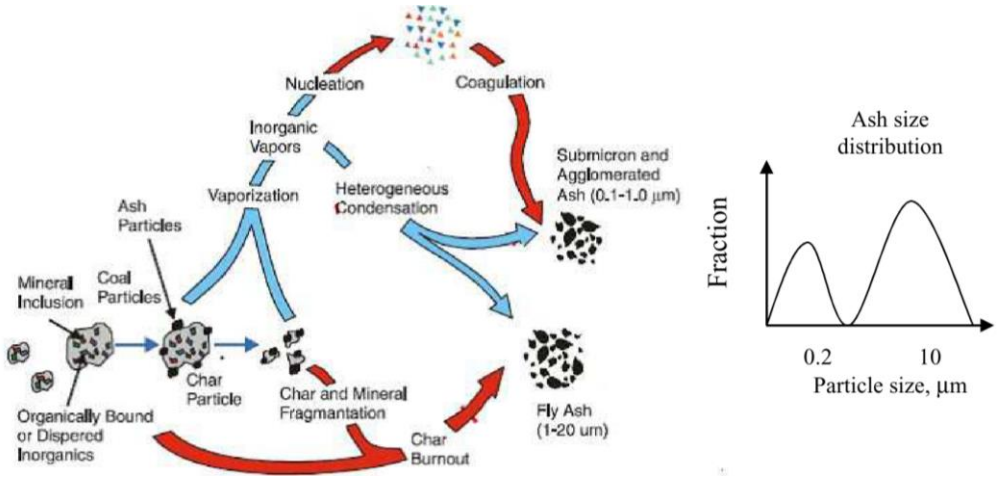


Figure 2-9: Ash formation during the combustion of solid fuels [18], [19], [23]

In the combustion process, ash forming components may be subject to a range of complex transformations and chemical reactions:

1. Inorganic species (alkali and heavy metals) released from the heating and burning of fuel and char and subsequent volatilisation [27], [29], [37]–[39].
2. Salt formation due to the interaction between inorganics in both the liquid and gaseous phases [29], [39]–[42].
3. Volatilised species from (1) interacting with components in the solid phase [26], [43]–[45].

4. Development of a molten phase comprised of alkali silicates (or other ash compounds that melt at a low temperature) after fusion or partial fusion [42], [46]–[49].
5. Residual char particulates and solid ash inserts are subsequently sintered as a result of (4) [18], [29], [47], [48].

Fuel, char and residual ash particles also undergo fragmentation and coalescence alongside the occurrences above [47], [48], [50].

2.2.4.1 Mineral Transformations

On combustion, the inorganics in coal undergo a transformation to an intermediary phase including gases and liquids, but essentially solid residues which may have a sticky surface. The exact characteristics of this intermediary phase are dependant on the make up of the ash, and the reaction conditions in the boiler. This phase manifests in the combustion zone at peak temperatures before flowing to the cooler parts of the boiler in which they condense and solidify.

Primarily, transformations depend on the inorganic components, however, they don't seem to be following a uniform trend, this makes predicting deposition behaviour complex [51]. Deposits found are often amorphous, which further adds to the difficulty.

Coals can be classified as having bituminous ash (sum of [CaO + MgO] is less than Fe2O3) and lignitic ash (sum is greater than Fe2O3). [52] It is possible for a coal to have an ash different to its rank. Ash types and characteristics:

Bituminous; Low level of organically-associated material; High proportions of SiO_2 and Al_2O_3; Moderate amount of Fe_2O_3; Small quantities of CaO, MgO, K_2O, Na_2O, and SO_3; Iron minerals: pyrite, illite, chlorite, siderite and ankerite; Lignitic; Salts of humic or carboxylic acids, often containing Ca, Na, and K; Montmorillonite, halite, and oxyhydroxides, pyrite, iron sulphates.

Vaporisation of organically associated compounds and alkali metals occurs at typical flame temperatures (1300–1500°C) which can condense in cooler zones. The in-flame and post-flame conditions are reducing and oxidising respectively, with iron being ferrous during combustion and the presence of oxygen post-flame [51].

Although Figure 2-10 gives discrete ranges for the decomposition temperatures high heating rates, temperature gradients and time lapses make predictability of chemical changes difficult. Dehydration, dihydroxylation, lattice degradation, and phase transformation of aluminosilicate minerals occurs within a fraction of a second of their temperature rising exemplifies the problem this poses [51].

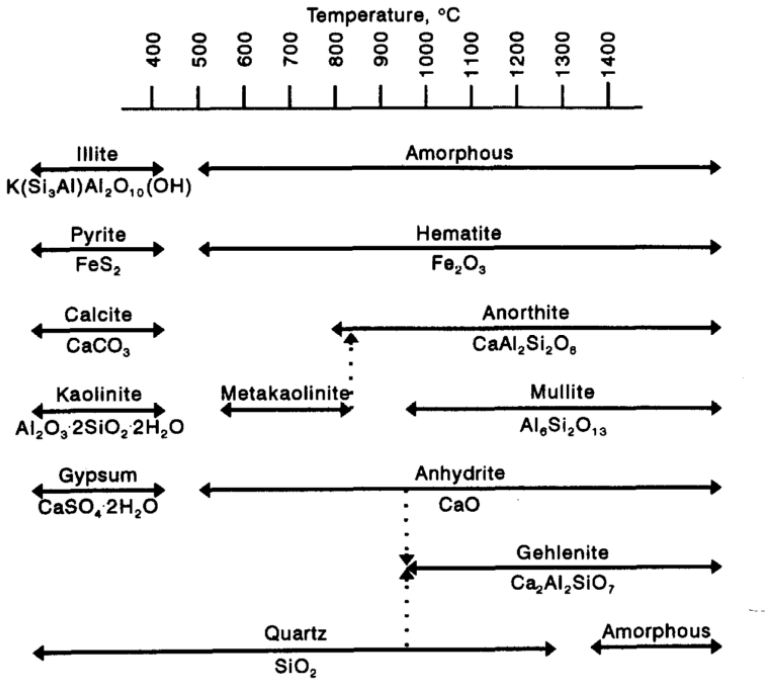


Figure 2-10. Thermal Decomposition of Major Coal Minerals [53]

The most common mineral in coal is Quartz, it has a melt T of 1723C but can form aluminosilicate melts above 1000C. The second major source of silica in coal is kaolinite which at 400°C it forms metakaolinite by the loss of water. As shown in the graphic, metakaolinite undergoes further changes to form mullite and amorphous quartz at around 800-900°C. Illite decomposes at 400°C with the loss of water to form aluminosilicates. A significant contributor to the deposit formation is pyrite which contains the majority of iron in coal. It decomposes at 300°C to pyrrhotite releasing sulphur oxidises to SO_2. The pyrrhotite then oxidises to haematite and magnetite At 500°C. Calcite decomposes at 800°C with the loss of CO_2 to form CaO [51].

Figure 2-11 shows the relationship between temperature and the percentage of inorganic phases [54]. Until 900C no major changes occur, then up to 1000°C wustite and other oxides rich in iron react with quartz and

kaolinite to form melts. The formation of hercynite slows the fluxing action of iron between 1000 and 1200°C. Above 1200°C all iron present has been incorporated into a viscous silicate liquid [51].

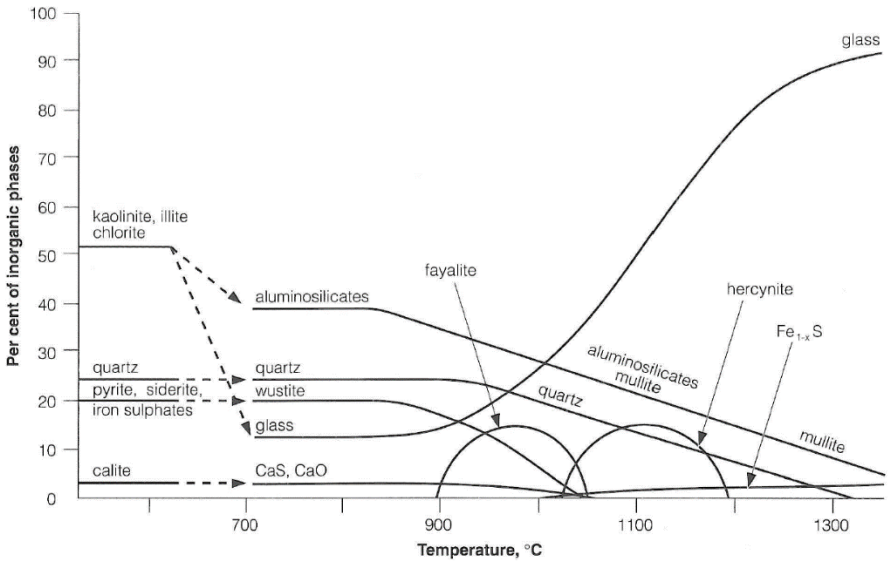


Figure 2-11. Phase Diagram of Changes in US Eastern Coal under Reducing Conditions [54]

Although glassy phases form more in reducing conditions, partial melting occurs at lower temperatures than those predicted by AFTs in both oxidising and reducing. This partial melting is important as up to 50% of ash may exist as glass at as much as 400°C below the quoted initial deformation temperature [51].

2.2.4.2 Deposition Mechanisms

The mechanisms of deposition are dependent on a multitude of factors including: physical state of the material, local temperature, flow patterns and the materials chemistry [21].

Baxter et al. describes the deposition mechanisms in terms of 4 principle categories, also illustrated in Figure 2-12 [55]: (A) Inertial deposition, the principal mechanism for slag formation [36], [56], commonly by larger particles, greater than 5-10 microns in size [21], [57], (B) Condensation, vapour passes over any cool surface, or entrained/deposited particle and the condensate forms a thin uniform boundary layer, this can be sticky and initiate deposit growth [21], [58]. Biomass contains a large amount of volatile inorganics, and this process is more profound in biomass than coal [36], [59], (C) Thermophoresis, a transport mechanism due to temperature gradient acting in the opposite direction, is mainly significant for finer particles [21], [36], [57], [59], (D) Chemical reaction, can determine if a deposit will stick. If it grows, these are strongly temperature dependant resulting in varying deposition relative to boiler position.

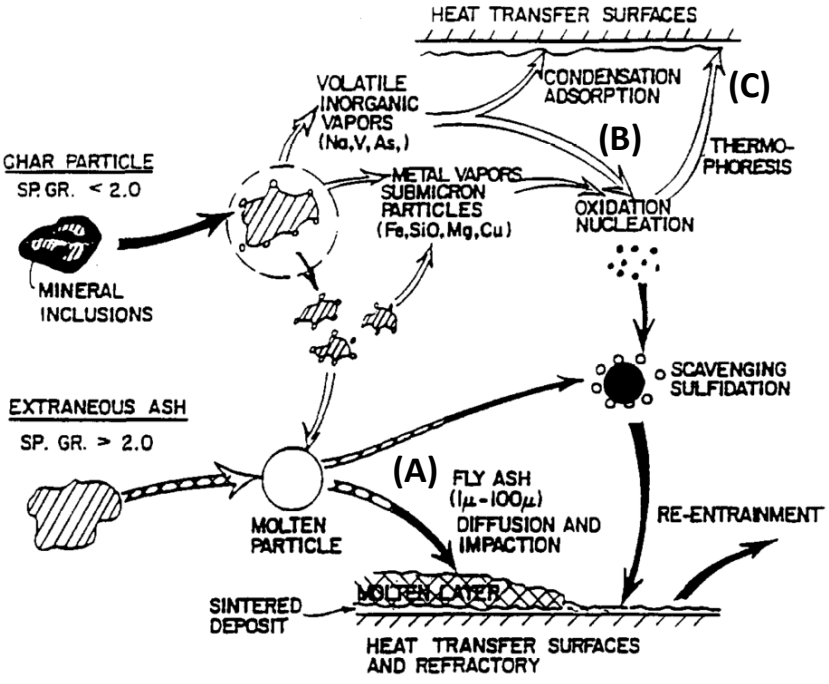


Figure 2-12. The fate of mineral matter in coal during combustion [18]**.**

2.2.5 Characteristics Responsible for Slagging And Fouling

In boilers, the problem of fouling and slagging can be attributed to the presence of 1 or more troublesome species within the combustion system [60]. The crucial element that is responsible for the creation of these problematic species is potassium. There are multiple routes to form these species at combustion temperatures including:

1. During the devolatilisation of fuel particles and char burnout, potassium salts such as KCl, K_2SO_4, and K_2CO_3 are formed and melt at low temperatures (as low as 770^oC) [37], [61]. The flow of gas can entrain such salts and hence result in fouling further down the boiler and foul heat exchanger tube surfaces [60].
2. Silicon and silicates from the fuel that react with the potassium salts to form differing potassium silicates in a binary system that initially melt at 600-700^oC. Some of these silicates, at normal biomass combustion temperatures (NBCTs) of 700-1000^oC, are in a viscous liquid form and have the propensity to cause sintering and agglomeration [39], [62].
3. Ternary K_2O-SiO_2-Al_2O_3 and K_2O-SiO_2-CaO systems form from melts and when the SiO_2 proportion of the system is high, the melting temperatures are even lower than 700^oC [28], [29], [63]. As a result, some systems with the required composition may melt at NBCTs causing ash sintering.

Potassium phosphates that have a high potassium content or high K/Ca ratio readily melt at NBCTs and result in ash sintering and slagging [40], [47], [48].

2.2.6 Cost to Industry of Fouling and Slagging

Several studies on US PF boilers relating to potential operational savings from reductions in slagging and fouling have quoted a range of values from various perspectives. Improvements in the abatement of ash deposition in all US boilers, attributing to a 1% decrease in heat rate and a 1% increase in availability, were quoted at a $400 million/year [64]. An assessment made on a poor quality lignite coal, with a high fouling propensity, attributed savings of around $8 million/year for a single boiler[65]. Furthermore, a review of 12 coal plants (8000MW capacity) in Pennsylvania for quality of coal utilised, estimated a saving of around $5 million/year [66].

In 1994, when the US proportion of coal fired capacity accounted for roughly 1 third of the world's coal consumption, it was projected from the previous reports indicated, that the global potential for saving from reductions in ash deposition would be in the region of $1000-1500 million/year [21]. It was also detailed that in reality there is a high likelihood of the top end estimate being correct, due to the increasing proportion of low grade coal being used globally.

Additionally, if this estimate were to be revised for the current market assuming similar saving potentials, with Figure 2-13 revealing a coal boom in the Asia Pacific region, the US now represents a mere 12.5% of the world's coal consumption. This dictates that the renewed estimate for the saving potential globally would equate to $2,400 – 3,600 million/year.

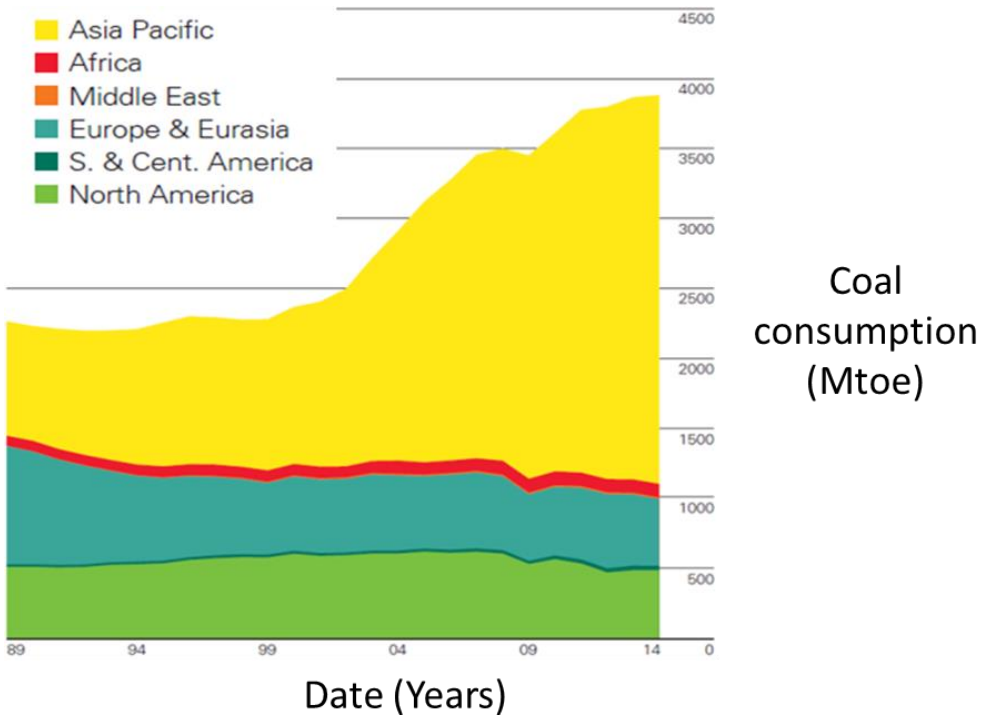


Figure 2-13.Coal consumption by region, million tonnes of oil equivalent [67]

This is estimate is subject to scrutiny over advances in operating performances by coal fired power stations, however, the vast majority of new capacity has come from china where the priority has been growth and not optimisation of efficiency. Moreover, the coal power stations in the rest of the world are reaching or have surpassed the end of their life span which brings with it inherent drops in efficiency. This analysis illustrates the vast economic potential for the prediction and thus prevention of fouling and slagging in PF coal boilers.

2.2.7 Methods of Mitigating Fouling And Slagging

To reduce potential slagging and fouling of coal and biomass, various methods have been developed. Such methods include attempts to identify potentially problematic fuels, improvements in operating conditions to suit localised or abundant coals, more recently additive measures to lower slagging

propensity, and the most common and necessary measures, remedial solutions once slagging and fouling have occurred.

2.2.7.1 ADDITIVE UTILISATION

It has been proposed by numerous researchers to use different mineral additives which can reduce deposits by shifting the ratios of compositions that favour slagging behaviour to 1 that have a lower propensity for fouling. Additives such as kaolin and calcite can considerably reduce super heater deposition and corrosion, and with slagging, the quantity decreases of 1 half and 1 third respectively [68]–[72]. Heat transfer surface deposition in biomass combustion can be prevented by the addition of high concentrations of aluminosilicate [73] with positive correlation between efficiency and levels of aluminium and silicon in the ash [74].

2.2.7.2 SOOT BLOWING

The most commonly used remedial/online cleaning mechanism is soot blowing; this is the removal of deposits using superheated steam, saturated steam, water or compressed air [75]. Steam and air tend to have the same impact on the boiler; saturated steam is less favourable due to its propensity to cause erosion [21]. Water is usually the chosen medium for strongly sintered deposits to provide greater thermal shock.

2.2.7.3 PREDICTIVE ANALYSIS

Increasing efforts are being made to be able to identify slagging and fouling propensities of coal and biomass. Proximate and ultimate analysis techniques are used to identify composition and attempt to correlate these 2

characteristics. However, understanding which components are responsible for slagging and fouling is only the first step. This can be used to select 1 fuel over another, or identify suitable pre-treatment, such as 3.4.1. Inevitably, whichever fuel has been selected will have some of these components regardless of treatment or fuel quality therefore, the next step is finding out at what temperature the ash will begin to slag. This process relates to the fusibility characteristics of the ash and the ash fusion test and is the current industry standard for assessing fusibility, thus predicting the onset of deposition.

2.3 Ash Fusibility

It is important to acknowledge the limitations of the ash fusibility test in its current state, including the inherent nature of the test and the heterogeneous nature of the solid fuels that are tested. It is also noted that slagging and fouling propensity is linked not only to ash characteristics but also boiler geometry and aerodynamics. It would be nearly impossible to create an all-encompassing test. However, there are significant improvements that can be made to the existing test and there is a lot of unused information in the current evolution of the test.

The ash fusion test, or ash fusibility test as it was initially called, was first used in the early 1900s, in order to attempt to predict the clinker forming characteristics in lump coal ash [11]. It has since become the principle test used in power stations to predict the slagging tendencies of pulverised coal ash. [19] However, its short-comings in repeatability and representing fusibility are widely documented and acknowledged.

2.3.1 The Standard Ash Fusion Test

The method for the test is outlined in multiple standards [12]–[15] (see Appendix). They cover the entire process from ash preparation and pelleting methodology, to calibration runs and the suitable set up for reducing and oxidising atmospheres. In a simplified test procedure, the samples are heated in a furnace, from 400°C to 1600°C at a heating rate of 8±3°C [15±5°F]/min. During the heating process the sample is observed and 4 characteristic temperatures are recorded, these are called the ash fusion temperatures.

2.3.1.1 ASH FUSION TEMPERATURES

These definitions are the descriptions that an operator would see for the critical temperature points to be observed. They are taken straight from the American standard[15] and are as follows:

2.3.1.1.1 INITIAL DEFORMATION TEMPERATURE, IDT

The IDT is the temperature that the apex of the cone begins to round. Shrinkage or warping of the cone is ignored if the tip remains sharp. In Figure 2-14, the first cone shown is an unheated one; the second cone is a typical cone at the initial deformation stage.

2.3.1.1.2 FLOW TEMPERATURE, FT

The temperature at which the fused mass has spread out in a nearly flat layer with a maximum height of 1.6 mm [1⁄16 in.] as shown by the fifth cone, FT, in Figure 2-14.

2.3.1.1.3 HEMISPHERICAL TEMPERATURE, HT

The temperature at which the cone has fused down to a hemispherical lump at which point the height is one half the width of the base as shown by the 4th cone, HT, in Figure 2-14.

2.3.1.1.4 SOFTENING TEMPERATURE, ST

The temperature at which the cone has fused down to a spherical lump in which the height is equal to the width at the base as shown by the third cone, ST, in Figure 2-14.

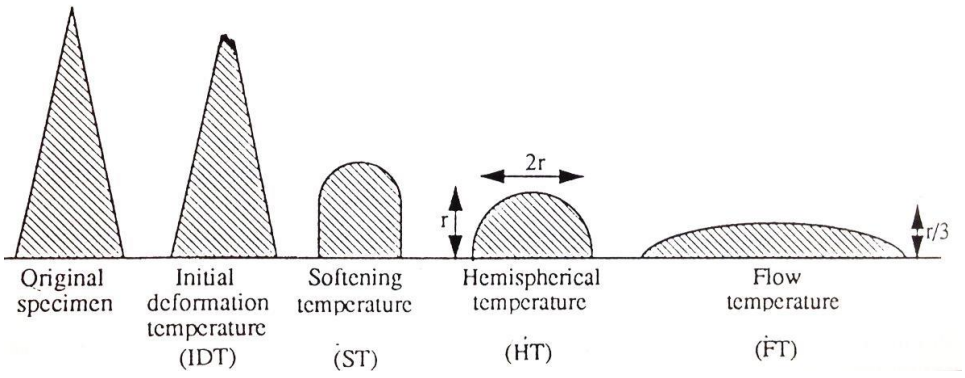


Figure 2-14. Characteristic profiles of key deformation events [34]

The test laid out in these standards has attempted to make a repeatable and reliable process for simulating and therefore predicting ash behaviour in a power station boiler. However, there are 2 key overriding problems concerning the AFT. Firstly, it is subjective in nature, and discrepancies have been experienced for identical coal ashes analysed in different laboratories. In some cases, differences of up to 400°C have been documented [16]. Figure 2-15 illustrates examples of the physical imperfections in cone samples. The main criticism of the standard ash fusion test however, is its unreliability in predicting

the behaviour of coal ashes in real combustion processes. The link between initial deformation temperature (IDT) and the onset of slagging has been scrutinised and in many cases found that the initial deformation of the cone may not be the key event that it was originally thought to be [16], [76]–[79].

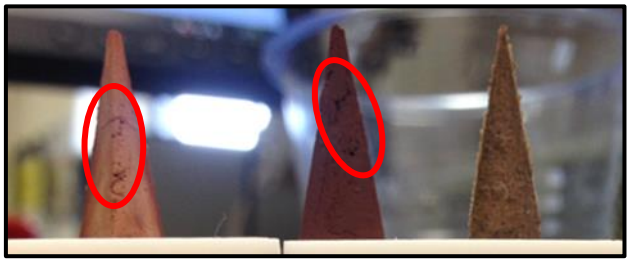


Figure 2-15: Standard AFT Cones Showing Cracks and Flaws

These deficiencies could have a detrimental influence on design parameters for boiler manufacturers and a fuel selection in relation to optimising efficiency. In response to the poor reproducibility and reliability, a series of developments to the original ash fusion test have arisen to improve the analysis.

2.3.1.2 INCONSISTENCY OF EXECUTION

Currently the pellets made for testing include a wide range of options, these include:

- Binder
    - Water, ethanol, dextrin, isopropanol and methanol.
- Shape and size (% of labs for biomass)
    - Cylinder (81%)
        - 3x3 (50%), 5x5 (18%), 4x4, 2x3, 3.5x2.5, 4x5mm (14%).
    - Cube (4%)
    - Pyramid (4%)
    - Cones (11%)
        - Height 12-19mm

2.3.1.3 ASH CHARACTERISTIC IMPACT ON THE STANDARD TEST

There have been many studies on coal ash fusion characteristics which closely relate SiO_2/Al_2O to the AFCs [80]–[82]. The IDT is primarily affected by an inversely proportional relationship to the concentration of K_2O [81]. A directly proportional relationship has been reported between IDT and MgO, CaO, Fe_2O_3 and Al_2O_3 concentrations [8]. The results from seaweed AFC and melting point analysis show very low melting temperatures, such that the Chinese and US national standards are not a suitable form of analysis [83].

2.3.2 Predictive Tools and Modelling of Ash Fusion Temperatures

The use of modelling has become more and more prominent in industry, in the hope that simulation can be used to save costly and time consuming experimental procedures. This has also found its way to the process of predicting ash fusion temperatures via empirical analysis using regressions or predictive algorithms.

2.3.2.1 SLAGGING AND FOULING INDICES

A range of indices, Table 2-3, are currently used as an indicator of which coals will have high or severe slagging propensity. They are simplified indicators for individual sets of analysis. These will be used as a reference to compare with when testing the large database of fuels.

Table 2-3: Slagging and Fouling Indices

Index	Formula	Slagging or fouling propensity			
		low	medium	high	severe
Ash fusion	Softening Temperature under reducing conditions	>1350		<1350	
Base-acid ratio	$\frac{Fe_2O_3 + CaO + MgO + Na_2O + K_2O}{SiO_2 + Al_2O_3 + TiO_2}$	< 0.4 or >0.7		0.4 -0.7	
Slagging factor	$\frac{Base}{Acid} \times Sulphur\ in\ Coal\ (d\%)$ (for bit ash where Fe_2O_3 > CaO+MgO)	<0.6	0.6-2.0	2.0-2.6	>2.6
Iron-calcium ratio	$\frac{Fe_2O_3}{CaO}$	<0.3 or >3.0	0.3-3.0		
Slagging index	$\frac{((\max HT) + 4 \times (\min IDT))}{5}$	>1340	1340-1230	1230-1150	<1150
Silica percentage	$\frac{SiO_2 \times 100}{SiO_2 + Fe_2O_3 + CaO + MgO}$	72-80	65-72		50-65

2.3.2.2 MULTI LINEAR REGRESSION

Early regression estimates were deemed as satisfactory [84] however, this was based on a now outdated view of the AFTs repeatability and reliability.

2.3.2.3 BACK-PROPAGATION (BP) NEURAL NETWORKS

These processes are, however, in themselves very complex. The BP neural network has been used predicting the ash fusion temperature from ash compositions [85]. Yin acknowledges that the work is extremely complex but it does yield reasonable correlation to softening temperature.

2.3.2.4 NON-LINEAR CORRELATION

Özbayočlu et al. compare the use of linear regression with non-linear. This illustrates that the reduction in variables and the inclusion of ash content, mineral matter content, specific gravity and Hardgrove index as independent variables for non-linear and gives a more accurate representation of AFTs.[86]

2.3.2.5 ACO-BP NEURAL NETWORK

The ACO-BP is an advance on 2.3.2.3 by using an ecology system algorithm called Ant Colony Optimisation (ACO) to relate the oxide content of coal ash to AFT temperatures. In the comparison of ACO-BP and BP algorithms, it is shown that the ACO-BP can be more accurate than the standard BP. When compared to empirical formulas, the average error is over both the ACO-BP and BP algorithms [87].

2.3.2.6 F*A*C*T PREDICTION

The F*A*C*T thermodynamic computer package working with a novel thermodynamic database, which simplifies coal ash composition to a 5-component system(Al-Ca-Fe-O-Si), has been used to predict the liquid temperatures of these individual components. This tool was demonstrated with excellent agreement with to the experimental AFT values, predicting the AFT's of 53% of the coals to within ±40C [88]. This predictive software has been used by many different researchers with areas of success in predicting ash fusion temperature but also correlating the data based on a range of 3 phase plots using the 5-component system for both coal and biomass [89]–[98].

After reviewing the estimation methods, assuming that the IDT is accurately being measured empirically, the F*A*C*T prediction model has produced the best correlations. This predictive method will be investigated from an empirical stand point in an attempt to find links the results to the AAFT.

The use of bulk properties together with predictive indices for such calculations is a helpful tool but may not fully represent the heterogeneous

nature of ash properties [99]. In PF combustion, not every particle plays a part in deposition, only specific particles in the ash adhere to the heat transfer surfaces and this is also dependant on boiler geometry [100]. To successfully create a predictive model for ash deposition it must include: detailed mineral matter of the coal, combustion transformations, boiler geometry and operating conditions and finally ash deposition characteristics throughout combustion [100]–[102].

2.3.3 Alternative Methodologies for Ash Fusion Testing

There are now a variety of analytical methods available that aim to improve upon the original AFT including, The ACIRL test, The HRL Test, and The CSIRO Test.

2.3.3.1 THE ACIRL TEST

The ACIRL test uses 2 plates to normalise the deformation (Figure 2-16), instead of 1 as the standard test does allowing the ash to deform freely in space. It measures the distance variation between the 2 tiles during the period of the test. The Australian Coal Industry Research Laboratories (ACIRL) designed the procedure aiming for a more precise analysis.

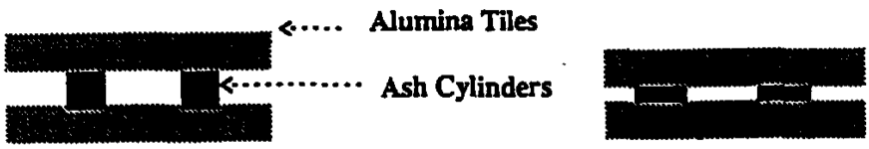


Figure 2-16. The ACIRL Test [79]

In the test, 4 ash cylinders (2 mm × 2 mm diameter) act as pillars that are used to separate 2 ceramic tiles. As in the standard AFT, the setup is heated

but, here the distance between the tiles is measured, this can be done continuously or up to 20°C temperature intervals, from 1000 to 1600°C. [79]

2.3.3.2 ACIRLS IMPROVED ASH FUSION TEST (IAFT)

The IAFT is an adjustment to the original ACIRL test where-by 6 ash pellets are used as cylindrical pillars between the plates and the methodology has been further refined. It requires 2 standard ash fusion ceramic tiles [25 × 25 × 6mm3] and 6 cylinders of ash of 2.0 mm diameter and 2.0 mm height (about 0.1 g) produced in a moulding device cited in the Australian Standards Association AS1038.15. [103] 6 cylindrical pellets of ash of 2 mm diameter and 2 mm height produced from the mould are disposed in 2 rows of 3 toward the corners on an ash fusion tile and a second tile is then placed on top of the pellets. A 3-D representation of this is layout can be see in Figure 2-17. The process then follows the same path for heating as the original AFT and ACIRL tests, except for explicitly stating a heat rate of 5C/min up to 1600C. In addition, the setup is photographed every 10-20C. The images are taken using a transmitted light microscope, and then the plate separation is measured from the negatives of each image and plotted on a graph of separation against temperature. A range of other variables can be recorded and analysed in the same way including; width of the ash pillars, estimated volume change for the coal ashes.

It is hoped that the parameters recorded in the experiment can be related to the stickiness in the ash; a notable event between the melting

temperature of the first liquid phase (at the point of highest viscosity) and the temperature at which it has minimum volume. [76], [77]

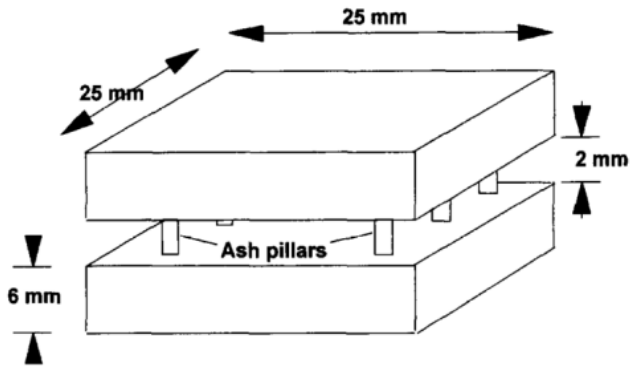


Figure 2-17. Diagramic representation of the ACRIL test [78]

2.3.3.3 THE HRL TEST

The HRL test utilises a completely different component to the deformation of ash, as opposed to just a visual analysis of physical deformation. The test measures electrical resistance and ash shrinkage alongside 1 another. HRL Technology Pty Ltd. developed the process, whereby 10% dextrin ash pellets (7 mm high × approx. 7 mm diameter, -0.3 g) are placed in a 10 mm diameter platinum crucible with a platinum disc situated on the top, see Figure 2-18.

An electrical circuit is then used to measure a standard resistance in series with the ash sample, but also conductance/resistivity via a pulsed voltage through it. Pellet height and change in voltage across the known resistance is observed simultaneously. Measurements are taken over the standard ash fusion temperature range however, the HRL test measurements start lower at 30^{o}C, and it can be drawn to a premature end when the top disc contacts the

platinum crucible. Each data point is measured at times of constant applied voltage (+ 2 V and - 2 V) [79], [104].

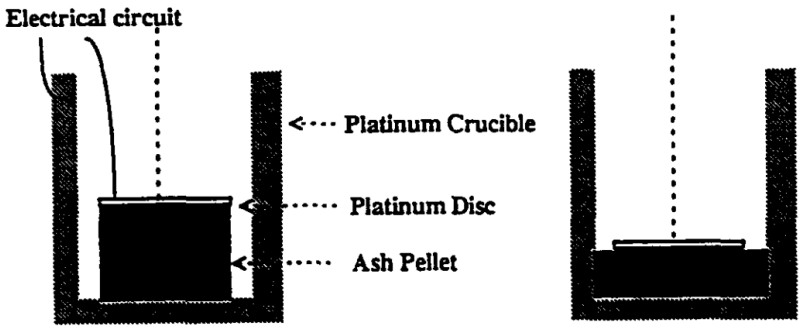


Figure 2-18. The HRL test [79]

2.3.3.4 THE CSIRO TEST

Unlike the other attempts to improve upon the AFT, the CSIRO test analyses loose ash instead of using a pellet. It was created by the CSIRO Division of Coal and Energy Technology. It follows the same heating range as the HRL test being heated from around 20-25C to 1600^{o}C, as it is not inhibited like the HRL at the top end by short circuiting. The setup includes a flat bottomed cylindrical container and a bar tapered at the face in contact with the ash (Figure 2-19). The loose ash is situated at the bottom of the container, with the tapered bar resting on it. As the temperature is increased, the ash melts and the bar sinks, gradually the ash flows as slag into the space between the bar and container. The container was specifically designed for a thermomechanical analysis machine (Setram TMA92).

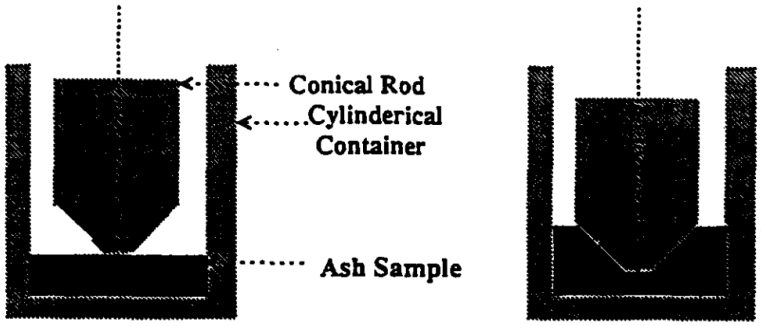


Figure 2-19. The CSIRO test [79]

2.3.3.5 TEST COMPARISONS

Currently, it is understood that onset of ash deposition is initiated when ash particles become 'sticky' and therefore will adhere to boiler surfaces. The temperature at which this occurs is what the ash fusion tests seek to identify. The standard test links this to deformation of a pyramidal pellet, whilst the newer tests aim to do this by measuring shrinkage and electrical resistance. The alternative methods are summarised in Table 2-4. The results from these new tests have shown shrinkage events well below the temperatures recorded for IDT for identical ash samples, and in some cases once the sample reaches IDT a substantial portion is in the liquid phase [79]. This is a clear indication that for the samples tested at least, the IDT isn't the lowest softening temperature. The CSIRO test identifies temperatures at points of rapid shrinkage during the heating of the ash. These events provide a legitimate alternative to AFT, and the ACRIL test can also achieve this when continuous measurements are obtained [79], [105]. The HRL test based on electrical resistance has not yet yielded characteristic events which can be related to AFT temperatures, but the

subtlety of the shrinkage measurements brought about by the use of non-pelleted ash may yet provide a useful indication of AFT temperatures [79], [104].

Table 2-4. Comparison of the alternative methodologies for ash fusion testing, modified from[79]

Test →	**ACIRL-IAFT**	**HRL**	**CSIRO**
Heating rate	8°C/min	8°C/min	8°C/min
Gas atmospheres	Reducing	Reducing	Inert gas
Amount of ash used	ACIRL~0.1 g	HRL ~ 0.3 g	CSIRO-35 mg
Ash compaction	Dextrin pellets	Dextrin pellets	loose ash
Initial temperatures	1000°C	900°C	900°C
Maximum temperature	1600°C	1350°C	1600°C
Data at temperature intervals	20°C	4°C	continuous
Monitoring	Shrinkage	Shrinkage & Electrical conductivity	Shrinkage

Stickiness has also been related to viscosity, which is then related to chemical composition thus, the composition of an ash sample can be used to calculate viscosity and provide another parameter for the prediction of stickiness. This parameter could also be linked to shrinkage temperatures [16].

Similar discrepancies have been found with the CSIRO and ACRIL tests as have previously been found with the standard ash fusion test relating to differences in results between lab ash and combustion ash from the same coals. This has been attributed to the higher temperatures experienced by the combustion ash which leads to the loss of potassium and further reactions not

experienced by lab ash[79]. These discrepancies illustrate the importance of including combustion ash in experimental investigations to obtain relevant data. Wall et al. showed that measuring the shrinkage data of power station combustion ashes can potentially provide a different approach to characterising slagging and fouling [79].

2.3.4 Automating the ash fusion test

Automation of the original processes has clear benefits with respect to precision and standardisation, purely based on the removal of the operator. This is 1 of the key problems identified with the existing ash fusion test, the reliance on visual observation rather than an objective physical measurement. This has been illustrated by discrepancies of up to 400^{o}C between different labs [9], [16]. This can be achieved using a camera in the furnace and the images are then analysed in a program based on the trigger points of deformation set out in the regional standards. Each run would then inherently identify the identical point each time. However, Pang et al have taken this approach 1 step further and attempted to characterise the complete behaviour of ashes with a fusion profile based on the height/initial height of the ash pellet sample (illustrated in Figure 2-20). Key event 'regions' are used to identify ash characteristic as opposed to individual temperatures however, these can easily be identified in the profile [9].

This new form of test shows the most promise in terms of potential to adapt the existing ash fusion test method in a minor way to appeal to industry for ease of applicability, whilst providing more incisive and complete analysis

in the identification of ash characteristics. Together with the improvements in accuracy, reproducibility and a pelleting process that includes no binders thus, less altering of the actual sample, the analysis can be viewed as a marked improvement. This type of set up, with the use of a camera and image analysis, is very flexible and could potentially be adapted to the tests shown in 2.3.3.

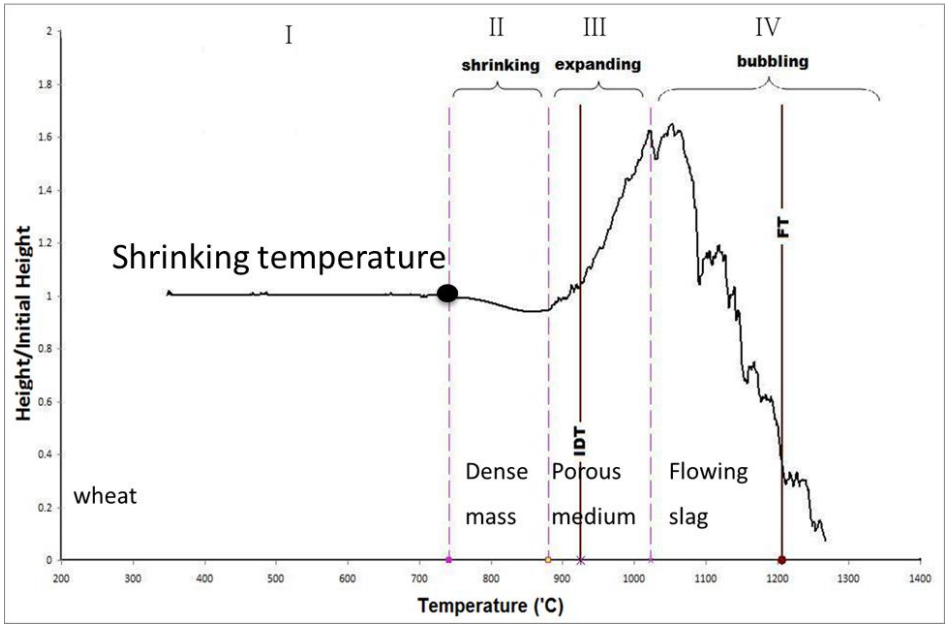


Figure 2-20: Fingerprint of the ash morphology change with characterised sections/phases

2.3.5 Current Market Review

The process described in the 2.3.4 whereby image analysis is used to automate the standard ash fusion test, has already been adopted by some companies in order to avoid the problem of operator error. These analysers follow the standard ash fusion test model and provide the 4 characteristic temperatures. A comparison of existing ash fusion test equipment are shown in Table 2-5

Table 2-5: Current market review of ash fusion test systems

Company	Model	Number of samples	Test duration (hours)*	Quote	Reference
Preiser Scientific	Auto Ash Fusion System	9	5	n/a	[106]
Leco Instruments UK Ltd.	AF700 Ash Fusion Determiner	6	4	£50,000.00	[107]
Carbolite	Carbolite CAF Digital Coal Ash Fusibility Furnace	12	3	n/a	[108]
Multimedia Comp. Research Laboratories	Ash Fusion Tester ASH-10	9	2	n/a	[109]

These analysers do not address the real issue which is, preparation of the samples and operator error and neither do they provide an answer to the problem highlighted by the attempts at improving the ash fusion test discussed in 6.2. These processes are still providing the standard ash fusion temperatures which are widely reported to have flaws in prediction slagging and fouling propensities of coal and biomass in pf boilers.

2.3.6 Quantitative Understanding of Ash Fusibility

There have been many attempts to quantify and understand the mineralogical changes that ash undergoes during deformation. The research is commonly carried out on a suite of relevant coals to local industry.

2.3.6.1 CHEMICAL INTERATIONS

The chemical composition of ash has been studied for a long time, with the intent of gaining understanding of what chemicals are responsible for behaviour of the ash. This research initially focused on the exact chemical compositions and these were used to describe ash composition but also as a basis for predictive modelling such as regression analysis, equilibrium calculation and AI. The results were inconsistent and weren't universally applicable to all samples. Thus, the move to modes of elemental combinations and with the arrival of better quantitative analysis techniques more comprehensive research has been carried out. Han et al. has mapped the modes of occurrence and behaviours for the mineral matter in Chinese coals by means XRD and focusing on the average number of mineral species and the amorphous substances for both high and low temperature ash. The behaviour of the mineral combinations or 'eutectics' are broken up into 3 phases with the exception of mullite containing ashes [110]. Some examples of the quantitative analysis can be seen graphically below (Figure 2-21) demonstrating the 3 phase melting processes, as well as the exception to the rule. Han et al. divides up the stages of heating into 'crystallisation' 815-1100C (1000C for low AFT), 'eutectics' 1100-1300C (1000C LAFT), and finally 'getting stable' 1300-1500C.

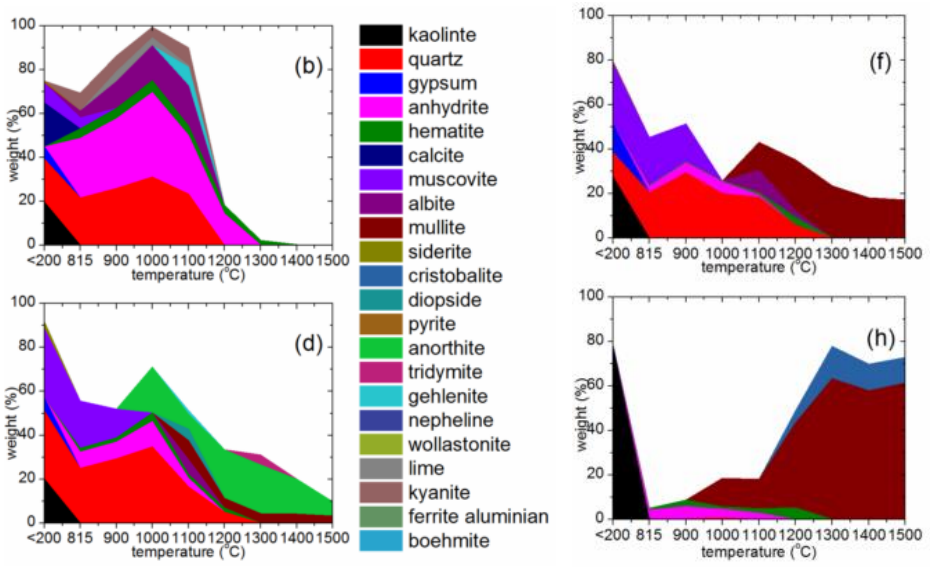


Figure 2-21: Changes of crystal and amorphous minerals in typical samples

AFT temperatures are related to the eutectic stage with IDT(DT) being at the start where there are less amorphous substances therefore has less links to the other AFT temperatures which occur with more amorphous substances present (Figure 2-22). Carbonates and sulphates are highlighted as promoting the eutectic mixtures from their decomposition products.

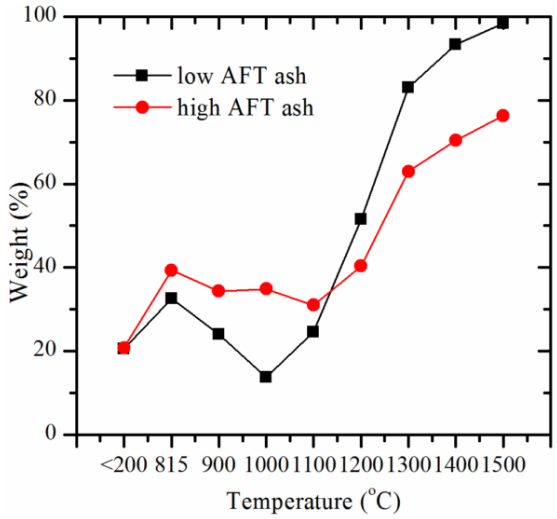


Figure 2-22: Changes of amorphous substances in low and high ash fusion temperatures ashes at different temperatures [110]

SiO_2 and Al_2O_3 are linked to high AFT temperatures. The latter phases were calculated using FactSage [110]. Arvelakis et al. carried out a study on coal and biomass ash which was done using similar but non-quantitative XRD which found that biomass ashes solidified at lower temperatures even though initial melt point is higher relative to coal. The addition of biomass to coal lowered the ash solidification points relative to coal due to increased amounts of alkali metals, calcium and magnesium. Furthermore, an increase in aluminium and decrease in alkali contents of the coal/biomass slags lead to lower melting points but higher solidification points relative to pure biomass [89]. Quantitative analysis whilst useful may not be the answer to the problem of a simple reliable test to predict the slagging and fouling propensities of solid fuels.

2.4 Conclusions

Coal fired boilers are a product of over a century of development, resulting in the pulverised fuel boilers used in the power industry today. Pulverised fuel boilers are capable of achieving efficiencies between 30-50%, depending on coal, boiler design and operating conditions. Slagging and fouling in pulverised fuel boilers have until recently been a background issue which reduce the efficiency of operation and require regular maintenance. Since the implementation of carbon budgets and the renewables boom however, the use of biomass in PF boilers has significantly increased in an attempt to reduce carbon emissions. Consequently, due to the increased propensity of biomass to cause slagging and fouling, these issues have come to prominence. The existing tool that is used by industry to predict the onset of fouling and slagging, the ash fusion test, has 2 well documented short comings that lead to inconsistencies. The method is inherently subjective as it relies on the observation of an operator to identify key events. This has seen discrepancies between results from different operators and laboratories. The adoption of automation using image analysis can successfully remove the subjectivity of the test. More importantly however, the test has been shown to be unable to accurately represent the onset of fouling and slagging. The attempts at addressing the second of the 2 issues have presented potential answers through the use of shrinking analysis or a more comprehensive analysis as shown by Pang et al., however further research is required in these areas. There is a clear potential for the development or adoption of these ideas to produce

a test that can more accurately and easily assess the slagging and fouling propensity of ash.

Chapter 3 : The Impact of Ash Pellet Characteristics and Pellet Processing Parameters on Ash Fusion Behaviour

3.1 Introduction

Slagging and fouling are key issues for the power industry and cause significant problems with continuous, long term boiler operation [18], [19]. Whilst there are various methods for the prediction of slagging and fouling such as, dilatometry/shrinkage tests [16], [77], [79], sinter strength tests [56], [111], viscosity measurements [112], [113], and a range of empirical indices [112], [114]–[117], the AFT is 1 of the most popular methods [111], [113], [115], [118], [119]. The AFT was developed in the early days of the power industry to predict clinker (large lumps of ash) forming characteristics in stoker furnaces [11]. It continues to be used, with minimal changes to the methodology since its inception in the early 1900s [11]. The current method of preparing samples for the AFT relies on hand-made cones or cylinders of ash, combined with a binder, sometimes with the use of a hand press. The use of hand pressed cones and can lead to poor repeatability [9], [11], [16], as well as uncertainty and subjectivity to the results. Attempts to make the test more analytical have been achieved by means of Thermo-mechanical Analysis (TMA) [16], [81], [120]–[122]. Further to the empirical tests, multiple predictive methods are documented [86]–[88], [96], [113], [117], [118]. A more recent review

correlates sticking probability to ash fusion temperatures alongside other modelling techniques [123].

During AFT, 4 discrete temperatures are noted; shrinkage temperature (SST) (biomass only), initial deformation temperature (IDT), softening temperature (ST) (coal only), hemisphere temperature (HT), and flow temperature (FT) based on shapes given by the regional standards [12]–[15]. These temperatures provide a prediction of slagging and fouling onset. The key temperatures utilised in power stations are IDT and FT. These temperatures are used to predict melting phenomena of a fuel ash in the boiler. In today's more sophisticated boilers, the test is used to inform fuel selection, as a method to identify the potential for unexpected slagging phenomena. Clearly this knowledge can be used by generators who use mixed fuels from a range of locations to create a blend with controlled slagging/fouling characteristics [124]. The repeatability of the test has been questioned with differences of up to 400^{o}C in IDT having been documented [16]. This uncertainty in IDT results makes it hard to make informed decisions based on melting temperature. Poorly identified melting characteristics of fuel ash could lead to premature outage or sourcing of unsuitable fuels. Thus, generators require a more reliable process with a clear illustration of behaviour.

Multiple efforts have been made to improve the ash fusion test [16], [79], [81], [104], [105], none of which have been adopted by industry. Questions surround the stability and consistency of the cone structure, and whether the toppling of the top of the cone is truly the first deformation of the

pellet. If any of these criteria are not satisfied by the current test method, then the cone pellet may not be the optimal shape to represent trigger points for deformation.

Ashing temperature (where the fuel is combusted to provide the ash for the AFT) is defined by standardised procedures [103], [125], since it has been shown that ashing temperature plays a significant role in the AFT [126]–[128]. Image analysis techniques have proven useful in aiding flame characterisation [129]–[131] and coal petrography [132]–[134]. Pang *et al*. [9] adopted the basis of the AFT but used an automated image analysis method to plot a curve of relative height of the pellet against temperature. This study focused on providing a characteristic curve for biomass ash however, the workers did not examine the effect of different pelleting methods on the AFT results.

The current coal standard cone theorises that the IDT is identified when the top point of the cone (considered to be a single point) melts [9]. The biomass standard uses cylinder which has 2 corners which enables 2 points to be averaged. However, the significance of this point of initial deformation is contentious in literature, as melting phases can be identified at earlier points in the test without a change in sample geometry [123], [135]. Thus, gaining more insight into the melting processes, as well as developing a more repeatable and reliable process are of paramount importance.

In this study, a range of pelleting processes have been investigated to identify the most repeatable and representative method of identifying the IDT. A progressive investigation was conducted to optimise each aspect of the

process, with the aim of producing a robust and highly repeatable ash fusion test. Additionally, a modified version of the picture analysis and graphing (PAnG) AAFT was used to provide novel analysis of the ashes and develop AFT characterisation curves which might provide an insight into the ash fusion behaviour of solid fuels. This study aims to address the issues with repeatability by presenting a fully mechanised pellet production process and automated AFT process using a novel image analysis technique. Furthermore, for the first time, a wide range of pelleting methods will be directly compared, and an optimal preparation methodology has been identified.

3.2 Materials and Methods

Kellingley is a typical UK coal provided by DRAX Power plc and was selected as the 'standard' for the optimisation of the test as it is well known throughout the industry and has been widely used in UK coal fired power stations. A further 4 fuels were selected to verify the findings of the optimised method; 2 international coals including a Colombian (La Loma) coal, and a South African (Zondag) coal; 2 white wood biomass, denoted B117 and EC78 supplied by DRAX Power plc.

3.2.1 Milling and Ashing

The coal was milled to below 212 µm in accordance with the ASTM standard [136], and the biomass was milled to below 1 mm to represent the size specification for biomass fired boilers [137]. The coals were then milled down using a Retsch Jaw crusher BB 100 mill from 10 cm down to 2-10 mm. The

samples were then milled sequentially using 3 screens of the Retsch SM2000 Knife mill to obtain a particle size of 70% below 325 µm (4 mm screen: 5 – 10 mm to 70% below 2 mm, 1.5 mm screen: to 70% below 750 µm, and 750 µm screen: to 70% below 325 µm). A TEMA machinery disc mill was then used to achieve a particle size of 100% below 212 µm. The biomass was milled below 1 mm using the Retsch SM2000 knife mill with 4 mm and 1.5 mm screens in series. This generated a particle size of 70% below 750 µm.

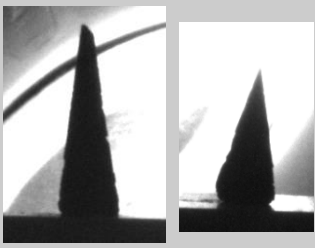
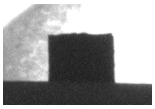
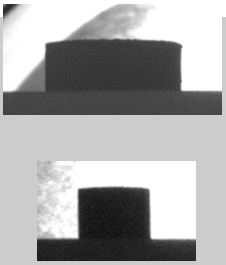
Coal samples were ashed at 815°C ± 15 [125] and biomass at 575°C ± 15 as required by the standards [138]. Large alumina rectangular crucibles (SS200S: L204 mm X W105 mm X H25 mm) from Almath Crucible LTD were used to maximise ash product. The ashing took place under a continuous air flow condition in a Carbolite GSM Ashing Furnace. Coal was raised to 500 ^{o}C and held for 1 hour, then raised to 815 ^{o}C and maintained for 3 hours. Biomass was raised to 575 ^{o}C and held there for 3 hours. After ashing, the ash was sieved to pass 75 µm sieve [14], [15], and a TEMA disc mill was used to ensure that any leftover particles passed through the sieve.

For the voidage study and the milled and un-milled study, 72 µm and 250 µm sieve screens were used to represent the milled ash based on the standards and non-milled ash, respectively. The ash was stored in sealed glass vials (until use) to minimise ash moisture uptake.

3.2.2 Pelleting Method Optimisation Study

6 pelleting methodologies were used in the Pelleting Method Optimisation study; the 12 mm and 18 mm cone presses (dimensions given in Table 3-1) were made according to the standards [15] using dextrin (Acros Organics) and cone moulds supplied by Carbolite with the Carbolite Ash Fusion furnace; 5 mm Carbolite hand press with dextrin (denoted CHPD) and without dextrin (denoted CHP), and a custom cylindrical hand press made by Carbolite for the purposes of the ash fusion test. Finally, 5 mm and 10 mm machine pressed pellets (denoted MPPs) were made using an Instron Universal testing system 3360 Series (IUTS 3360) using varying pressures as detailed in Table 3-1.

Table 3-1: Pelleting shape descriptions

Shape/standard	Description	Diagram
COAL: **CONE MOULD WITH DEXTRIN**	The 2 cones shall be 19 mm [3⁄4"] and 13 mm [1/2"] in height and 6.4 mm [1⁄4"] in width.	
BIOMASS: **CHP**	This method involves making a, roughly, 5 mm high x 5 mm diameter pellet, with a handheld press.	
MPPs	10 mm and 5 mm dies are used to make pellets under 5000psi (34.47 Mpa) of pressure (2707N and 677N, respectively) and held for 1 minute. Pressing profiles shown in Figure 3-1.	

During the voidage investigation the IUTS 3360 was used to study additional pressures of 2500 psi and 7500 psi for pelleting the 5 mm pellet. Once pressed, the pellets were stored in a glass vial for protection to minimise moisture uptake.



Figure 3-1: Profiles for the MPPs tested during the pelleting method optimisation study

3.2.2.1 Cumulative Pelleting, Preparation and Ashing Study

To validate the investigations of the pelleting and preparation studies, a milled and unmilled matrix was created to test a range of fuels, detailed in Table 3-2. Included in the study was the addition of 2 different ashing temperatures to assess the impact. All milled and un-milled samples were pelleted at 2500 and 7500 psi to establish the scenarios.

Table 3-2: Sample preparation of the high pressure milled and low pressure un-milled scenarios

Sample	Ashing Temperature	Milling	Pelleting Pressure
High pressure milled	575	Milled < 75 µm	7500 psi
Low pressure un-milled	575	Un-milled	2500 psi
High pressure milled	815	Milled < 75 µm	7500 psi
Low pressure un-milled	815	Un-milled	2500 psi

3.2.3 Advanced Ash Fusion Test (AAFT)

The AAFT profiles were obtained using the Carbolite Gero Ash Fusibility Test Furnace - CAF G5 (Figure 3-2). Samples were place on Carbolite 25 mm x 25 mm recrystallised alumina (RCA) ceramic tiles and loaded in the furnace. The furnace temperature was increased from 25 ^{o}C to 1600 ^{o}C at a rate of 7 ^{o}C/min under oxidising condition (air flowrate of 4 l/min at 27.5 kPa (4 psi)). Images were taken every 1 ^{o}C on an integrated HD 1.3 Mb camera with an image size of 1280 by 1024 pixels. MATLAB (version R2017b) was used to analyse each image in a process adapted from work by Pang and co-workers [9]. The images are cropped automatically based on the starting location of the sample. The pellet was then automatically tracked during the experiment using a combination of edge detection and thresholding techniques. 5 thresholding techniques were used in total including Canny [139], Otsu [140], Prewitt [141], Bradley Adaptive Thresholding [142], and Log methods [139]. These techniques were chosen based on the different image histograms obtained at different

points in the test. Canny and Otsu were both suited to the early test back lit range of images (0-500 ^{o}C). Prewitt was used in the transition where the back light turns off and the radiative light begins (500 – 800 ^{o}C). Finally, the Bradley and log methods were better suited to the end test images (800 – 1600 ^{o}C). These techniques are used to create a pellet outline.

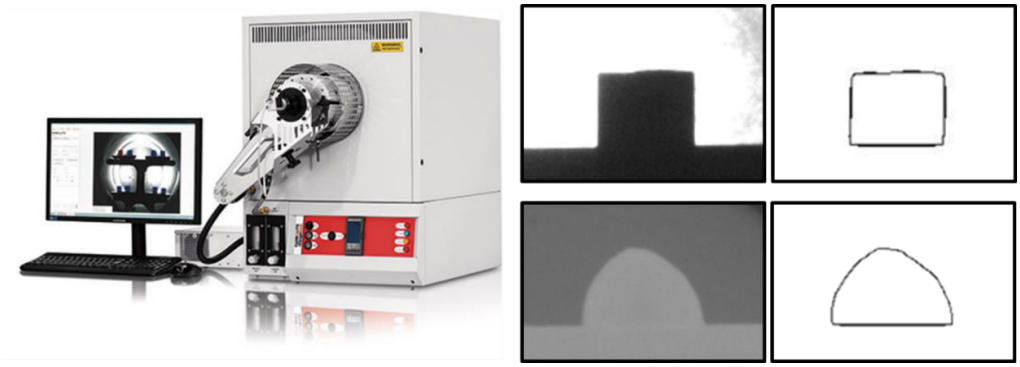


Figure 3-2: CAF furnace, images generated, and processed images

This outline was then used to capture the height and centroid parameter of the pellet. The centroid was used to track the location of the sample and the height was compared to the initial height of the pellet to plot relative height. Each sample was run in triplicate, with the average displayed on the AAFT plot. The standard deviation of the 3 runs is displayed on the AAFT profile as a shaded-out area and illustrated in Figure 3-3.

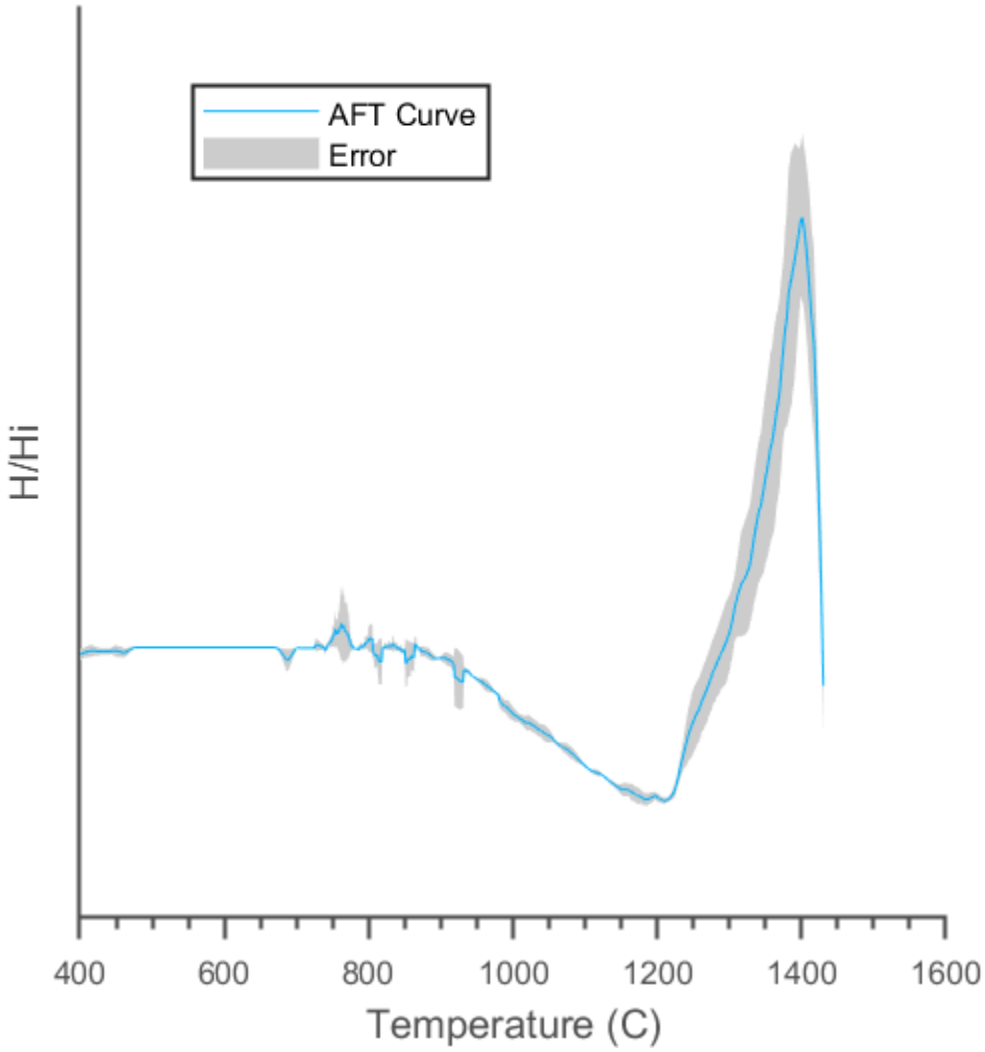


Figure 3-3: Typical AAFT profile (250 µm sample, voidage investigation)

3.2.4 Thermogravimetric analysis (TGA)

Proximate analysis was carried out using TGA. Thermal profiles were produced using TA Instruments Q500 TGA. Tests used 10-15mg of sample with a particle size range of 75-300µm. The sample was heated in a furnace at 5 °C.min^{-1} in 100 ml.min^{-1} of nitrogen from atmospheric temperature to 900°C, after which the gas was switched to air at 100 ml. min^{-1}. The composition of the samples is given by moisture, dry ash free volatile, fixed carbon, and dry ash contents. In addition, the percentage of volatiles at 575°C, 815°C and 900°C was obtained from the profiles[143].

3.2.5 Pelleting Mould Type Selection Criteria

4 criteria were selected to evaluate the optimal pellet mould type for the AAFT. Repeatability, error, morphology and IDT 'trigger' (defined in Table 3-3) were selected and each were given a weighting based on discussions with industrial end users and the key parameters taken from the AFTT. This is summarised in Table 3-3, a higher value represents higher importance. The performance of each pellet was ranked from 1-6, with 6 being the best.

Table 3-3: Selection criteria for evaluating pelleting process

Criteria	Description	Evaluation	Importance value (Low: 1 – High: 5)
Repeatability	How closely the key temperatures of the same sample match	Based on how close IDT readings are for repeat samples	5
Error	How close each plot matches the plot of repeats at the IDT	Average standard deviation (Av(SD (H/H_i))) of the repeat samples between 1100 – 1300 ^oC	3
Morphology	How much the gradient of the plot changes at the IDT	Based on the sum of change in gradient ($\sum\Delta H$) between 1100 – 1300 ^oC	3
IDT Trigger	How early the plot displays IDT	Based on the average IDT for repeat samples	5

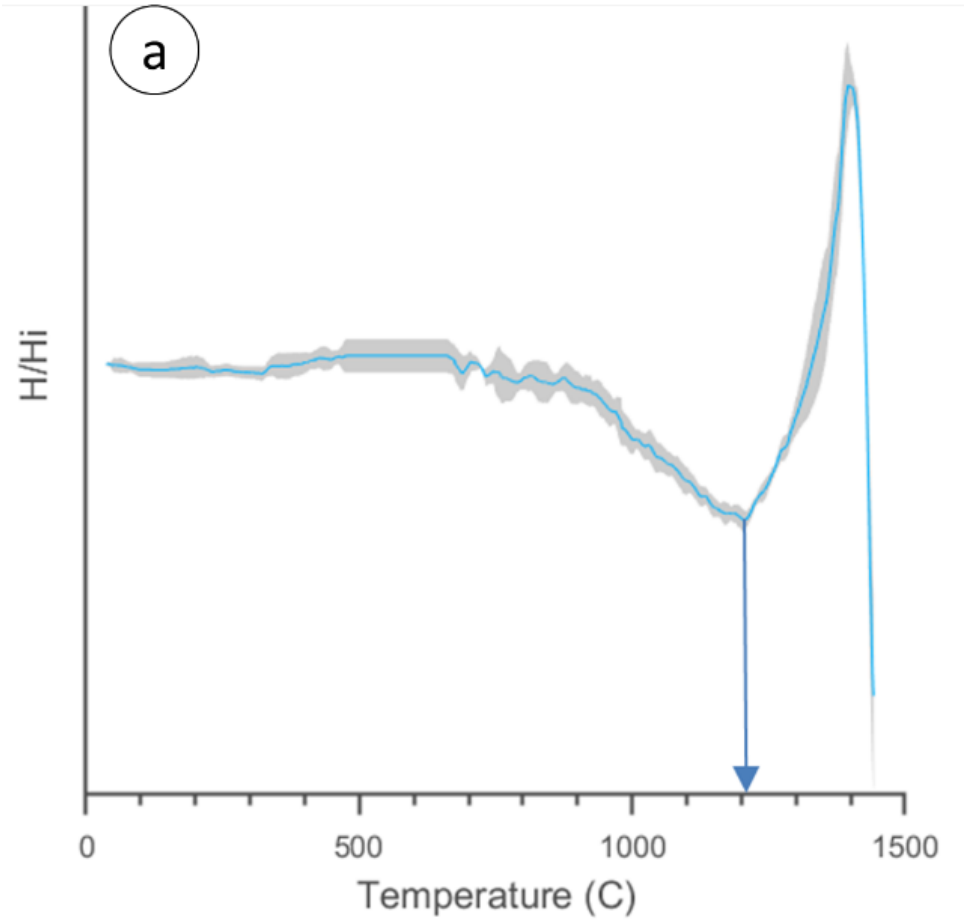
3.3 Results and discussions

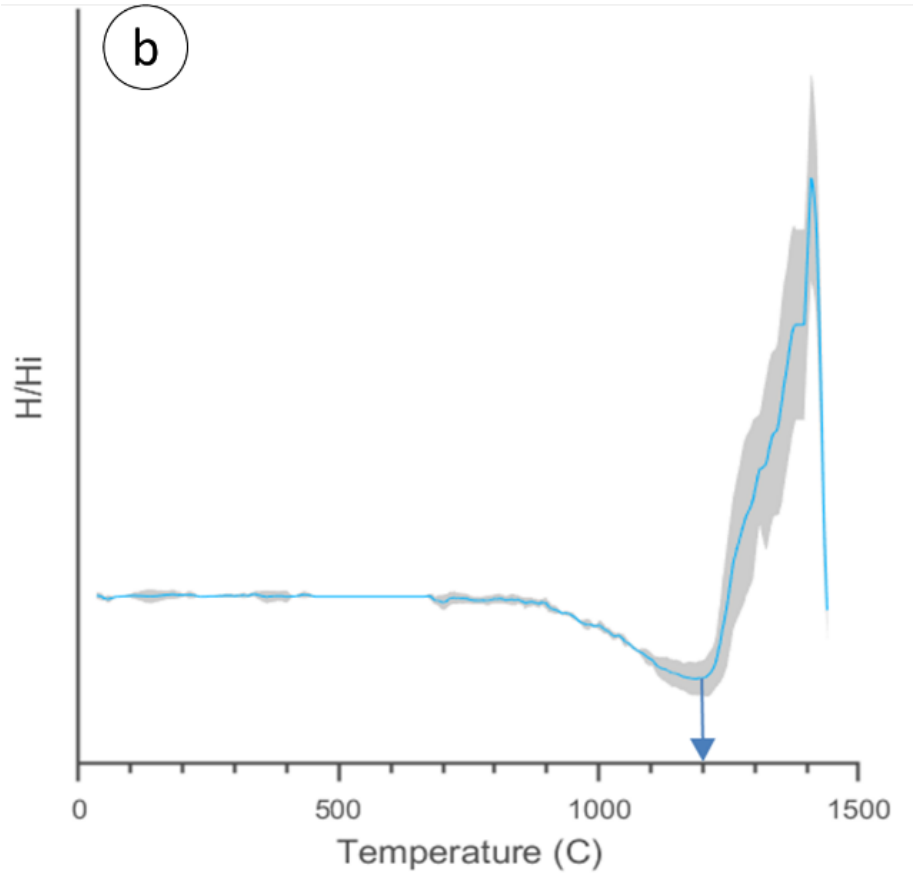
3.3.1 Impact of pellet type on the AAFT

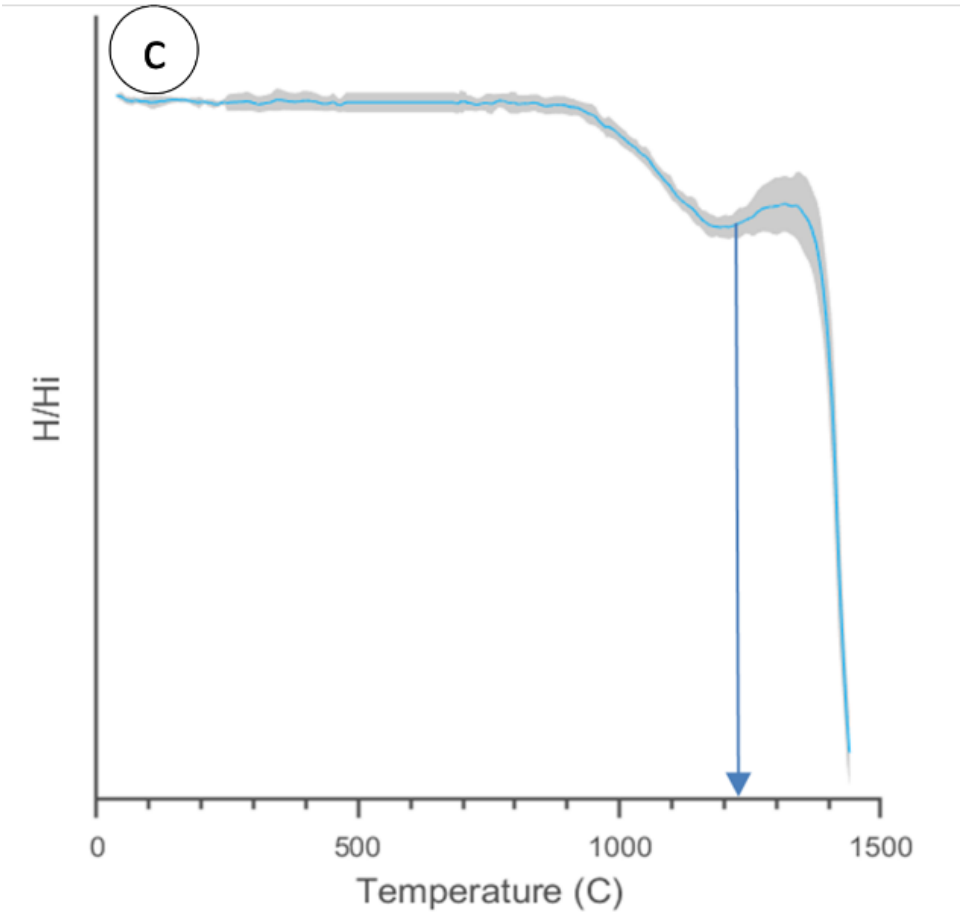
In this section Kellingley coal ash has been pelleted using a range of different methods and tested in the Carbolite CAF G5 furnace. Image analysis was used to produce a plot of relative height of the pellet during melting and manual analysis was done to highlight the IDT trigger, which is defined as the first deformation after shrinkage. Due to the evidence that melt phases occur earlier than that identified by the traditional AFT method [123], [135], it has been assumed that the earlier the first significant visible melting event occurs, the more accurate the measure of the actual IDT trigger will be.

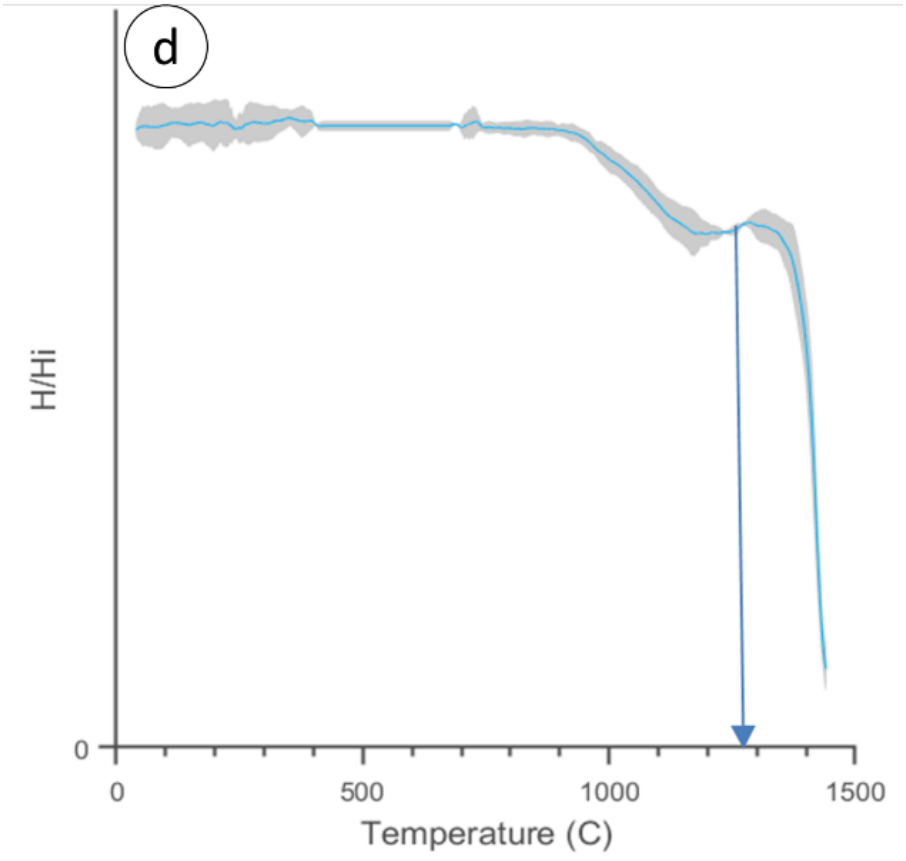
3.3.1.1 Repeatability

The first stage of the study explored the repeatability of the different mould processing methods. Figure 3-4 displays the AAFT curves for each of the moulds tested. As noted in Table 3-3, the error is represented by the shaded area between 1100-1300 ^{o}C, which is the key area of interest. Morphology is represented by the total change in height (ΔH) over the range of 1100–1300 ^{o}C. Finally, the IDT trigger point is denoted by the arrow on each curve.


a
H/Hi
0
500
1000
1500
Temperature (C)


b
H/Hi
0
500
1000
1500
Temperature (C)


c
H/Hi
0
500
1000
1500
Temperature (C)


d
H/Hi
0
0
500
1000
1500
Temperature (C)

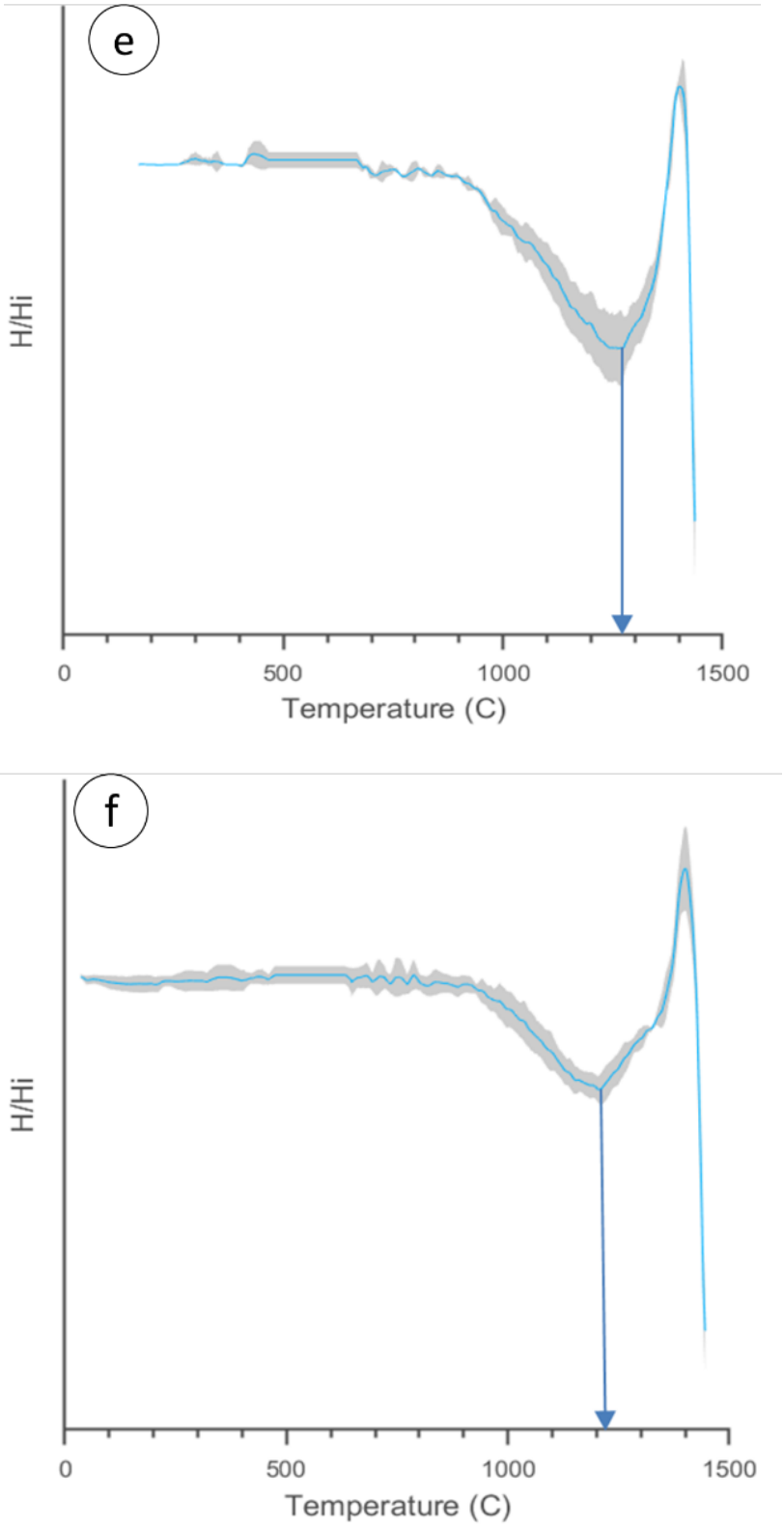


Figure 3-4: Plots demonstrating the error, morphology, and IDT trigger of each pelleting method; a) 5 mm MPP, b) 10 mm MPP, c) 12 mm cone, d) 18 mm cone, e) CHP, f) CHPD (n=3)

1 of the fundamental aspects of the test is how repeatable it is. Table 3-4 shows the variability of IDT for different mould samples for Kellingley ash. The 5 mm MPP was the most repeatable (< 10 ^{o}C), while the 12 mm cone performed the poorest with a variance of 100 ^{o}C. The variance in the results shows that, on average, cones had significantly more variation in IDT than cylinders, with the MPPs and hand presses showing a variance 4 times lower (±20 °C) than that of cones (±90 °C). The CHP (20 °C) and CHPD (40 °C) display comparable repeatability to the MPPs with a simpler pelleting method. When compared to the British standards for coal fusibility repeatability guidelines for deformation temperature (30 °C, Table 3-5) , only the 5 mm and 10 mm MPP and the CHP meet the standards. This investigation would need to be repeated to evaluate reproducibility.

Table 3-4: Selectivity matrix ranks for the pelleting methods in the categories on repeatability, error, morphology, and IDT trigger

Sample	Repeatability (°C)	Error Av(SD (H/H_i))	Morphology ∑(ΔH)	Trigger IDT (°C)
MPP (5 mm)	<10	0.0133	0.118	1204
MPP (10 mm)	<20	0.0803	0.363	1200
Cone (12 mm)	100	0.0179	0.059	1320
Cone (18 mm)	80	0.0135	0.033	1256
CHP (5 mm)	20	0.0368	0.093	1270
CHPD (5 mm)	40	0.0210	0.086	1220

Table 3-5: Maximum acceptable differences between results [28]

	All atmospheres	
Fusibility of ash	Repeatability (°C)	Reproducibility (°C)
Deformation temperature, DT *a*	30	80

a If the sphere temperature is not reached, the precision on deformation temperature might not be achievable.

3.3.1.2 Error

There are no units for error as it is a relative value of height/initial height. The averaged results from the error study for cones (12 and 18 mm) compared to cylinders (CHP and CHPD), would suggest that the cones performed best (0.0157) when compared to the cylinders (0.0379). The 2.5x reduction in error can be attributed to the lack of change in morphology displayed in Figure 3-4, which hinders the indication of IDT. Furthermore, Figure 3-4 shows that the low error may be a result of coincidental crossing of the plot as opposed to common curve shape. The 5 mm MPP gives the most repeatable curve with an average error of 0.0133. This is attributed to the smaller size of the pellet as well as the consistency of the pelleting process. The 10 mm MPP appears to be an outlier, not least because it is made using the same process as the 5 mm MPP but it produces the highest error of 0.0803. In contrast to the 5 mm pellet, its size allows greater scope for error in repeatability of the curve shape shown in Figure 3-4. This suggests that minimising the size of the pellet in the analysis will give less error and probably create a more consistent morphological change.

3.3.1.3 Morphology

When comparing the morphology, the IDT is best represented by the cylindrical pellets (0.093, 0.086, 0.118, 0.363), as the cones (0.059, 0.033) do not drastically change shape at the key trigger temperature. This is illustrated visibly by the plots in Figure 3-4, and by the low ∑ΔH in Table 3-4, which is, on average, 4x greater deformation displayed by the cylinders. A similar change is seen when handmade pellets (0.059, 0.033, 0.093, 0.086) are compared with the MPPs (0.118, 0.363). This suggests that the increase in morphology is linked to the MPPs as opposed to the change in shape. The means that making the pellets at a higher pressure will result in greater change in morphology and easier indication of the IDT. The 10 mm MPP showed the greatest change (0.363) however, this was at the expense of increased error as it also displayed the greatest error (0.0803).

3.3.1.4 IDT trigger level

Alongside the repeatability, the IDT trigger is of equal importance. If the IDT trigger can be reduced, earlier melting will be indicated, and thus the allowable limits for IDT may need to be shifted. Table 3-4 shows that the range in IDTs identified by all the tests was 116 ^{o}C. This illustrates the extent that the relevance of pellet type has on IDT. The lowest IDT achieved was 1200 ^{o}C by the 10 mm MPP, closely followed by the 5 mm MPP (1204 ^{o}C). Although the CHP (1270 °C) was more repeatable than the CHPD (1220 °C) the dextrin appeared to improve the IDT trigger of the CHP. The clear results in Table 3-6

originate from the 5 mm MPP. The 5 mm pellet was therefore carried forward to the next stage of testing.

Table 3-6: Selectivity matrix summary for the mould type analysis

Criteria (weighting)	5 mm MPP	10 mm MPP	12 mm Cone	18 mm Cone	Hand press	Hand press w/d
Repeatability (5)	6	5	1	3	4	2
Error (3)	6	1	4	5	2	3
Morphology (3)	5	6	1	2	3	4
IDT Trigger (5)	5	6	1	3	2	4
Totals out of 96	93	71	25	51	45	51

3.3.2 Impact of material preparation and furnace heating rate for the 5 mm MPPs

Factors such as mineralogy, particle size, water content and applied pressure affect thermal conductivity of a material [144], [145]. The size of the ash particles in the pellets, and the pressure with which they are made will determine the physical void fractions thus, the degree of differential temperature and stress within the pellet. The results from the previous study highlighted the 5 mm MPP as the best option for pelleting. This pelleting method will be used to investigate the impact of particle size, pelleting pressure and heating rate on the IDT trigger. Kellingley ash was again used to study 2 particle sizes, 4 pressures and 3 heating rates.

3.3.2.1 Particle size

To examine the impact of particle size, 2 extremes were tested. A particle size of <72 µm, (according to the ash fusibility standards [14], [15]), and <212 µm (the standard for coal milling prior to pf combustion [136]) were used. This has been designed to investigate how an additional ash milling stage impacts on the results. Table 3-7 shows that the <72 µm (No. 400) particle size sample gave an IDT of 1200 ^{o}C which matches the outcome of the 5 mm MPP from the previous mould study. The <212 µm (No. 60) resulted in an IDT of 1220 ^{o}C, a difference of 20 ^{o}C. This difference in IDT is attributed to the increase in particle size and therefore, an increase in voidage in the pellet which reduces the heat transfer through the pellet.

Table 3-7: IDTs of the particle size, pressure and heating rate investigations on Kellingley coal

Sample	Particle size		Pressure		Heating rate		
	72-µm	212-µm	2500 psi	7500 psi	4 ^{o}C /min	7 ^{o}C /min	10 ^{o}C /min
IDT (^{o}C)	1200	1220	1228	1200	1196	1198	1210

3.3.2.2 Pelleting Pressure

The next investigation studied the impact of increased pressure during the pelleting process displayed in Table 3-7. As before, 2 extremes were used, 2500 psi which was at the low end of pressure and produced an IDT of 1228 ^{o}C, and 7500 psi and gave 1200 ^{o}C. Increasing the pressure during the pelleting process decreases the IDT of a sample by 28^{o}C, this is comparable to the

difference from the MPPs and the standard hand press with dextrin. The difference is that the low MPP still had excellent repeatability, but with a delayed response to IDT. The delay in IDT can be attributed to increased voidage in the pellet. Whereas non-uniform particle size will increase voidage, the increase in pressure applied to the pellet will reduce the voidage in the pellet and increase particle to particle contact improving heat transfer.

3.3.2.3 Heating rate

The heating rate was varied to investigate the sensitivity of the key melting phenomena and the characteristic profile. 3 heating rates were used, 4 ^{o}C/min, 7 ^{o}C/min, and 10 ^{o}C/min as displayed in Table 3-7, the resultant IDTs for each were 1196 ^{o}C, 1198 ^{o}C, and 1210 ^{o}C, respectively. The slower the heating rate, the lower the measured IDT. This marginal decrease in IDT can be attributed the slower heating rate allowing the pellet more time to heat up and reach the specified temperature.

3.3.3 Cumulative Influence of Pelleting, Preparation and Ashing on 5 Different Fuels

This study has already shown that the temperature of the first melting phenomenon can be reduced by using machine made pellets and ensuring that the ash being used in the pellets has been pre-milled. The maximum IDT range were 28 ^{o}C and 20 ^{o}C based on pelleting pressure and particle size, respectively. The following section investigates whether these effects are cumulative. Furthermore, it is still speculated as to whether ashing temperature has a significant impact on the AFT[126], [128], [146], [147]. 4 additional fuels were

selected to examine the impact of pelleting method, preparation and ashing temperature.

Initially proximate analysis was carried out on the 5 fuels to identify differences in volatile content at different points in the ashing process. This was broken down into moisture in the coal, dry ash %, fixed carbon %, and the amount of volatiles released at the low ashing temperature, 575 ^{o}C , the high ashing temperature, 815 ^{o}C, and the total volatiles released at the end of the test, 900 ^{o}C. The fixed carbon, dry ash, and volatiles at 900 ^{o}C sum to 100 %.

Table 3-8 shows that as temperature increases, the coal samples observed the greatest change in thermal decomposition, which released double the volatile contents at 815 ^{o}C compared to 575 ^{o}C.

Table 3-8: Comparison of the change in thermal decomposition with increasing ashing temperature

Sample	Moisture Content (%)	Dry Volatiles @575^{o}C (%)	Dry Volatiles @815^{o}C (%)	Dry Volatiles @900^{o}C (%)	Fixed Carbon (%)	Dry Ash (%)
Kellingley	2.7	15.65	27.64	28.2	47.7	24.1
La Loma	3.6	19.7	30.3	30.2	51.3	19.2
Zondag	4.9	14.3	27.0	27.6	63.2	9.1
B117	6.5	80.3	83.9	84.7	13.8	1.4
EC78	6.4	79.9	82.9	83.6	14.3	2.1

Section 3.3.1 highlights the optimum pelleting methodology to be used. Any further variation in this test is due to the preparation of the ash or pressure during pelleting. The key temperatures used to compare the Impact of pellet type on were IDT, and the FT.

3.3.3.1 Impact of pelleting on IDT trigger level

Table 3-9 shows that the IDT is delayed from the milled to un-milled case pellets and this effect is consistent across all samples. The average increase in IDT is 32 ^{o}C, and in some cases, there is as great a difference of up to 58 ^{o}C (EC78). This large change suggests there is a cumulative impact (for biomass) on the IDT from both increased pelleting pressure and no pre-milling.

Table 3-9: Comparing pellet preparation methods on IDT trigger

Sample	High pressure milled 575 (^{o}C)	Low pressure un-milled 575 (^{o}C)	Difference (^{o}C)	High pressure milled 815 (^{o}C)	Low pressure un-milled 815 (^{o}C)	Difference (^{o}C)
Kellingley	1168	1220	52	1194	1238	44
B117	1208	1211	3	1314*	1238	-76*
EC78	917	975	58	920	1040	120
Laloma	1169	1194	25	1181	1192	11
Zondag	1272	1298	26	1275	1292	17

*Note: The B117 ashed at 815 and pelleted at 7500 psi gave inconsistent outputs even with multiple repeats.

Table 3-9 also shows that a similar phenomenon was observed when the same samples were ashed at 815 ^{o}C. The average increase in IDT in this case was 47 ^{o}C, excluding the B117 sample. The average in this instance is skewed by the EC78 sample, but even so, there is a general increase in IDT of 24 ^{o}C, which is comparable to the results of the 575 ^{o}C ash. This suggests that the difference between the milled and unmilled methods is responsible for an average delay in IDT trigger of 28 ^{o}C. The results illustrate there can be a cumulative impact of pressure and particle size, but there is a delay in IDT due to poor preparation methods. These results were obtained with excellent repeatability, by using the most repeatable pelleting method (MPP) from Section 3.3.1. The milled and un-milled pelleting condition supports the results of the voidage study with the optimum method consistently reducing the IDT. In the case of EC78, the improvement was as high as 120 ^{o}C. There is an indication from the results that the relative change in IDT for biomass bigger than for coal. It is possible that some fuels are more impacted than others. Further work is required to explore this for a greater range of biomass and emerging fuels such as algae and refuse derived fuels.

3.3.3.2 Impact of ashing temp on IDT trigger level

Table 3-10 illustrates that there was a small impact on IDT as a result of ashing temperature. For the milled scenario, the average reduction in IDT was 11 ^{o}C, and for the un-milled case, no general trend was observed. Increasing the ashing temperature delayed the IDT for both biomass samples. The impact

was not consistent for the coal samples in the un-milled-case scenario, with the majority seeing negligible impact.

Table 3-10: Comparing effects of ashing temperature on IDT trigger

Sample	High pressure milled 575 (°C)	Low pressure un-milled 575 (°C)	Difference (°C)	High pressure milled 815 (°C)	Low pressure un-milled 815 (°C)	Difference (°C)
Kellingley	1168	1194	29	1220	1238	18
B117	1208	1314*	107*	1211	1238	28
EC78	917	920	3	975	1040	65
Laloma	1169	1181	12	1194	1192	-3
Zondag	1272	1275	4	1298	1292	-6

There are no trends to link to the TGA volatile release data from Table 3-8, which showed that 50% of the volatilised species were loss after 575 °C in the coal samples. This suggests that any effects of ashing on the IDT or FT may be linked to the release of residual volatiles. It can be concluded that the release of volatiles between 575 °C and 815 °C does not play a role in AAFT. Whilst the biomass samples did not show a greater volatiles release between 575 °C and 815 °C, there was a delay in the IDT in the un-milled-case samples. This further supports that volatile release and ashing temperature does not play a role in ash fusibility. This supports the conclusions from some literature[127], whilst contradicting the findings of other researchers [126], [128]. The latter clearly states that an increased ashing temperature increases IDT. The method of pelleting for these studies were the standard cone press, which has been shown to have poor repeatability and delayed IDT trigger. A

larger investigation including a wider range of fuels, using the optimised method would provide a strong conclusion to the impact of ashing temperature on AAFT behaviours.

3.3.3.3 Flow temperature

The impact of pelleting, preparation and ashing on FT was negligible, and proved to be less affected by varying the particle size, pelleting pressure and ashing conditions. On average, the difference in FT for coal milled and un-milled cases was 3 ^{o}C, and for the ashing comparison was 14 ^{o}C. The biomass results showed a reduction in FT of 12 ^{o}C for the milled-unmilled comparison. The ashing study revealed a 28 ^{o}C general increase in FT for the 815 ^{o}C ash compared with the 575 ^{o}C ash, but this was the only instance that showed comparable change to the IDT study.

3.3.4 The optimised advanced ash fusion test (OAAFT)

The optimised version of the AAFT satisfies the need to create a standardised test that is clearly repeatable whilst giving the best representation of the first point of melting. The equipment used to create the MPPs, IUTS 3360, is common in mechanical engineering test laboratories throughout the world, is low cost and requires low skill to operate. The potential impact on standard fusibility tests for coals [14], [15] may require increased detail in preparation of ash and adopting of 5 mm MPPs. Furthermore, the repeatable nature of the OAAFT test curve means that there is a potential to utilise this characteristic curve to understand more about ash

behaviour in relation to onset of slagging and fouling. This curve is unique to the fuel being tested and a database of fuels might then be used to help predict blending properties. The OAAFT process includes:

- The selected fuel milled to below 212 µm
- Ashed at 575/815 ^{o}C (biomass/coal)
- Ash milled to below 76 µm (if any particles do not pass include them in the sample)
- 0.100g of ash (± 0.05g) compressed into 5 mm pellet at 7500psi
- Ash fusion test run at 7 ^{o}C/min from room temp (or 300 ^{o}C for consecutive tests) to 1600 ^{o}C/completion of the test (or capacity of the furnace)

This test used a novel pelleting methodology to provide greater repeatability, change in morphology and earlier indication of IDT. It has been verified by 5 different fuels including 3 coals and 2 biomasses and reinforces the importance of consistent ash preparation.

3.4 Conclusions

This study investigated the different pelleting types used during the ash fusion test to develop an optimised preparation technique with enhanced accuracy and reliability. This method was then applied to a range of other fuels to verify the technique and assess the significance of ash preparation. A modified version of the AAFT was used to generate the AFT profiles and highlight key temperatures. The novelty of the work identifies a new pelleting

method for the AAFT and identifies its impact on a range of industrially used coals and biomass. The findings which can be drawn from this study are:

- For the first time, it has been shown that cones and the hand pressed pellets do not have good repeatability and delay the response of the IDT when compared directly to the MPPs.
- The 5 mm MPP provided excellent repeatability, identified the 2nd earliest IDT (after the 10 mm MPP), gave the least error and displayed the greatest change in H/Hi to enable easier identification.
- Reducing maximum ash particle size to less than 72 µm and increasing the pressure of the pelleting process can produce a 120 ^{o}C reduction in the IDT, with an average reduction of 40 ^{o}C.
- A reduced ashing temperature for coal and biomass resulted in no evidence to support ashing temperature plays a role in IDTs therefore, volatiles lost during ashing played no part in the change in IDTs.
- Preparation of ash and pelleting method has a greater impact on biomass ash compared to coal ash.
- An optimised advanced ash fusion test (OAAFT) has been developed.

The optimised version of the AAFT creates a standardised test that is repeatable and gives the best representation of the first point of melting. This test will be useful to generate comparable results to aid in boiler operation and fuel selection decisions which might help prevent premature outages and the sourcing of unsuitable fuels.

Chapter 4 : Automated Image Processing and Shape Analysis and Clustering

4.1 Introduction

The previous chapter illustrated the significant improvement in repeatability made to the AAFT by scrutinising the pelleting process. The OAAFT offers a vastly more repeatable and accurate test with a curve profile instead of the traditional temperatures. This chapter will discuss the development of functions to enable fully automated image processing and the clustering of shape parameters to find the optimum characteristic profile.

4.1.1 Automated Image Analysis

The use of image analysis to automate processes, once thought not possible for computers, is increasing. Computer vision has grown rapidly in recent years from uses such as sign recognition for driving assisted cars to facial recognition for security purposes. The availability of high quality cameras and large storage devices facilitates the use of image analysis on simple applications.

There are a range of ways to identify features in an image including Scale-Invariant Feature Transform (SIFT), Speeded-Up Robust Features (SURF) and Histogram Oriented Gradients (HOG) descriptors. SIFT and SURF are useful for identifying unique points of interest however, the images obtained from the CAF furnace have many ‘unique’ features, not just the samples which are the target. Corner detection algorithms suffer from the same hindrance of multiple detectable non-target corners. Features of stock sample images are

obtained using the HOG descriptors and these features are fed into a support vector machine (SVM). The SVM essentially clusters the images into images that contain samples and images that don't contain samples. Deep learning, such as convolutional neural networks, could also be used however, these methods are way too computationally expensive, and the desired outcome can be achieved with less overheads.

To obtain the shape data for the plots an image is taken of the stage every 1 ^{o}C. The test starts at 30 ^{o}C and finishes at 1600 ^{o}C therefore, there are more than 1000 images to process. In the traditional CAF furnace, the samples could be run from 815 – 1600 ^{o}C. By which time the light radiating from the heat in the furnace would be enough to highlight the samples and perform analysis. However, the new CAF test furnace includes a back light to enable analysis of the samples at lower temperatures. This is useful when testing biomass due to its lower melting temperatures. This set up creates a complex change in contrast between the artificial light form the back light between 0 – 400, the transition period between 400 – 800 and the natural light from the heat from 800 – 1600.

During analysis, the digital images are viewed as 2-D matrices where each value represents a small square area of the image called a pixel [148]. Segmentation techniques are the first step in classifying or cropping an image for analysis and many are case specific [149]. There are no '1 size fits all' segmentation techniques [150], and with a set of changing images, it may be required to use multiple methods. 1 of the most common techniques is

thresholding, which isolates the subject by removing the background. This is achieved by analysing an images histogram frequency and locating the clear divide in peaks. This can be problematic when the image histogram is not as straight forward [148], [151], [152].

The main types of edge detection can be grouped into 2 categories, gradient and Laplacian [153]. They use first derivative maximum and minimum and second derivative zero crossing respectively. Direct comparisons have been made which illustrate drawbacks in both methods due to large contrasts between images [153]–[155].

There have been a range of studies whereby obtaining data from complex images is achieved and optimised using a range of different edge detection and thresholding techniques [148], [153], [156], [157]. The best way to identify the optimum technique is to test a wide range of methods.

4.1.2 Shape Analysis and Clustering

The PaNG profile uses the height of the pellet which isolates analysis to a single point. Whilst this simplifies the analysis, there is a lot of unharnessed information from the deformation being missed. There are multiple raw variables, such as area, perimeter, height, width etc., changing during deformation whilst and there are further manipulations based on these raw variables that can be calculated. Such variables and manipulations have been compared and categorised before in characterising the morphology of volcanic ash [158]. The use of standard scores or ‘Z scores’ can be used to compare the parameter which have large differences in scale [159].

Furthermore, the standard ash fusion has 4 discrete temperatures which have subjective descriptions and shape guidelines as shown in Figure 4-1 from the standards. The conversion of these descriptions into code would create a repeatable point of reference as opposed to a subjective operator observation. PaNG denotes 4 phases which are clearly linked to height of an ideal curve shown in Figure 2-20. These regions relate to the sintering strength and porosity of the ash during these phases. Linking these existing triggers to shapes and identifying the morphological properties of these shapes are the first steps in identifying these trigger points.

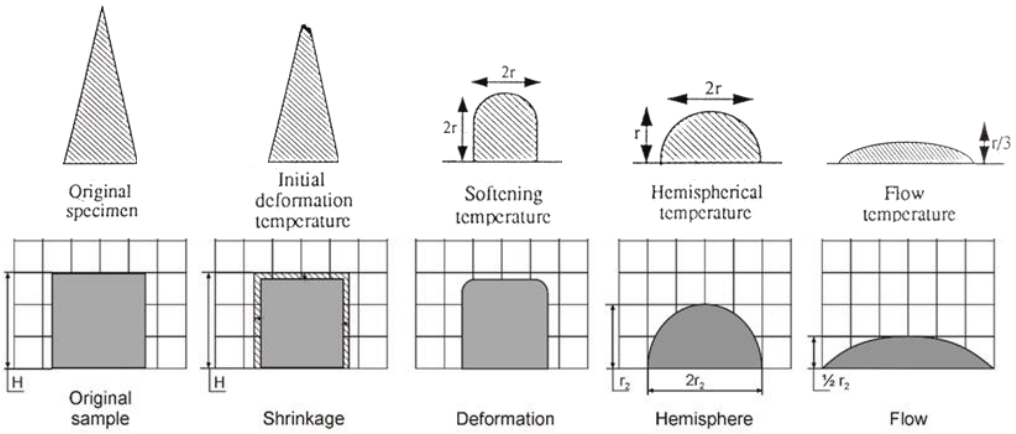


Figure 4-1: Ash Fusion Test Shape Guidelines for Coal (Cone) and Biomass (Cylinder)

In this chapter, works have been carried out on a coal sample (Kellingley) and a biomass sample (olive cake) which generate the 2 types of characteristic profile. These images were used to develop an auto-location technique using hog predictors and to analyse problem images with a range of thresholding and edge detection techniques. Furthermore, a wide range of shape parameters and manipulations have been analysed to identify the set that gives the best

representation of change. The ash fusion temperature definitions have also been interpreted in relation to the OAAFT curve.

4.2 Materials And Methods

The OAAFT pelleting method documented in the previous chapter was used to prepare a coal sample (Kellingley) and a biomass sample (olive cake). The samples were run in the CAF furnace and image analysis was carried out on each. 3 different methods were used in the development of analysis: Auto-location was achieved using HOG descriptors to recognise the pellet shape; a range of thresholding and edge detection techniques were used to obtain shape data from the images; and Z-score clustering was used to evaluate the shape parameters.

4.2.1 Thresholding and Edge-Detection Techniques

The thresholding techniques include Bradley, ISODATA, Minimum error, Moment preserving, and PUN. These were adapted from the research on bread crumb features [148]. The study also included Binarize Global, an inbuilt function in MATLAB which utilises OTSU thresholding [160]. The edge detection techniques include Approximate canny, Canny, Log, Prewitt, Roberts, Sobel and Zerocross. All these edge detection functions are inbuilt to MATLAB. Chen-vese algorithm is also included which is adapted from papers by Chan [161]. These functions have been compared to a manual analysis of the pellet creating an ideal analysis. Once the pellet was found, a range of parameters were chosen including; Number of particles found; Area; Perimeter; Eccentricity; Axial ratio and Aspect ratio. This was then compared relatively to the manual analysis.

4.2.2 Shapes and Clustering Analysis

The full range of raw shape parameters shown in Table 4-1 were obtained from the region properties function in MATLAB. These parameters almost explicitly relate to the size of an object however, when combined they can be used to relate to the shape of an object shown in Table 4-2. To identify the best parameter, they were clustered using Z-score, then each cluster was interpreted, and the most visually representative parameter was selected.

Z-scores measure the distance of a data point from the mean in terms of the standard deviation. The standardized data set used here has a mean of 0 and standard deviation 1.5 and retains the shape properties of the original data set. This has been visually illustrated in Figure 4-2 at the range of temperatures where the initial deformation occurs. The Z-score was computed as a function in MATLAB, the shape and size parameters were then plotted in a dendrogram cluster tree shown in Figure 4-3.

Table 4-1: Raw Size Parameters Obtained from Matlab

Symbol	Definition	Parameter type
H	Height of the bounding box	Size
W	Width of the bounding box	Size
Ap	Area of the particle	Size
Ach	Area of the convex hull	Size
Pp	Perimeter of the particle	Size
Cen	Centroid	Location
AXmax	Length (in pixels) of the major axis of the ellipse that has the same normalized second central moments as the region.	Size
AXmin	Length (in pixels) of the minor axis of the ellipse that has the same normalized second central moments as the region.	Size
Fmax	Maximum Feret Diameter, or longest internal line segment of the particle	Size
De	Diameter of equivalent area circle (Heywood diameter) computed as sqrt(4*Ap/pi)	Size

Table 4-2: Size Parameter Combinations to Create Shape parameters

Shape Parameter	Abbreviation	Formula	Parameter type
Circularity	1/C	(4*pi*Ap)/Pp^2	Shape
Alt Circularity	√C	Pp/ (2*√(pi*Ap)	Shape
Convextity feret	CVX_F	(pi*Dmaxferet)/Pp	Shape
Rectangularity	RECT	Pp/(2H+2W)	Shape
Square deviation	A/ABB	Ap/(H*W)	Shape
Roundness	RDN	4A/(pi*Dmaxferet^2)	Shape
PaNG	PaNG	H/Hi	Size
Eccentricity	ECC	See 0 Appendix	Shape
Solidity	SLD	Ap/Ach	Shape
Axial Ratio	AXR	Axmin/Axmax	Shape
Aspect Ratio or Height:Width Ratio	AR, H:W ratio	H/W	Shape

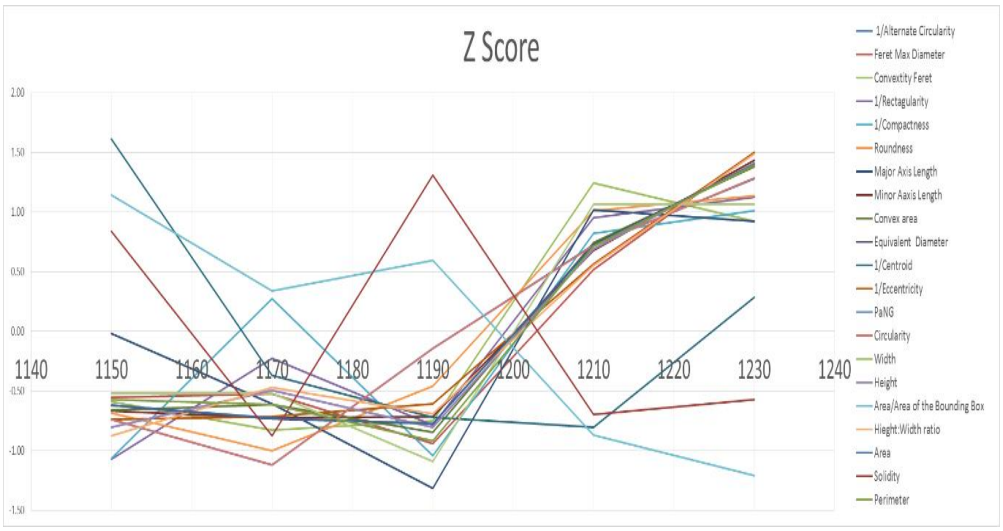


Figure 4-2: Visual Representation of Z-score comparison at IDT

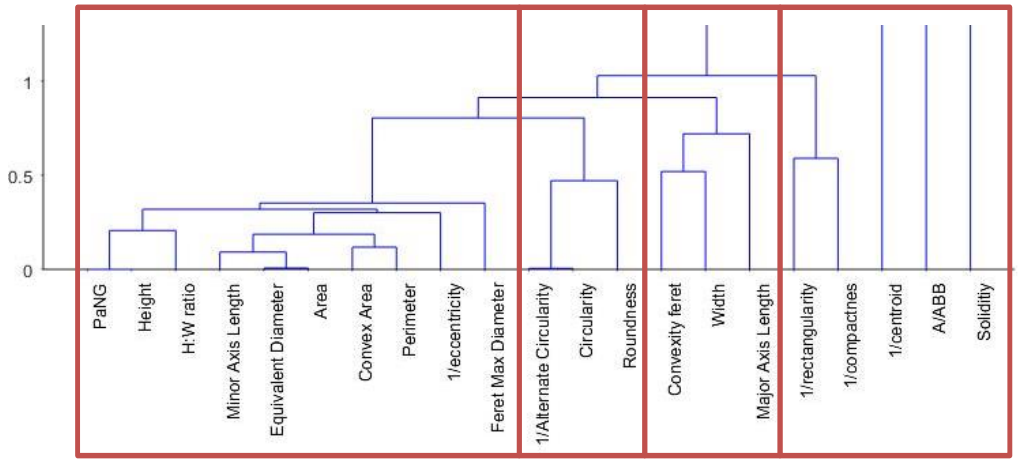


Figure 4-3: Illustration of the clustering groups identified using z-score and clustering

4.3 Results and Discussions

4.3.1 Thresholding and edge detect analysis

Thresholding performance was assessed by 2 criteria: closeness of the edge to original image and 'noisiness' of the background. Pellet features; area, perimeter, axial ratio, aspect ratio, and eccentricity, were computed for each method on 30 different images from 4 tests at a range of temperature variations shown in Figure 4-4. The main objective is to conclude the optimum process for defining the ash pellet through the various changes in contrast. An added complexity arises from the changes in the exposure from the camera (set manually), the changes in light emitting radiation from the increase in temperature from 0 – 1600 ^{o}C and the temperature at which the back light is turned off. Therefore, the contrast is not directly linked to temperature and a direct analysis of the image is required. This is illustrated clearly in images 16,17 and 19 in Figure 4-4. Images 5-13 present the biggest problem for analysis due to poor contrast.

Figure 4-6 and Figure 4-7 show the analysis of image 5, the 460 ^{o}C pellet. The histogram peaks are far apart and the top 5 clusters support the analysis. When the clusters are far apart, the analysis is possible and the optimum analysis as shown in Table 4-3 were approximate canny, sobel and prewitt.

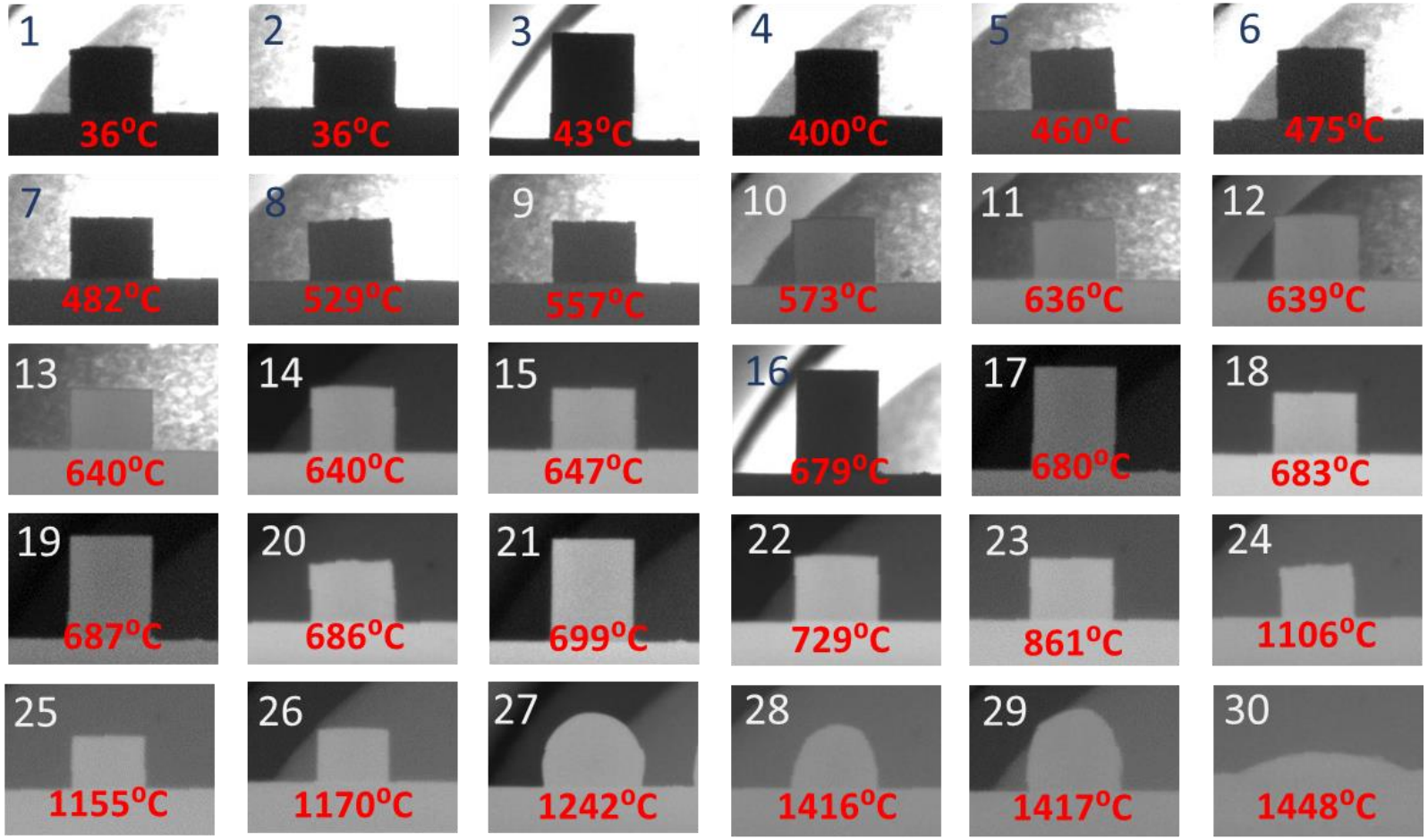


Figure 4-4: 30 cropped images from the CAF test furnace and temperatures at which they were taken

Figure 4-8 and Figure 4-9 show the analysis of image 11, the 636 ^{o}C pellet. The obvious difference is the lack of reasonable pellet in the top 3 analysis methods. In Figure 4-8 it is clear from the histogram that it is harder to separate the background from the pellet. Both the y axis and the x axis have changed in Figure 4-8B whereby the peak counts are an order of magnitude lower, from 8000 to 800 and similarly the grey scale range is greatly reduced, from >200 to <20. This is a clear indicator of the quality of the image and can inform the software if the segmentation method will work or not.

4.3.1.1 Creating the functions: Cluster Peak Distance and Grey Clustering Range

Now that a clear difference has been identified in the image histograms, the analysis of the methods (Table 4-3), on the 30 images, highlighted which method to use for each range. In the temperature range of 0 to 400 ^{o}C, contrast doesn't impact analysis, and Binarize Global (or OTSU global) and Canny edge detection are the best options. The contrast problem occurs in the range of 400 to 800 ^{o}C. There are 2 ways to indicate if a selected image is suitable for analysis; the first is the range of the grey scale values (GreyClusterRange Figure 4-5); the second is the distance between the 2 peaks (ClustPeakDists Figure 4-5). If the grey scale range is less than 90 then analysis is not possible thus the image will be bypassed. If the grey scale requirements are satisfied, then the distance between the 2 peaks must be greater than 50 grey scale points. Once passed 800 ^{o}C, the contrast no longer impacts the analysis. In the temperature range of 800 to 1600 ^{o}C, Bradley and log edge detection are the best options.

In the regions which don't require the extra analysis, the 2 best techniques are both executed and the outcomes are averaged to safeguard against anomalous results.

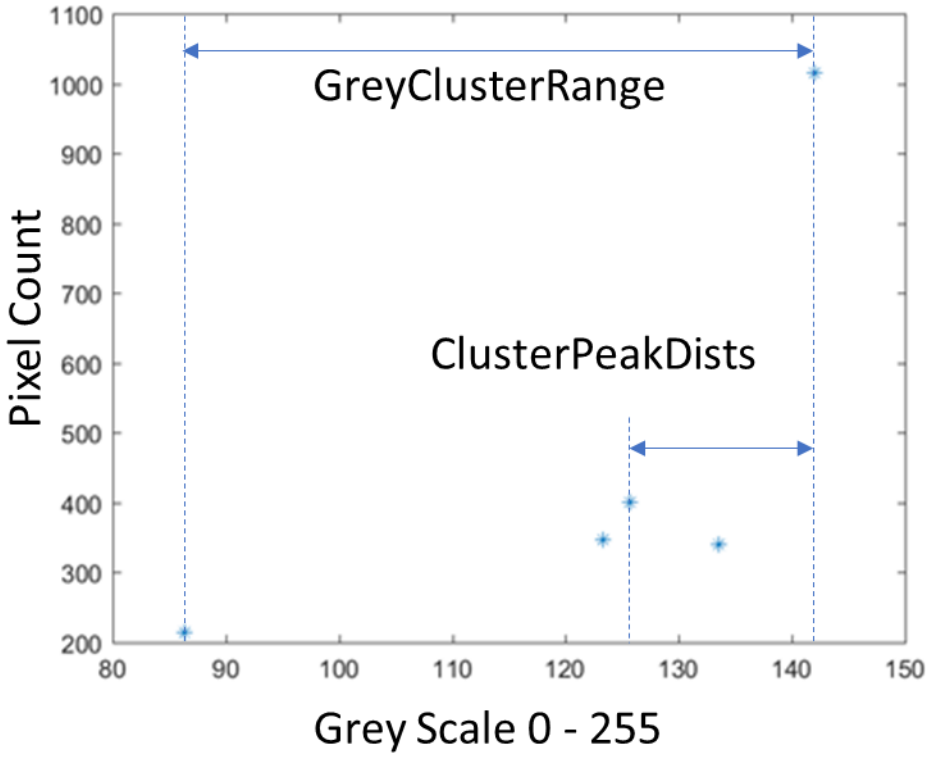


Figure 4-5: Top 5 histogram clusters for image 13 demonstrating analysis functions

4.3.1.2 Concluded classification system

```
At (if) T = 0 – 400
        Otsu global-Canny Average
At (if) T = 400 – 800
        if GreyClusterRange < 90
                I2   = [];  % Image is too complex to analyse, use the previous
        elseif ClustPeakDists > 50
                Prewitt
At (if) T = 800 – 1600
        Bradley-Log average
```

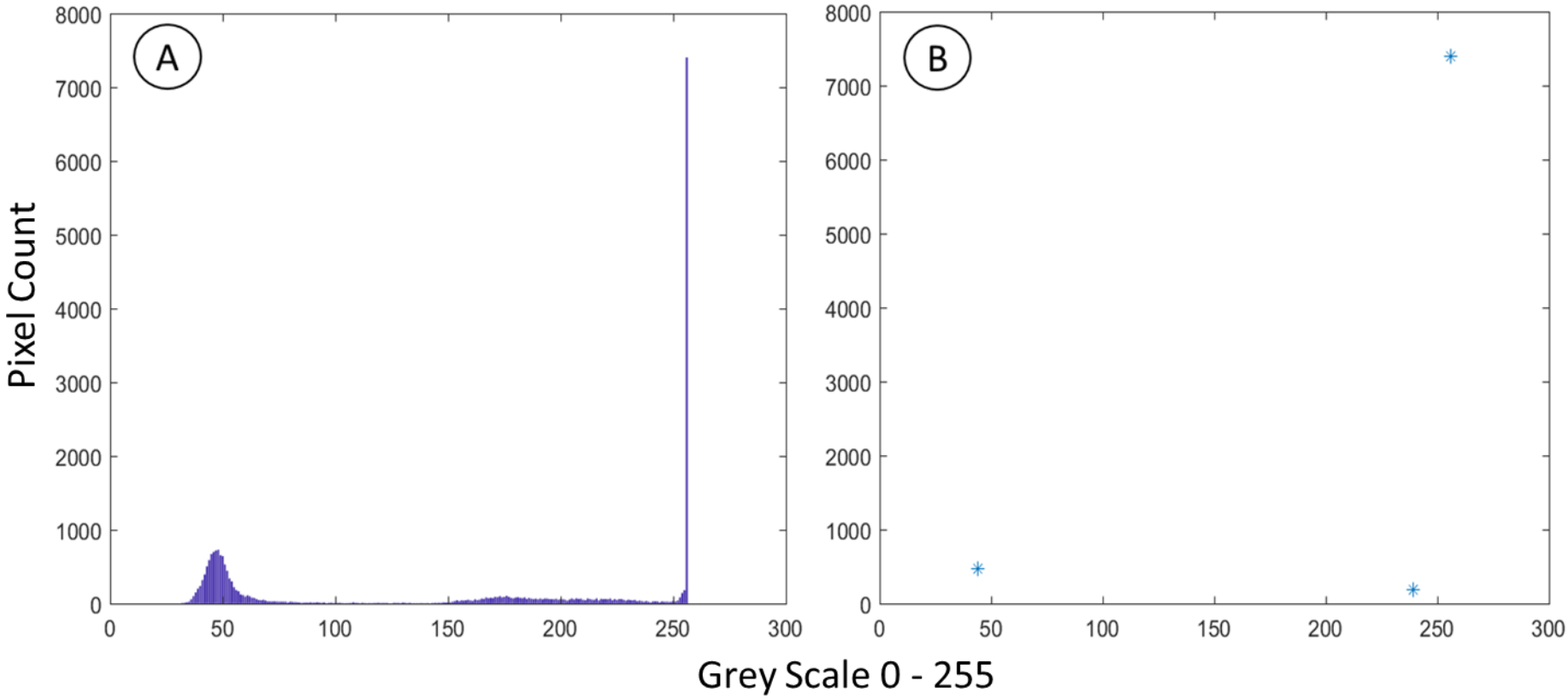


Figure 4-6: A) Histogram of pixel counts for the 460 ^{o}C Image; B) Top 5 clustered pixel counts from the histogram

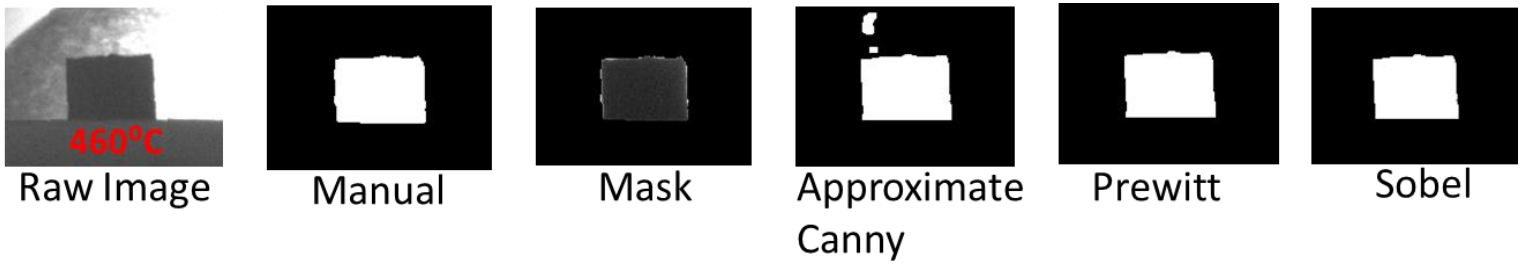


Figure 4-7: Raw Image, Manual Thresholding and the Top 3 Methods for Image5

Table 4-3:Difference in value of the manual threshold and the different threshold techniques for a range of shape parameters

Function Name	Number of particles found	Area	Perimeter	Eccentricity	Axial ratio	Aspect ratio	Average difference from manual
Approximate Canny	3	0.0077	0.0161	0.0065	0.0060	0.0133	0.0099
Canny	1	0.0173	0.0350	0.0219	0.0197	0.0232	0.0234
Chenvese	1	0.0125	0.0116	0.0425	0.0371	0.0325	0.0272
Log	1	0.0085	0.0127	0.0336	0.0316	0.0443	0.0262
Prewitt	1	0.0085	0.0113	0.0067	0.0061	0.0133	0.0092
Roberts	0	1.0000	1.0000	1.0000	1.0000	1.0000	1.0000
Sobel	1	0.0051	0.0090	0.0058	0.0053	0.0133	0.0077

BinarizeGlobal	1	0.0059	0.0071	0.0338	0.0318	0.0316	0.0220
Bradley	9	0.8542	0.4286	0.1786	0.1962	0.0370	0.3389
ISODATA	1	0.0056	0.0063	0.0334	0.0314	0.0316	0.0217
MinimumError	0	1.0000	1.0000	1.0000	1.0000	1.0000	1.0000
PreservingMoments	1	0.0194	0.0121	0.0329	0.0309	0.0443	0.0279
Pun	1	0.0082	0.0071	0.0346	0.0325	0.0443	0.0254
Zerocross	1	0.0085	0.0127	0.0336	0.0316	0.0443	0.0262

Note: top 3 highlighted in yellow

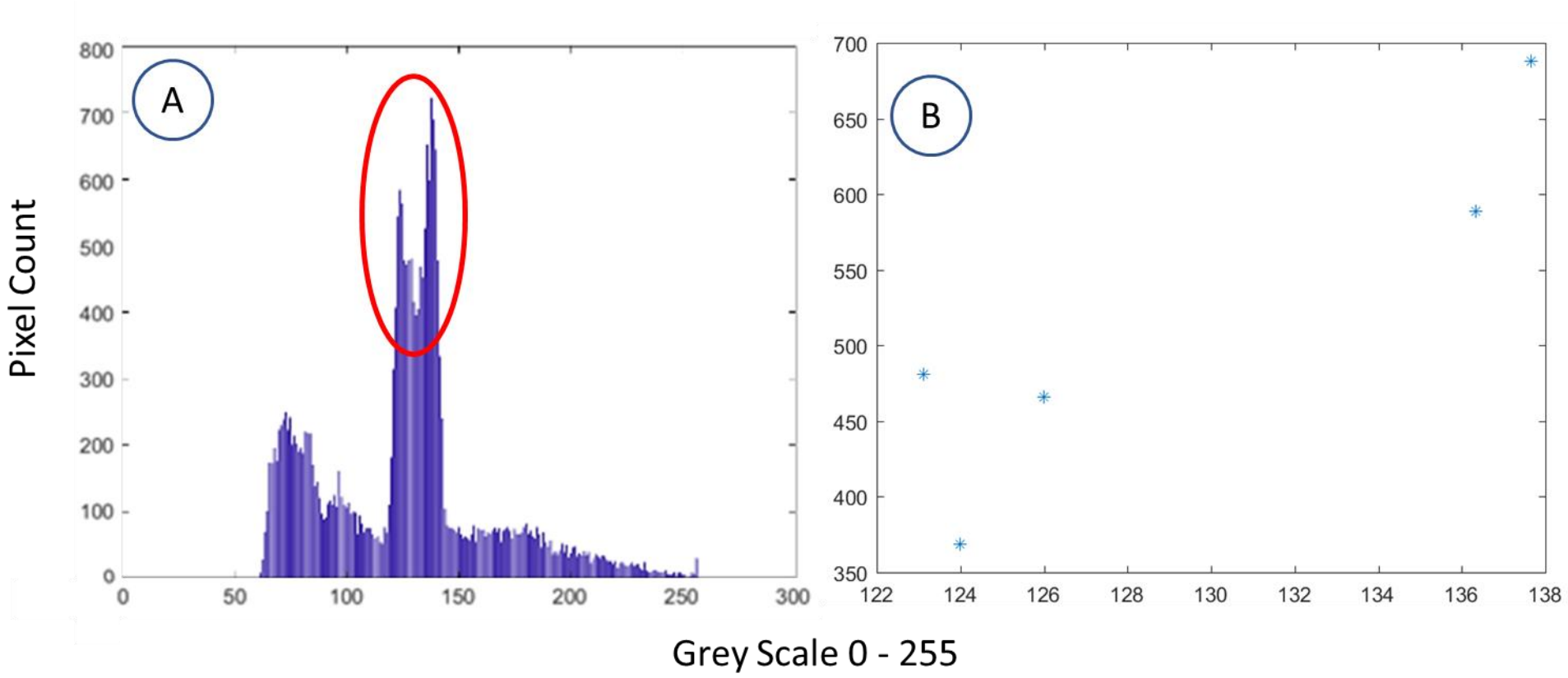


Figure 4-8:A) Histogram of pixel counts for the 636 ^{o}C Image; B) Top 5 clustered pixel counts from the histogram

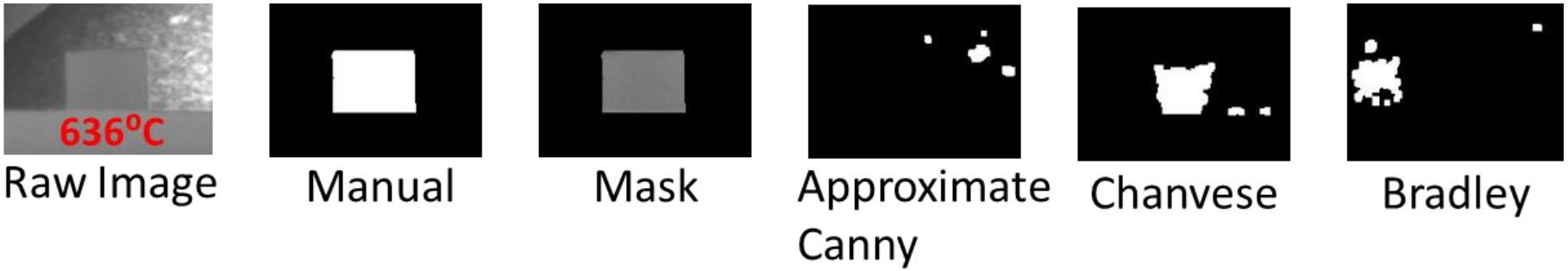


Figure 4-9:Raw Image, Manual Thresholding and the Top 3 Methods for Image 11

4.3.2 Clustering the Profile Using Z-Score

There are generally 2 types of profiles for ash fusion tests, a shrinking-expanding curve and a collapsing curve illustrated in Figure 4-10. The former is generally simpler to analyse as the phases of the test are clearly defined and is more common in coals. The latter curve is more prominent in biomass samples and the shrinking and the IDT phases are difficult to distinguish between. This makes it complicated to analyse, especially using only height. Therefore, it is important to analyse both types of curve to identify which parameter at most useful. The parameters were clustered for each phase of the expanding profile, SST (Figure 4-11), IDT (Figure 4-13), slope analysis (Figure 4-15), and the collapsing curve only has 1 phase (Figure 4-17). The parameters from groups which showed the greatest magnitude of change and represented the key features relating to each phase were selected. These parameters are listed in Table 4-4, Table 4-5, Table 4-6, and Table 4-7, for SST, IDT, slope analysis and collapsing curve respectively. Once the key parameters were highlighted for each phase, they were broken down into their fundamental components to discount similar identical analysis and then combined to formulate the most useful parameter/s. The most representative variable was then chosen as the indicator for each respective portion of the curve.

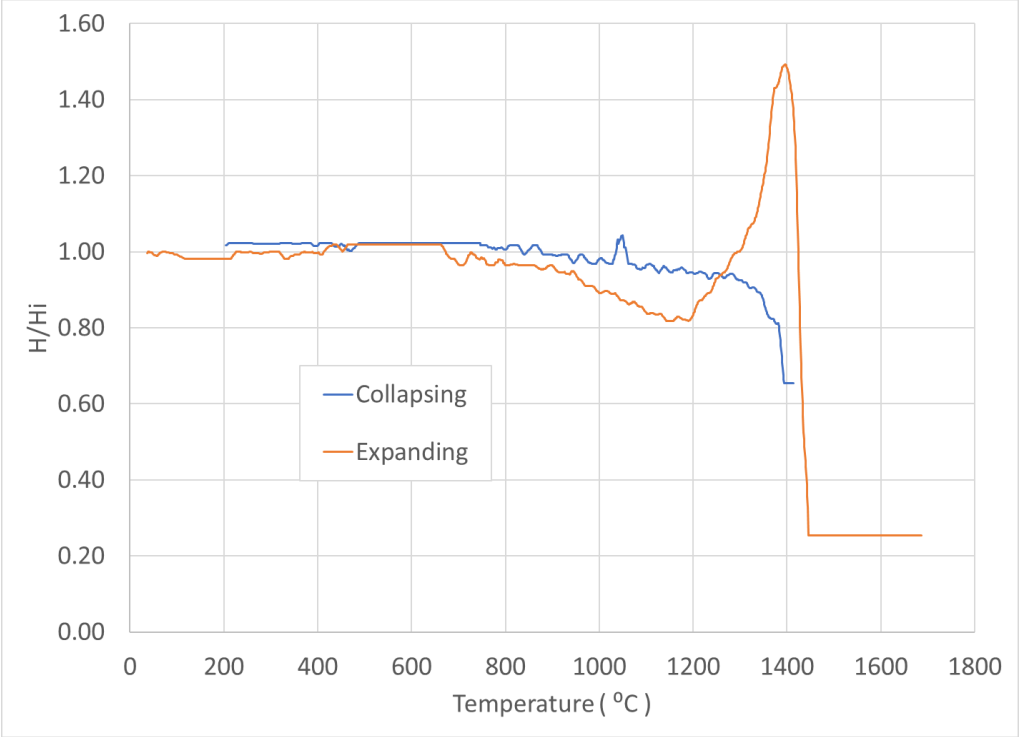


Figure 4-10: PaNG (H/Hi) curves for the collapsing (Olive cake) and expanding (Kellingley) curves

4.3.2.1 CLUSTERING FOR SHRINKING-EXPANDING PROFILES

4.3.2.1.1 Clustering the SST

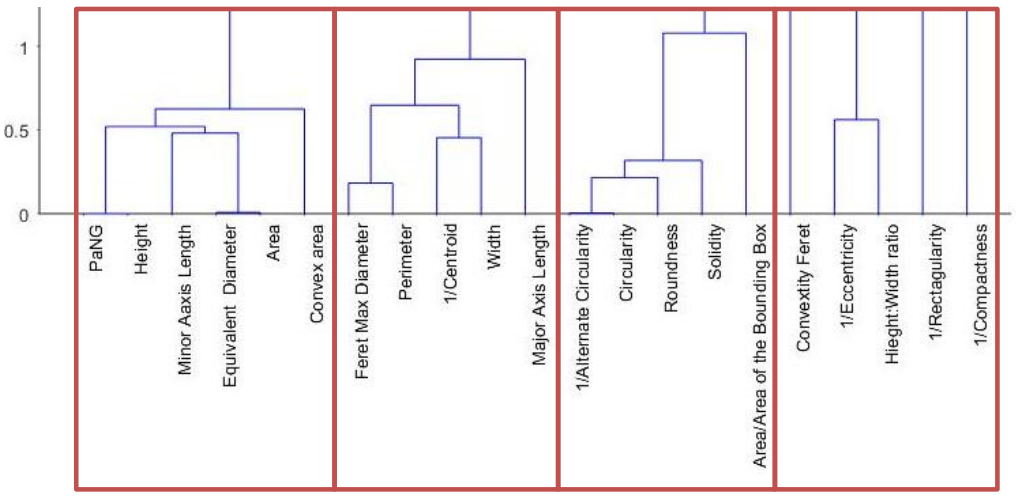


Figure 4-11: Grouping the clusters for the expanding curve SST analysis

GROUP 1: Displays a link to the shrinking point with a noisy change of gradient.

GROUP 2: Similar trend to group 1 but with significantly less noise which offers a far clearer representation the first shrinking phase. The centroid is misleading in this instance as it cannot be guaranteed that the change is due to the pellet, and not to the image error as it is the only parameter relative to the co-ordinates.

GROUPS 3 & 4: No significant change obverted in groups 3 & 4 linking to the shrinking point therefore, these variables can be ignored during this phase of analysis.

Table 4-4: The variables to be considered from the slope phase of the clustering

Shape Parameter	Inclusion	Link	Cluster group	Parameter Type
PaNG	H/Hi	Height	1	Size
Area	A_P	Area	1	Size
Convex Area	A_{CH}	Area	1	Size
Minor Axis Length	AX_{MIN}	Height	1	Size
Equivalent diameter	sqrt(4*A_P/pi)	Area	1	Size
Feret Max Diameter	F_{MAX}	Fmax	2	Size
Perimeter	P_P	Perimeter	2	Size and Shape
Width	W	Width	2	Size
Major Axis Length	AX_{MAX}	Width	2	Size

The group 1 cluster is built up of Area and Height manipulations, and as shrinkage of the particle is more comprehensively captured by the Area compared to the singular point of Height, area of the particle, A_P, will be taken from group 1. Group 2 is composed of width and perimeter parameters,

similarly with group 1, comparing the discrete line such as width to holistic parameter such as perimeter. The analysis of the group 1 curves showed that they had a greater fluctuation but also showed greater overall change. The group 2 curves give a smoother curve, but the overall change is smaller. Group 1 and 2 were best represented by area and perimeter respectively shown in Figure 4-12. The noise in group 1 can be avoided by smoothing of the curve and the trigger for shrinkage is based on the area of the pellet. Thus, the only parameter needed to analyse the shrinkage is **area**.

Stage 1 SST Analysis: $\mathbf{A_P}$

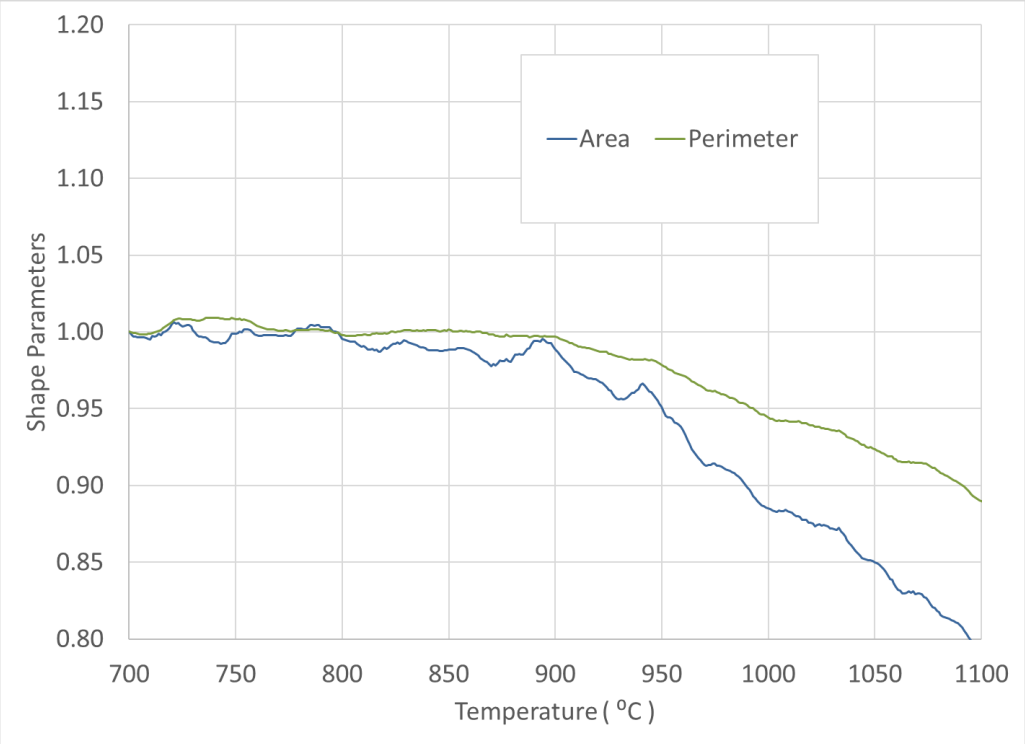


Figure 4-12: Shrinking phase curve shape comparisons for Perimeter and Area

4.3.2.1.2 Clustering the IDT Trigger

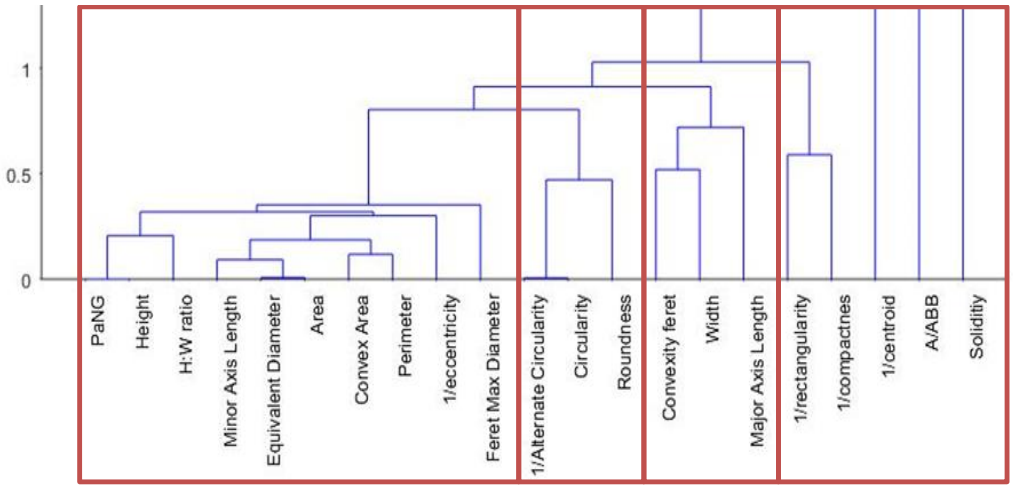


Figure 4-13: Grouping the clusters for the expanding curve IDT analysis

GROUP 1: All the variables show a clear significant change of gradient at the IDT, whilst 3 of the variables (Feret Max Diameter, Minor Axis Length and Perimeter) show a less distinct change.

GROUPS 2, 3 & 4: Variables including Width, Roundness and 1/rectangularity showed a lesser magnitude of change than Group 1 variables but enough to be considered as significant. No significant change is observed by the rest of the variables in these groups that link to the IDT point therefore, most of these variables can be ignored during this phase of analysis.

Table 4-5: The variables to be considered from the slope phase of the clustering

Shape Parameter	Inclusion	Link	Cluster Group	Parameter Type
PaNG	H/Hi	Height	1	Size
Area	Ap	Area	1	Size
Convex Area	Ach	Area	1	Size
Minor Axis Length	AXmin	Elipse height	1	Size
Height to weight ratio (AR)	H/W	Height and width	1	Shape

Perimeter	Pp	Perimeter	1	Size & shape links
Width	W	Width	1	Size
Equivalent diameter	sqrt(4*A_P/pi)	Area	1	Size
Feret Max Diameter	Fmax	Fmax	1	Size
Eccentricity	ECC*	Ellipse height and width	1	Shape
Roundness	4A/(pi* F_{MAX}^2)	Area, Fmax	2	Shape
1/Rectangularity	Pp/(2H+2W)	Perimeter, height, and width	4	Shape

This group of clusters is built up of **Area**, **Height**, **Width**, **Perimeter** and **Fmax** and manipulations containing them. As all the plots show a similar trend during the stretch of SST to the initial curve of deformation, it is important now to consider which parameters are encapsulating this stage of the deformation. In the previous phase the only parameter changing was size, during this phase size increases as well as a transition from a square/rectangle to a circle-like shape. Therefore, at least 1 parameter for both size and shape should be integrated in the analysis. The raw outputs such as **height** and **width** are far more subject to minor variations whereas, the ellipse equivalents return a more consistent output thus highlighting macro changes. **Roundness** outputs a noisier profile and **rectangularity** doesn't display enough change. Area and Eccentricity represent size and shape respectively and are illustrated in Figure 4-14.

Stage 2 IDT Analysis: **A_P*ECC**

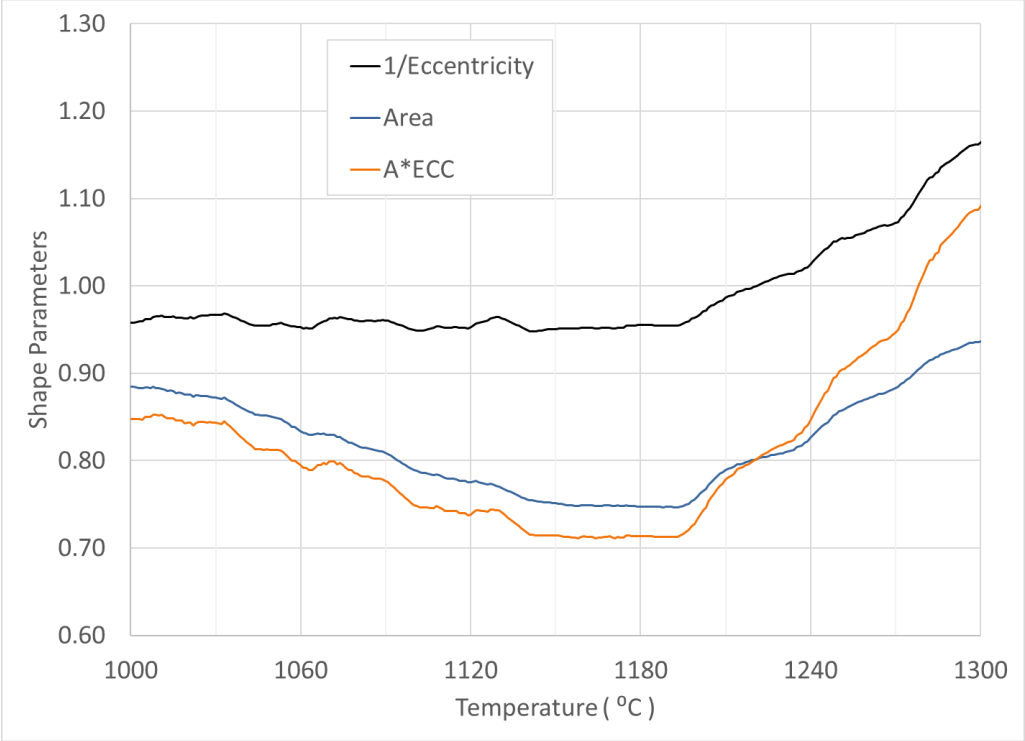


Figure 4-14: IDT phase comparisons for Eccentricity and Area

4.3.2.1.3 Clustering the Slope

Defining the phase between the traditional IDT point and the FT point is the most challenging, as there are multiple ways to define the deformation that takes place. It is also not known if this phase will lead to any significant triggers for slagging and fouling therefore, is it important to characterise as many of the different features as possible.

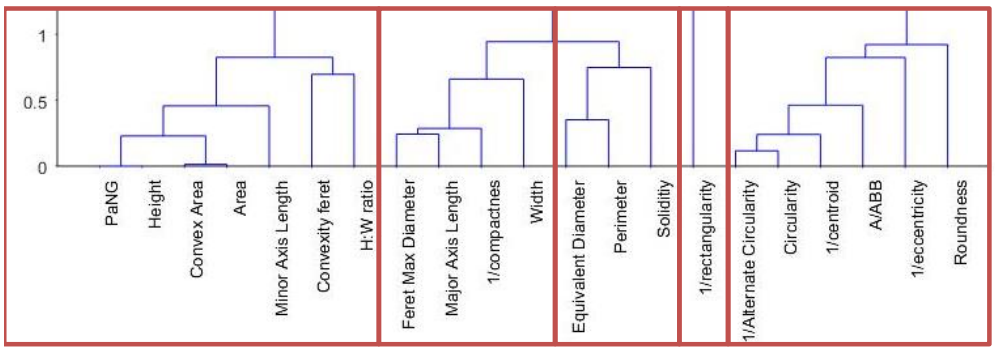


Figure 4-15: Grouping the clusters for the expanding curve slope analysis

GROUPs 1 & 3: Both groups display a similar trend of gradual increase until the trend rounds to a peak and continues to round to a decline and then a trough, like the traditional PaNG curve. There are 2 exceptions in Solidity and Convexity Feret which are linked but have a vastly lower magnitude of change. All the variables show a clear significant change of gradient at the IDT, whilst 3 of the variables (Feret Max Diameter, Minor Axis Length and Perimeter) show a less distinct change.

GROUPs 2 & 4: The variables in groups 2 & 4 generally show a later peak closer to the traditional FT, with a slope of increased gradient and a steep drop after the peak. These variables don't add to the trigger points that are already accounted for in group 1&3 and therefore can be ignored.

Group 5: These variables follow a gradual increase of small magnitude akin to groups 1 and 3, but towards the end of the deformation all the plots contain a clear change. This group also contains eccentricity which follows a similar pattern with a unique characteristic change as the shape becomes more circular relative to the best fit ellipse. Eccentricity should be carried forward. The exceptions to this trend are the A/ABB which follows a similar shape, is offset to the other profiles and doesn't show any links to the deformation.

Table 4-6: The variables to be considered from the slope phase of the clustering

Shape Parameter	Inclusion	Link	Cluster Group	Parameter Type
PaNG	H/Hi	Height	1	Size
Area	A_P	Area	1	Size
Convex Area	A_{CH}	Area	1	Size
Minor Axis Length	AX_{MIN}	Ellipse height	1	Size
Height to weight ratio	H/W	Height and width	1	Shape
Perimeter	P_P	Perimeter	3	Size & shape links
Equivalent diameter	D_E	Area	3	Size
Alternative Circularity	P_P/ (2*√(pi*AP_P)	Area and perimeter	4	Shape
Circularity	(4*pi*A_P)/P_P^2	Area and perimeter	4	Shape
Eccentricity	ECC*	Ellipse height and width	4	Shape
Roundness	4A/(pi*F_{MAX}^2)	Area and Fmax	4	Shape

Although eccentricity was considered an important variable, its unique change is not representative of any significant trigger. The peak seems to be a special case for the specific dimensions taken between 1330 and 1390.

The morphology change that takes place here is a general increase in size with the continued rounding of the edges until the base widens and the shape becomes a rough semi-circle, reducing to a line segment. The chemical change taking place is the slag becoming gradually more porous until the peak at which the slag starts becoming a fluid. The height to width ratio is the best representation of this change, especially as the base widens and the slag begins to transition from the porous phase to the fluid phase. Size (area) and aspect

ratio are the key changes that take place and are depicted in Figure 4-16. Therefore:

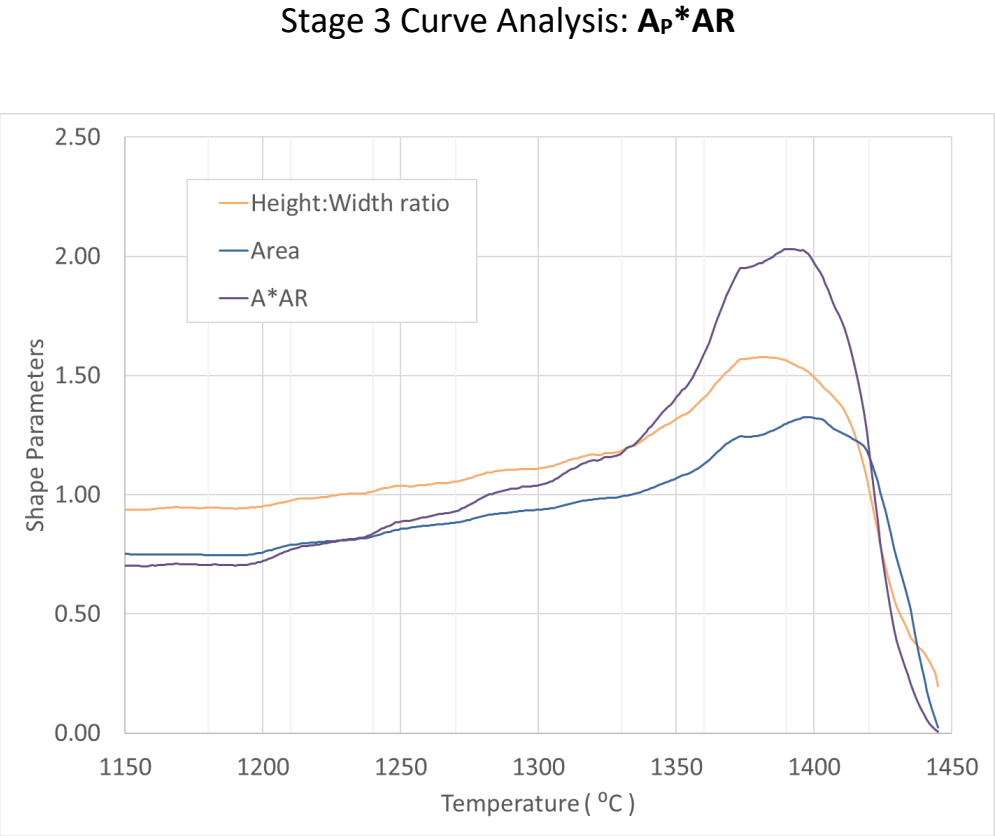


Figure 4-16: Expanding curve shape comparisons for Aspect ratio and Area

4.3.2.2 CLUSTERING FOR COLAPSING PROFILES

In the collapsing curve type, the expanding phase of the plot is removed. The significance of this transition from shrinking to expanding is that it gives a clear point to indicate initial deformation. Without this, the IDT trigger is harder to identify. The z-score of these clusters shown in Figure 4-17 are relatively low when compared to the previous clusters, this means that the trends are very close together. This is not surprising due to the minimal deformation change taking place in the collapsing profile.

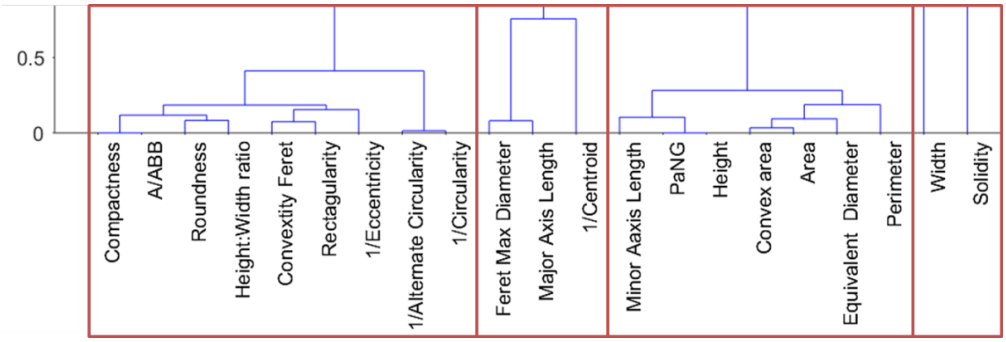


Figure 4-17: Z-score clustering for shape parameters during the collapsing profile

GROUP 1: These variables do not change greatly over the duration of the test until the IDT and FT which occur within 20 ^{o}C of each other. The **Roundness**, and **Circularity** parameters are linked very closely to the IDT. Eccentricity and Height-Width ratio only show a link to the FT, and the rectangularity and compactness show no clear link to any triggers.

GROUP 2 & 4: Both groups result show similar trends reducing during the shrinkage phase and then increasing up until the FT. The magnitude of change of the parameters in this group is not comparable to those in groups 1 or 3 and therefore can be discarded.

Group 3: This group contains the size parameters such as height and area. The curves in this cluster reduce during the shrinking phase and then steadily decline until the FT. The problem with these variables is that they do not identify the IDT when there is no expansion phase. The Area is the best indicator of shrinkage as in the expansion curve however, it will need to be combined with a shape parameter to enable IDT identification.

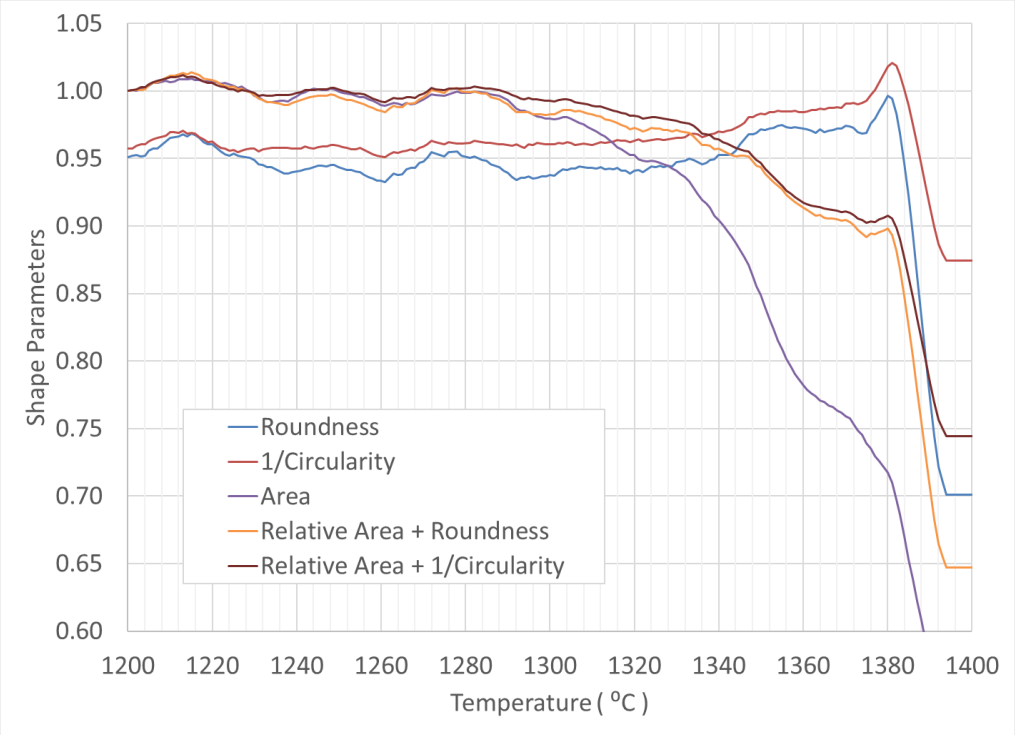
Table 4-7: The variables to be considered from the collapsing curve clustering

Shape Parameter	Inclusion	Link	Cluster Group	Parameter Type
1/Circularity	$(4*pi*A_P)/P_P\text{^}2$	Area and Perimeter	1	Shape
Roundness	$4A/(pi*F_{MAX}^2)$	Area and Fmax	1	Shape
Area	A_P	Area	3	Size

The key difference for this type of curve is that there is a very limited change in size of the sample compared to the expanding curve. This means that the shape parameters such as, circularity and roundness play a more significant role in identifying the IDT.

Therefore:

Collapsing Analysis: relative (Ap + 1/C)



4.3.2.3 CONCLUSIONS FROM KEYS AREA CLUSTERING FOR EACH CURVE TYPE

2 types of curve have been analysed in this investigation; the expanding curve; and the collapsing curve. The expanding curve was broken down into 3 key areas, the shrinking phase, IDT trigger, and expansion phase:

- Shrinking phase: **Area** best represent the stinking process and shows the greatest change in size when plotted.
- IDT Trigger: **Area** and **Eccentricity** give the greatest magnitude of change during the IDT region of the curve. Area represents the change in size that occurs in the expanding curves and eccentricity represents the shape change.
- Expansion phase: **Area** and **Aspect Ratio** describe the shape of the pellet during the transition from IDT to FT.

The collapsing curve lacks the expansion phase during deformation and therefore shape parameters become more significant. Thus, the combination of **Area** and **1/Circularity** best represents the change in morphology.

These parameters will be used as indicators for different phases. Although Eccentricity and Aspect ratio help track deformation, they do not offer key morphological changes for visual representation. **Area** is the most representative parameter for all the phases of change. It will be the parameter displayed in combination with **1/Circularity** which enables identification of the IDT in collapsing curve data as shown in Figure 4-18.

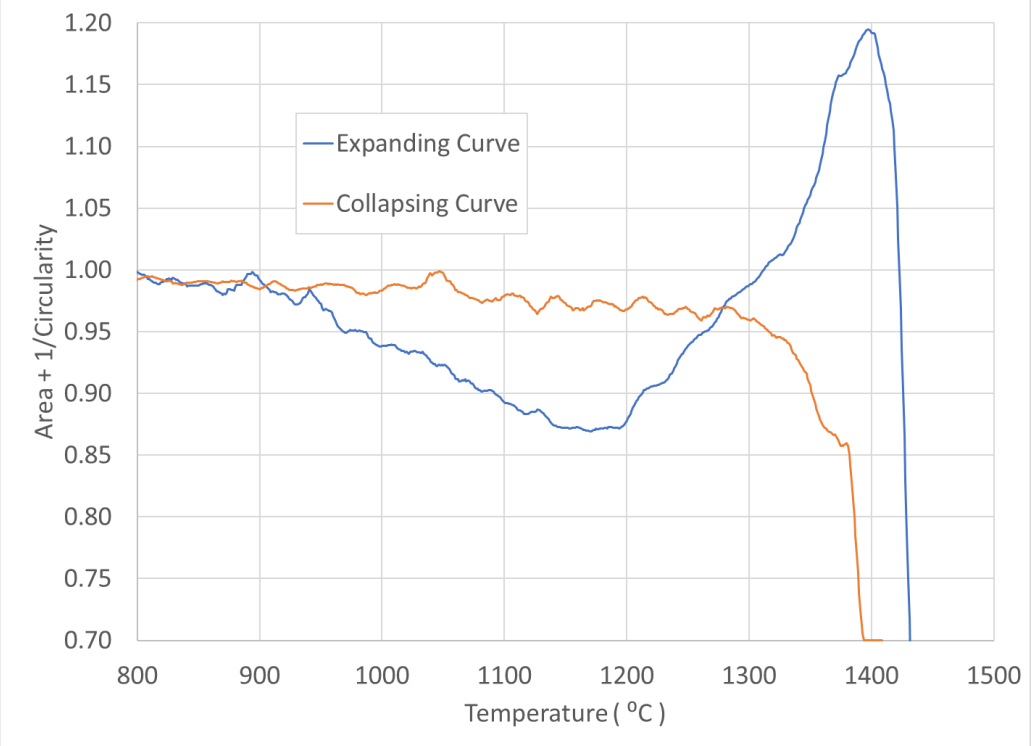


Figure 4-18: Finalised Expanding and Collapsing Curve Profiles

4.3.3 Ash Fusion Temperature Definitions in Relation To The OAAFT Curve

The national standards dictate the point at which to record the ash fusion temperatures based on a description such as:

- **SST** – The temperature when the area of the test piece falls below 95 % of the original test piece area.
- **DT -** Temperature at which the first signs of rounding, due to melting, of the tip or edges of the test piece occur
    - NOTES: Shrinkage or distortion of the test piece, or rounding of cracks and fins, are not criteria for deformation and should be ignored if the tip and edges remain sharp. However, for some solid mineral fuels, the temperature at which the test piece shrinkage begins can be of interest and should be reported as a feature noted during the determination.
- **ST (cone) -** The temperature at which the height is equal to the width of the base.
- **ST (Cylinder & truncated cone) -** The temperature at which the edges of the test pieces become completely round with the height remaining unchanged.
- **HT -** Temperature at the height becomes equal to half the base diameter.
- **FT** - Temperature at which the height of which is 1-third of the height of the test piece at the hemisphere temperature.

Some of these descriptions translate to code very easily, and other parts of the descriptions do not. Furthermore, there are different trigger descriptions for the cone shapes and the cylinders. The OAAFT method only needs to consider the cylinder description, this is how the descriptions translate to code:

- **SST** – Temp @ A = Ai*0.95
- **DT** – N/A
- **ST** – N/A
- **HT** – Temp @ H= W*0.5 = H_{HT}
- **FT** – Temp @ H = $H_{HT}/3$

The deformation and softening temperatures are very difficult to quantify as shape parameters. The OAAFT has enabled the indication of IDT using image analysis. The shape analysis from Chapter 4.3.2 has Identified Area and 1/Circularity as key parameters for representing the curve highlighting IDT.

4.3.4 Alternative data collection

The OAAFT not only captures a complete characteristic profile of the ash sample, it enables the collection of alternative data not possible to obtain otherwise. Rather than a single temperature to highlight the start of shrinking, the extent of the shrinkage can be captured from the area parameter as a percentage, and the range over which the shrinkage takes place. A similar result can be obtained for the expansion properties of the sample. This alternative data is documented in Table 4-8 and an illustration how the data is obtained is shown in Figure 4-19.

Table 4-8: Alternative data collection for the OAAFT for the Expanding and Collapsing curves

	Expanding Curve	Collapsing curve
Total shrinkage (%)	25	28
Shrinkage range (^{o}C)	380	450
Total expansion (%)	56.6	n/a
Expansion range (^{o}C)	220	n/a

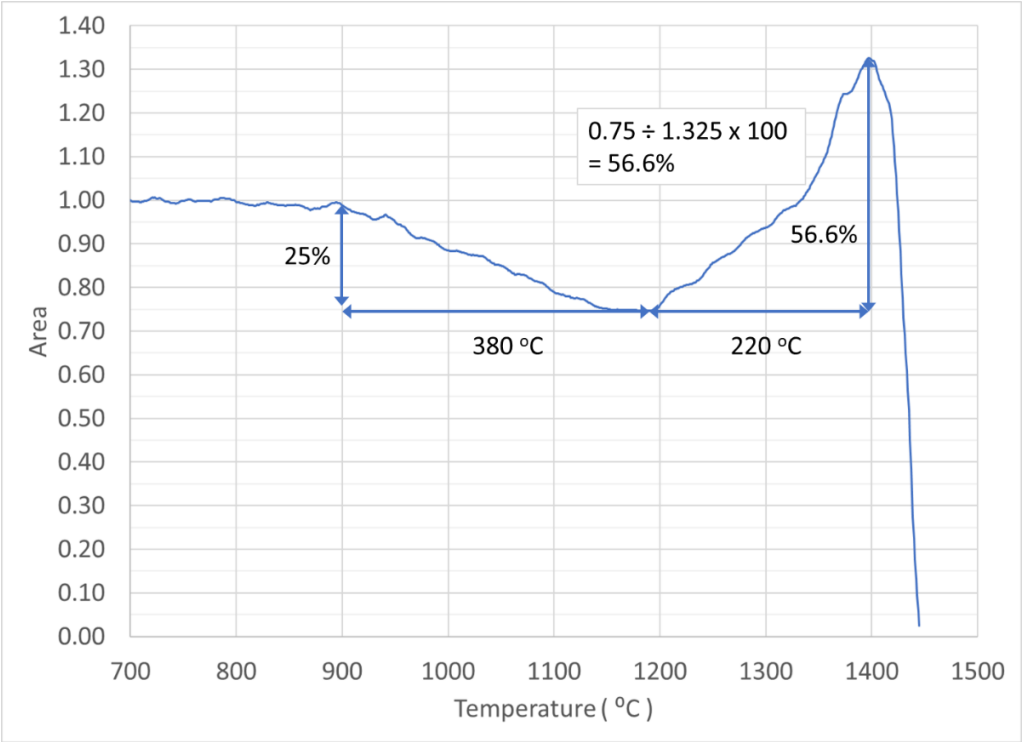


Figure 4-19: Illustration of the shrinkage and expansion calculations

4.4 Significance of Data

The full automation of the analysis completely removes any subjectivity or requirements from the operator of the test. Together with the optimised pelleting process from Chapter 3, the entire ash fusion test has been made highly repeatable. The function developed in this chapter enables smooth analysis of the complex range of contrast in the CAF furnace. The potential for lost information is still a problem if the camera set up is poor or if the images are of low quality.

4.5 Conclusions

In this chapter an auto-location technique using hog predictors was developed alongside the optimisation of the image analysis method using thresholding and edge detection techniques. The best representation of change has also been defined using a range of shape parameters and manipulations.

Image Processing: 3 regions of analysis requiring different segmentation techniques were identified. Binarize global threshold and canny edge detection are used from 0-400 ^{o}C. Histogram analysis was incorporated to classify images from 400-800 ^{o}C and prewitt edge detection is used. Finally, Bradley threshold and log edge detection are used from 800- 1600 ^{o}C.

Shape Analysis: Area in combination with 1/Circularity is the most representative parameter for all the phases of change. It enables identification of the IDT in both expanding and collapsing curve data. The OAAFT also enables quantitative analysis of shrinkage and expansion.

Chapter 5 The Impact of Individual Components on Pseudo Ash Pellet AFT Temperatures And OAAFT Curves

5.1 Introduction

Coal ash is predominantly made up of 4 major elements which account, on average, for 88% of the database investigated. The other inclusions occur at lower average concentrations but can spike sporadically in some coals. These major minerals include; Al_2O_3, SiO_2, CaO, & Fe_2O_3 with lesser common minerals being MgO, K_2O and SO_3. The ratio of these main mineral inclusions plays a pivotal role in determining melting characteristics. The 5-component relationship of Al-Si-Ca-Fe-O has been used in the F*A*C*T computing package to predict the phase equilibria of coal ash slags. There have been successful attempts to validate FactSage models using pseudo ash samples [162], [163]. To date, the impact of individual components of the OAAFT curve has not been investigated. The purpose of this investigation is to reaffirm the impact of individual components on ash fusion temperatures and identify any impact of individual components on the OAAFT curve.

Empirical investigations of these components and their impact on ash fusion temperatures has been done previously. 4 papers directly compared the impact of the component oxides Al_2O_3, SiO_2, CaO, & Fe_2O_3 to the ash fusion temperatures of the samples [8], [128], [163], [164]. 3 of the studies created pseudo pellets and 1 directly compared the impact of each component from raw coals. Liu et al. and Song et al. analysed 34 and 33 pseudo ashes

respectively. Both sets of ashes were composed of the 4 major elements Al_2O_3, SiO_2, CaO, & Fe_2O_3 however, Liu added K_2O whilst Song added MgO. Liu used a carbon atmosphere[22] (assumed to be reducing [164]) to analyse the ash fusion temperatures, whist Song used an inert Ar atmosphere. The ash fusion temperatures were recorded under air or oxidising conditions, and this may have led to differences in results. All the components were varied to compare S/A ratio, and w/w % of Fe_2O_3, CaO, K_2O and MgO. Each study found that higher Fe_2O_3 content resulted in lower AFT temperatures. The studies directly contradict each other, with Liu finding that increasing the S/A ratio reduced ash fusion temperatures by 200 ^oC and Song finding the opposite[163], [164]. The CaO content displayed a low 'trough' of AFT temperatures in both studies at 30% (Liu) and 35% (Song) weight but increase either side of this point. The later 'trough' for Liu can be attributed to the reduced step size of weight %. The K_2O displayed no significant change in Lui's study whilst Song found that increasing MgO generated an 's' shaped curve, initially decreasing ash fusion temperatures, then increasing, before finally greatly reducing ash fusion temperatures. Niu et al. carried out a study for synthetic biomass ashes, whilst not directly comparable to coal ashes due to the different make up, they found an increase in acid base ratio reduces the IDT if the ratio is less than 1.4 [8]. A further study by Yan focused only on S/A ratio under inert conditions, finging similar results to Liu but also linked shrinkage to slag formation rate [165].

Since the development of the AAFT and the subsequent optimisation of the AAFT (OAAFT), the output of a characteristic curve has been generated. The

influence of individual elements and their eutectics on the characteristic curve has not been investigated. The effect of individual elements on ash fusion temperatures have been shown [8], [113], [128], [163], [164]. The use of 3 phase plots to link multiple phases has helped in relating acid-base ratio comparisons.

In this chapter, experiments have been carried out using the 5 key individual components of coal to create a mineral database for the AAFT curve. Each mineral used has been given its own characteristic curve along with other common minerals found in coals. Pseudo pellets were created based on a coal sample database collated from literature. The OAAFT curves were compared with the raw AFT temperatures to verify reliability of the pseudo pellet trends. Further links to 3 phase plots have been examined to assess eutectic trends.

5.2 Materials and Methods

5.2.1 Ash Database

A database was populated using existing studies in literature including typical trade coals with UK bituminous coals and brown coals from the EU [19] and Chinese coal and a range of international coals [164] shown in Table 0-1. These coal compositions were collated and used to generate and 'average' coal ash consisting of only SiO_2, Al_2O_3, Fe_2O_3, CaO, and MgO.

5.2.2 Synthetic ash samples

The average ash values were used as a basis to examine the impact of the individual coal constituents. Silica-Alumina ratio (0.5-4), and weight percentages of CaO (0-40%), Fe_2O_3 (0-40%) and MgO (0-25%) were

investigated. The extremes in variations of individual components were based on previous studies [163], [164] and the range in values in the database. The chemical compositions of SiO_2, Al_2O_3, CaO, Fe_2O_3, and MgO for the 20 pseudo coal ash samples are given in Table 5-1. The Al_2O_3 (Aluminum oxide, powder, <10 um avg. part), SiO_2 (Quartz, Sand, White quartz), Fe_2O_3 (Iron(III) oxide, powder, <5 micron, >=99), the CaO (CALCIUM OXIDE, REAGENT GRADE) and MgO (MAGNESIUM OXIDE, -325 MESH, >=99% TRACE) were sourced from Sigma Aldrich. Each component was weighed out and added to its respective sample. Each sample was then milled using a pestle and mortar and then ashed at 815^{o}C using the British standard for coal ashing[166]. All Samples were analysed using XRF to verify that the composition had not changed during this process.

5.2.3 Ash Fusion Temperatures and Test Curves

The OAAFT profiles were obtained using the methodology documented in Chapter 4.

Table 5-1: major oxides in samples 1 - 20 of the pseudo pellets

Sample		Weights % (XRF)						B-A ratio	I-C ratio	Silica %	AFT temperatures (^oC)	
		SiO_2	Al_2O_3	Ratio	Fe_2O_3	CaO	MgO				IDT	FT
CaO	1	54	28	1.9	18	0	0	0.22	0.0	75	1460	1538
	2	48	25	2.0	16	11	0	0.37	1.5	64	1319	1363
	3	43	22	2.0	14	20	0	0.53	0.7	56	1353	1385
	4	37	20	1.9	12	31	0	0.76	0.4	46	1307	1344
	5	33	16	2.0	11	41	0	1.05	0.3	39	1266	1295
Fe2O3	6	56	29	1.9	0	15	0	0.17	0.0	79	1403	1482
	7	51	26	2.0	10	13	0	0.30	0.8	69	1329	1399
	8	45	23	2.0	20	12	0	0.48	1.7	58	1299	1359
	9	39	20	2.0	31	11	0	0.71	2.9	48	1306	1356
	10	33	17	2.0	41	9	0	0.98	4.5	40	1330	1386
MgO	11	47	24	2.0	16	13	0	0.40	1.3	62	1305	1364
	12	47	24	1.9	16	13	5	0.47	1.3	58	1298	1321
	13	47	24	2.0	16	13	11	0.55	1.3	55	1225	1292
	14	47	25	1.9	16	12	18	0.64	1.3	51	1211	1250

	15	47	24	2.0	16	13	25	0.76	1.2	47	1254.5	1286
S/A	16	25	48	0.5	16	12	0	0.39	1.3	47	1401.5	1451.5
	17	36	36	1.0	15	13	0	0.40	1.2	56	1352.5	1405
	18	48	25	1.9	16	12	0	0.39	1.3	63	1307.5	1361.5
	19	54	18	3.0	16	12	0	0.39	1.3	66	1226	1346
	20	57	15	3.9	16	12	0	0.39	1.3	67	1189	1320.5

IDT, initial deformation temperature; ST, spherical temperature; HT, hemispherical temperature; FT, flow temperature. Ash oxide compositions and standard ash fusion temperatures of a range of international Coals.

All % are w/w %

5.3 Results and Discussions

5.3.1 Pseudo Pellet Individual Element analysis

In this section the individual component effects on ash fusion temperatures will be examined and compared with literature. Furthermore, the curve shapes of each of these samples will be compared to other samples and the single component pellets in Figure 5-1.

MgO – The magnesium oxide curve reaches the end of the test without completion of the curve shape. It is likely that the reduction shown is shrinkage before a further deformation phase based on the change in gradient between 1500 – 1600 ^{o}C.

CaO – Calcium oxide is the only component that reaches Flow Temperature (at 1500 ^{o}C). There is only a marginal shrinkage period of around 5-10%.

Al_2O_3 – Aluminium shows very little change over the range 0 – 1600 ^{o}C, a very small level of shrinkage, around 1-5%, at around 1450 to 1600 ^{o}C.

Fe_2O_3 – The iron oxide curve displays clear shrinking properties for a sharp increase. This is like many traditional coal ashes and is likely to be the component responsible for this behaviour.

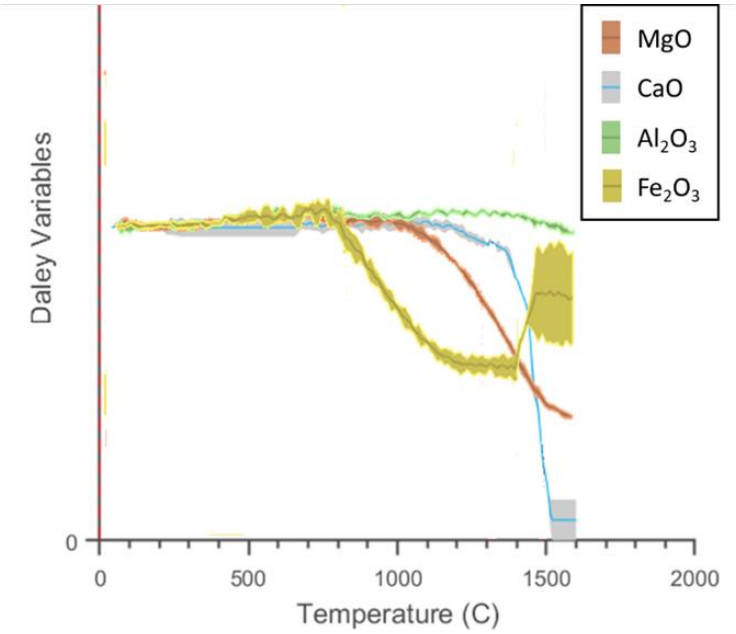


Figure 5-1: Individual component curves from the OAAFT.

Note: It was not possible to make a pellet of SiO_2.

5.3.1.1 CaO comparisons

The CaO content was varied between 0% and 40% based on the range of international fuels taken from literature. CaO can be used as a fluxing agent to reduce the AFT temperatures of coal ashes [117], [167]. This is supported by all the data in Figure 5-2, up to the point of 30 ^{o}C. There is rapid decrease in AFT temperatures (~200 ^{o}C) between 0 and 10% weight, 20 ^{o}C/w%. Once this effect has occurred there is a plateau between 10% and 40% where the AFT temperatures generally decrease but only by 100 ^{o}C, 3.3 ^{o}C/w%. As the other data sets pass 40% the AFT temperatures begin to increase again at a similar rate. There are discrepancies in the data, the OAAFT shows no minimum point and the studies by Lui et al and Song et al show a minimum at 30 and 35 ^{o}C respectively. A second order polynomial fits the dataset of Lui and Song

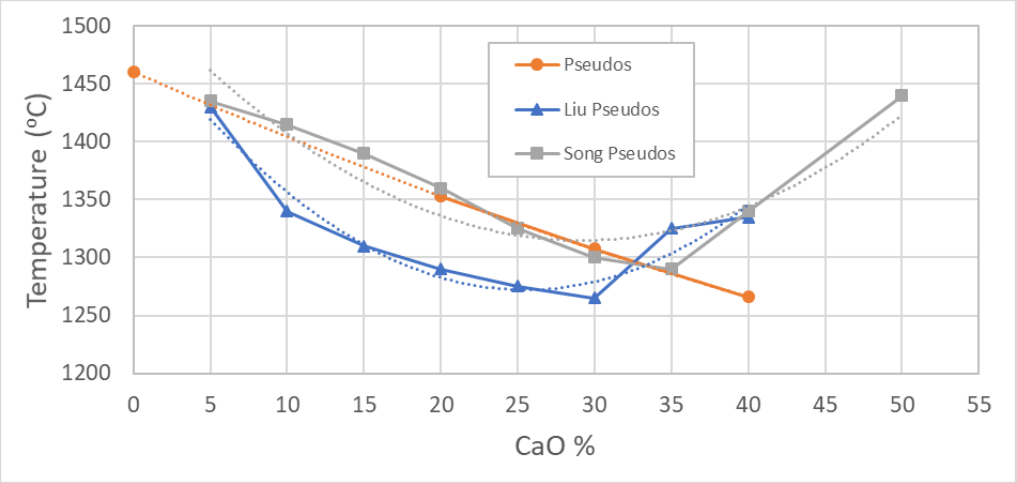


Figure 5-2: Ash fusion temperatures for CaO at 0-40%

however, the OAAFT datapoints could be linear (Figure 5-2, Table 5-2). The other plots display sharp increase at the minimum point which does suggest that the OAAFT plot would be parabolic if the concentration was increased further. Lui's explanation for the rapid reduction in the AFT temperatures, then rapid increase passed 40% weight shown in Figure 5-2, has been attributed to low melting eutectics of CaO with other minerals, whilst at higher concentrations, high melting CaO monomers form to raise the AFT temperatures [164]. The lack in rapid increase for the OAAFT could be down to the high-pressure pellets enabling eutectics at higher concentrations. Song, however, observed a shift in subliquidous phase from low-melting gehlenite to high-melting mullite from 5%-35% and then back when the weight % increased from 35-40% over the range of concentrations [163].

Table 5-2: Line equations and R-squared values for the CaO investigations

	Equations	Minimum point	R^2
OAAFT pseudo pellets	$y = 0.025x^2 - 5.86x + 1460$	117%	1
Liu pseudo pellets	$y = 0.35x^2 - 17.86x + 1500$	25.5%	0.936
Song pseudo pellets	$y = 0.25x^2 - 14.64x + 1528$	29%	0.859

The atmospheric conditions of the tests appear to have made an impact on results. The reducing conditions have shifted the late increase in deformation temperature to 30% whereas, the inert conditions show the shift at 35% and the oxidising doesn't show the phenomena at all. Furthermore, the AFT temperatures under reducing atmosphere are generally, around 50-100 ^{o}C lower than that of the oxidising and reducing conditions. Figure 5-3 presents the OAAFT curve for the CaO pseudo pellets which go through a drastic transformation from 0 to 40% weight. The difference between IDT and FT continuously shrinks as the CaO is increased. At 0% the difference is over 50 ^{o}C, and by 40% the difference is down to 25 ^{o}C. The addition of CaO reduces the shrinkage of the samples therefore, there is no sign of sintering before IDT. The most obvious change that can be seen is the loss of the expanding phase completely from the curve. The closest example of the raw CaO curve is the 40% weight samples, which is to be expected with the highest concentration of CaO. The only difference is that the IDT comes at around 100 ^{o}C earlier.

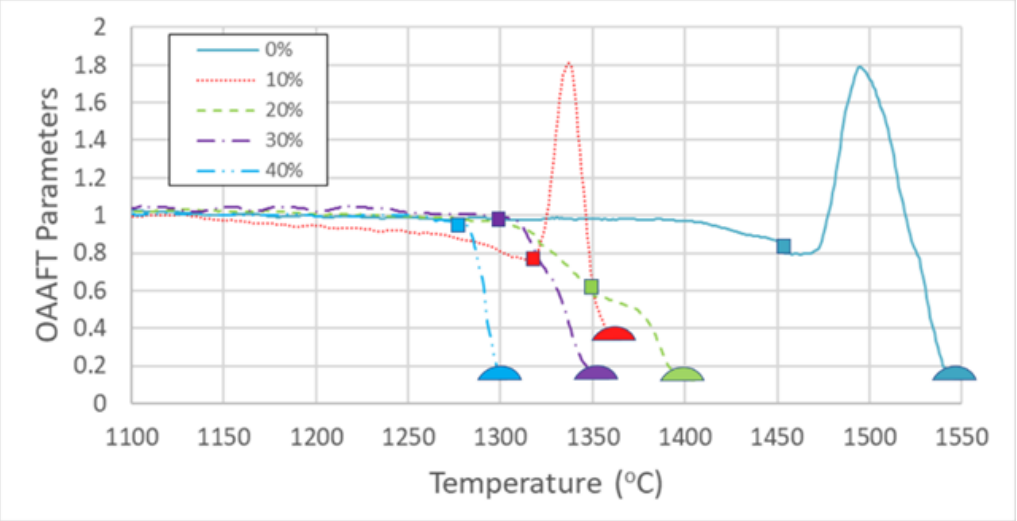


Figure 5-3: OAAFT curves for the CaO pseudo pellets ranging from 0 - 40% weight

5.3.1.2 Fe2O3 comparisons

Iron occurs in coal mainly as ferric iron in both oxidising and reducing conditions [164], [168]. Under reducing conditions, the iron take ferrous or metallic forms [163], [164]. Liu comments that specifically the valence state of iron plays a large role in melting behaviour [164]. The Fe_2O_3 studied in this investigation ranges from 0-40% based on the range in coal ashes in Table 0-1. The comparisons of the 2 studies in literature are displayed in Figure 5-4 and show good correlation in trends of the IDT.

The IDT decreases from 0 to 30% with the minimum being 100 ^{o}C and maximum being 275 ^{o}C. 1 of the studies finishes at 30% however, this study and that of Song continue to 40% which show a slight increase in IDT. The greatest impact on IDT is seen between 0-20%, as the Fe_2O_3 composition increases the trend levels off.

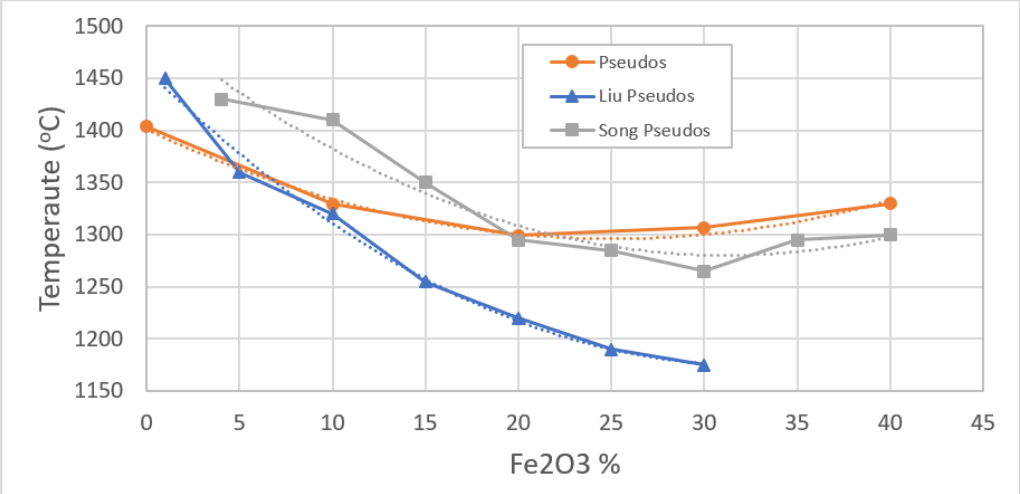


Figure 5-4: Comparison of pseudo pellet deformation temperatures with existing literature

Whereas the CaO investigation displayed an earlier 'trough' under reducing atmosphere, increasing to inert and then oxidising, this investigation shows the opposite trend. As shown in Table 5-3 the 'trough' or minimum point in the oxidising curve is seen at 25% whilst inert is at 31%. Although the reducing curve has not yet reached its minimum point, the minimum point of the line of best fit suggest a minimum point shortly after the final data point. Similarly to the CaO investigation, the reducing AFT temperatures are lower however, more consistently at 100 ^{o}C less. In the reducing investigation, the general trend shown in AFT temperatures is attributed to an increase in FeO, rather than Fe_2O_3. This is due to new chemical bonds forming between Fe(II), and unsaturated O_2 and subsequent eutectic compounds between the FeO and other oxides at high temperatures [164]. This could explain the shift in trend whereby oxygen is more readily available and stems the increase in FeO.

Table 5-3: Line equations and R-squared values for the Fe_2O_3 investigations

	Equations	Minimum point	R^2
OAAFT pseudo pellets	$y = 0.1661x^2 - 8.3379x + 1400.8$	25%	0.988
Liu pseudo pellets	$y = 0.2667x^2 - 17.391x + 1458.1$	33%	0.933
Song pseudo pellets	$y = 0.2287x^2 - 14.242x + 1501.9$	31%	0.992

The comparison of the individual components in Figure 5-1 identified Fe_2O_3 as the component with greatest and earliest change in morphology. It can be seen in Figure 5-5 that the addition of Fe_2O_3 has an instant impact on the shape of the OAAFT curve.

The addition of iron initiates a shrinking and expanding phase. All the samples containing Fe_2O_3 shrink by 30-40% and from the sintered size all

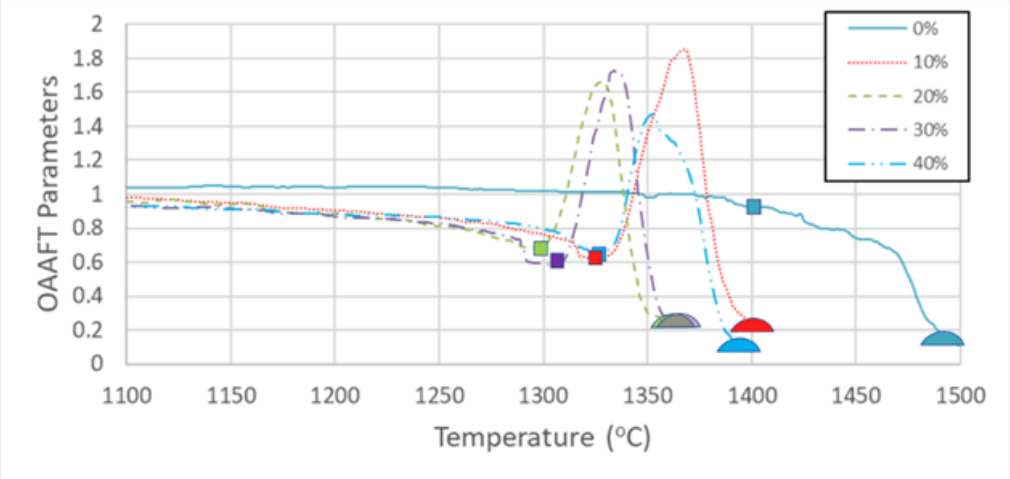


Figure 5-5: OAAFT curves for the Fe2O¬3 pseudo pellets ranging from 0-40% weight

samples appear to at least double in size, which is in stark contrast to CaO. When the CaO concentration increases, it depresses and finally removes the peak from the curve. It seems that the iron in the sample is either responsible for the expanding phase or at the very least doesn't inhibit it. The AFT range stays constant throughout all the samples, suggesting that Fe_2O_3 has no impact.

5.3.1.3 Silica-Alumina (S/A) Ratio

S/A ratio is known to play an important role in AFT temperatures and ash melting properties [169]. In this study 5 pseudo ash pellets were created to cover the range of S/A ratios (0.5-4) whilst reflecting the compositions of the range of coal ashes from Table 0-1. The DT of the samples were then plotted and compared to current literature in Figure 5-6.

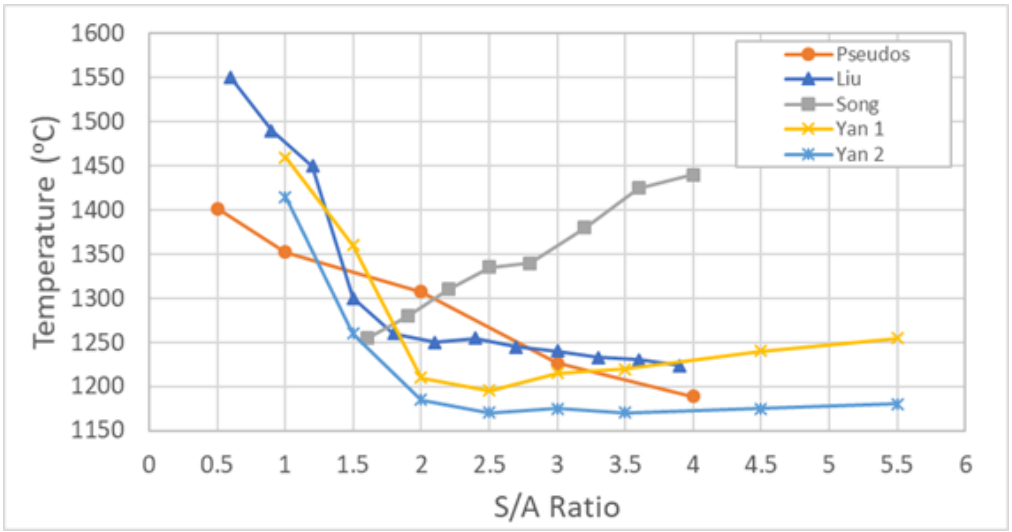


Figure 5-6: Comparison of pseudo pellet deformation temperatures with existing literature

Yan investigates the 2 groups of samples where the CaO has been increased in Yan 2 (from 16 to 23) to shift the acid-base ratio [165]. The drop from Yan 1 to Yan 2 can be explained by the 7% decrease of CaO. Within this range on average, it decreases the DT by 25 ^{o}C as show in the study above. All the investigations have slightly differing components in each of their pseudo pellets, which is due to the coals that they are attempting to reflect. This has the impact of causing slightly varying trends. In most cases however, there is a general trend that increasing the S/A ratio results in reducing the DT. It is difficult to explain the result found by Song as there are clear outliers compared to the other studies. The only difference in Song's study is that it includes minor constituents, MgO, TiO_2, Na_2O and K_2O in all samples in small quantities. The other investigations only add MgO and K_2O into specific tests to identify the impact of each individual component. These minor constituents may have cumulatively impacted on the overall eutectics of the mixture. 3/5 of the studies identified a steep drop of roughly 200 ^{o}C in DT between a S/A of 1 and 2 before a plateau at S/A of over 2. Further increasing the S/A has no effect on DT. The trend found using the OAAFT shows a linear decrease in AFT temperatures. As it is the only test done in an oxidising environment, this may have elongated the general trend seen by shifting the plateau, something that has been seen in the other individual component studies. The impact of atmosphere on the OAAFT should be investigated in further research.

The S/A ratio clearly has a large impact on both the shape of the OAAFT curve (Figure 5-7) and the AFT temperature range. The most obvious change is

that increasing the ratio firstly adds an expansion and sintering phase, and then increases the magnitude of the expansion phase.

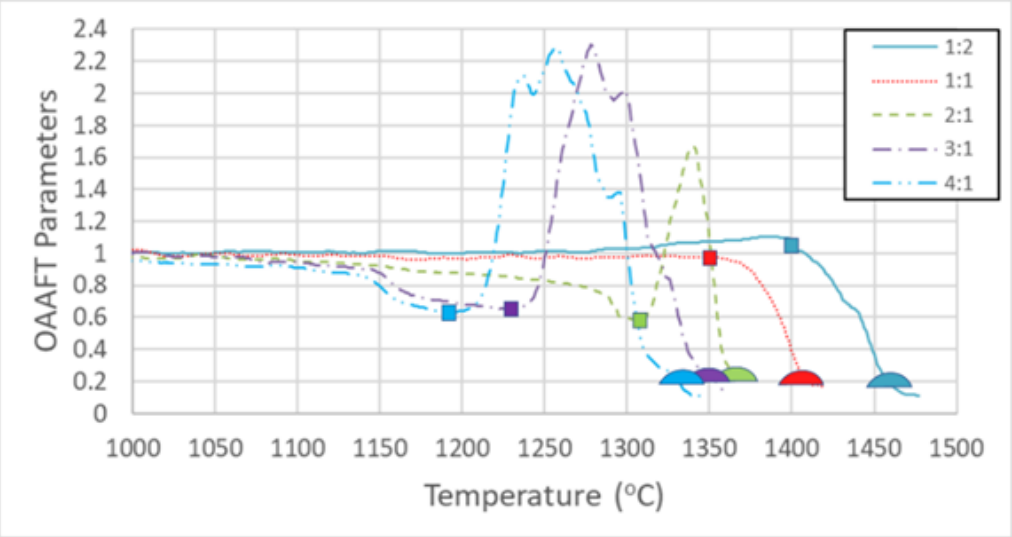


Figure 5-7: OAAFT curves for the pseudo pellets ranging from S/A of 0.5 to 4

The expansion increases from 0 to 60% from 1:1 to 2:1, and another 60% to 3:1. The 1:1 sample displays no sintering phase whilst the 2:1 sample shrinks by 40%. This would suggest that the sintering strength of the samples increases with S/A ratio. The increase in AFT temperature range where a low DT is paired with a high FT, can be a severe problem for boiler operation. This characteristic can cause deposition and lead to stickiness at low temperatures [165], [170], [171].

5.3.1.4 MgO comparison

Magnesium oxide is a minor component to most coal ashes however, it is a basic oxide and, even at low concentrations can impact the melting characteristics. Increasing the concentration can lead to lower AFT temperatures and prove beneficial to flow properties of coal ash slag samples

[99], [163]. In this study, 5 pseudo ash pellets were created to cover the range of MgO weight percentages (0-30) whilst reflecting the compositions of the range of coal ashes from Table 0-1. The DT of the samples were then plotted and compared to current literature in Figure 5-8. The trends from Song do not match exactly with the findings from this study however, they display a general decrease from 0-15% of around 100 ^{o}C.

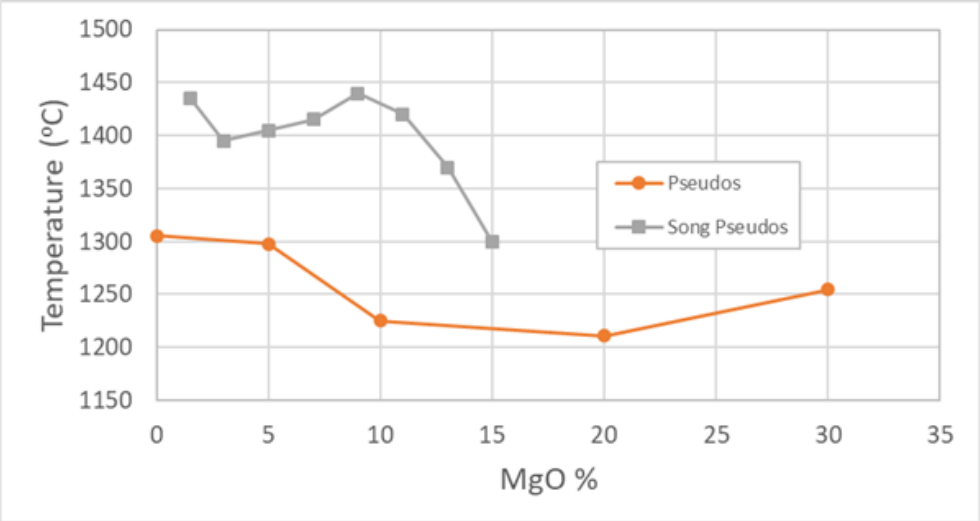


Figure 5-8: Comparison of pseudo pellet deformation temperatures with existing literature

The results reflect a similar behaviour to iron, a minimum point at 20% weight with increasing IDTs either side. However, both curves fit a 3rd order polynomial, displayed in Table 5-4, better than 2nd order as the previous trends.

As shown in

Figure 5-9 when the MgO is increased the OAAFT curve changes in shape similarly to that of the CaO OAAFT but with increased potency.

Table 5-4: Line equations and R-squared values for the MgO investigations

	Equations	R^2
OAAFT pseudo pellets	$y = 0.0102x^3 - 0.1608x^2 - 6.2085x + 1311.8$	0.8836
Song pseudo pellets	$y = -0.3339x^3 + 6.8755x^2 - 40.012x + 1474$	0.9623

The expansion phase is completely lost with only 5% weight of MgO added and the AFT range is reduced by half. The sintering phase is sustained until 10% weight is added. Unlike CaO, which trends towards is individual component curve shape, the MgO curves trend towards the CaO curve shape with no sintering and minimal AFT range. The exception to this is that at 30% MgO the expansion phase returns, and the sample expands by 20% after the IDT.

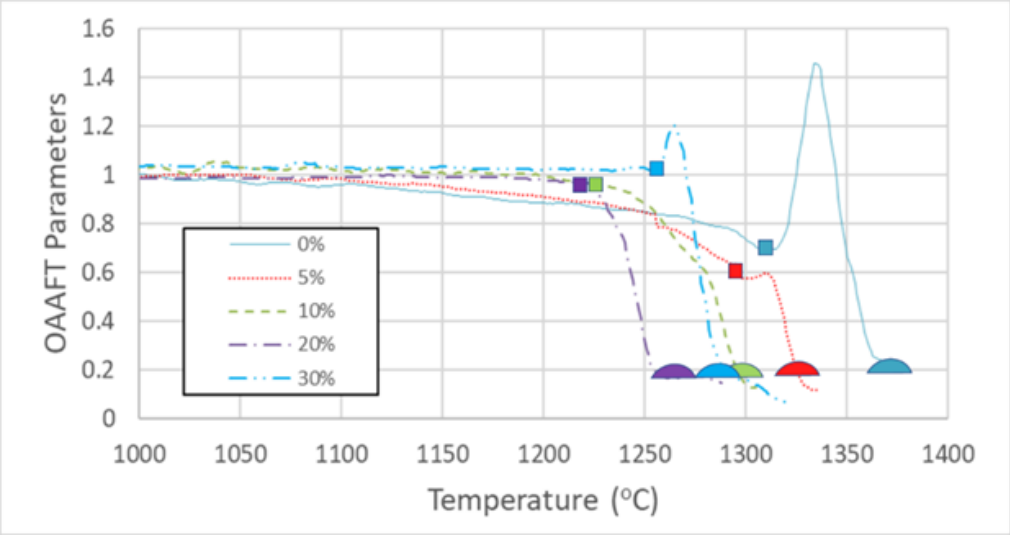


Figure 5-9: OAAFT curves for the pseudo pellets ranging from MgO of 0 to 30

5.3.1.5 U-shaped trend

The CaO, Fe_2O_3 and the MgO IDT trends all displayed a parabolic trend as the concentration for each component was increased. This phenomenon suggests that the effect of adding these is reversed when the concentration becomes too high. Each of the investigations show an optimum low melting point in relation to the component in question. This, however, is not consistent across literature and that suggests that the ratios of the other components has a significant impact on the IDT. Thus using these components as an additive is possible, but the extent of the impact on the IDT is dependent on the ratios of the other components.

5.4 Significance of Data

The significance of the OAAFT curves responding to changes in individual elements means that it can potentially be used to highlight 'problem' cases. The profiles appear to fingerprint the behaviour of the different components. Furthermore, should a problem arise from swelling or sintering, the OAAFT could be used to test if mineral additives, such as CaO and MgO will work to modify the behaviour.

5.5 Conclusions

In this chapter, the ash fusion temperatures and OAAFT curves have been measured for a set of pseudo ash pellets based on a range of 31 international coals from literature simplified to a 4-component system of SiO_2, Al_2O_3, CaO, and Fe_2O_3, with 1 5-component system including MgO. Each component oxide was studied to show its effect on the AFT temperatures and OAAFT curves.

AFT temperatures : Fe_2O_3 and MgO initially reduced the AFT temperatures by 100 ^oC until a minimum at 20% weight, before increasing and resulting in parabolic shaped curves. The AFT temperatures decreased linearly with increasing CaO and S/A ratio. These results aligned well with literature however, the difference in atmosphere shifted the AFT temperatures in some studies. Furthermore, the investigations in literature were replicating different average coals, this meant that the ratios of components that were not the focus of each investigation, were not identical. This is another factor in shifting the general trend of each test set.

OAAFT curves: As the CaO is increased the AFT range halves, and the sintering and expanding phases are lost from the curve the 40% curve closely resembles the raw CaO OAAFT curve. The addition of Fe_2O_3 initiates a 30-40% shrinkage during the sintering phase and an expansion phase that doubles in size from the sintered size. Iron is 1 of the components necessary for the expanding phase in coal ash. Increasing the S/A ratio adds an expansion phase which then doubles over the range, and a sintering phase is added with a 40% shrinkage. When the MgO is increased by only 5% weight the expansion phase is completely lost. The AFT range is reduced by half and the sintering phase is sustained until 10% weight is added.

5.6 Further work

It was noted during the chapter that the some of the results deviate from other findings in literature. A factor that could explain these differences would be the ratio of the other elements to the 1s of interest, (i.e. if CaO is the focus,

the ratio of components Fe_2O_3, SiO_2, Al_2O_3 and MgO). An alternative way to compare the results would be to model the samples using FactSage, in the same way that Song investigates[163]. Rather than directly comparing the AFT temperatures of each study, comparing the closeness of the results to the thermodynamics package. This would give a reference point which considers the entirety of each sample whilst further validating the package. Furthermore, the investigation of K_2CO_3 was dropped from the research program due to time constraints. A similar investigation including K_2CO_3 would be an interesting addition as K is known to have a strong impact on AFT temperatures. To add to the existing OAAFT curves, it would be interesting to investigate if the trends identified in this chapter are reflected in naturally occurring coal ashes. To add to this, an investigation could also use a standard coal ash to which individual components are added to identify the impact of raw CaO, Fe_2O_3 etc. on naturally occurring samples OAAFT.

Chapter 6 : Assessing the Link Between the Optimised Advanced Ash Fusion Test Curve and FactSage Modelling for A Range of Coals and Biomasses

6.1 Introduction

Ash melting temperature has long been used as an indicator for the onset of slagging and fouling in coal and biomass power stations. The main empirical test method being the ash fusion test. This test has been known to have issues with repeatability and reliability which have been addressed in Chapters 3 and 4. Industry still uses the results to inform decision making during fuel selection and fault finding. The recent development of the optimised advanced ash fusion test delivers a highly repeatable version of the test. It provides the opportunity to better understand how fuel ashes are behaving during the melting process, as well as a reliable indicator of traditional ash fusion temperatures. Continuous improvement in predictive modelling of mineral transformation during heating of ash is being made using modelling software FactSage. These 2 forms of analysis offer an opportunity to better understand the link between triggers for ash melting and mineral transformations. In turn, they can be used to enhance fuel selection predicting slagging and fouling propensities of fuels. Furthermore, the maceral data of the coal via petrographic analysis and the mineral data of the ash has been collected. This holistic approach to characterising the database of fuels will be used to find any trends in pre or post ashing analysis. After identifying individual mineral impact on the AFT temperatures and the OAAFT curve in Chapter 5, this chapter looks

at a wide range of coal and biomasses mineral data to identify if these conclusions hold up to empirical testing.

In this Chapter, a range of 20 BF2RA coal bank and international coals & 11 Biomasses were tested to identify the OAAFT curve using the previously refined method. Petrographic analysis has been run on the coals to assess the impact of rank and maceral content on the OAAFT. Fused bead X-ray fluorescence was run on all the fuels to obtain high quality mineral data. This was input to the FactSage model to predict liquidus temperatures and compare to the OAAFT curve. Furthermore, the aim for the chapter is to identify groups of OAAFT curves and to potentially link behaviour to a general shape.

6.2 Materials and Methods

6.2.1 Petrographic Analysis

When preparing the coals for petrographic analysis, the fine particles in the sample need to be removed to enable characterisation using image analysis software. The fuel is milled as documented in chapter 3.2.1 and then jet sieved using a 20 µm screen to remove the fines.

The prepared coals were mixed with simplex rapid powder at a ratio of 4:1, powder to sample. The mixture was pressed into blocks at 30 kN, heated for 9 mins and cooled for 6 mins. These were then backed with resin, 25 parts resin and 3 parts hardener, to enable polishing. The polishing method was 600 under 25N for 1 min, 1200 under 25N for 2 mins, 2400 under 15N for 1 min, and finally 9 µm with diamond solution for 2 mins. The petrographic images were taken using a high definition microscope.

6.2.2 Fused Bead X-ray fluorescence (XRF)

To obtain elemental data of high enough accuracy for the FactSage analysis, fused bead XRF was carried out. The ash samples were first ignited at 900 ^{o}C to drive off any volatiles, the loss in % weight is recorded in the table as loss on ignition (LOI). Once ignited, the samples were mixed with a fluxing agent at a ratio of 10:1, fluxing agent to sample. The mixture was then heated in a platinum pot with an oxygenated flame. The molten mixture was poured into a mould and air cooled. The beads were then analysed using a PANalytical Axios-Advanced XRF spectrometer.

6.2.3 FactSage Thermochemical calculations

Thermochemical calculations of the mineral phases were executed by FactSage™ using version 7.2 [91]. Herein, the data bases of FToxid, FTmisc, FTsalt, and FactPS were regarded in that order. Solution species are selected in accordance with [95]. The input data for the calculations are: all oxides from the XRF (see Table 6-1), and an air atmosphere composed of an average ratio between the 3 main components (75.56 wt% N2, 23.15 wt% O2, and 1.29 wt% Ar). A surplus of air was considered by the 20-fold mass of the total oxides. The graphical representation of slag content is shown in Figure 6-1.

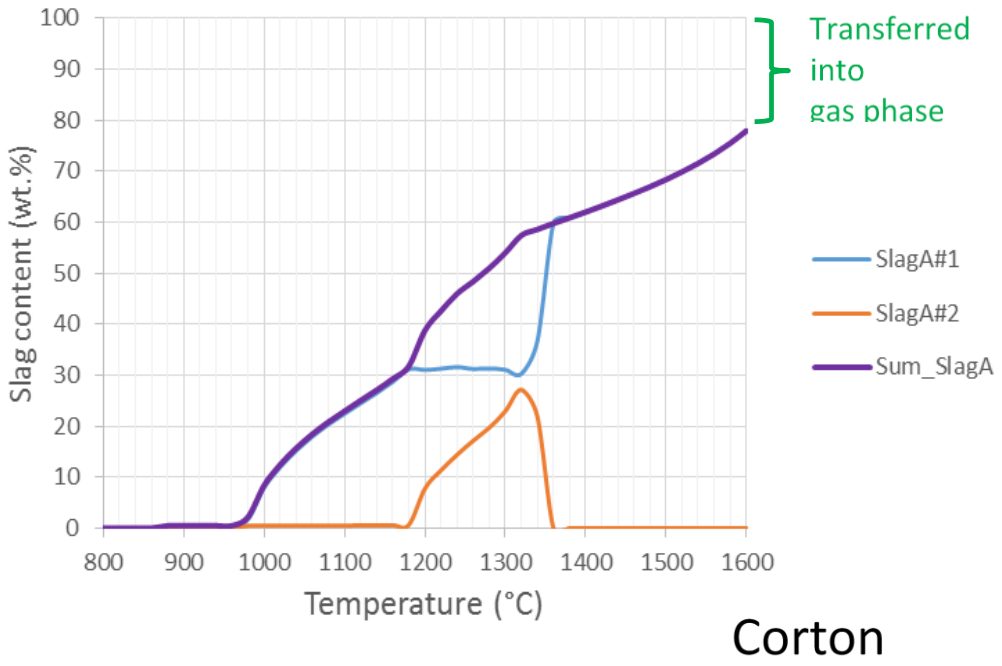


Figure 6-1: Illustration of Slag content analysis from FactSage (SlagA with 2 potentially immiscible phases) vs. temperature

6.2.4 Fuel Characterisation

Table 6-2 notes the maceral content and vitrinite reflectance of the coals. The data shows that the database contains a wide range different rank coals including lignite's and an anthracite. Rank does not play a role in ash fusion behaviour. Table 6-1 shows the XRF data for the coal and biomass; a wide scope of mineral content in these fuels is evident. This gives a broad range to reference for the analysis.

Table 6-1: Fused Bead XRF Data for the Coal and Biomass Database

Sample	SiO_2	TiO_2	Al_2O_3	Fe_2O_3	MgO	CaO	Na_2O	K_2O	P_2O_5	SO_3	SrO*	BaO*	ZnO*	LOI	Total
Gedling	34.9	1.1	29.6	5.4	1.5	6.2	7.8	0.5	1.2	6.8	0.5	2.1	0.0	2.0	100.3
Corton Wood	51.2	2.7	35.5	3.0	0.4	0.9	0.9	0.8	0.2	0.4	0.1	0.4	0.0	1.1	98.4
Kellingly	45.0	0.9	29.2	13.1	1.7	1.4	1.2	3.8	0.1	2.1	0.0	0.3	0.0	1.4	100.5
CWD	32.6	0.9	38.1	2.3	0.2	2.4	0.9	0.3	10.2	1.7	5.4	2.4	0.0	0.9	98.6
Cresswell	36.1	1.3	32.3	15.1	0.8	3.0	5.6	0.8	0.2	2.9	0.1	0.6	0.0	1.5	100.8
Jagua	44.0	1.2	35.8	4.9	0.9	3.4	1.1	0.4	1.5	1.8	0.7	1.2	0.0	2.0	99.3
Littleton	36.7	0.9	26.6	9.6	2.4	6.4	3.8	2.4	0.3	7.4	0.1	0.3	0.1	2.7	100.0
Golden hope	56.9	1.7	29.6	5.3	0.8	0.8	0.3	2.9	0.1	0.5	0.1	0.3	0.0	0.9	100.4
Taff merth	48.7	1.1	35.8	2.8	0.7	1.6	1.2	1.3	1.2	0.3	0.5	0.7	0.0	2.3	98.5
Tillman stone	36.0	0.7	28.0	22.2	0.7	3.1	0.8	2.0	0.2	2.3	0.1	0.3	0.0	2.4	99.2
Markham	27.8	0.9	23.3	20.4	1.2	5.6	6.7	0.8	0.5	6.5	0.1	0.4	0.0	4.0	98.9
Yanoice	38.0	1.2	32.5	9.5	1.8	3.7	1.6	2.2	2.8	1.5	0.4	1.1	0.1	2.5	99.2
Trentham	31.9	0.8	27.2	15.6	1.7	7.2	3.0	0.7	1.8	5.5	0.2	0.4	0.1	2.6	99.2
Seaham	37.1	1.1	22.6	19.9	2.5	3.9	2.7	0.8	0.2	4.8	0.1	0.8	0.2	1.8	99.0
Indonesian	44.5	1.0	23.1	13.2	2.0	5.1	0.8	2.3	0.4	3.2	0.1	0.5	0.0	2.8	99.6
Pittsburg no.7	43.0	0.9	20.3	14.4	1.5	5.8	0.5	1.9	0.4	6.2	0.1	0.3	0.0	3.2	98.7
USA Blue Creek	47.7	1.4	31.1	7.3	1.2	2.0	0.9	2.4	1.2	0.5	0.3	0.8	0.0	2.4	99.4
La loma	53.6	0.9	21.7	8.9	2.0	4.8	1.4	2.4	0.4	1.9	0.1	0.4	0.0	0.5	99.1
Zondag	42.7	1.4	28.5	3.7	3.5	9.0	0.4	0.8	0.6	3.5	0.3	0.6	2.6	0.9	98.8
Pond fines	55.2	1.0	25.6	6.2	1.7	1.1	0.7	4.2	0.1	0.9	0.0	0.3	0.0	1.2	98.2
B139	56.8	0.0	0.8	0.7	2.3	8.6	0.4	14.6	2.7	4.6	0.0	0.1	0.0	6.6	98.3
MV Flevoborg	9.3	0.1	1.8	1.0	4.8	36.2	0.4	9.5	3.4	3.5	0.1	0.1	0.3	28.3	99.6

Sunflower	3.7	0.0	0.5	0.7	9.7	14.9	0.6	35.9	4.8	14.0	0.1	0.0	0.1	15.2	100.3
BKE Palm Kernel	1.4	0.0	0.1	0.4	10.8	5.1	0.4	35.1	23.8	4.3	0.0	0.0	0.1	10.3	91.9
Bagasse	67.1	0.6	12.2	4.7	1.8	3.1	0.2	4.6	1.6	1.0	0.0	0.1	0.0	2.7	99.8
B586	55.3	0.0	2.2	0.4	3.6	5.1	0.6	14.8	9.7	3.9	0.0	0.0	0.1	3.9	99.7
Jatrophe seed	1.3	0.0	0.3	0.2	10.2	5.2	0.4	35.5	22.3	3.9	0.0	0.0	0.1	10.4	89.8
Eucalyptus	25.4	0.3	7.8	5.6	5.5	18.9	2.5	8.7	2.3	9.9	0.2	0.3	0.1	11.2	100.9
Olive Cake	13.4	0.1	2.8	1.2	3.9	9.8	1.6	30.0	4.0	3.4	0.0	0.0	0.0	17.5	87.8
EC78	56.8	0.1	2.1	1.5	1.9	7.3	0.4	12.8	3.3	4.5	0.0	0.1	0.1	7.7	99.1
B117	24.0	0.2	2.3	1.0	6.8	22.6	1.9	10.5	3.3	4.5	0.1	0.2	0.2	21.6	100.1
Ollerton	36.9	1.6	26.9	18.9	0.6	3.6	5.6	0.7	0.6	1.9	0.1	0.4	0.0	2.2	100.5
G1-A	4.0	0.2	3.0	8.8	14.9	32.1	5.5	0.4	0.0	31.2	0.2	0.3	0.0	-0.3	100.5
G2-A	10.4	0.2	4.9	24.7	10.3	26.1	0.0	0.2	0.0	24.2	0.3	0.1	0.0	-0.8	101.1
G3-A	45.3	0.0	0.4	9.4	2.1	21.1	0.0	0.0	0.0	24.3	0.1	0.1	0.0	0.8	103.7
G4-A	46.1	1.1	6.6	1.9	2.5	16.9	2.2	0.5	0.1	25.0	0.2	0.2	0.0	0.7	104.4
G5-A	31.4	2.6	25.6	1.3	2.3	17.8	0.1	0.7	0.3	17.6	0.1	0.5	0.0	2.6	103.1
G6-A	38.2	0.8	13.8	16.0	2.5	11.3	0.0	1.1	0.1	15.0	0.2	0.1	0.0	3.3	102.6
G7-A	22.6	0.5	10.5	16.0	7.7	17.5	0.0	0.7	0.1	24.1	0.2	0.2	0.0	1.0	101.4

Note:* not used in the FactSage analysis

Table 6-2: Maceral Analysis and Vitrinite Reflectance for the Coal Database

MACERAL ANALYSIS	Gedling	Corton Wood	Kellingly	CWD	Cresswell	Jagua	Littleton	Golden hope	Taff merth
Vitrinite	76	59	82	40	79	73	64	81	77
Liptinite	4	16	2	17	2	1	10	3	0
Semi-Fusinite	4	18	8	29	14	5	12	7	15
Fusinite	16	7	8	14	5	21	14	9	8
VITRINITE REFLECTANCE									
Average	0.55	0.95	0.72	0.96	0.77	0.58	0.61	0.70	1.60
Minimum	0.45	0.76	0.63	0.74	0.66	0.40	0.47	0.44	0.99
Maximum	0.69	1.09	0.85	1.16	0.87	0.88	0.76	0.90	2.27
St.Dev.	0.053	0.080	0.055	0.085	0.059	0.092	0.059	0.097	0.259
MACERAL ANALYSIS	Tillman stone	Markham	Yanoice	Trentham	Seaham	Indonesian	Pittsburg no.7	USA Blue Creek	La loma
Vitrinite	93	82	70	86	81	77	76	81	86
Liptinite	0	6	8	4	6	6	0	1	0
Semi-Fusinite	1	3	8	3	3	9	12	4	3
Fusinite	6	9	14	7	10	8	12	14	11
VITRINITE REFLECTANCE									
Average	1.36	0.59	0.69	0.78	0.80	0.63	0.72	0.99	0.55
Minimum	1.08	0.43	0.53	0.57	0.66	0.49	0.57	0.82	0.39
Maximum	1.52	0.75	1.00	1.02	0.95	0.87	0.90	1.17	0.70
St.Dev.	0.104	0.076	0.098	0.092	0.067	0.089	0.080	0.073	0.071
MACERAL ANALYSIS	Zondag	Pond fines	Ollerton	G1-A	G2-A	G3-A	G4-A	G5-A	G6-A	G7-A

Vitrinite	30	85	78	100	89	95	97	98	94	98
Liptinite	0	1	7	0	11	2	2	1	6	2
Semi-Fusinite	61	7	9	0	0	2	1	0	0	0
Fusinite	9	7	6	0	0	1	0	1	0	0
VITRINITE REFLECTANCE										
Average	0.80	0.85	0.64	0.33	0.31	0.33	0.29	0.28	0.30	0.31
Minimum	0.57	0.61	0.54	0.25	0.25	0.23	0.20	0.20	0.20	0.23
Maximum	1.46	1.08	0.73	0.43	0.43	0.53	0.38	0.35	0.44	0.47
St.Dev.	0.232	0.073	0.049	0.048	0.040	0.062	0.046	0.032	0.058	0.051

6.3 Results and Discussions

6.3.1 FactSage comparison

Below are Figure 6-2 - 6-21 where the OAAFT curves are plotted with the FactSage predicted liquidous temperatures. The OAAFT curve tracks the external shape change plotted against the left axis, and the Slag % tracks the percentage of the samples that has become molten or liquid phase and is plotted against the right axis.

6.3.1.1 Coal OAAFT Curves vs FactSage

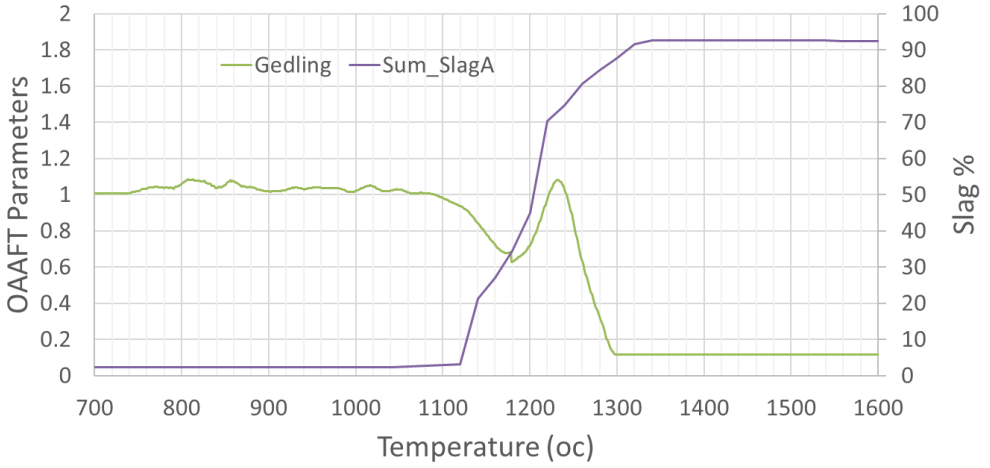


Figure 6-2: Gedling OAAFT vs FactSage

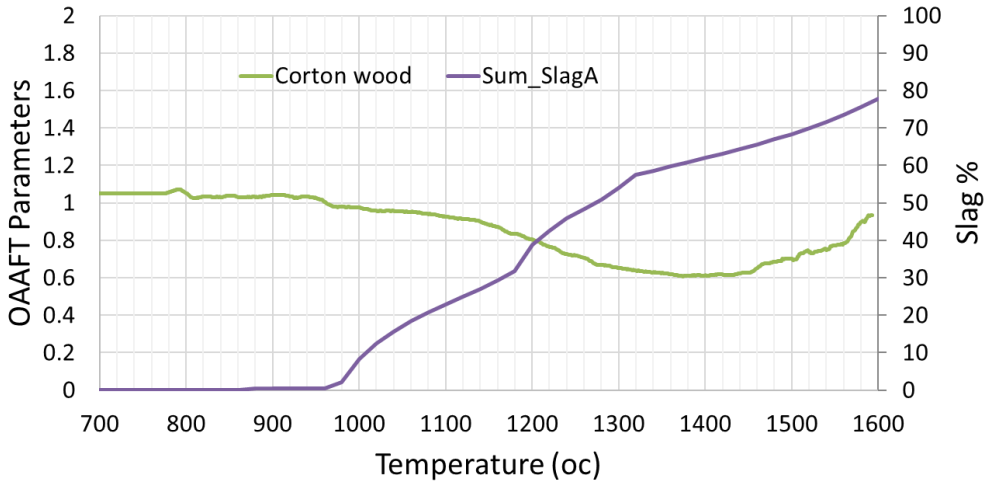


Figure 6-3:Corton Wood OAAFT vs FactSage

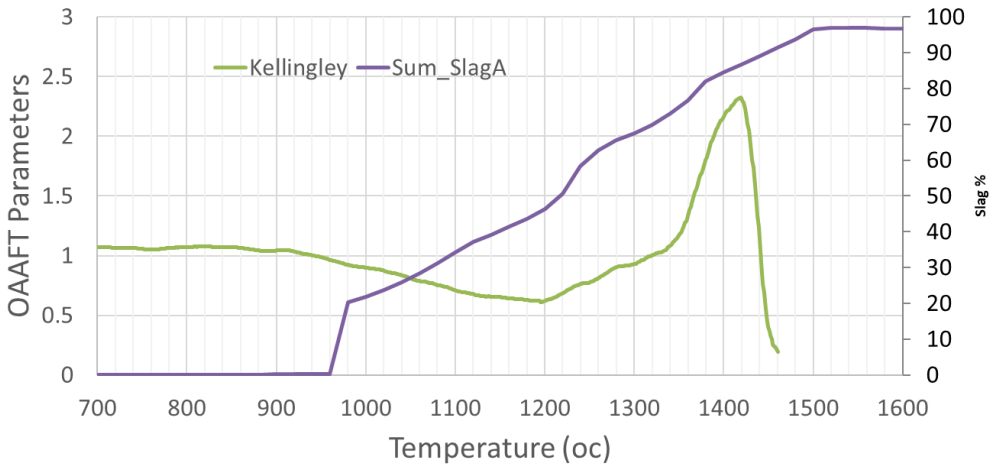


Figure 6-4: Kellingley OAAFT vs FactSage

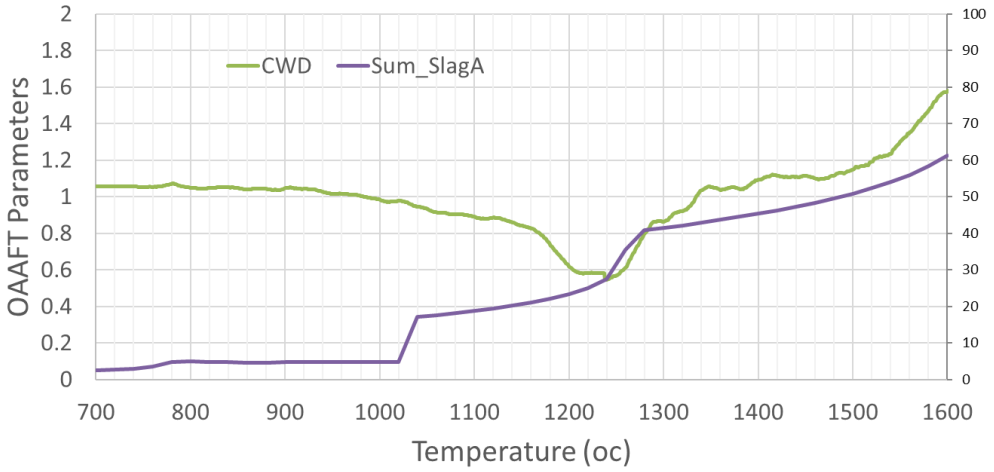


Figure 6-5: CWD OAAFT vs FactSage

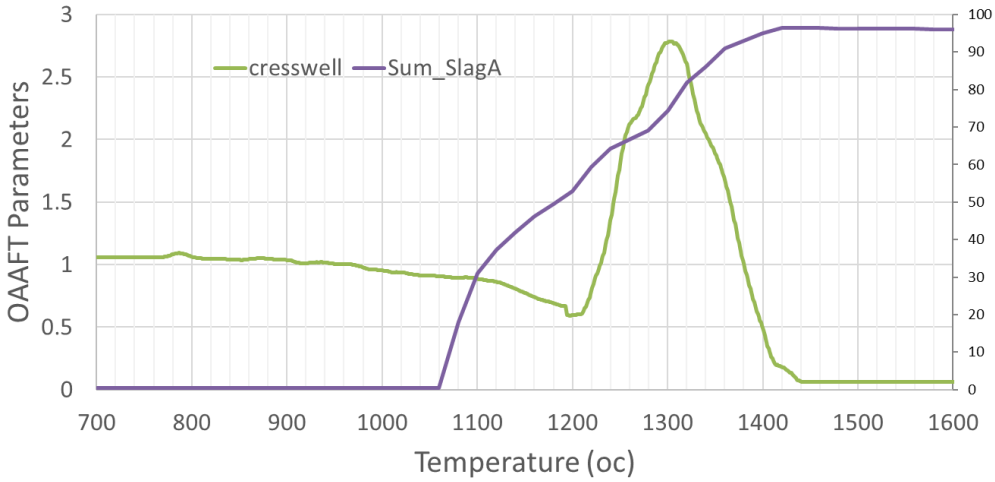


Figure 6-6: Cresswell OAAFT vs FactSage

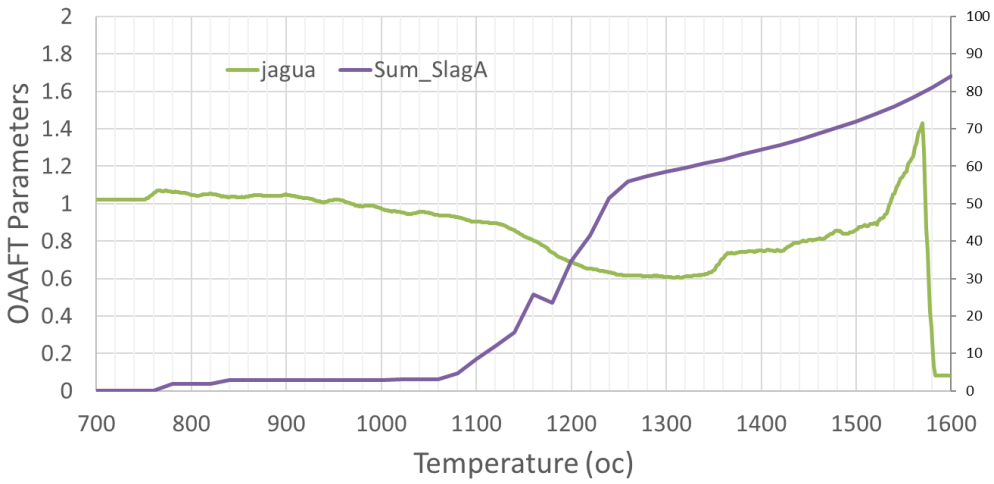


Figure 6-7: Jagua OAAFT vs FactSage

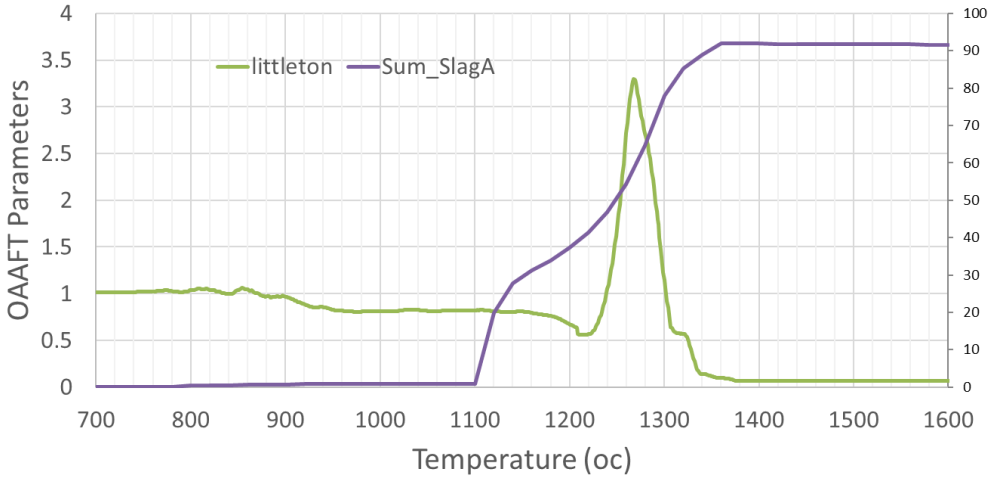


Figure 6-8: Littleton OAAFT vs FactSage

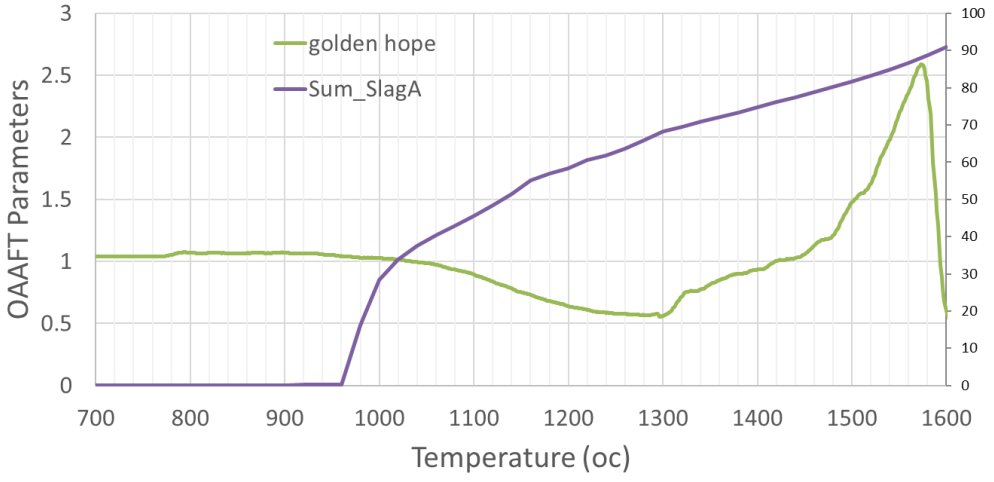


Figure 6-9: Golden hope OAAFT vs FactSage

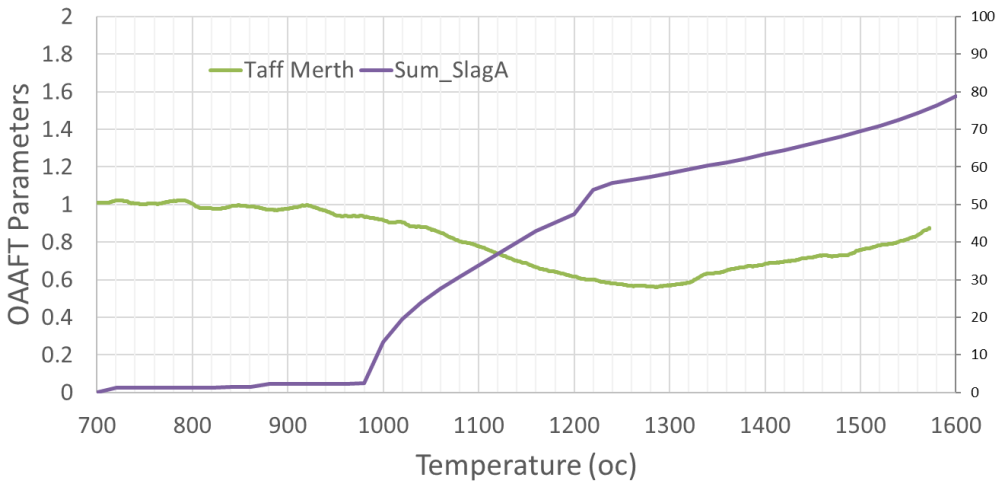


Figure 6-10: Taff Merth OAAFT vs FactSage

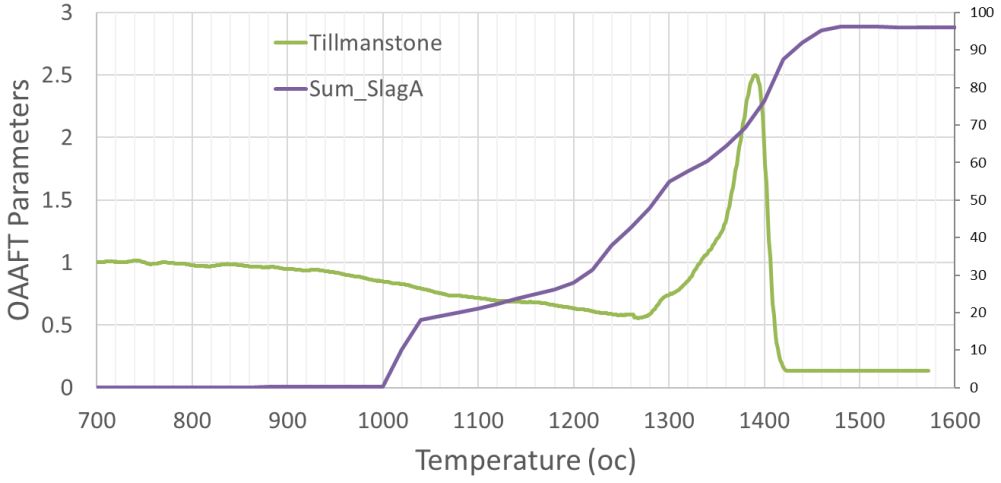


Figure 6-11: Tillman Stone OAAFT vs FactSage

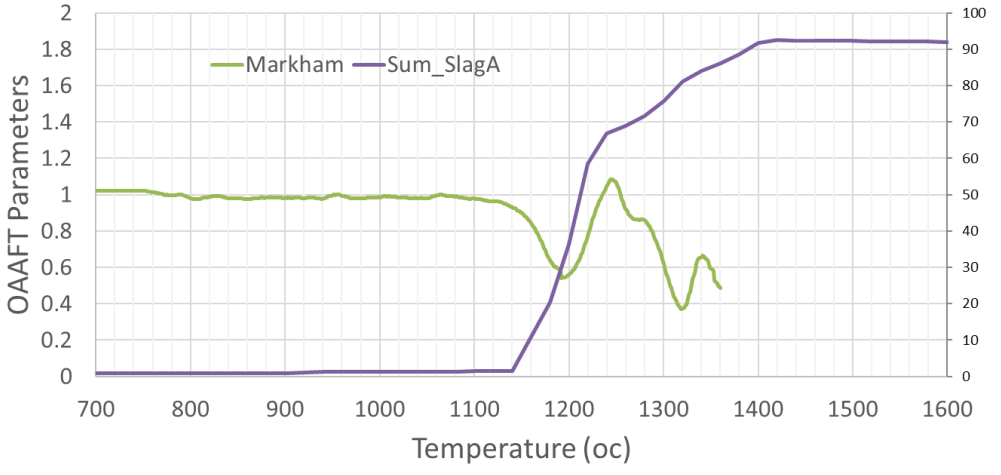


Figure 6-12: Markham OAAFT vs FactSage

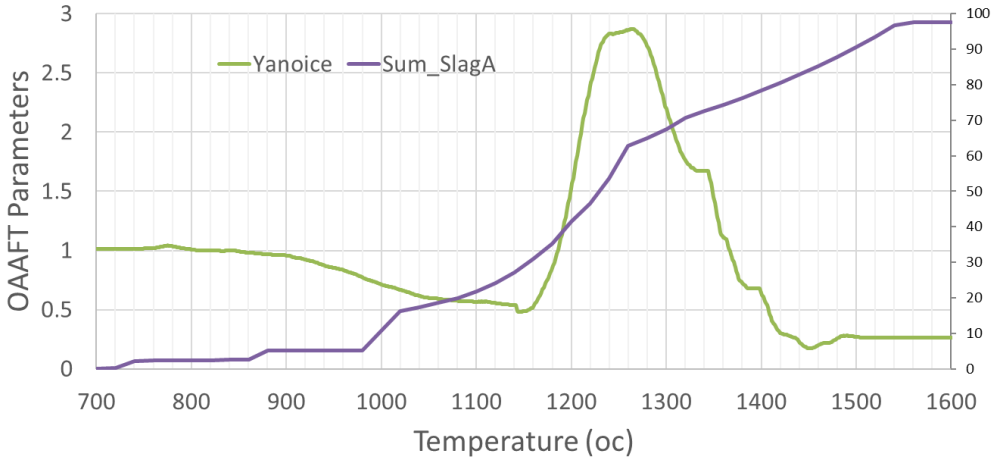


Figure 6-13: Yanoice OAAFT vs FactSage

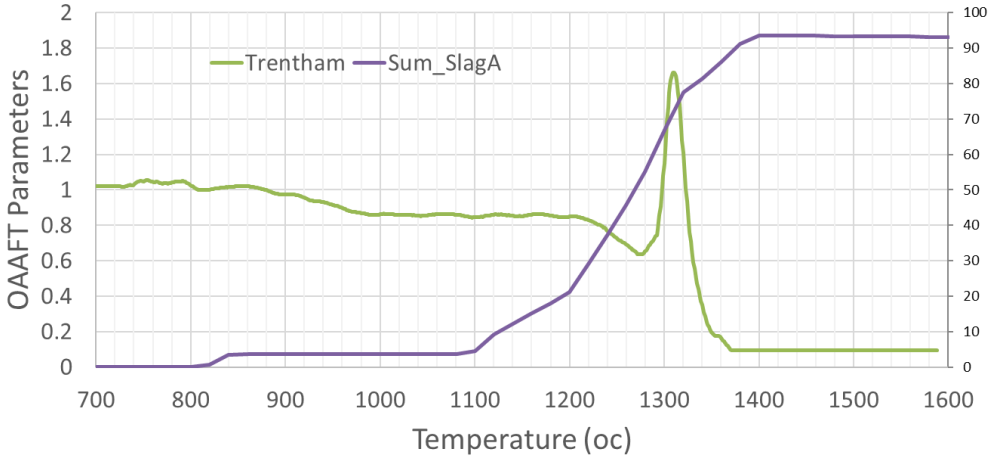


Figure 6-14: Trentham OAAFT vs FactSage

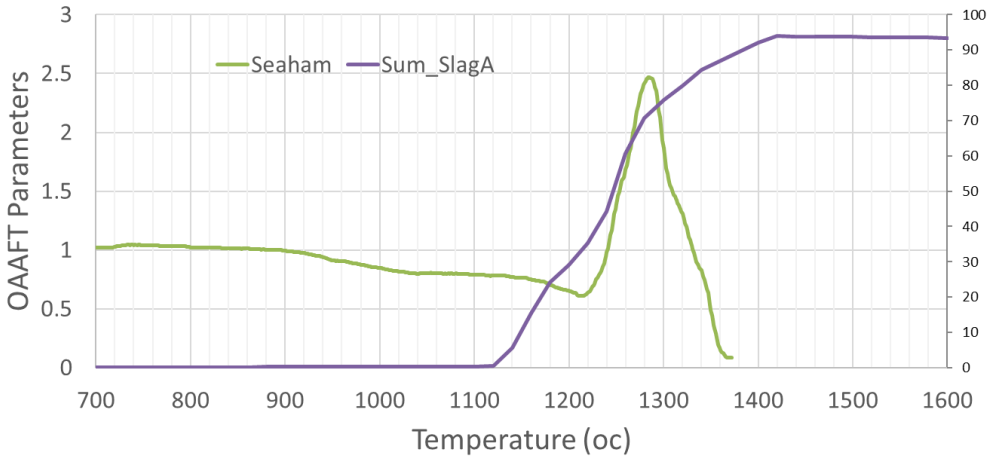


Figure 6-15: Seaham OAAFT vs FactSage

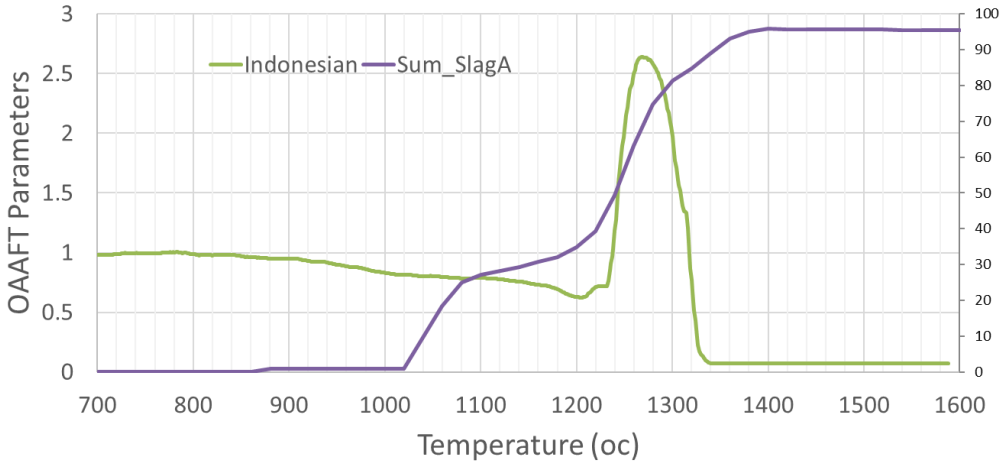


Figure 6-16: Indonesian OAAFT vs FactSage

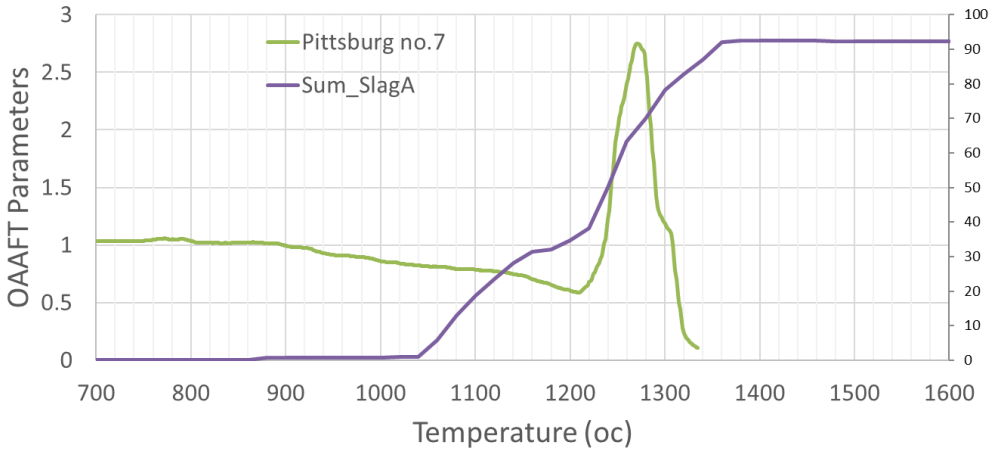


Figure 6-17: Pittsburg No.7 OAAFT vs FactSage

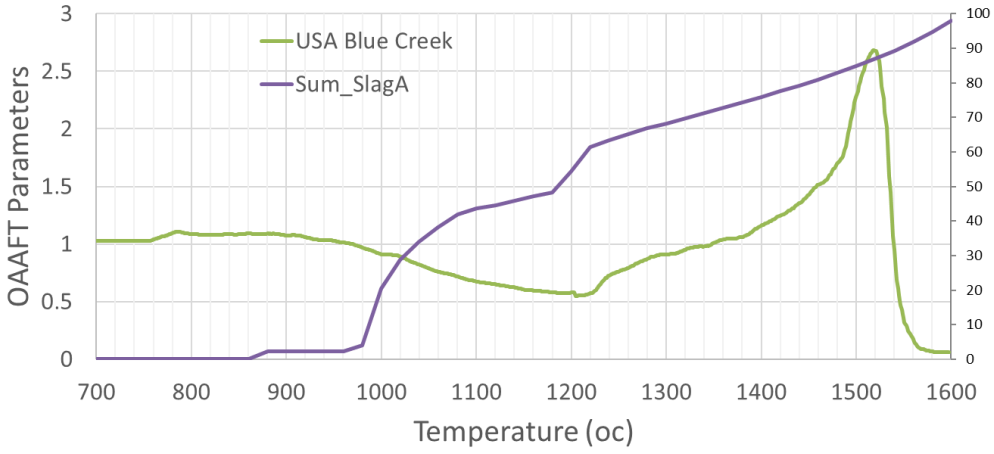


Figure 6-18: USA Blue Creek OAAFT vs FactSage

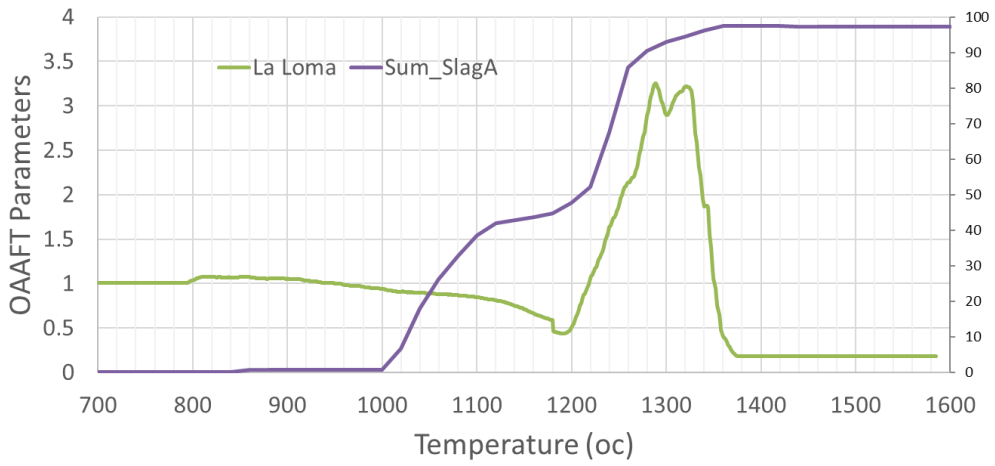


Figure 6-19: La Loma OAAFT vs FactSage

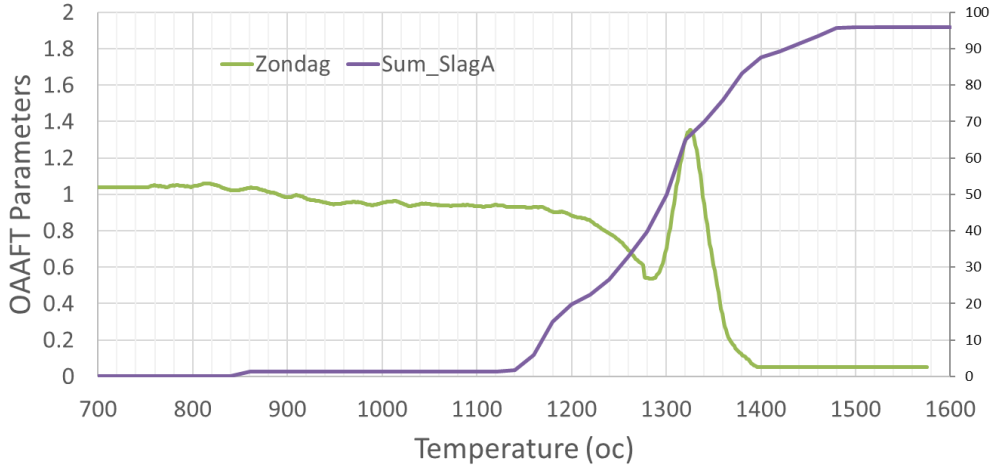


Figure 6-20: Zondag OAAFT vs FactSage

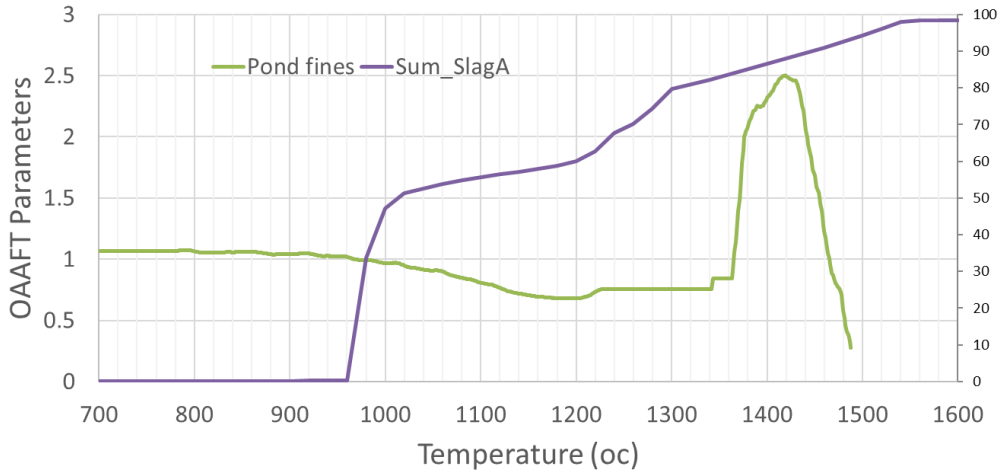


Figure 6-21: Pond Fines OAAFT vs FactSage

Table 6-3: Coal Ash Fusion Temperatures and Slag %s at the Key Temperatures

			Temperature (^{o}C)					Slag %				
Sample #	Name	Coal/Biomass	SST	IDT	Peak	HT	FT	SST	IDT	Peak	HT	FT
1	**Gedling**	Coal	1128	1183	1237	1272	1311	11	34	74	82	89
2	**Corton Wood**	Coal	1150	1450	>1603	>1603	>1603	28	65	>77	>77	>77
3	**Kellingly**	Coal	900	1194	1420	1456	1468	0	46	87	90	92
4	**CWD**	Coal	1075	1246	>1603	>1603	>1603	18	30	>61	>61	>61
5	**Cresswell**	Coal	980	1191	1300	1404	1455	0	51	74	94	96
6	**Jagua**	Coal	1057	1335	1569	>1598	>1598	3	60	79	>83	>83
7	**Littleton**	Coal	850	1210	1269	1322	1401	0	39	59	85	91
8	**Golden hope**	Coal	1070	1295	1570	1603	>1603	41	68	88	91	>91
9	**Taff merth**	Coal	895	1300	>1603	>1603	>1603	2	58	>78	>78	>78
10	**Tillman stone**	Coal	973	1276	1390	1415	1418	0	45	73	84	86
11	**Markham**	Coal	1162	1209	1250	1372	1389	10	36	68	87	90

12	**Yanoice**	Coal	831	1142	1260	1404	1507	3	27	63	78	90
13	**Trentham**	Coal	921	1271	1310	1336	1360	4	55	72	80	86
14	**Seaham**	Coal	937	1208	1290	1356	1389	0	32	74	87	91
15	**Indonesian**	Coal	809	1208	1270	1319	1327	0	35	69	85	87
16	**Pittsburg no.7**	Coal	907	1200	1276	1314	1368	0	35	68	81	92
17	**USA Blue Creek**	Coal	967	1203	1520	1553	1572	2	54	87	90	93
18	**La loma**	Coal	908	1181	1300	1329	1370	1	45	93	95	97
19	**Zondag**	Coal	1220	1275	1323	1362	1403	23	38	66	76	88
20	**Pond fines**	Coal	952	1209	1420	1484	1524	0	61	89	93	96
							Average:	7.3	45.7	75.5	86.1	90.9

6.3.1.2 Summary of the FactSage Analysis

The averages in Table 6-3 show that the FactSage analysis is predicting that almost 50% of the sample is molten at the point of IDT. Furthermore, at the shrinking temperature, on average, about 7% of the sample is molten and 90% at the flow temperature. This indicates and excellent alignment of the OAAFT with the FactSage modelling analysis. This is not the case for the biomass samples, this can be seen in Figure 6-22 – 6.32. Table 6-4 confirms that they do not align well with the FactSage model. Around 70% of the sample molten at IDT and a higher molten content at HT (86.4%) than at FT (86.1%). Some of the samples including B139, Eucalyptus, EC78 and B117 gave comparable results to the coal analysis. The reasoning for this is not clear as these sample do not all represent coal-like ashes, with would explain why the model could process them accurately.

6.3.1.3 Biomass OAAFT Curves vs FactSage

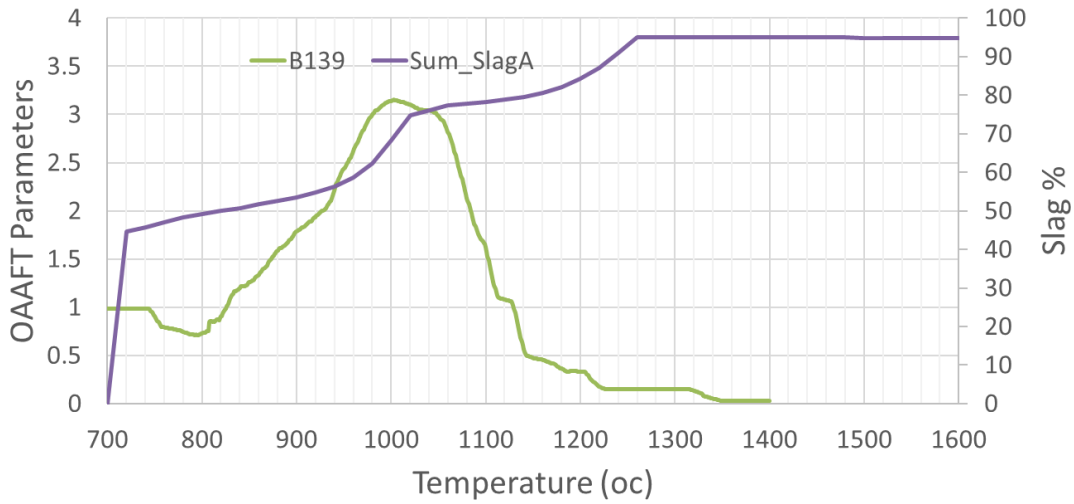


Figure 6-22: B139 OAAFT vs FactSage

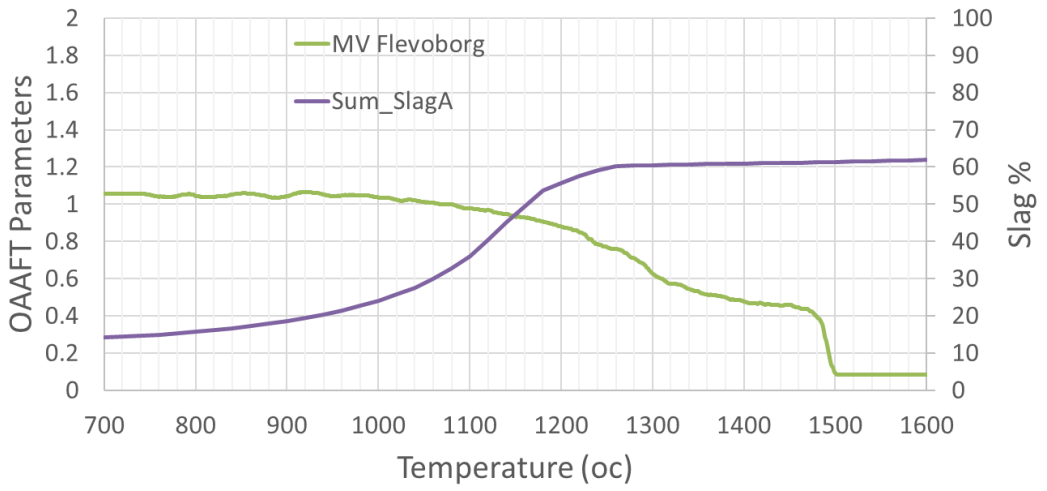


Figure 6-23: MV Flevoborg OAAFT vs FactSage

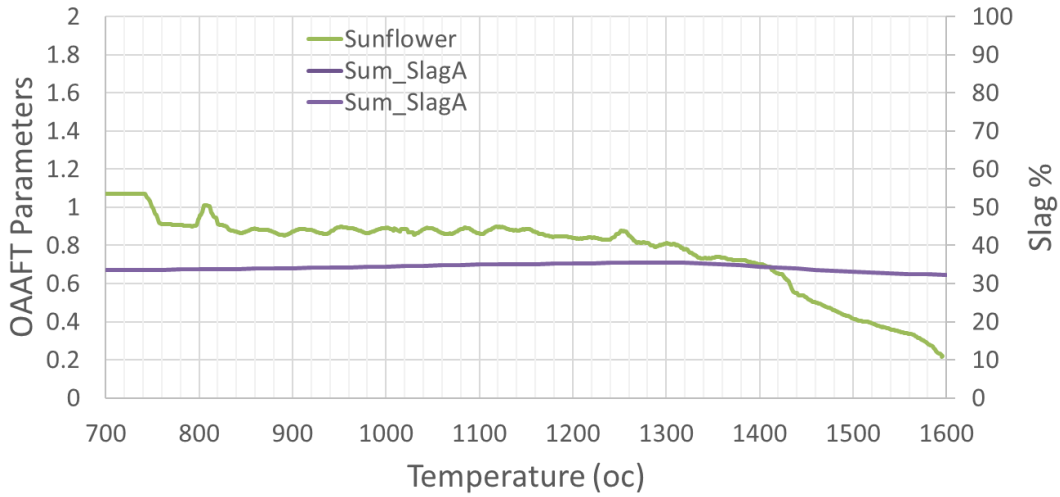


Figure 6-24: Sunflower OAAFT vs FactSage

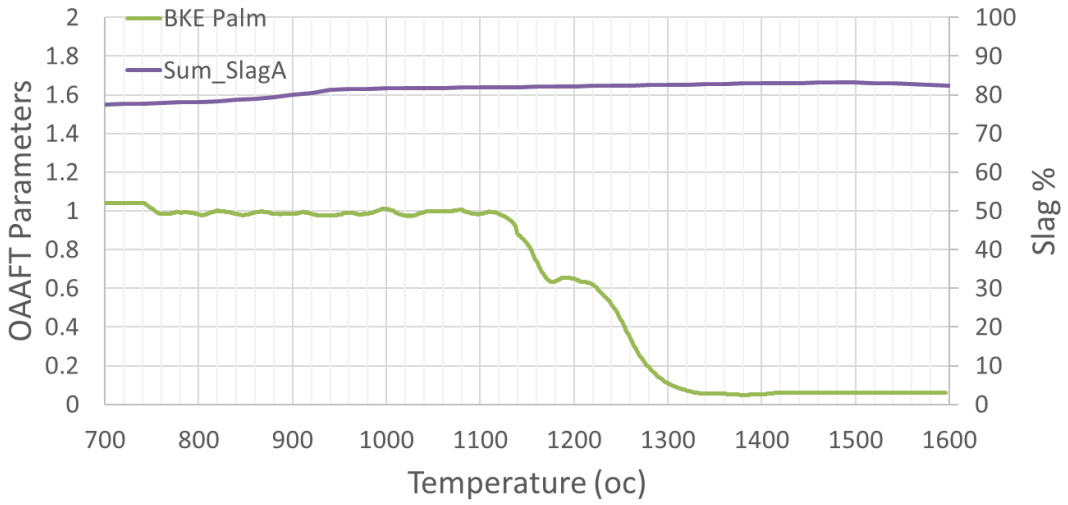


Figure 6-25: BKE Palm OAAFT vs FactSage

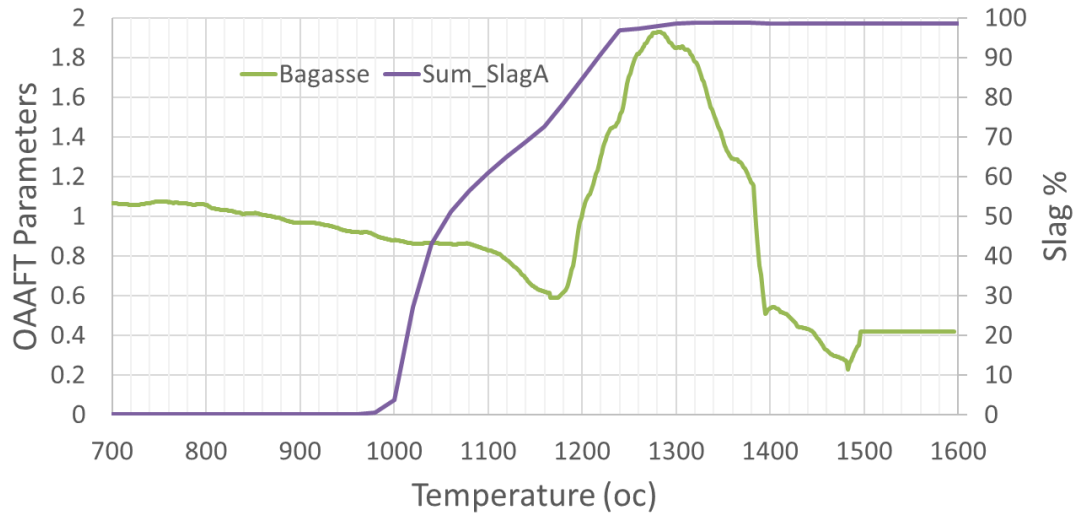


Figure 6-26: Bagasse OAAFT vs FactSage

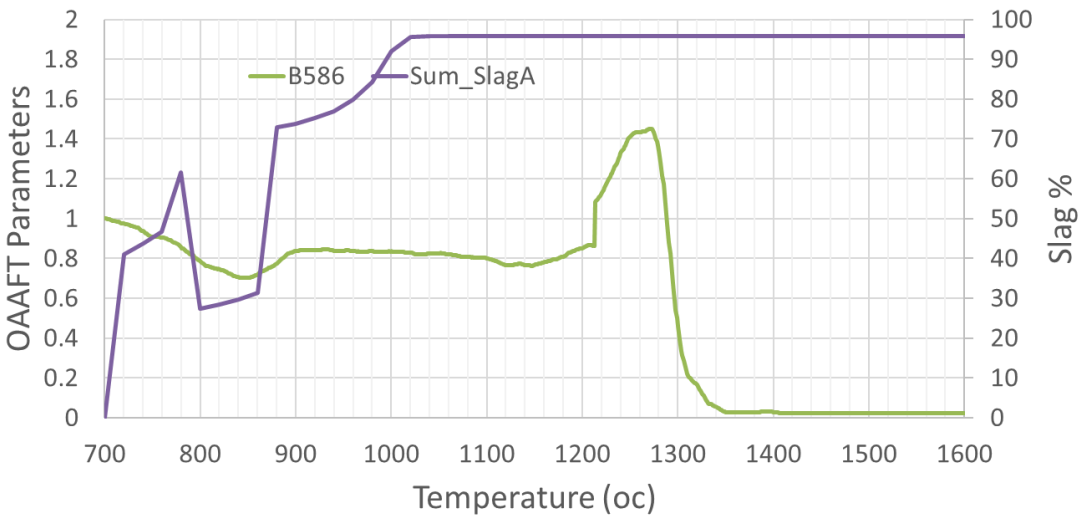


Figure 6-27: B586 OAAFT vs FactSage

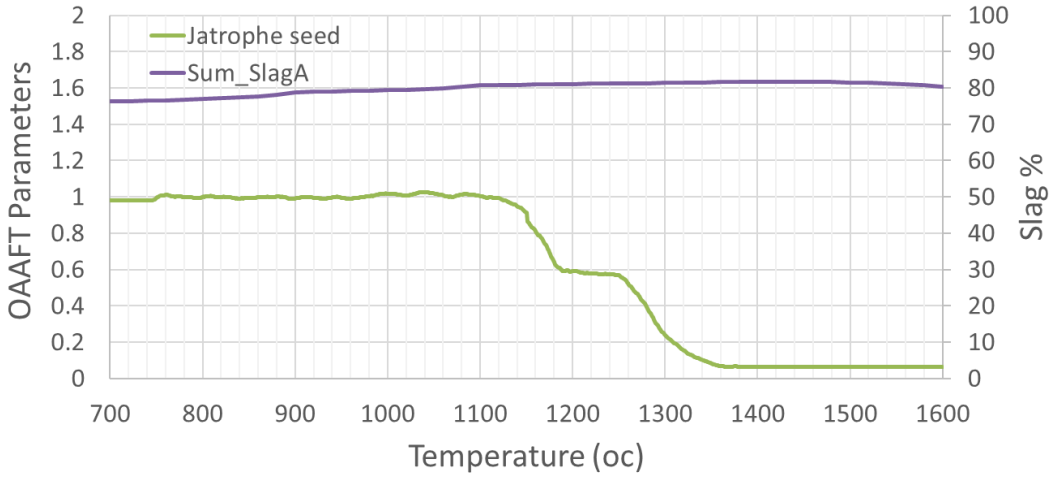


Figure 6-28: Jatrophe Seed OAAFT vs FactSage

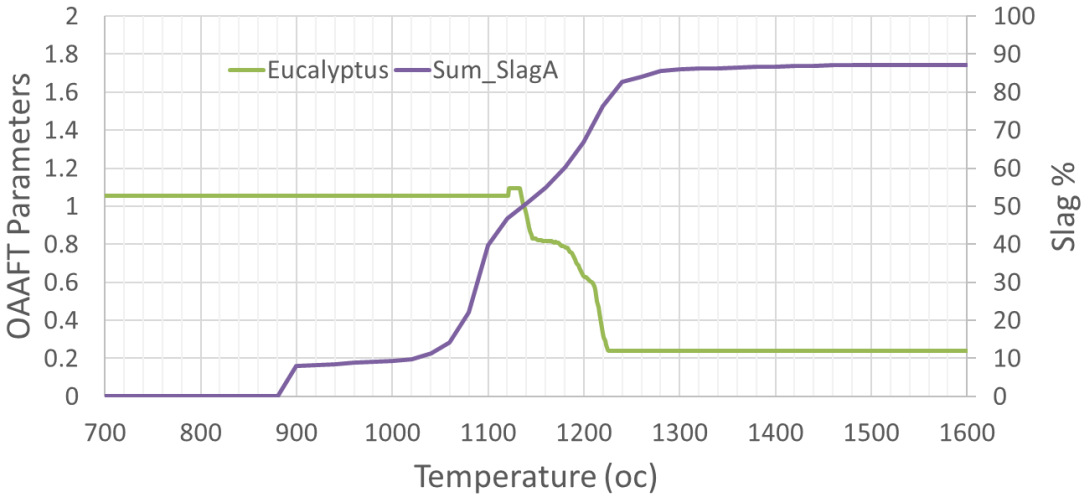


Figure 6-29: Eucalyptus OAAFT vs FactSage

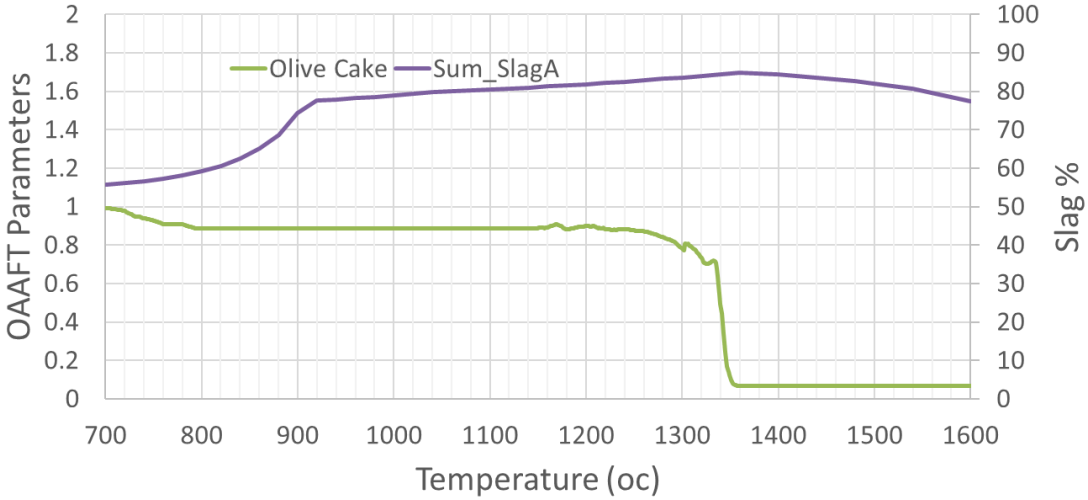


Figure 6-30: Olive Cake OAAFT vs FactSage

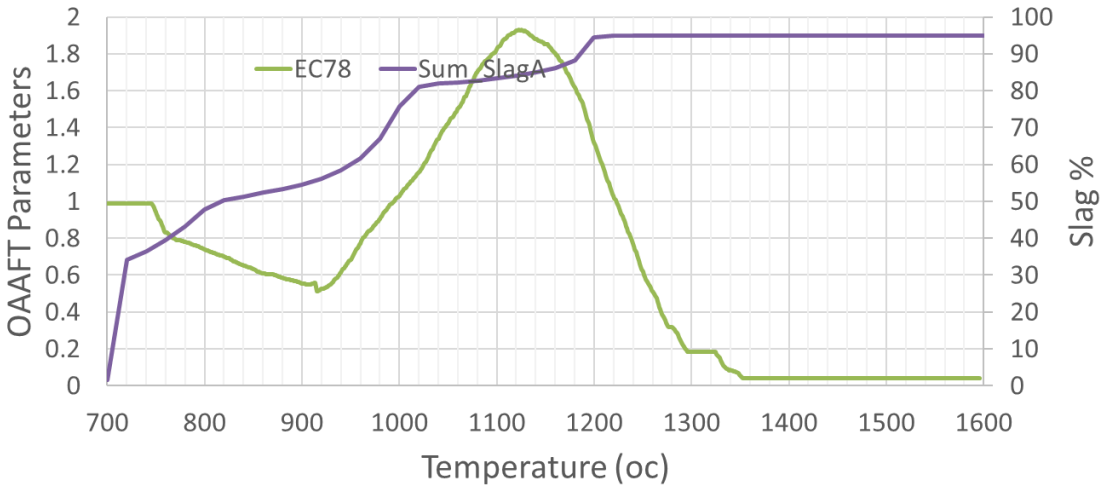


Figure 6-31: EC78 OAAFT vs FactSage

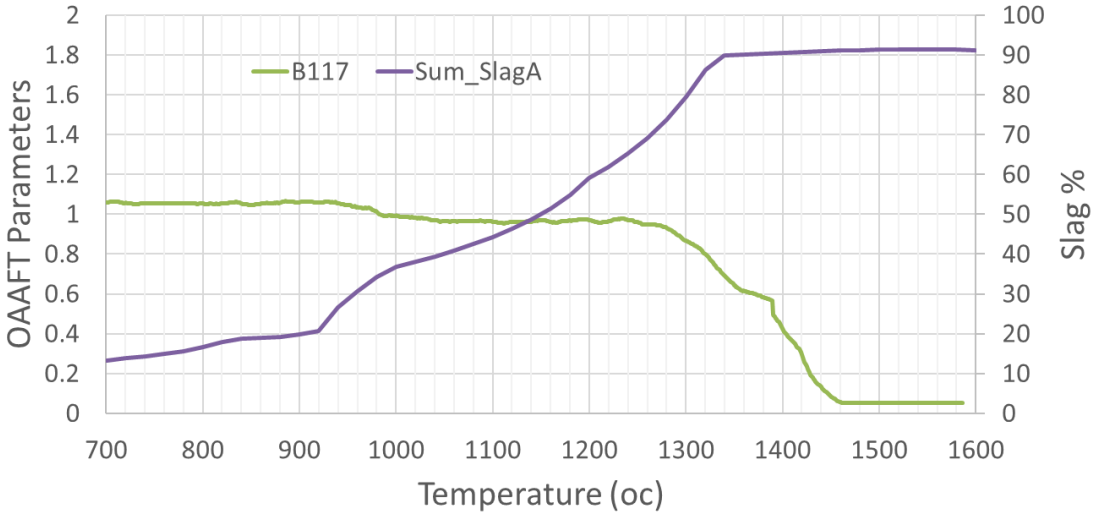


Figure 6-32: B117 OAAFT vs FactSage

Table 6-4: Biomass Ash Fusion Temperatures and Slag %s at the Key Temperatures

			Temperature (^{o}C)					Slag %				
Sample #	Name	Coal/Biomass	SST	IDT	Peak	HT	FT	SST	IDT	Peak	HT	FT
21	B139	Biomass	748	807		1147	1335	46	49		80	94
22	MV Flevoborg	Biomass	1010	1485		--	1504	25	61		--	61
23	Sunflower	Biomass	1350	--		--	--	35	--		--	--
24	BKE Palm Kernel	Biomass	1138	1182		1283	1340	82	82		82	83
25	Bagasse	Biomass	1114	1165		1453	>1604	63	74		98	98
26	B586	Biomass	736	1150		1308	1348	43	96		96	96
27	Jatrophe seed	Biomass	1141	1212		1355	1603	81	81		81	80
28	Eucalyptus	Biomass	1092	1199		1227	1239	31	67		78	82
29	Olive Cake	Biomass	800	1349		1392	1401	59	82		82	82
30	EC78	Biomass	752	917		1293	1411	35	56		95	95
31	B117	Biomass	989	1174		1318	1341	35	53		86	90
							Average:	48.6	70.1		86.4	86.1

6.3.2 OAAFT grouping

The OAAFT curve defines a characteristic profile for each sample, and thus it is possible to compare tests based on these curves. In this section, it will be attempted to identify common properties in curves and draw links to ash composition. Furthermore, there are standard indices to predict slagging and fouling propensity (SFP) based on ash composition Figure 6-33. The samples that indicate high or severe propensity will be plotted together to see if they show any similar attributes.

Index	Formula	Slagging or Fouling Propensity			
		Low	Mediu m	High	Severe
Base - Acid Ratio	$\frac{Fe_2+CaO+MgO+Na_2O+K_2O}{SiO_2+Al_2O_3+TiO_2}$	<0.4 or > 0.7		0.4 to 0.7	
Iron Calcium ratio	$\frac{Fe_2O_3}{CaO}$	<0.3 or > 3.0	0.3 to 3.0		
Silica Percentage	$\frac{SiO_2\times100}{SiO_2+Fe_2O_3+CaO+MgO}$	72-80	65-72		50-65

Figure 6-33: Traditional Slagging and Fouling Indices

6.3.2.1 Coal Curve Shape

Figure 6-34 illustrates the range of coals with a sharp expansion curve after the IDT. This is the most common curve type in the database. The range of base/acid ratio is 0.2-0.5 with the average being 0.4. which puts it on the fringe of high/severe SFP. The iron/calcium range is 0.4-7.1 with a 3.3 average, this puts the group on the fringe of this indices but mostly outside the range. The silica % varies across the entire range of indices whilst the S/A ratio ranges from 1.1-2.5, averaging 1.6.

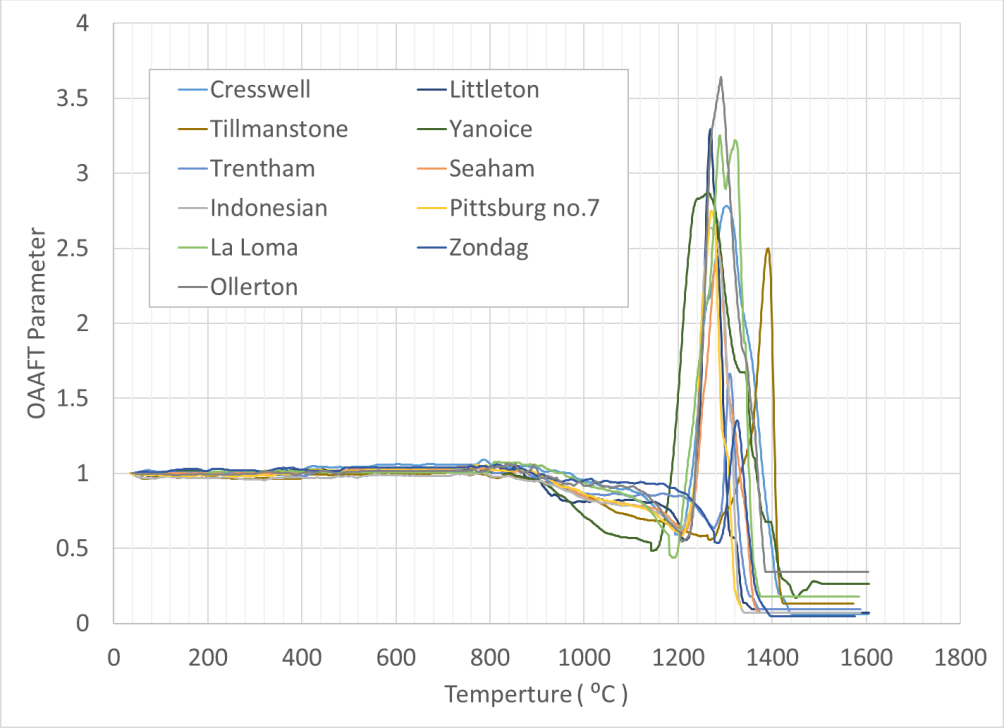


Figure 6-34: OAAFT Coal Samples with Sharp Expansion Curve Grouping

The next potential grouping is the gradual transition to expansion phase, this is represented in Figure 6-35. The base/acid ratio ranges from 0.1 to 0.3 however the average is 0.1. This lies well outside the high SFP range. The silica % is very high ranging from 73.4-90.5, averaging 84.1. Both indices would suggest low SFP. The iron/calcium indices show no trend.

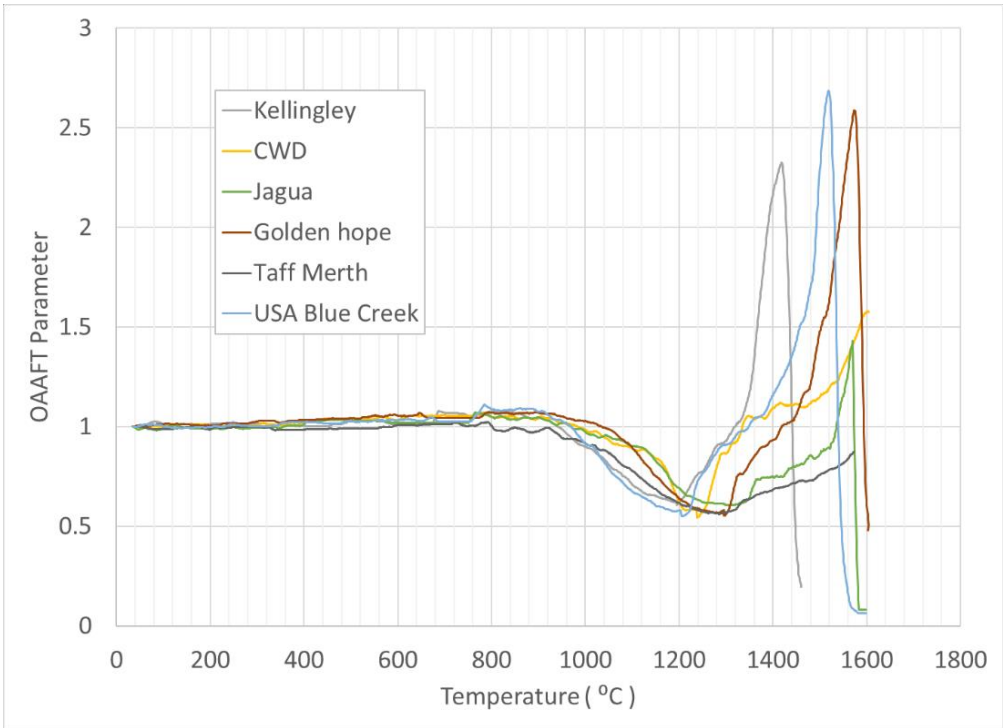


Figure 6-35: OAAFT Coal Samples with Gradual Transition into Expansion Phase

6.3.2.2 Coal Expansion Extent

An alternative way to group the curve is by the amount of expansion of the sample. The example are: greater than 1.5%, less than 1.5% and no expansion. This group is essentially a combination of the 2 previous groups. Figure 6-36 shows that most of the coals in the database expand to greater than 1.5%. No general trends can be seen in the iron/calcium, base/acid or Si % indices. The < 1.5% expansion group is shown in Figure 6-37, and similarly to the >1.5% curves, there are no general trends within this magnitude of expansion. The final group of this type is the collapsing curve which has no expanding phase at all (Figure 6-38). All these samples are high in CaO and SO_3. The Si % of these coals are all very low, they range from 35-68, with an average of 47. 2 of these coals have a slight expansion phase in G5 & G6, both have

comparatively lower SO_3 levels when compared with the others. The G5 sample also has vastly higher Al_2O_3. G1 is the only sample that shows shrinkage however, vastly different MgO content, B/A ratio and Silica % makes it hard to define the cause.

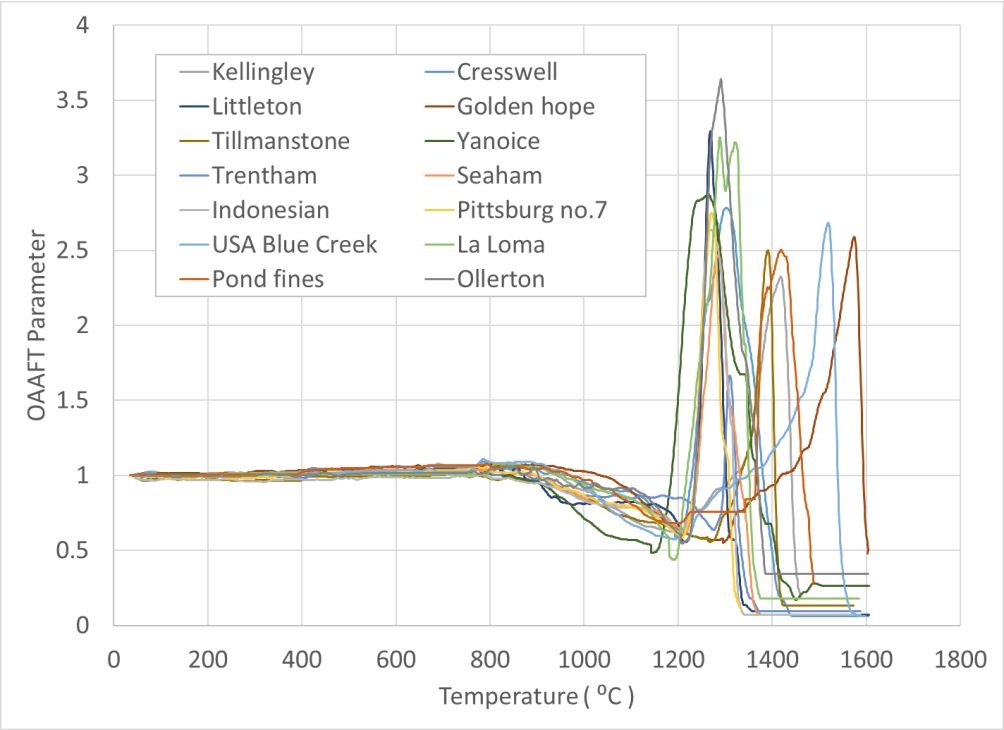


Figure 6-36: OAAFT Coal Samples with an Expansion of >1.5%

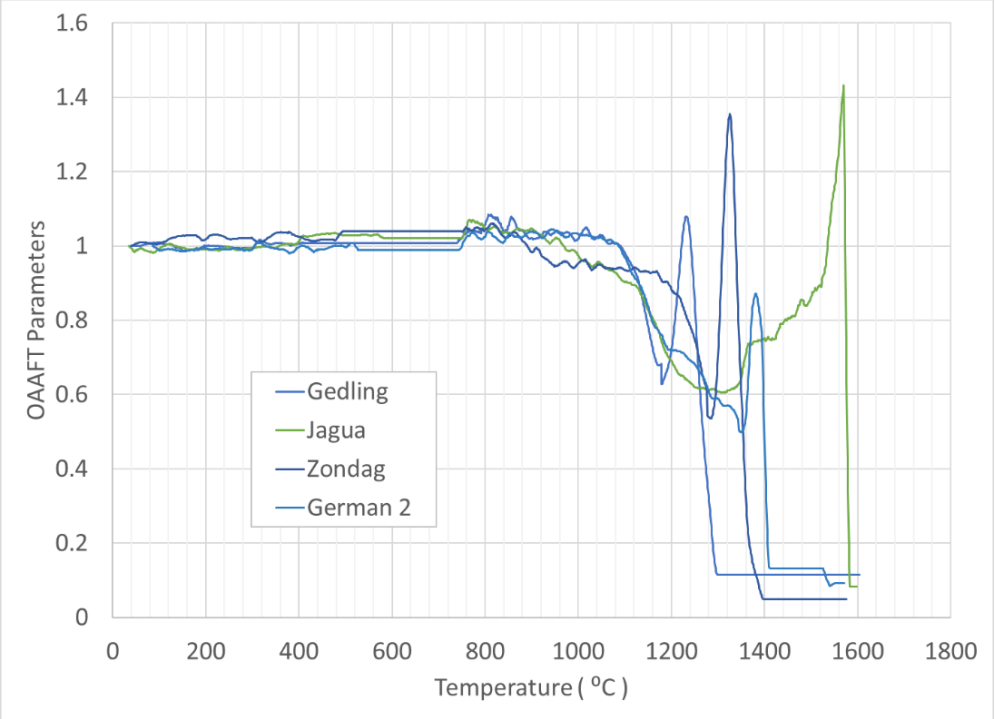


Figure 6-37: OAAFT Coal Samples with an Expansion of <1.5%

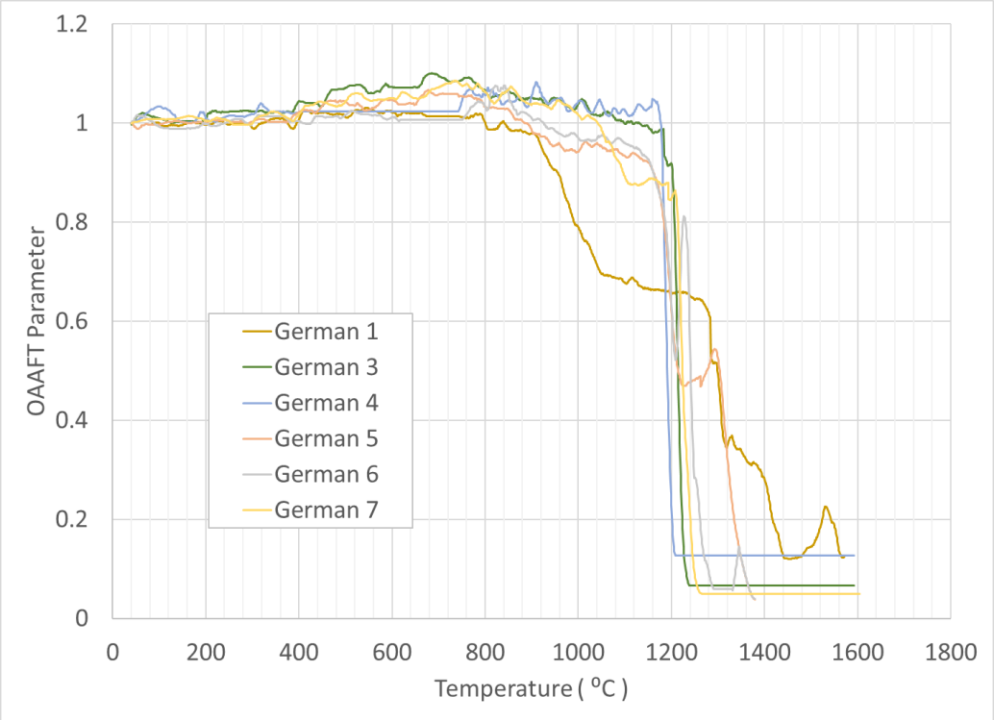


Figure 6-38:OAAFT Coal Samples with No Expansion Phase

6.3.2.3 Biomass

In contrast to the coal samples from Figure 6-34, Figure 6-39 represents the most common shape in the biomass database, a collapsing curve. The indices for SFP will have been designed for coals, and the components of biomass are vastly different. This set of biomasses have very low levels of Al_2O_3, a range of 0.1-7.8 and an average of 2.2. This is like the collapsing data for coal and could link Al_2O_3 to the expansion phase. BKE Palm kernel and Jatropha Seed have very similar elemental data, as both are seeds. They also share extremely similar profiles, which suggests that even different species will behave similarly in the OAAFT. Furthermore, the characteristic profile is linked to the elemental composition. Figure 6-40 shows the biomass samples with an expansion phase. All these samples have very high Si %s and low levels of CaO, K_2P, and P_2O_5 compared with the Figure 6-39.

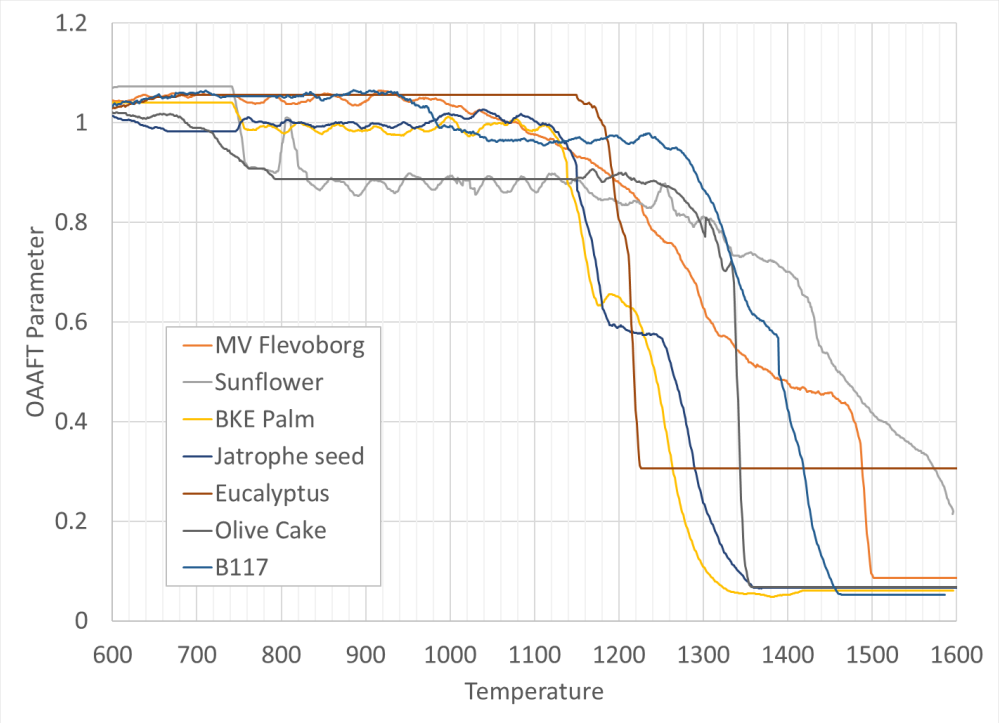


Figure 6-39:OAAFT Biomass Samples with No Expansion Phase

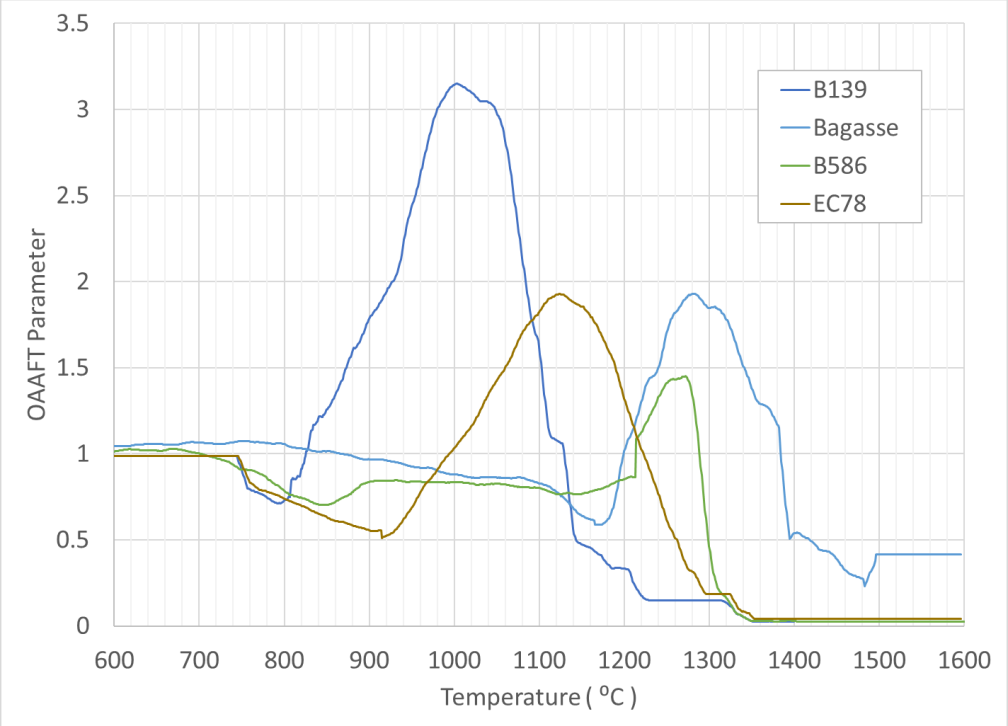


Figure 6-40: OAAFT Biomass Samples with An Expansion Phase

Table 6-5 compares the average elemental values and indices from the OAAFT curve grouping. The expansion phase of the curve is linked to greater levels of SiO_2 and lower levels of CaO and SO_3. These individual components lead to a similar trend shown in the B/A ratio. This relatively small database of coals and biomasses has yielded some promising indications of trends within the OAAFT curve. Further work should be carried out to improve the database not only to identify further links to the curve but also to create repeatable and reliable ash fusion test reference data.

6.4 Relevance of Data

The FactSage modelling results have supported its predictive capabilities for coal liquidous temperatures alongside the OAAFT. The OAAFT not only produces highly repeatable ash fusion temperatures, but the characteristic curve profile has been shown to indicate higher or lower elemental concentrations. These could be used as an indicator for further testing however, further work is required to validate the trends.

Table 6-5: Comparing the Averages for the Different OAAFT Curve Groupings

Fuel	Group name	SiO_2	Al_2O_3	Fe_2O_3	MgO	CaO	Na_2O	K_2O	P_2O_5	SO_3	LOI	S/A	F/C	B/A	Si %
Coal	Sharp expansion	39.7	26.3	13.7	1.8	5.1	2.4	1.6	0.7	3.7	2.1	1.6	3.3	0.4	65.8
	Gradual expansion	45.8	33.3	5.9	0.9	1.9	0.9	1.9	2.4	1.1	1.6	1.4	3.9	0.1	84.1
	>1.5	42.7	26.9	12.8	1.5	3.7	2.1	2.1	0.6	3.0	2.0	1.6	4.3	0.3	70.1
	<1.5	33.0	24.7	9.7	4.0	11.2	2.3	0.5	0.8	9.1	1.0	1.5	0.9	1.2	60.7
	No expansion	31.3	10.0	8.9	5.3	19.5	1.3	0.6	0.1	22.9	1.4	20.7	0.5	2.0	47.4
Biomass	No expansion	11.2	2.2	1.4	7.4	16.1	1.1	23.6	9.1	6.2	16.4	6.8	0.1	13.0	26.3
	Expansion	59.0	4.3	1.8	2.4	6.0	0.4	11.7	4.3	3.5	5.3	32.0	0.5	0.4	85.1

6.5 Conclusions

In this chapter, the OAAFT curve for both coal and biomass was compared with a reliable slag formation prediction method. A large database of coal and biomass was tested to generate OAAFT curve and the characteristics were grouped to identify links to elemental composition.

- Coal FactSage modelling shows an excellent relationship to the OAAFT curve.
- Biomass molten phase are not predicted well, samples do not correlate to curve shape.
- Preliminary work suggests that the OAAFT can be used to identify links to species in samples.
    - The expansion phase of the curve is linked to greater levels of SiO_2 and lower levels of CaO and SO_3.

Chapter 7 : Industrial Case Study OAAFT of Stoker Furnace Coals

7.1 Introduction

The origins of the ash fusion test attempted to predict clinker formation in stoker furnaces. A clinker is a sintered block of ash. Stoker furnaces work by burning fuel on a grate conveyor allowing air flow though the bed to enable combustion. The formation of clinkers corrupts the porosity of the bed and inhibits combustion conditions [11]. The residence time for stoker furnaces is such that near total burnout will occur without milling fuels to a fine powder. However, in some cases a fuel will reach a ceiling of low burnout irrespective of residence time [172]. The aim for this work is to gain greater insight into the low burnout of Colombian coals used in 2 Colombian stoker furnaces Mayaguez and La Cabaña using the OAAFT.

The fuel on the conveyor appears to be swelling and agglomerating thus trapping unburned coal with an ash shell. The purpose of this industrial investigation is to identify if the problematic swelling comes from the coal or the ash, or both at furnace operating conditions of 900^{o}C. The OAAFT developed in earlier chapters is used to track the shape change of an ash sample during the ash fusion test. This process will be adapted to perform the same analysis on coal particles during combustion. Attempts to make this form of testing more analytical have been achieved by means of Thermo-mechanical Analysis (TMA) [16], [81], [120]–[122]. This analysis will be cross-referenced by TMA data between 0-1000 ^{o}C, any data above this will be only OAAFT data.

Bryant claims that TMA aligns better with predicted liquidous temperatures than AFT temperatures [169]. The OAAFT alongside TMA analysis will validate the OAAFT data which combines the tracking of the TMA with the analysis of AFT temperatures.

In this chapter, 5 coals and their respective ashes have been tested using the OAAFT to investigate the swelling characteristics. Furthermore, TMA has been used alongside the OAAFT to validate the data obtained.

7.2 Materials and Methods

7.2.1 Samples Used

This study includes 5 domestic Colombian coals used in local stoker furnaces; Patia, Antioquia, Cundinamarca, Valle, and a blend. These fuels were ashed individually to assess their unique ash characteristics. The furnace bottom ashes (FBA) and fly ashes from the stoker furnaces in Colombia (Cabana and Mayaguez). A typical stoker furnace is represented in Figure 7-1 for reference of where the FBA and fly ash are taken.

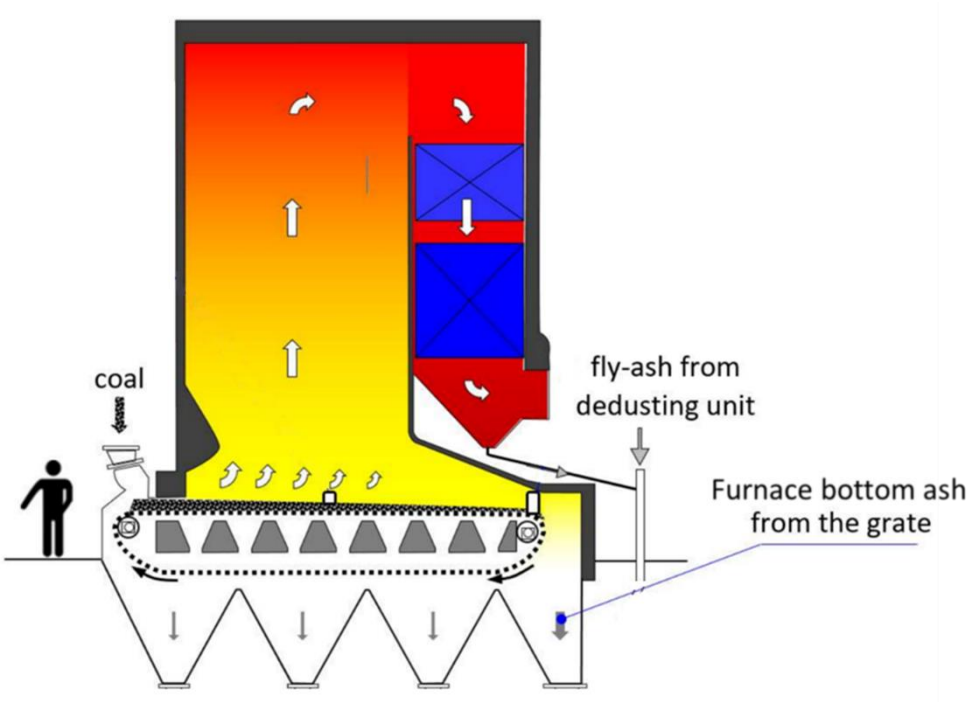


Figure 7-1: A Typical Stoker Furnace To Illustrate Where The Fly Ash And The Furnace Bottom Ash Is Collected – Edited From [173]

7.2.2 TMA

Thermomechanical analysis (TMA) was used to track the mechanical change of samples between 25^{o}C and 1000^{o}C at a rate of 10^{o}C/min. All 17 samples were tested. Between 0.05gs and 0.1gs of sample was pressed at 7500 psi using a 5mm mechanical press mould. This pelleting process was developed in chapter 3. The mass of the samples was varied to ensure the height of the samples was between 3-4mm. Sample height was tracked with an accuracy of X using a quartz probe and 2 quartz plates.

7.2.3 Coal Combustion Imaging (CCI)

This test is *ad-hoc* in nature however, the procedure is the same as the OAAFT apart from the sample preparation. Roughly 5mm diameter pieces of

the coal rock were broken off into large pieces and positioned on the samples holder. The coal was then tested in a Carbolite Gero Ash Fusibility Test Furnace - CAF G5. Samples were place on ceramic tiles and loaded in the furnace and the temperature was increased from 25 ^{o}C to 1000 ^{o}C at a rate of 4 ^{o}C/min under oxidising condition (air). The relative height of the pellet was output for direct comparison with the TMA data. Area is can also be plotted which is a better representation of swelling.

7.2.4 Ash Fusion Testing

The OAAFT developed in previous chapters was used to analyse the ash. As with the CCI above, the relative height of the pellet was output for direct comparison with the TMA data.

7.3 Results and Discussion

7.3.1 Ash Fusion Test with TMA Analysis

In this section, the OAAFT curves for the 14 samples in the investigation are displayed in Figure 7-2 – 7-10. The orange line represents the OAAFT analysis with the H/Hi output obtained using image processing. The Blue line represents the H/Hi TMA data which is obtained using a quartz probe to physically track the top of the sample. A force is applied to the sample in the TMA analysis therefore, there is an inherent slight difference in the analysis with the OAAFT being free standing and the TMA sample being compressed.

Even with this difference in analysis, the tests showed excellent correlation. The analysis was such that the TMA could only catch the edge of the deformation of the ash pellet. Though this was enough to validate the

OAAFT, it is a clear indicator that the OAAFT is the better option for ash fusion analysis. Of all the ashed samples, only Mayaguez FBA swelled during the range of the stoker furnace operating conditions. This could be due to containing unburned coal which is released upon milling. Mayaguez must contain 1 or a combination of the indigenous coals and since none of those ashes swell, there must be another competent causing the swelling.

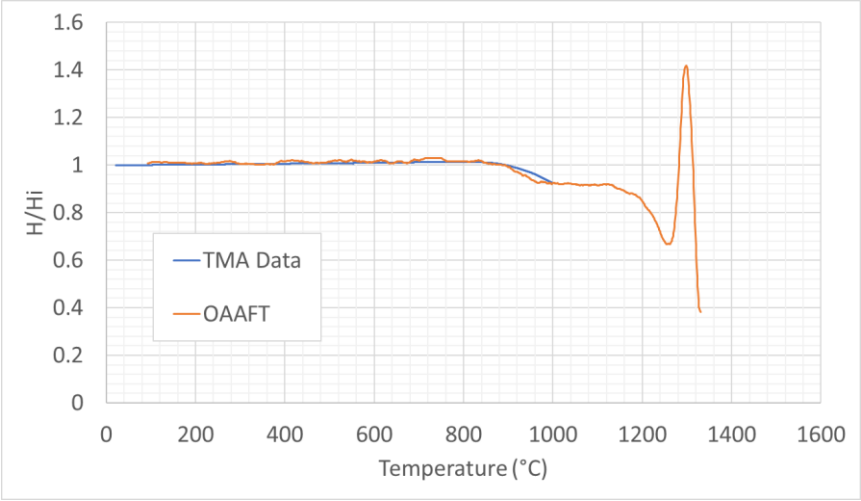


Figure 7-2: Antioquia OAAFT Curve Plotted with The TMA Analysis

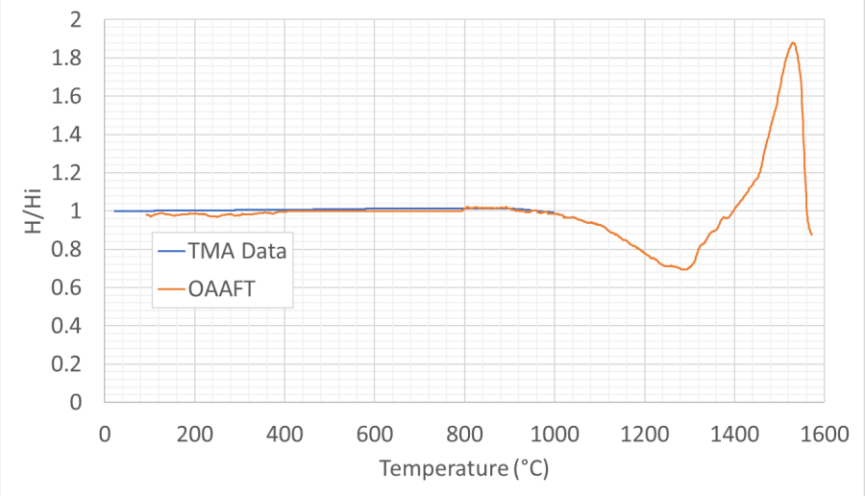


Figure 7-3: Blend OAAFT Curve Plotted with The TMA Analysis

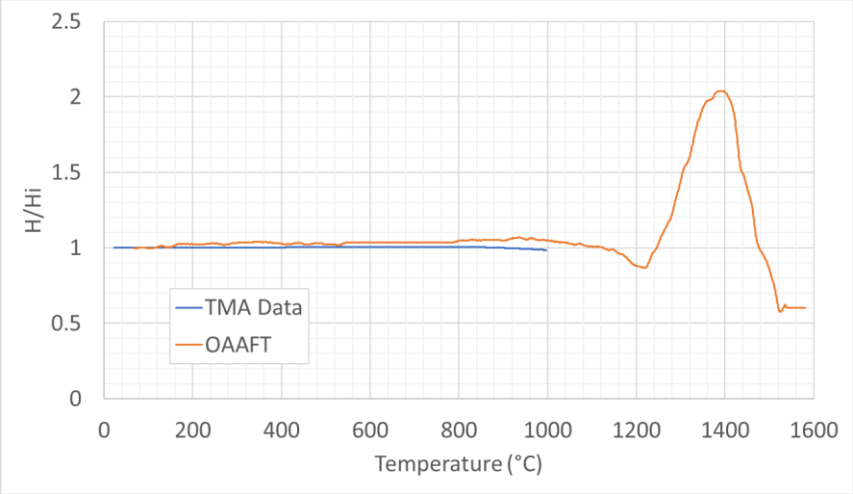


Figure 7-4: La Cabaña FBA OAAFT Curve Plotted with The TMA Analysis

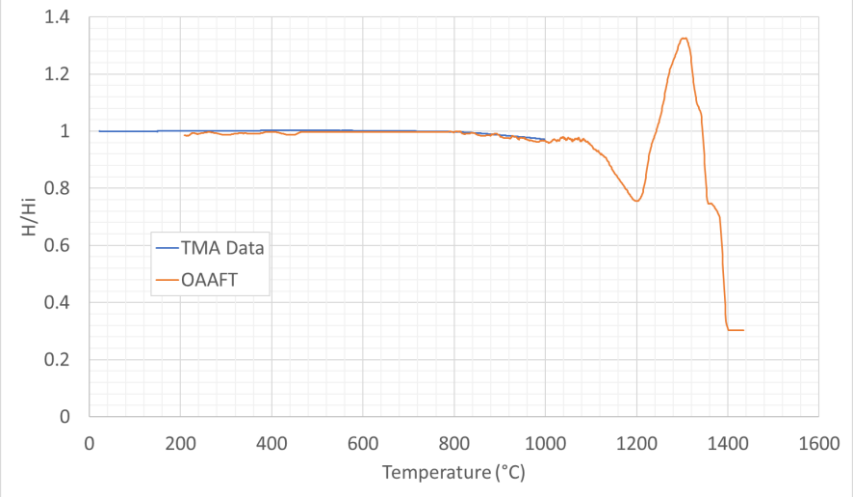


Figure 7-5: La Cabaña Fly ash OAAFT Curve Plotted with The TMA Analysis

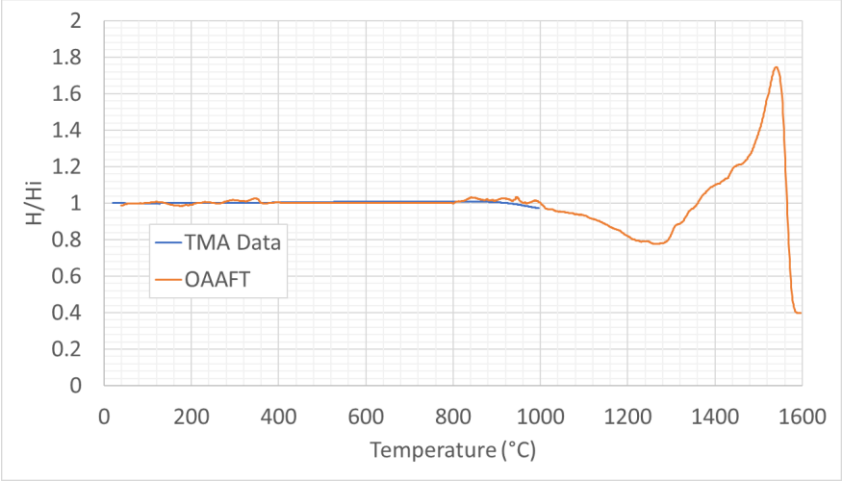


Figure 7-6: Cundinamarca OAAFT Curve Plotted with The TMA Analysis

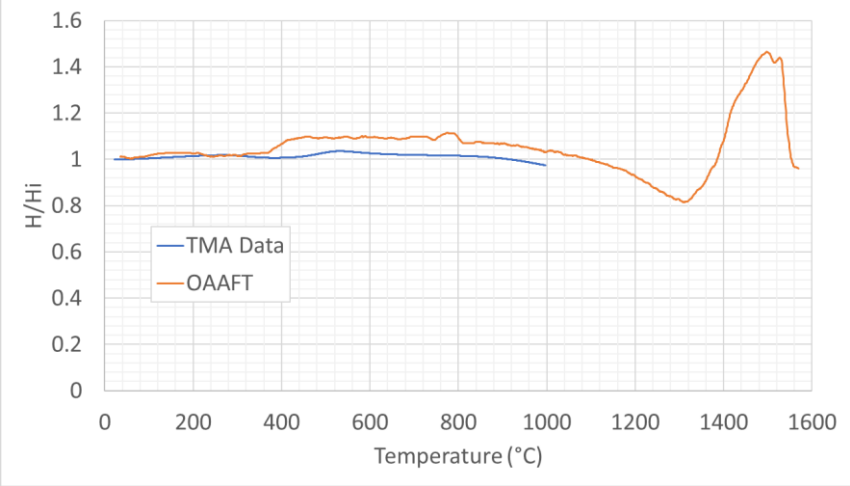


Figure 7-7: Mayaguez FBA OAAFT Curve Plotted with The TMA Analysis

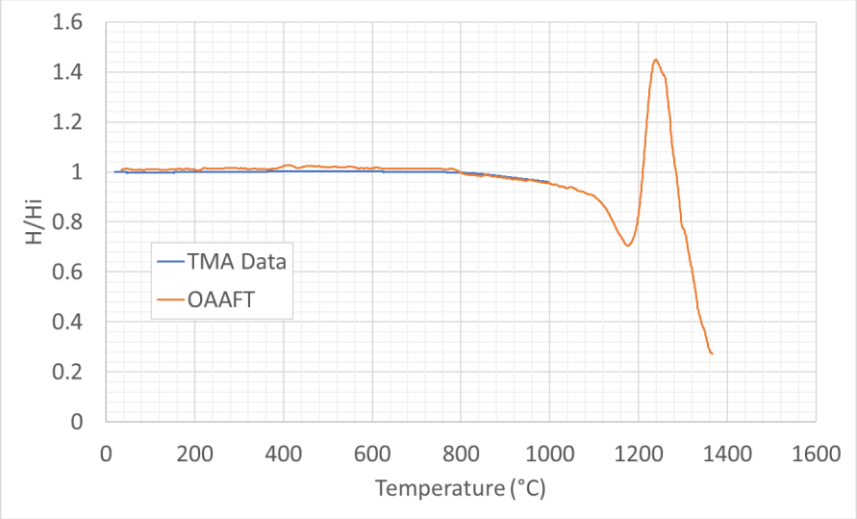


Figure 7-8: Mayaguez Fly OAAFT Curve Plotted with The TMA Analysis

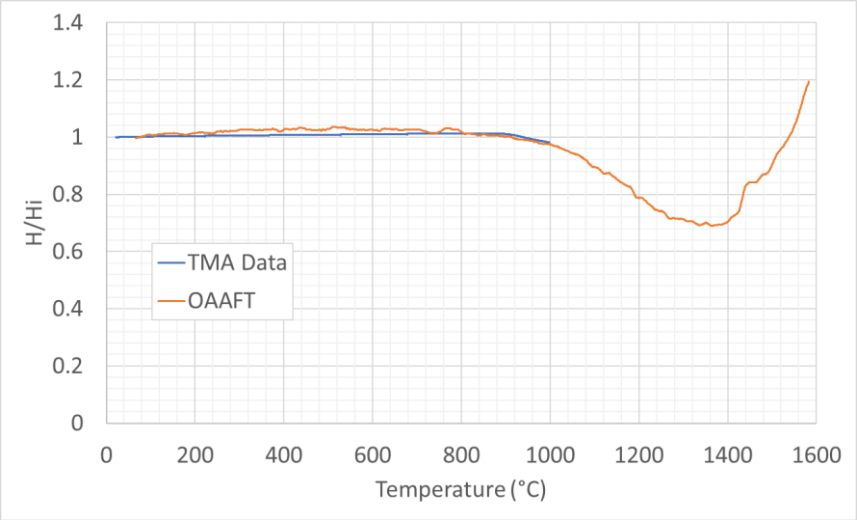


Figure 7-9: Patia OAAFT Curve Plotted with The TMA Analysis

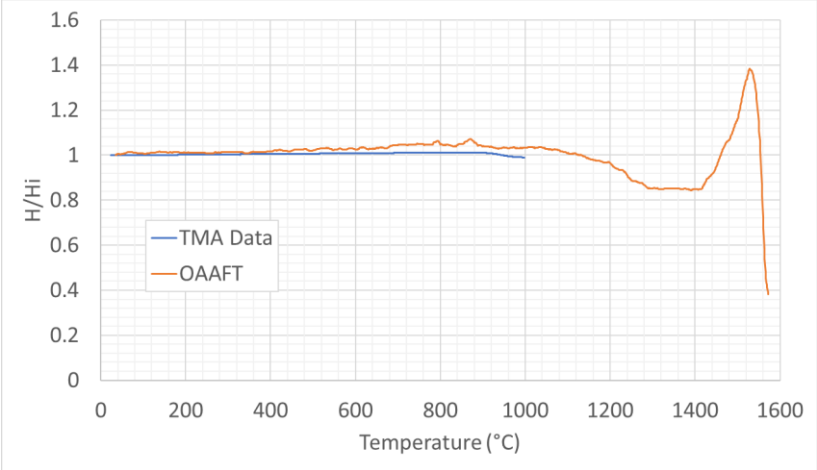


Figure 7-10: Valle OAAFT Curve Plotted with The TMA Analysis

The traditional AFT are reported in Table 7-1 & 2, they do not yield any insight into the problem of swelling in the stoker furnace. The modelling in the previous chapter indicated that up to ~50% of the sample was in the slag phase by the IDT. The Valle and Patia samples have late IDT however very early shrinking temperature, this suggests that melting and sintering phenomena could be occurring at lower temperatures. This could add to the agglomeration of the coal ash on the surface areas exposed to heat in the furnaces.

Table 7-1: Ash Fusion Temperatures of The Coal Samples

Sample	SST	IDT	ST	FT
Antioquia	1062	1250	1285	1322
Blend	1116	1289	1516	0
Cordina	1026	1279	1543	1574
Patia	815	1410	0	0
Valle	907	1401	1516.5	1564

Table 7-2: Ash Fusion Temperatures of The Fly Ash And FBA

Sample	SST	IDT	ST	FT
Cabana FBA	994	1211	1391	1520
Cabana Fly	948	1198	1289	1387
Mayaguez FBA	997	1324	1483	0
Mayaguez Fly	800	1172	1228	1321

7.3.2 Coal Combustion Imaging (CCI) with Thermomechanical analysis

In this section, the 5 raw coals used in Colombia were tested and the CCI curves and TMA plots are displayed in Figure 7-11 – 7-15 with the same formatting as the previous section. TMA is a very accurate form of measurement and supplies useful shrinkage data. The probe represses the sample, this provides a different form of measurement to the CCI. The CCI allows the sample to move freely during testing and subsequently in most of the samples, earlier swelling is observed. It should be noted that only 1 sample was analysed due to time constraints and visual impairment of the camera. Due to the heterogeneity of coal, unprepared pieces could lead to different swelling curves. Further tests should be run to confirm the swelling data for the CCI.

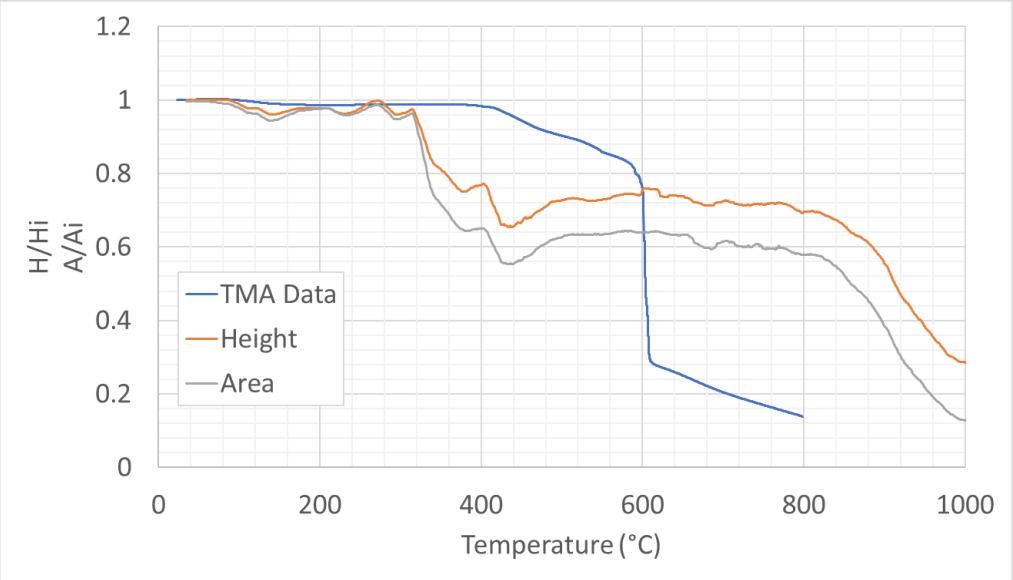


Figure 7-11: Antioquia Comparison of CCI vs TMA

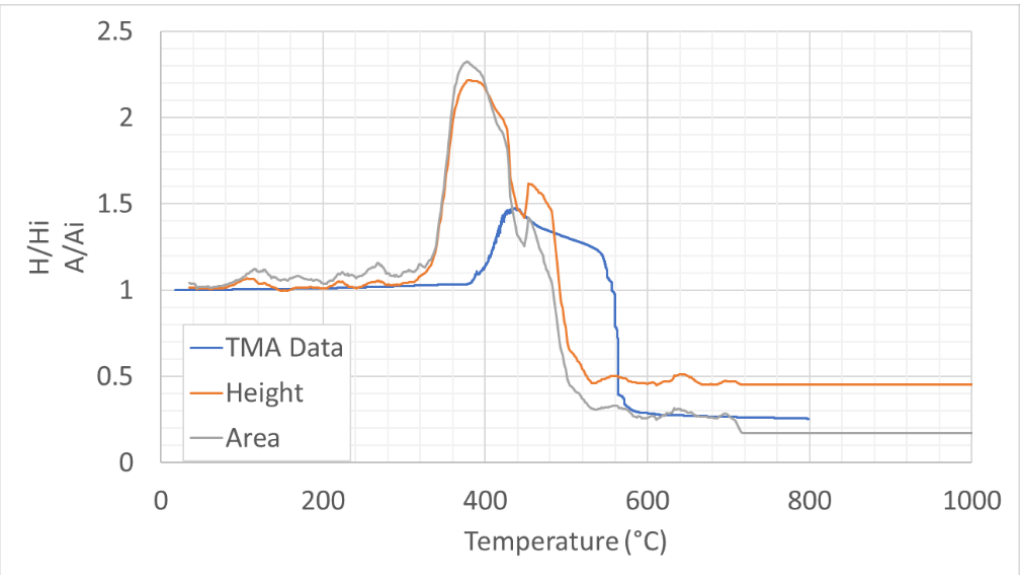


Figure 7-12: Blend Comparison of CCI vs TMA

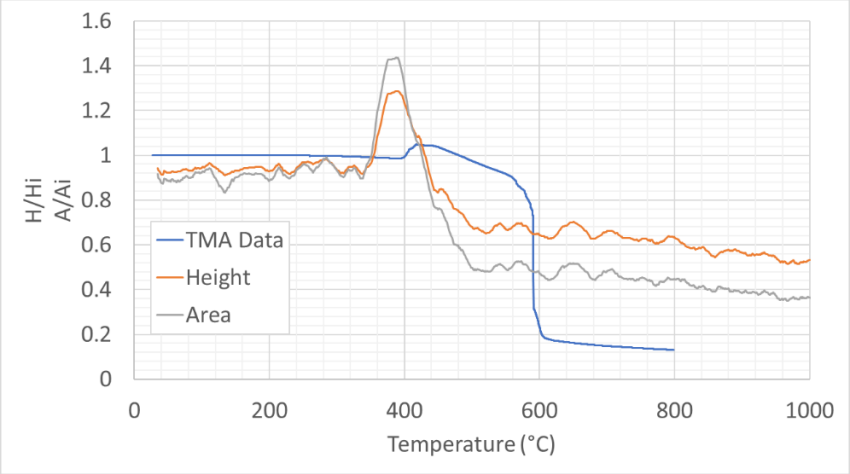


Figure 7-13: Cundinamarca Comparison of CCI vs TMA

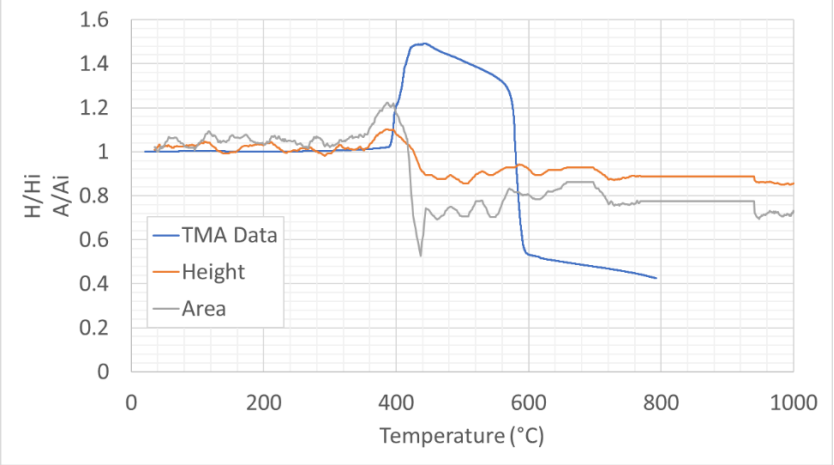


Figure 7-14: Patia Comparison of CCI vs TMA

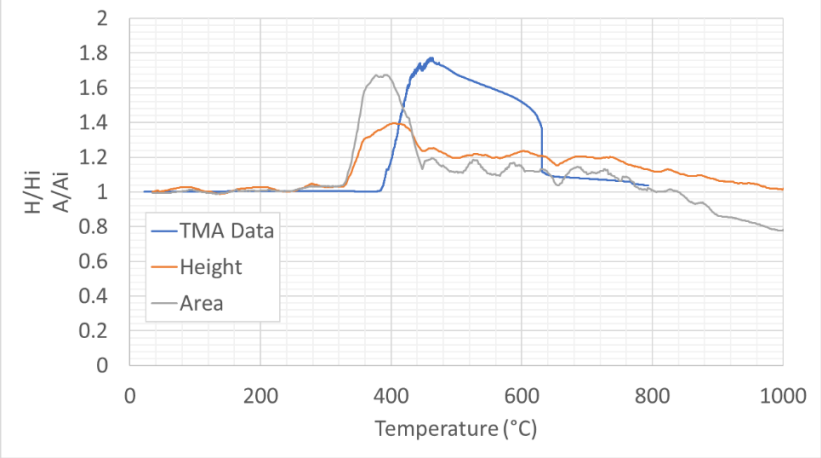


Figure 7-15: Valle Comparison of CCI vs TMA

4 of the coal samples from Colombia displayed swelling properties, Antioquia was the only coal not to do so. The TMA data suggests that Valle expanded the most, swelling by 80%. Blend and Patia swelled by 50%, and Cundina only swelled by 5%. The CCI data agreed that Antioquia did not swell however, showed slightly different values for Valle, Blend, Patia and Cundina, 40%, 120%, 10%, and 30% respectively. Furthermore, in every sample there is roughly a 150 ^{o}C delay post-swelling shrinkage between the TMA and the CCI. This is unexpected due to the force applied to the samples during mechanical testing. Capturing the area with the CCI reveals as the actual swelling may be greater than the height data suggests as shown in Table 7-3.

Table 7-3: Comparing the extent of Swelling between TMA Height, CCI Height and CCI Area

Samples	TMA	CCI	
	Height (%)	Height (%)	Area (%)
Antioquia	0	0	0
Blend	50	120	130
Cundinamarca	5	30	40
Patia	50	10	20
Valle	80	40	70

7.4 Significance of Findings

This chapter documents a novel Coal/fuel swelling analysis test, and in theory, the methodology is very transferable for analysis of other materials, including liquidous contact angle. Any material of interest that is required to undergo high temperatures can be analysed using this method and the furnace has the potential for alternative atmospheres.

7.5 Conclusions

In this chapter, 5 indigenous Colombian coals were tested to investigate low burnout experienced in 2 Colombian stoker furnaces, Mayaguez and Cabaña. The stoker fuel bed appeared to be swelling and agglomerating and forming a shell around the unburned coal. The OAAFT revealed no swelling from the ash samples, except Mayaguez FBA which may contain unburnt carbon. The CCI revealed swelling of up to 130% in some of the coals. This could potentially double the size of the stoker furnace bed and smother the remaining fuel. The options for enabling greater levels of burnout with the indigenous fuels are:

- Milling the fuel to increase the surface area of coal.
- Agitation mechanisms on the stoker bed conveyor to break up the forming slag bed fuel and expose residual unburnt carbon inside.

Chapter 8 : Conclusions

8.1 Chapter 3

A novel pelleting method was developed for the AAFT and for the first time it has been shown that cones and the hand pressed pellets do not have good repeatability and delay the response of the IDT. The optimum pelleting method for the AAFT was the 5 mm machine pressed pellet which displayed repeatability of ±5 ^{o}C. Reducing the particle size and increasing the pressure of the pelleting lowered the IDT of the sample, and the cumulative impact in some cases produced a 120 ^{o}C reduction in the IDT

The optimised version of the AAFT (OAAFT) creates a standardised test that is repeatable and gives the best representation of the first point of melting. This test will be useful to generate comparable results to aid in boiler operation and fuel selection decisions which might help prevent premature outages and the sourcing of unsuitable fuels.

8.2 Chapter 4

In this chapter, a fully automated technique for ash fusion analysis was developed with the use of hog predictors to locate the samples, and histogram analysis to create an automated segmentation technique. Area in combination with 1/Circularity was identified as the best plot against temperature to represent change in morphology during the test.

8.3 Chapter 5

SiO_2, Al_2O_3, CaO, Fe_2O_3, and MgO were studied using pseudo pellets to show each components effect on AFT temperatures and OAAFT curves. Parabolic curves were obtained in the Fe_2O_3 and MgO studies with the minimum point at 20% weight. A linear decrease in AFT temperatures was found in the CaO and S/A ratio investigation. Both results aligned well with results from literature however, some variance was seen due to the investigations in literature replicating different average coals. This meant that the ratios of components that were not the focus of each investigation, were not identical. When individual components were increased:

- **CaO** halved the AFT range and removed the sintering and expanding phases.
- **Fe_2O_3** initiates a 30-40% shrinkage during the sintering phase and an expansion phase that doubles in size from the sintered size.
- **S/A** ratio adds an expansion phase which then doubles over the range, and a sintering phase is added with a 40% shrinkage.
- **MgO** removes the expansion phase completely and halves the AFT range.

8.4 Chapter 6

In this chapter, the OAAFT curve for both coal and biomass was compared with a reliable slag formation prediction method. A large database of coal and biomass was tested to generate OAAFT curves. The FactSage modelling of the coal ashes showed excellent correlation to the OAAFT curve. The biomass

molten phases however were not predicted well and do not correlate to curve shape. Preliminary work on grouping the OAAFT suggested that it can be used to identify links to species in samples. The key trends show that greater levels of SiO_2 and lower levels of CaO and SO_3 result in an expansion phase.

8.5 Chapter 7

Fuel feed stocks for 2 Colombian stoker furnaces were tested using the OAAFT (ash) and CCI (coal). The ash samples did not swell in the range of the stoker furnace operating conditions. The CCI revealed swelling of up to 130% in some of the coals. This is deemed to have caused the swelling and agglomeration found on the stoker furnace bed and reduced the coal burn out by trapping unburnt coal. The options for enabling greater levels of burnout with the indigenous fuels are milling the fuel or agitating the stoker bed conveyor to break up the fuel.

8.6 Future work

The lack of reducing atmosphere testing is a clear gap in the research matrix from the thesis. This was excluded due to safety complications and time constraints. Further work should be carried out to replicate the works in this thesis under reducing conditions. More work is required to increase the size and scope of the OAAFT database to include more international coals and relevant industrial coals. Working more closely with industry will lead to more insightful information about what different melting characteristics in the OAAFT mean. This could give added value to the untapped information that the OAAFT offers.

It was noted during chapter 5 that an alternative way to compare the results would be to model the samples using FactSage, in the same way that Song investigates[163]. Rather than directly comparing the AFT temperatures of each study, comparing the closeness of the results to the thermodynamics package.

A further component study of K_2CO_3 was dropped from the research program due to time constraints. A similar investigation including K_2CO_3 would be an interesting addition as K is known to have a strong impact AFT temperatures. A further investigation into the effect on real coal and biomass ashes of adding the individual components, raw CaO, Fe_2O_3 etc would be interesting. This would support the findings from chapter 5 in AFT temperatures and the OAAFT curves.

Testing the impact of blending on the OAAFT curve would be the most interesting and industrially relevant investigation. It has been stated that predictive methods yield poor replication of blending properties.[97] This suggest that empirical methods are currently the best source of information on blending properties. The OAAFT is the most suitable path forward for predicting blend melt behaviours.

Finally, once enough of a database has been generated, works can begin on creating a method for predicting the OAAFT curve based on ash composition.

References

[1] J. Harris, “The electricity of holborn,” *New Sci.*, vol. 93, no. 1288, p. 88, 1982.

[2] K. Gravett, “The Electric Light at Godalming, 1881,” *Surrey Hist.*, vol. 2, no. 3, 1981.

[3] K. S. Vorres, *Users Handbook for the Argonne Premium Coal Sample Program*. United states dept. of commerce, 1993.

[4] J. G. Speight, “Handbook of Coal Analysis,” vol. 182, no. 0, 2015.

[5] J. G. Speight, *Coal-Fired Power Generation Handbook*. John Wiley & Sons, 2013, 2013.

[6] DECC, “The Carbon Plan: Delivering our low carbon future,” *Energy*, no. December, p. 218, 2011.

[7] A. Demirbaş, “Biomass resource facilities and biomass conversion processing for fuels and chemicals,” *Energy Convers. Manag.*, vol. 42, no. 11, pp. 1357–1378, 2001.

[8] Y. Niu *et al.*, “Study on fusion characteristics of biomass ash,” *Bioresour. Technol.*, vol. 101, no. 23, pp. 9373–9381, 2010.

[9] C. H. Pang, B. Hewakandamby, T. Wu, and E. Lester, “An automated ash fusion test for characterisation of the behaviour of ashes from biomass and coal at elevated temperatures,” *Fuel*, vol. 103, pp. 454–466, 2013.

[10] C. Heng, S. Gaddipatti, G. Tucker, E. Lester, and T. Wu, “Bioresource Technology Relationship between thermal behaviour of lignocellulosic components and properties of biomass,” *Bioresour. Technol.*, vol. 172, pp. 312–320, 2014.

[11] A. C. Fieldner, A. E. Hall, and A. L. Feild, “The fusibility of coal ash and the determination of the softening temperature,” *Bur. Mines*, vol. 129, p. 19, 1918.

[12] S. Australia, “Australian Standard ™ Coal and coke — Analysis and testing Part 17 : Higher rank coal — Moisture-holding capacity (equilibrium moisture),” 2000.

[13] British Standards Institution, “Methods for the Analysis and Testing of Coal and Coke,” *Br. Stand. Inst.*, vol. BS 1016, 1970.

[14] ISO540, “Hard coal and coke. Determinstion of Ash Fusibility,” *Int. Organ. Int. Stand.*, 2013.

[15] A. S. for T. and M. ASTM, “Standard Test Method for Fusibility of Coal and Coke Ash,” *Combustion*, vol. i, no. Reapproved 2010, pp. 1–5, 2011.

[16] S. Gupta, T. F. Wall, R. a. Creelman, and R. Gupta, “Ash fusion temperatures and the transformations of coal ash particles to slag,” *ACS Div. Fuel Chem. Prepr.*, vol. 41, no. 2, pp. 647–649, 1998.

[17] F. Biedermann and I. Obernberger, “Ash-related Problems during Biomass Combustion and Possibilities for a Sustainable Ash Utilisation Friedrich Biedermann,” *Proceeddings Int. Conf. “World Renew. Energy Congr.*, no. x, p. 8, 2005.

[18] R. W. Bryers, “Fireside Slagging, Fouling, and High-Temperature Corrosion of Heat-Transfer Surface Due To Impurities in Steam-Raising Fuels,” *Prog. Energy Combust. Sci.*, vol. 72, 1995.

[19] P. P. Płaza, “The Development of a Slagging and Fouling Predictive Methodology for Large Scale Pulverised Boilers Fired with Coal / Biomass Blends By,” 2013.
[20] E. Raask, *Mineral Impurities in Coal Combustion*. 1985.
[21] G. Couch, *Understanding fouling and slagging during pf combution*. London: IEA Coal Research, 1994.
[22] P. J. Jackson and A. R. Jones, “Fireside fouling experience in large CEGB boilers,” in *1981 conference on fouling and slagging resulting from impurities in combustion gases*, 1981, pp. 1–15.
[23] L. Baxter and G. Richards, “Application of advanced technologies to ash-related problems in boilers,” *Conf. Eff. Coal Qual. Boil. Perform.*, no. January, 1995.
[24] P. G. Bv, J. Koppejan, and P. Group, “The Handbook of Biomass Combustion and Cofiring The Handbook of Biomass Combustion and Co-firing Edited by,” no. January, 2016.
[25] F. J. Frandsen, “Ash Formation , Deposition and Corrosion when Utilizing Straw for Heat and Power Production,” pp. 1–341, 2011.
[26] F. J. Frandsen *et al.*, “Quantification of the release of inorganic elements from biofuels,” *Fuel Process. Technol.*, vol. 88, no. 11–12, pp. 1118–1128, 2007.
[27] F. Frandsen, P. Glarborg, P. A. Jensen, and S. C. van Lith, “Release to the Gas Phase of Inorganic Elements during Wood Combustion. Part 2: Influence of Fuel Composition,” *Energy & Fuels*, vol. 22, no. 6, pp. 1598–1609, 2008.
[28] M. Hupa, “Ash-related issues in fluidized-bed combustion of biomasses: Recent research highlights,” *Energy and Fuels*, vol. 26, no. 1, pp. 4–14, 2012.
[29] J. N. Knudsen, P. a Jensen, and K. Dam-Johansen, “Quantification of the Release of Cl, K and S to the Gas Phase from Combustion of Annual Biomass,” *Prepr. Pap. - Am. Chem. Soc., Div. Fuel Chem.*, vol. 49, no. 1, pp. 93–94, 2004.
[30] S. C. van Lith, V. Alonso-Ramírez, P. a. Jensen, F. J. Frandsen, and P. Glarborg, “Release to the gas phase of inorganic elements during wood combustion. Part 1: Development and evaluation of quantification methods,” *Energy and Fuels*, vol. 20, no. 3, pp. 964–978, 2006.
[31] M. Zevenhoven-Onderwater, J. P. Blomquist, B. J. Skrifvars, R. Backman, and M. Hupa, “Prediction of behaviour of ashes from five different solid fuels in fluidised bed combustion,” *Fuel*, vol. 79, no. 11, pp. 1353–1361, 2000.
[32] M. J. F. Llorente, P. D. Arocas, L. G. Nebot, and J. E. C. García, “The effect of the addition of chemical materials on the sintering of biomass ash,” *Fuel*, vol. 87, no. 12, pp. 2651–2658, 2008.
[33] S. A. Benson, M. L. Jones, and J. N. Harb, “Ash formation and deposition,” in *Fundamentals of of coal combustion for clean and efficient use, Smoot L D*, Amsterdam, The Netherlands: Elsevier science publishers, 1993.
[34] D. W. Van Krevelen, *Coal: Typology, Physics, Chemistry and Constitution*. 1993.

[35] R. Gupta, T. Wall, and L. Baxter, *The impact of mineral impurities in solid fuel combustion*. 621, 525, 247, 23, 1, 2007.
[36] C. H. Pang, "The Characterisation of Biomass and Biomass/Coal Blends," Nottingham, 2012.
[37] L. L. Baxter *et al.*, "The behavior of inorganic material in biomass-fired power boilers: field and laboratory experiences," *Fuel Process. Technol.*, vol. 54, no. 1–3, pp. 47–78, 1998.
[38] L. Wang, Ø. Skreiberg, M. Gronli, G. P. Specht, and M. J. Antal, "Is elevated pressure required to achieve a high fixed-carbon yield of charcoal from biomass? Part 2: The importance of particle size," *Energy and Fuels*, vol. 27, no. 4, pp. 2146–2156, 2013.
[39] P. Thy, B. M. Jenkins, S. Grundvig, R. Shiraki, and C. E. Lesher, "High temperature elemental losses and mineralogical changes in common biomass ashes," *Fuel*, vol. 85, no. 5–6, pp. 783–795, 2006.
[40] D. Boström *et al.*, "Ash transformation chemistry during combustion of biomass," *Energy and Fuels*, vol. 26, no. 1, pp. 85–93, 2012.
[41] P. Thy, B. M. Jenkins, C. E. Lesher, and S. Grundvig, "Compositional constraints on slag formation and potassium volatilization from rice straw blended wood fuel," *Fuel Process. Technol.*, vol. 87, no. 5, pp. 383–408, 2006.
[42] P. Piotrowska, M. Zevenhoven, M. Hupa, J. Giuntoli, and W. De Jong, "Residues from the production of biofuels for transportation: Characterization and ash sintering tendency," *Fuel Process. Technol.*, vol. 105, pp. 37–45, 2013.
[43] M. Theis, C. Mueller, B. J. Skrifvars, M. Hupa, and H. Tran, "Deposition behaviour of model biofuel ash in mixtures with quartz sand. Part 1: Experimental data," *Fuel*, vol. 85, no. 14–15, pp. 1970–1978, 2006.
[44] A. Pettersson, L. E. Åmand, and B. M. Steenari, "Chemical fractionation for the characterisation of fly ashes from co-combustion of biofuels using different methods for alkali reduction," *Fuel*, vol. 88, no. 9, pp. 1758–1772, 2009.
[45] H. Wu, P. Glarborg, F. J. Frandsen, K. Dam-Johansen, and P. A. Jensen, "Dust-firing of straw and additives: Ash chemistry and deposition behavior," *Energy and Fuels*, vol. 25, no. 7, pp. 2862–2873, 2011.
[46] B. M. Steenari and O. Lindqvist, "High-temperature reactions of straw ash and the anti-sintering additives kaolin and dolomite," *Biomass and Bioenergy*, vol. 14, no. 1, pp. 67–76, 1998.
[47] C. Gilbe *et al.*, "Slagging characteristics during residential combustion of biomass pellets," *Energy and Fuels*, vol. 22, no. 5, pp. 3536–3543, 2008.
[48] E. Lindström, M. Sandström, D. Boström, and M. Öhman, "Slagging characteristics during combustion of cereal grains rich in phosphorus," *Energy and Fuels*, vol. 21, no. 2, pp. 710–717, 2007.
[49] B. M. Steenari, A. Lundberg, H. Pettersson, M. Wilewska-Bien, and D. Andersson, "Investigation of ash sintering during combustion of agricultural residues and the effect of additives," *Energy and Fuels*, vol. 23, no. 11, pp. 5655–5662, 2009.
[50] L. Wang, G. Skjevrak, J. E. Hustad, and M. G. Gronli, "Effects of sewage

sludge and marble sludge addition on slag characteristics during wood waste pellets combustion," *Energy and Fuels*, vol. 25, no. 12, pp. 5775–5785, 2011.

[51] G. Couch, *Understanding slagging and fouling during pf combustion*. London: IEA Coal Research, 1994.

[52] J. F. Unsworth, D. J. Barratt, and P. T. Roberts, *Coal quality and combustion performance: an international perspective*. Elsevier, 1991.

[53] R. W. Bryers, "Fireside slagging, fouling, and high-temperature corrosion of heat-transfer surface due to impurities in steam-raising fuels," *Prog. Energy Combust. Sci.*, vol. 22, no. 1, pp. 29–120, Jan. 1996.

[54] G. P. Huffman and F. E. Huggins, "Reactions and Transformations of Coal Mineral Matter at Elevated Temperatures," in *Mineral Matter and Ash in Coal*, American Chemical Society, 1986, pp. 100–113.

[55] L. L. Baxter, G. H. Richards, D. K. Ottesen, and J. N. Harb, "In situ, real-time characterization of coal ash deposits using Fourier transform infrared emission spectroscopy," *Energy & Fuels*, vol. 7, no. 6, pp. 755–760, 1993.

[56] S. V. Loo and J. Koppejam, *Handbook of Biomass Combustion and Co-firing*. 2008.

[57] X. Gaus-Liu, *High-Temperature Chlorine Corrosion during Co-Utilisation of Coal with Biomass or Waste*. Cuvilliar Verlag, 2008.

[58] L. L. Baxter and R. W. DeSollar, "Ash Deposition as a Function of Coal Type, Location in a Boiler, and Boiler Operating Conditions: Predictions Compared to Observations," in *International Conference on Environmental Control of Combustion Processes*, 1991.

[59] A. Zbogar, F. Frandsen, P. A. Jensen, and P. Glarborg, "Shedding of ash deposits," *Prog. Energy Combust. Sci.*, vol. 35, no. 1, pp. 31–56, 2009.

[60] L. Wang, J. E. Hustad, Ø. Skreiberg, G. Skjevrak, and M. Grønli, "A critical review on additives to reduce ash related operation problems in biomass combustion applications," *Energy Procedia*, vol. 20, no. 1876, pp. 20–29, 2012.

[61] F. J. Frandsen, "Utilizing biomass and waste for power production - A decade of contributing to the understanding, interpretation and analysis of deposits and corrosion products," *Fuel*, vol. 84, no. 10, pp. 1277–1294, 2005.

[62] J. Werther, M. Saenger, E. U. Hartge, T. Ogada, and Z. Siagi, "Combustion of agricultural residues," *Prog. Energy Combust. Sci.*, vol. 26, no. 1, pp. 1–27, 2000.

[63] M. Öhman and A. Nordin, "The Role of Kaolin in Prevention of Bed Agglomeration during Fluidized Bed Combustion of Biomass Fuels," *Energy & Fuels*, vol. 14, no. 3, pp. 618–624, 2000.

[64] J. J. Helble, S. Srinivasachar, and A. A. Boni, "Factors influencing the transformation of minerals during pulverised coal combustion.," *Prog. energy combution Sci.*, vol. 16, no. 4, 1990.

[65] F. I. Honea, G. G. Montgomery, and M. L. Jones, "Recent research on ash fouling in combustion of low rank coals.," in *Proceedings of the eleventh biennial lignite symposium - technology and the use of lignite.*,

Springfield, USA: Department of Commerce, National Technical Information Service, 1981.

[66] R. P. Johnson, R. G. Plangeman, and M. D. Rehm, “Coal quality effects on voiler performance - and Eastern utility perspective,” in *Proceedings of the second international conference on the effects of coal quality on power plants*, 1991.

[67] British Petroleum, “BP Statistical Review of World Energy,” no. June, 2013.

[68] K. O. Davidsson, L. E. Åmand, B. M. Steenari, a. L. Elled, D. Eskilsson, and B. Leckner, “Countermeasures against alkali-related problems during combustion of biomass in a circulating fluidized bed boiler,” *Chem. Eng. Sci.*, vol. 63, no. 21, pp. 5314–5329, 2008.

[69] K. O. Davidsson, B. M. Steenari, and D. Eskilsson, “Kaolin addition during biomass combustion in a 35 MW circulating fluidized-bed boiler,” *Energy and Fuels*, vol. 21, no. 4, pp. 1959–1966, 2007.

[70] P. a. Jensen, M. Stenholm, and P. Hald, “Deposition Investigation in Straw-Fired Boilers,” *Energy & Fuels*, vol. 11, no. 5, pp. 1048–1055, 1997.

[71] L. S. Johansson, B. Leckner, C. Tullin, L. E. Åmand, and K. Davidsson, “Properties of particles in the fly ash of a biofuel-fired circulating fluidized bed (CFB) boiler,” *Energy and Fuels*, vol. 22, no. 5, pp. 3005–3015, 2008.

[72] S. Xiong *et al.*, “Slagging characteristics during combustion of corn stovers with and without kaolin and calcite,” *Energy and Fuels*, vol. 22, no. 5, pp. 3465–3470, 2008.

[73] M. Aho and E. Ferrer, “Importance of coal ash composition in protecting the boiler against chlorine deposition during combustion of chlorine-rich biomass,” *Fuel*, vol. 84, no. 2–3, pp. 201–212, 2005.

[74] A. A. Khan, M. Aho, W. de Jong, P. Vainikka, P. J. Jansens, and H. Spliethoff, “Scale-up study on combustibility and emission formation with two biomass fuels (B quality wood and pepper plant residue) under BFB conditions,” *Biomass and Bioenergy*, vol. 32, no. 12, pp. 1311–1321, 2008.

[75] S. C. Stultz and J. B. Kitto, *Steam - Its generation and use*. Ohio, USA: Babcock & Wilcox co, 1992.

[76] a. P. Reifenstein, H. Kahraman, C. D. a Coin, N. J. Calos, G. Miller, and P. Uwins, “Behaviour of selected minerals in an improved ash fusion test: Quartz, potassium feldspar, sodium feldspar, kaolinite, illite, calcite, dolomite, siderite, pyrite and apatite,” *Fuel*, vol. 78, no. 12, pp. 1449–1461, 1999.

[77] H. Kahraman, a. P. Reifenstein, and C. D. a Coin, “Correlation of ash behaviour in power stations using the improved ash fusion test,” *Fuel*, vol. 78, no. 12, pp. 1463–1471, 1999.

[78] H. Kahraman, F. Bos, A. Reifenstein, and C. D. a. Coin, “Application of a new ash fusion test to Theodore coals,” *Fuel*, vol. 77, no. 9–10, pp. 1005–1011, 1998.

[79] T. F. Wall, R. a. Creelman, R. P. Gupta, S. K. Gupta, C. Coin, and a. Lowe, “Coal ash fusion temperatures—New characterization techniques, and

implications for slagging and fouling," *Prog. Energy Combust. Sci.*, vol. 24, no. 4, pp. 345–353, 1998.

[80] H. Gao, Z. Zhang, Y. Lai, J. Li, and Y. Liu, "Structure characterization and electrochemical properties of new lithium salt LiODFD for electrolyte of lithium ion batteries.," *J. Cent. South Univ. Technol. (Engl. Ed.)*, vol. 15, no. 6, pp. 830–834, 2008.

[81] S. K. Gupta, R. P. Gupta, G. W. Bryant, and T. F. Wall, "The effect of potassium on the fusibility of coal ashes with high silica and alumina levels," *Fuel*, vol. 77, no. 11, pp. 1195–1201, 1998.

[82] W. Song *et al.*, "Fusibility and flow properties of coal ash and slag," *Fuel*, vol. 88, no. 2, pp. 297–304, 2009.

[83] S. Wang, X. M. Jiang, X. X. Han, and H. Wang, "Fusion characteristic study on seaweed biomass ash," *Energy and Fuels*, vol. 22, no. 4, pp. 2229–2235, 2008.

[84] W. G. Lloyd, J. T. Riley, M. A. Risen, B. Green, and R. L. Tibbitts, "Estimation of ash fusion temperatures from elemental composition: a strategy for regressor selection," *Amer. Chem. Soc. Divn. Fuel Chem. Prepr. 36, 325.*, 1989.

[85] C. Yin, Z. Luo, M. Ni, and K. Cen, "Predicting coal ash fusion temperature with a back-propagation neural network model," *Fuel*, vol. 77, no. 15, pp. 1777–1782, 1998.

[86] G. Özbayočlu and M. Evren Özbayočlu, "A new approach for the prediction of ash fusion temperatures: A case study using Turkish lignites," *Fuel*, vol. 85, no. 4, pp. 545–552, 2006.

[87] Y. P. Liu, M. G. Wu, and J. X. Qian, "Predicting coal ash fusion temperature based on its chemical composition using ACO-BP neural network," *Thermochim. Acta*, vol. 454, no. 1, pp. 64–68, 2007.

[88] E. Jak, "Prediction of coal ash fusion temperatures with the F*A*C*T thermodynamic computer package," *Fuel*, vol. 81, no. 13, pp. 1655–1668, 2002.

[89] and H. J. Arvelakis S, Folkedahl B, Dam-Johansen K, "Studying the Melting Behavior of Coal , Biomass , and Coal / Biomass Ash Using Viscosity and Heated Stage XRD Data," *Energy & Fuels*, vol. 20, no. 11, pp. 1329–1340, 2006.

[90] C. W. Bale *et al.*, "FactSage thermochemical software and databases — recent developments," *CALPHAD Comput. Coupling Phase Diagrams\penalty \z@ \protect \futurelet \@let@token Thermochem.*, vol. 33, no. 2, pp. 295–311, 2009.

[91] C. W. Bale *et al.*, "Reprint of: FactSage thermochemical software and databases, 2010–2016," *Calphad Comput. Coupling Phase Diagrams Thermochem.*, vol. 55, pp. 1–19, 2016.

[92] M. V Nel, C. A. Strydom, H. H. Schobert, J. P. Beukes, and J. R. Bunt, "Reducing atmosphere ash fusion temperatures of a mixture of coal-associated minerals — The effect of inorganic additives and ashing temperature," *Fuel Process. Technol.*, vol. 124, pp. 78–86, 2014.

[93] M. V Nel *et al.*, "Ash melting behavior and slag infiltration into alumina refractory simulating co-gasification of coal and biomass," *Fuel*, vol. 139,

no. 2, pp. 457–465, 2015.
[94] M. Reinmöller, M. Klinger, M. Schreiner, and H. Gutte, “Relationship between ash fusion temperatures of ashes from hard coal, brown coal, and biomass and mineral phases under different atmospheres: A combined FactSage™ computational and network theoretical approach,” *Fuel*, vol. 151, pp. 118–123, 2015.
[95] M. Reinmöller, M. Schreiner, S. Guhl, M. Neuroth, and B. Meyer, “Formation and transformation of mineral phases in various fuels studied by different ashing methods,” *Fuel*, vol. 202, pp. 641–649, 2017.
[96] T. Sasi, M. Mighani, E. Örs, R. Tawani, and M. Gräbner, “Prediction of ash fusion behavior from coal ash composition for entrained-flow gasification,” *Fuel Process. Technol.*, vol. 176, no. March, pp. 64–75, 2018.
[97] P. Xing, L. I. Darvell, J. M. Jones, L. Ma, M. Pourkashanian, and A. Williams, “Experimental and theoretical methods for evaluating ash properties of pine and El Cerrejon coal used in co-firing,” *Fuel*, vol. 183, pp. 39–54, 2016.
[98] T. Rizvi, P. Xing, M. Pourkashanian, L. I. Darvell, J. M. Jones, and W. Nimmo, “Prediction of biomass ash fusion behaviour by the use of detailed characterisation methods coupled with thermodynamic analysis,” *Fuel*, vol. 141, pp. 275–284, 2015.
[99] L. Yan, R. P. Gupta, and T. F. Wall, “The implication of mineral coalescence behaviour on ash formation and ash deposition during pulverised coal combustion,” *Fuel*, vol. 80, no. 9, pp. 1333–1340, 2001.
[100] D. Zhang FTSE, *Ultra super critical coal power plants*, First edit. Woodhead publishing, 2013.
[101] L. Baxter and R. W. Desollar, “A mechanistic description of ash deposition during pulverised coal combustion: predictions compared to with observations,” *Fuel*, vol. 72, no. 10, pp. 1411–1418, 1992.
[102] L. Yan, R. P. Gupta, and T. F. Wall, “A mathematical model of ash formation during pulverized coal combustion,” *Fuel*, vol. 81, no. 3, pp. 337–344, 2002.
[103] ASME, “Methods for the Analysis and Testing of Coal Ash and Coke Ash, AS1038.15,” 1987.
[104] G. C. Ellis, “The thermomechanical, electrical conductance and chemical characteristics of coal ash deposits,” 1989.
[105] C. Coin, A. P. Reifenstein, and H. Kahraman, “Improved ash fusion test,” in *Proceedings of the Engineering Foundation Conference on Application of Advanced Technology to Ash- Related Problems in Boilers*, 1996, pp. 187–200.
[106] Preciser Scientific, “Auto Ash Fusion System,” 2009.
[107] Quote from: Leco, “AF700 Ash fusion,” 2015.
[108] Carbolite, “Coal Ash Fusibility Furnaces,” 2013.
[109] MCRlab, “Operation Manual for ash fusion tester ASH-10,” 2012.
[110] K. Han, K. Qiu, Z. Huang, and Z. Wang, “Ash fusibility based on modes of occurrence and high-7 temperature behaviors of mineral matter in coals,” *Energies*, vol. 8, pp. 1–19, 2015.

[111] I. W. Cumming, W. I. Joyce, and J. H. Kyle, “Advanced Techniques for the Assessment of Slagging and Fouling Propensity in Pulverized Coal Fired Boiler Plant,” *J. Inst. Energy*, pp. 169–175, 1985.
[112] D. H. H. Quon, S. S. B. Wang, and T. T. Chen, “Viscosity Measurements of Slags From Western Canadian Coals,” 1984.
[113] S. a. Lolja, H. Haxhi, R. Dhimitri, S. Drushku, and A. Malja, “Correlation between ash fusion temperatures and chemical composition in Albanian coal ashes,” *Fuel*, vol. 81, no. 17, pp. 2257–2261, 2002.
[114] G. Dunnu, J. Maier, and G. Scheffknecht, “Ash fusibility and compositional data of solid recovered fuels,” *Fuel*, vol. 89, no. 7, pp. 1534–1540, 2010.
[115] J. W. Regan, “Impact of coal characteristics on boiler design,” *Coal Technol.*, vol. 3, 1982.
[116] J. C. Van Dyk, L. L. Baxter, J. H. P. Van Heerden, and R. L. J. Coetzer, “Chemical fractionation tests on South African coal sources to obtain species-specific information on ash fusion temperatures (AFT),” *Fuel*, vol. 84, no. 14–15, pp. 1768–1777, 2005.
[117] M. Seggiani, “Empirical correlations of the ash fusion temperatures and temperature of critical viscosity for coal and biomass ashes,” *Fuel*, vol. 78, no. 9, pp. 1121–1125, 1999.
[118] J. C. Van Dyk, S. a. Benson, M. L. Laumb, and B. Waanders, “Coal and coal ash characteristics to understand mineral transformations and slag formation,” *Fuel*, vol. 88, no. 6, pp. 1057–1063, 2009.
[119] T. F. Wall, S. K. Gupta, R. P. Gupta, R. H. Sanders, R. a. Creelman, and G. W. Bryant, “False deformation temperatures for ash fusibility associated with the conditions for ash preparation,” *Fuel*, vol. 78, no. 9, pp. 1057–1063, 1999.
[120] T. Yan, L. Kong, J. Bai, Z. Bai, and W. Li, “Thermomechanical analysis of coal ash fusion behavior,” *Chem. Eng. Sci.*, vol. 147, pp. 74–82, 2016.
[121] J. H. Kim, G. B. Kim, and C. H. Jeon, “Prediction of correlation between ash fusion temperature of ASTM and Thermo-Mechanical Analysis,” *Appl. Therm. Eng.*, vol. 125, pp. 1291–1299, 2017.
[122] J. J. C. Vijay, A. Lawrence, and G. Arthanareeswaran, “Analytical tool for analysing slagging characteristic of high ash coals in utility boilers,” *Int. J. Mech. Eng. Technol.*, vol. 8, no. 3, pp. 185–196, 2017.
[123] U. Kleinhans, C. Wieland, F. J. Frandsen, and H. Spliethoff, “Ash formation and deposition in coal and biomass fired combustion systems: Progress and challenges in the field of ash particle sticking and rebound behavior,” *Prog. Energy Combust. Sci.*, vol. 68, pp. 65–168, 2018.
[124] J. Xie, J. Weidong Fan, and I. Zhang, “Study of Gas Temperature Characteristics at the Bottom of the Platen Heaters of Boiler Employing Shenhua Bituminous Coal Based on Two-Level Air Staging Combustion System,” *ASME Proc. | Fuels, Combust. Mater. Handl.*, vol. Volume 1, 2017.
[125] A. S. for T. and M. ASTM, “D3174-12 Standard Test Method for Ash in the Analysis Sample of Coal and Coke from Coal,” pp. 1–6, 2011.
[126] R. Xiao, X. Chen, F. Wang, and G. Yu, “The physicochemical properties of

different biomass ashes at different ashing temperature," *Renew. Energy*, vol. 36, no. 1, pp. 244–249, 2011.
[127] X. Fang and L. Jia, "Experimental study on ash fusion characteristics of biomass," *Bioresour. Technol.*, vol. 104, pp. 769–774, 2012.
[128] Q. H. Li, Y. G. Zhang, a. H. Meng, L. Li, and G. X. Li, "Study on ash fusion temperature using original and simulated biomass ashes," *Fuel Process. Technol.*, vol. 107, pp. 107–112, 2012.
[129] H. W. Huang, Q. Wang, H. J. Tang, M. Zhu, and Y. Zhang, "Characterisation of external acoustic excitation on diffusion flames using digital colour image processing," *Fuel*, vol. 94, pp. 102–109, 2012.
[130] Y. Yan, G. Lu, and M. Colechin, "Monitoring and characterisation of pulverised coal flames using digital imaging techniques," *Fuel*, vol. 81, no. 5, pp. 647–656, 2002.
[131] H. W. Huang, J. Yang, Q. Wang, and Y. Zhang, "Variation of hydrocarbon compositions and ignition locations on the radiative flame initiation characteristics through multi-dimensional DFCD incorporated image analysis," *Fuel*, vol. 103, pp. 334–346, 2013.
[132] G. O'Brien, B. Jenkins, J. Esterle, and H. Beath, "Coal characterisation by automated coal petrography," *Fuel*, vol. 82, no. 9, pp. 1067–1073, 2003.
[133] E. Lester, "The characterisation of coals for combustion," 1994.
[134] J. A. Minkin, C. L. Thompson, and E. C. T. CHAO, "Application of Automated Image Analysis to Coal Petrography," *Int. J. Coal Geol.*, vol. 2, 1982.
[135] J. C. van Dyk, F. B. Waanders, S. A. Benson, M. L. Laumb, and K. Hack, "Viscosity predictions of the slag composition of gasified coal, utilizing FactSage equilibrium modelling," *Fuel*, vol. 88, no. 1, pp. 67–74, 2009.
[136] P. Coal and S. Analysis, "Standard Method of Preparing Coal Samples for Analysis 1," *Measurement*, vol. 05, no. 4, pp. 133–143, 1988.
[137] O. Williams *et al.*, "Influence of mill type on densified biomass comminution," *Appl. Energy*, vol. 182, pp. 219–231, 2016.
[138] ISO 18122, "Solid biofuels - Determination of ash content," *18122*, no. JANUARY, pp. 1–6, 2015.
[139] J. Canny, "A Computational Approach to Edge Detection," *IEEE Trans. Pattern Anal. Mach. Intell.*, vol. Vol. PAMI-, no. 6, pp. 679–698, 1986.
[140] N. Otsu, "A threshold selection method from grey-level histograms," *IEEE Trans. Syst. Man Cybern.*, vol. 9, no. 1, pp. 62–66, 1979.
[141] A. Seif and E. Al., "A hardware architecture of Prewitt edge detection," *Sustain. Util. Dev. Eng. Technol.*, vol. IEEE Confe, 2010.
[142] D. Bradley and G. Roth, "Adaptive Thresholding using the Integral Image," *J. Graph. Tools*, vol. 12, no. 2, pp. 13–21, 2007.
[143] E. Lester, M. Gong, and A. Thompson, "A method for source apportionment in biomass/coal blends using thermogravimetric analysis," *J. Anal. Appl. Pyrolysis*, vol. 80, no. 1, pp. 111–117, 2007.
[144] C. Dixon, M. R. Strong, and S. M. Zhang, "Transient plane source technique for measuring thermal properties of silicone materials used in electronic assemblies," *Int. J. Microcircuits Electron. Packag.*, vol. 23, no. 4, pp. 494–500, 2000.

[145] J. Lee, T. S. Yun, and S. U. Choi, “The effect of particle size on thermal conduction in granular mixtures,” *Materials (Basel).*, vol. 8, no. 7, pp. 3975–3991, 2015.
[146] R. Gupta, “Advanced coal characterization: A review,” *Energy and Fuels*, vol. 21, no. 2, pp. 451–460, 2007.
[147] W. Z. Cheng X, Han K, Huang Z, “Ash Fusibility Based on Modes of Occurrence and High-Temperature Behaviors of Mineral Matter in Coals,” *Energy Resour. Technol.*, 2016.
[148] U. Gonzales-Barron and F. Butler, “A comparison of seven thresholding techniques with the k-means clustering algorithm for measurement of bread-crumb features by digital image analysis,” *J. Food Eng.*, vol. 74, no. 2, pp. 268–278, 2006.
[149] K. S. Fu and J. K. Mui, “A survey on image segmentation,” *Pattern Recognit.*, vol. 13, no. 1, pp. 3–16, 1981.
[150] N. R. PAL, “A Review on Image Segmentation Techniques.” 1993.
[151] M. Sonka, V. Hlavac, and R. Boyle, “Image Processing, Analysis, and Machine Vision,” *Thomson Learn.*, p. 812, 2008.
[152] I. T. Young, J. J. Gerbrands, and L. J. van Vliet, “Fundamentals of Image Processing (v.2.3),” pp. 1–112, 2007.
[153] G. T. Shrivakshan and C. Chandrasekar, “A Comparison of various Edge Detection Techniques used in Image Processing,” *Int. J. Comput. Sci. Issues*, vol. 9, no. 5, pp. 269–276, 2012.
[154] W. Gao, L. Yang, X. Zhang, and H. Liu, “An improved Sobel edge detection,” *Proc. - 2010 3rd IEEE Int. Conf. Comput. Sci. Inf. Technol. ICCSIT 2010*, vol. 5, pp. 67–71, 2010.
[155] C. Ma, W. Gao, L. Yang, and Z. Liu, “An improved Sobel algorithm based on median filter,” in *2nd International Conference on Mechanical and Electronics Engineering*, 2010.
[156] Y. Bao-liang, J. Feng-ming, and L. Ming-dong, “The Analysis and Implementation of Edge Detection Algorithms in Image Processing Based on Matlab,” no. Icectt, pp. 387–391, 2015.
[157] R. Maini and H. Aggarwal, “Study and comparison of various image edge detection techniques,” *Int. J. Image Process.*, vol. 3, no. 1, pp. 1–11, 2009.
[158] E. J. Liu, K. V. Cashman, and A. C. Rust, “Optimising shape analysis to quantify volcanic ash morphology,” *GeoResJ*, vol. 8, pp. 14–30, 2015.
[159] D. M. Diez, “OpenIntro Statistics: Second Edition,” vol. 1, p. 426, 2012.
[160] N. Otsu, “A Threshold Selection Method from Gray-Level Histograms,” *IEEE Trans. Syst. Man, Cybern.*, vol. 9, 1979.
[161] T. F. Chan and L. A. Vese, “Active contours without edges,” *IEEE Trans. Image Process.*, 2001.
[162] W. J. Song, L. H. Tang, X. D. Zhu, Y. Q. Wu, Z. B. Zhu, and S. Koyama, “Prediction of Chinese coal ash fusion temperatures in Ar and H2 atmospheres,” *Energy and Fuels*, vol. 23, no. 4, pp. 1990–1997, 2009.
[163] W. J. Song, L. H. Tang, X. D. Zhu, Y. Q. Wu, Z. B. Zhu, and S. Koyama, “Effect of coal ash composition on ash fusion temperatures,” *Energy and Fuels*, vol. 24, no. 1, pp. 182–189, 2010.

[164] B. Liu, Q. He, Z. Jiang, R. Xu, and B. Hu, “Relationship between coal ash composition and ash fusion temperatures,” *Fuel*, vol. 105, pp. 293–300, 2013.
[165] T. Yan, J. Bai, L. Kong, Z. Bai, W. Li, and J. Xu, “Effect of SiO2/Al2O3on fusion behavior of coal ash at high temperature,” *Fuel*, vol. 193, pp. 275–283, 2017.
[166] BS, *Methods for analysis and testing of coal and coke. Analysis of coal ash and coke ash*. 2017.
[167] M. Seggiani and G. Pannocchia, “Prediction of coal ash thermal properties using partial least-squares regression,” *Ind. Eng. Chem. Res.*, vol. 42, no. 20, pp. 4919–4926, 2003.
[168] S. V. Vassilev, D. Baxter, L. K. Andersen, and C. G. Vassileva, “An overview of the chemical composition of biomass,” *Fuel*, vol. 89, no. 5, pp. 913–933, 2010.
[169] G. W. Bryant *et al.*, “The fusibility of blended coal ash,” *Energy Fuel*, no. 14, pp. 316–325, 2000.
[170] E. Lindstroem, M. Oehman, R. Backman, and D. Bostroem, “Influence of sand contamination on slag formation during combustion of wood derived fuels.,” *Energy Fuel*, vol. 22, p. 2216–20., 2008.
[171] J. C. Van Dyk, “Understanding the influence of acidic components (Si , Al , and Ti) on ash flow temperature of South African coal sources,” vol. 19, pp. 280–286, 2006.
[172] A. A. Bhuiyan, A. S. Blicblau, A. K. M. S. Islam, and J. Naser, “A review on thermo-chemical characteristics of coal/biomass co-firing in industrial furnace,” *J. Energy Inst.*, vol. 91, no. 1, pp. 1–18, 2018.
[173] T. Aspects, “Technical Aspects and Energy Effects of Waste Heat Recovery from District Heating Boiler Slag,” *Energies*, vol. 11, no. 4, p. 796, 2018.

Appendix

Shape definitions

The eccentricity, F/A, is the ratio of the distance between the foci of the ellipse, F, and its major axis length, A, see Figure 0-1.

- The foci, F = square root((major radius, A)^2 – (minor radius, B)^2).
- The value is between zero and 1.
- An ellipse whose eccentricity is 0 is a circle, while an ellipse whose eccentricity is 1 is a line segment.

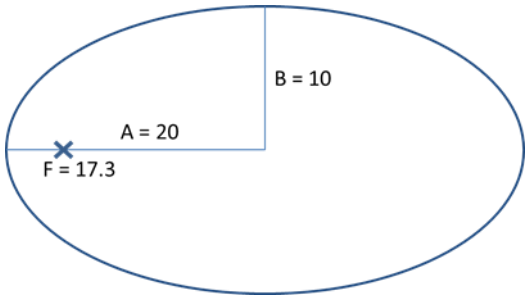


Figure 0-1: Demonstration of Where the Foci Of An Ellipse Is

Pseudo Pellet Literature Samples Database

Table 0-1: Major oxide compositions of a range of coals and their ash fusion temperatures

	Ash Samples	Content of oxides						AFT temperatures (°C)	
		SiO2	Al2O3	S/A	Fe2O3	CaO	MgO	IDT	FT
Chinese coals	Shanxi Datong	56.6	25.4	2.2	6.5	3.7	1.4	1239	1352
	Heilongjiang Jixi	64.1	27.2	2.4	2.9	0.9	0.5	>1450	>1450
	Shandong Xinwen	52.9	31.9	1.7	4.9	2.7	1.2	>1450	>1450
	Anhui Huainan	50.8	36	1.4	6.1	1.9	0.6	>1450	>1450
	Neimenggu lijiata	41.7	23	1.8	7.1	13.1	2.1	1141	1177
	Liaoning Fuxin	52.7	33.5	1.6	5.9	1.8	1.1	>1450	>1450
	Shanxi Huating	39.7	18.2	2.2	17.1	17.5	0.9	1160	1300
	Shandong Zaozhuang	34.9	16.5	2.1	8	37.1	2	1180	1230
	Shandong yanzhou	23	34	0.7	22.1	17.3	1.7	1155	1225
	Shanxi gujiao	24.2	27.1	0.9	25.2	18	0.7	1220	1280
Imported bituminous	Sofia Bulgaria	32	11.3	2.8	10.6	27.7	2.8	1100	1225
	Montana US	44.5	20.3	2.2	1.6	15.7	3.5	1125	1205
	Miike Japan	47.7	20.8	2.3	10.2	9.7	1.5	1165	1320

	New Hope Australia	62.5	30	2.1	2.6	0.9	0.4	>1450	>1450
	Mafty Russia	60.6	21.9	2.8	5.1	5	1.9	1170	1360
	Coal Mountain Canada	39.9	27.3	1.5	2.5	22.1	3.2	1200	1450
	Donbass Ukraine	53.8	20.4	2.6	15.1	2.8	1.3	1150	1370
	RUS	55.6	24.5	2.3	7.15	3.15	0.88	1290	1460
	Columbian	61.8	21.1	2.9	6.6	2.2	2.1	1250	1410
	SA	43.7	34	1.3	3	7.2	2.2	1390	1500
	US high S	43.5	22.6	1.9	21.2	4.03	0.84	1070	1300
	IND	25.6	7.5	3.4	11.2	14.3	4.8	1080	1140
	Polish	46.8	21.8	2.1	9.6	5.8	3.5	1182	1350
UK Bituminous coals	low Si	31.4	17.6	1.8	23.2	12.5	0.6	1040	1110
	Low Si	36.8	23.9	1.5	11.2	12	2.5	1240	1320
	Low Si	34.3	23.8	1.4	26.3	3.3	0.7	1060	1220
	High Si	47.8	26.8	1.8	16.6	1.3	1.1	0	0
	High Si	47	25.5	1.8	14.1	6.4	3	0	0
Brown Coals	Greek	31.07	12.85	2.4	7.69	38.92	4.45	1238	1280
	German	1.3	1.5	0.9	18.6	35.8	16.3	1310	1350
	Polish	55	24.1	2.3	9.3	3.4	1.5	1250	1480

Top 20 clustering function code

```
function [ ClustPeakDists, GreyClusterRange ] = TopTwentyClustering( I )
%UNTITLED2 Summary of this function goes here
%   Detailed explanation goes here
H = imhist(I);

%% Maximum points
   % max 1
      [y1,x1] = max(H);
      H1     = H < y1;
      H1     = H.*H1;
   % max 2
      [y2,x2] = max(H1);
      H2     = H1 < y2;
      H2     = H1.*H2;
   % max 3
      [y3,x3] = max(H2);
      H3     = H2 < y3;
      H3     = H2.*H3;
   % max 4
      [y4,x4] = max(H3);
      H4     = H3 < y4;
      H4     = H3(H4);
   % max 5
      [y5,x5] = max(H4);
      H5     = H4 < y5;
      H5     = H4(H5);
   % max 6
      [y6,x6] = max(H5);
      H6     = H5 < y6;
      H6     = H5(H6);
   % max 7
      [y7,x7] = max(H6);
      H7     = H6 < y7;
      H7     = H6(H7);
   % max 8
      [y8,x8] = max(H7);
      H8     = H7 < y8;
      H8     = H7(H8);
   % max 9
      [y9,x9] = max(H8);
      H9     = H8 < y9;
      H9     = H8(H9);
   % max 10
      [y10,x10]   = max(H9);
      H10        = H9 < y10;
```

```
    H10       = H9(H10);
  % max 11
    [y11,x11]  = max(H10);
    H11       = H10 < y11;
    H11       = H10(H11);
  % max 12
    [y12,x12]  = max(H11);
    H12       = H11 < y12;
    H12       = H11(H12);
  % max 13
    [y13,x13]  = max(H12);
    H13       = H12 < y13;
    H13       = H12(H13);
  % max 14
    [y14,x14]  = max(H13);
    H14       = H13 < y14;
    H14       = H13(H14);
  % max 15
    [y15,x15]  = max(H14);
    H15       = H14 < y15;
    H15       = H14(H15);
  % max 16
    [y16,x16]  = max(H15);
    H16       = H15 < y16;
    H16       = H15(H16);
  % max 17
    [y17,x17]  = max(H16);
    H17       = H16 < y17;
    H17       = H16(H17);
  % max 18
    [y18,x18]  = max(H17);
    H18       = H17 < y18;
    H18       = H17(H18);
  % max 19
    [y19,x19]  = max(H18);
    H19       = H18 < y19;
    H19       = H18(H19);
  % max 20
    [y20,x20]  = max(H19);

%% Creating the arrays for the table
    Greyscale  = [x1;x2;x3;x4;x5;x6;x7;x8;x9;x10;x11;x12;x13;x14;x15;x16;x17;x18;x19;x20];
    Count      = [y1;y2;y3;y4;y5;y6;y7;y8;y9;y10;y11;y12;y13;y14;y15;y16;y17;y18;y19;y20];
  % combine the array
    PeakPoints  = [Greyscale(:,1), Count(:,1)];

%% Clustering the peaks
```

```
%% 5 clusters

        % Clustering function
           % turn annoying warnings off
           warning('off');

          %gm        = fitgmdist(Data     ,# of clusters,                 ,  );
           gm        = fitgmdist(PeakPoints,5          ,'RegularizationValue',0.1);
           [idx,D,E]   = cluster(gm,PeakPoints);

           % turn warnings back on
           warning('on');

        % Cluster points
           cluster1    = (idx == 1); % |1| for cluster 1 membership
           cluster2    = (idx == 2); % |2| for cluster 2 membership
           cluster3    = (idx == 3); % |3| for cluster 3 membership
           cluster4    = (idx == 4); % |4| for cluster 4 membership
           cluster5    = (idx == 5); % |5| for cluster 5 membership

        % Obtaining the averages
           cluster1a = [PeakPoints(cluster1,1),PeakPoints(cluster1,2)];
           cluster1b = [mean(cluster1a(:,1)),mean(cluster1a(:,2))];
           cluster2a = [PeakPoints(cluster2,1),PeakPoints(cluster2,2)];
           cluster2b = [mean(cluster2a(:,1)),mean(cluster2a(:,2))];
           cluster3a = [PeakPoints(cluster3,1),PeakPoints(cluster3,2)];
           cluster3b = [mean(cluster3a(:,1)),mean(cluster3a(:,2))];
           cluster4a = [PeakPoints(cluster4,1),PeakPoints(cluster4,2)];
           cluster4b = [mean(cluster4a(:,1)),mean(cluster4a(:,2))];
           cluster5a = [PeakPoints(cluster5,1),PeakPoints(cluster5,2)];
           cluster5b = [mean(cluster5a(:,1)),mean(cluster5a(:,2))];

           Clusters  = cat(1, cluster1b, cluster2b, cluster3b, cluster4b, cluster5b);     %
Creating a clustered array
           Clusters( ~any(Clusters,2), : ) = [];                          % Removing any empties

%% manipuating the clustered data
   % finding the distance between the min and max peeks
   Max              = max(Clusters(:,1));
   Min              = min(Clusters(:,1));
   GreyClusterRange    = Max - Min;

   % finding the distance between the two greatest count peaks
      %%% Peak 1
      [Peak1X,Peak1Y]     = max(Clusters(:,2));
      Peak1Grey          = Clusters(Peak1Y,1);
```

```
%%% Peak 2
   % Adjusting the array to remove the first maximum
   Clusters2          = Clusters < Peak1X;
   Clusters2          = Clusters.*Clusters2;

% Finding the 2nd max
[Peak2X,Peak2Y]     = max(Clusters2(:,2));
Peak2Grey          = Clusters(Peak2Y,1);
ClustPeakDists      = sqrt((Peak1Grey - Peak2Grey)^2);

% removing the cluster if it is very close to another 1

if ClustPeakDists < 10
   % Adjusting the array to remove the first maximum
   Clusters2          = Clusters < Peak2X;
   Clusters2          = Clusters.*Clusters2;
   % Finding the 2nd max
   [Peak2X,Peak2Y]     = max(Clusters2(:,2));
   Peak2Grey          = Clusters(Peak2Y,1);
   ClustPeakDists      = sqrt((Peak1Grey - Peak2Grey)^2);
end
   if ClustPeakDists < 10
      % Adjusting the array to remove the first maximum
      Clusters2          = Clusters < Peak2X;
      Clusters2          = Clusters.*Clusters2;
      % Finding the 2nd max
      [Peak2X,Peak2Y]     = max(Clusters2(:,2));
      Peak2Grey          = Clusters(Peak2Y,1);
      ClustPeakDists      = sqrt((Peak1Grey - Peak2Grey)^2);
   end
      if ClustPeakDists < 10
         % Adjusting the array to remove the first maximum
         Clusters2          = Clusters < Peak2X;
         Clusters2          = Clusters.*Clusters2;
         % Finding the 2nd max
         [Peak2X,Peak2Y]     = max(Clusters2(:,2));
         Peak2Grey          = Clusters(Peak2Y,1);
         ClustPeakDists      = sqrt((Peak1Grey - Peak2Grey)^2);
      end

end
```

“All we have to decide is what to do with the time that is given us.”

– J.R.R. Tolkien, The Fellowship of the Ring